WWTP Process Tank Modelling

The Integration of Advanced Hydrodynamicand Microbiological Models

Laursen, Jesper

Publication date:
2007

Document Version
Publisher's PDF, also known as Version of record

Preface

The present thesis, *WWTP Process Tank Modelling - The Integration of Advanced Hydrodynamic and Microbiological Models*, has been prepared in connection with a Ph.D. study carried out in the period September 2002 to October 2005 at the Hydraulic and Coastal Engineering Section at the Department of Civil Engineering, Aalborg University, Denmark. The Ph.D. study was financially supported by the Department of Civil Engineering.

I would like to thank my supervisor Associate Professor, M.Sc. Michael R. Rasmussen. His interest, enthusiasm and encouragement through the study is greatly appreciated.

Also I would like to thank the laboratory staff at the Hydraulic and Coastal Engineering Section for their always kind attitude and helpfulness during the experimental work in the laboratory and the field. Special thanks is given to M.Sc. Palle Meinert for helping out with the laser profiling.

I would like to thank Krüger A/S, the staff at Hals Central Wastewater Treatment Plant and the staff at Frederikshavn Central Wastewater Treatment Plant for delivering material for the case studies.

I would also like to thank Dr. Ewen McLean and the rest of the staff at Virginia Tech Aquaculture Center at Blackburg, Virginia for a fruitful and pleasant stay at the research center.

Finally, I would like to thank my girlfriend Birgitte, my family and my friends for their moral support and understanding throughout the process of finishing this thesis.

Salten, November, 2006

Jesper Laursen

Summary in English

The present thesis considers numerical modelling of activated sludge tanks on municipal wastewater treatment plants. Focus is aimed at integrated modelling where the detailed microbiological model the Activated Sludge Model 3 (ASM3) is combined with a detailed hydrodynamic model based on a numerical solution of the Navier-Stokes equations in a multiphase scheme.

After a general introduction to the activated sludge tank as a system, the activated sludge tank model is gradually setup in separate stages. The individual sub-processes that are often occurring in activated sludge tanks are initially investigated individually, with the purpose of obtaining a better understanding before the final integrated model is setup. In the sub-process investigations focus is addressed especially at aeration by bottom mounted diffusers and mechanical mixing of the activated sludge suspension via slowly rotating hydrofoil shaped propellers. These two sub-processes deliver the main part of the supplied energy to the activated sludge tank, and for this reason they are important for the mixing conditions in the tank. For other important processes occurring in the activated sludge tank, existing models and measurements conducted by other investigators have given basis to the model. This applies to especially the ASM3, the sedimentation model and the rheology model. The main task has for these models has mainly been to perform a suitable integration into the existing commercial Navier-Stokes solver.

After completion of the sub-process models, the last part of the thesis, where the integrated process tank model is tested on three examples of activated sludge systems, is initiated. The three case studies are introduced with an increasing degree of model complexity. All three cases are take basis in Danish municipal wastewater treatment plants.

The first case study involves the modelling of an activated sludge tank undergoing a special controlling strategy with the intention minimising the sludge loading on the subsequent secondary settlers during storm events. The applied model is a two-phase model, where the sedimentation of sludge flocs is modelled through an altering of the inter-phase friction forces occurring between sludge flocs and wastewater. The purpose of the simulations is to optimise the flow conditions during the sedimentation phase of the process tank. This is done through a numerical testing of different inlet configurations that are all constructed with a decrease in inlet impulses and the thereby derived rotation flow in the tank in mind.

Case two concerns the modelling of a hydrodynamically and biologically complex OCO process tank. Since the OCO-tank is constructed with the promotion of parallel aerobic and anoxic zones in mind, its special construction poses strict demands to the hydrodynamic model. In case study three the model is extended to a three-phase model where also the injection of air bubbles during the aeration process is modelled. The aeration of sludge is controlled through a simple expression for the reoxygenation of the wastewater phase as a function of the local volume fraction of air and the concentration of soluble oxygen. A simple model for the bulk consumption of oxygen is linked to the reoxygenation expression in order to model measured oxygen concentrations in the suspension.

In the final case study, the ASM3 is integrated in the hydrodynamic model and the model is calibrated and validated against both online and manual measurements performed in the tank. The model calibration is performed by systematically changing the standard values of the model.

Finally an assessment of the models strengths and weaknesses are conducted and proposals for future extensions to the model are given.

Summary in Danish

Nærværende afhandling omhandler modellering af aktiv-slam tanke på kommunale renseanlæg. Der er lagt vægt på en integreret model, hvor den detaljerede mikrobiologiske model Activated Sludge Model 3 (ASM3) kombineres med en detaljeret hydrodynamisk model baseret på numerisk løsning af Navier-Stokes ligninger i et flerfase skema.

Efter en generel introduktion til aktiv-slam tanken som system, bygges aktiv-slam tanks modellen gradvist op i etaper. De specifikke delprocesser som ofte er forekommende i aktiv-slam tanke undersøges først hver for sig, med henblik på at sikre en forståelse af disse inden den samlede model afprøves. I denne undersøgelse af delprocesser er der lagt vægt på især beluftning vha. bundmonterede diffusorer samt den mekaniske omrøring af aktiv-slam suspensionen via langsomt roterende miksere. Disse to leverer hovedparten af energien til aktiv-slam tanken, og er derfor af stor betydning for opblandingsforholdene i tanken. For andre vigtige processer i aktiv-slam tanken er der taget udgangspunkt i eksisterende modeller og måledata udviklet af andre forfattere. Her tænkes især på aktiv-slam, sedimentations- og rheologimodellen. Hovedopgaven har for disse modeller bestået i at udføre en hensigtsmæssig integration af disse processer i den eksisterende kommercielle strømningsløser.

Efter modelleringen af delprocesserne indledes afhandlingen sidste fase, hvor den integrerede proces tank model afprøves på tre eksempler på aktiv-slam tank systemer. De tre *cases* introduceres med stigende grad af kompleksitet. Alle tre cases tager udgangspunkt i Danske kommunale renseanlæg.

Den første case omhandler modelleringen af en aktiv-slam tank som undergår en speciel styringsstrategi som har til hensigt at minimere slambelastningen på efterklaringstankene under kraftige regnvejrshændelser. Den opstillede model er en to-fase model, hvor sedimentationen af slam modelleres gennem en styring af interfase friktionskræfterne mellem slampartikler og spildevand. Formålet med beregningerne er at optimere strømningsforholdene under sedimentation i aktiv-slam tanken. Dette er gjort vha. numerisk afprøvning af forskellige indløbskonfigurationer der alle har til formål at nedsætte impulsen i indløbene og den deraf genererede roterende strømning i tanken.

Case nummer to omhandler modelleringen af en hydrodynamisk og biologisk kompleks OCO-proces tank. OCO-tanken sætter strenge krav til den hydrodynamiske model idet tanken med sin specielle opbygning er konstrueret med henblik på at fremme områder med både aerobe og anoxiske forhold på samme tid. Modellen udvides i denne sammenhæng til en tre-fase model hvor også indblæsningen af luftbobler under beluftningen modelleres. Beluftningen af slammet styres gennem et simpelt udtryk for geniltningen af vandet som funktion af den lokale volumen fraktion af luft og koncentrationen af ilt i vandet. En simpel model for det samlede forbrug af ilt er tilknyttet geniltningsudtrykket med henblik på at modellere målte iltkoncentrationer i suspensionen.

I den sidste case integreres Activated Sludge Model 3 i den hydrodynamiske model, og modellen kalibreres og valideres op mod online målinger og flow og iltmålinger målt manuelt i tanken. Modelkalibreringen udføres ved systematisk at ændre standardværdierne i modellen.

Slutteligt omhandler afhandlingen en vurdering af modellens styrker og svagheder, samt forslag til fremtidig udvidelse af modellen.

Contents

CHAPTER 1
Introduction

The main purpose of domestic wastewater treatment plants (WWTP) is to reduce the impact of pollutants of larger cities on the ambient nature and environment. In the WWTP, pollutants are typically removed by either turning soluble compounds into gas or settling out particulate matter incorporated into biomass. The main part of the turn over of nutrients and organic matter is in many advanced WWTP performed in biological removal units, in high advanced plants often of the activated sludge type. In Denmark, all cities have implemented wastewater treatment with biological removal units. In Denmark, the introduction of the Environmental Plan in 1987 (Miljøministeriet, 1987) resulted in extensive upgrading of both the capacity and the technology of the existing plants. Today the capacity of the existing wastewater treatment plants are in general sufficient. By process optimization it has been possible for many plants to gradually increase their capacity without actually making physical extensions.

With the focus on capacity increments on the basis of process optimization in mind, the need for thorough insight in the functioning of the different operational units of the WWTP is present. The large expansion of the WWTP, starting at the introduction of the Environmetal Plan in 1987 (Miljøministeriet, 1987), has resulted in a diversity of different process tank types. The activated sludge system has been the preferred system responsible for the biological treatment on many Danish plants. The activated sludge process tanks occurring at these plants have however often been designed by different consultant companies with a resulting diversity in tank design. Often the design has been based upon former experiences and thereby derived *rules of thumbs*. By the introduction of the Activated Sludge Models (ASM), attention has been given towards detailed modelling of the biological processes occurring at activated sludge systems. The high level of insight in the biological processes has until now not been followed up by the same level of insight in the hydrodynamics occurring in the process tanks. In order to to fully use the power of the detailed biological models, the distribution of important parameters like soluble and particulate compounds, the fraction of biomass and the level of available oxygen needs to be known in the tank. Since the hydrodynamics of the tank are governing the transport of these parameters, a linkage between the hydrodynamics and the biology is necessary in order to obtain complete insight in the functioning of an existing process tank configuration. With the integration of hydrodynamic and biological modelling, an effective tool towards future wastewater treatment optimization can be developed. The present work is focused towards the integration of detailed hydrodynamic and biological modelling of process tanks.

1.1 WWTP terminology

The overall structure of a typical municipal wastewater treatment plant is outlined on figure 1.1:

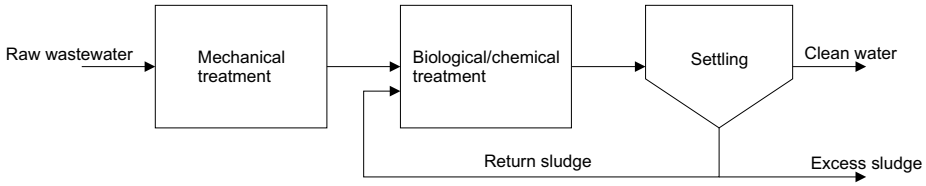

Figure 1.1 Outline of the structure of a typical activated sludge wastewater treatment plant.

Three main treatment steps may appear in a WWTP:

- Mechanical treatment
- Biological treatment
- Chemical treatment

Included in the mechanical treatment are mechanical separation by grates, sand and grease traps and separation by settling. Mainly particulate organic matter is removed during the mechanical treatment steps. The biological treatment includes the removal of organic matter and nutrients, whereas chemical treatment most frequently involves removal of phosphorous by precipitation.

The work in the present thesis is mainly focused on the physical and biological treatment on the WWTP. In most advanced wastewater treatment plants, the microbiological treatment can roughly be sub divided into two different treatment methods:

- Biofilter systems
- Activated sludge systems

In the biofilter system, the bacteria are attached to a biofilm on a biofilter media. When the polluted water gets in contact with the biofilm, the pollutants are removed by the bacteria. The biofilter media can be either fixed or in suspension in the system. Biofilters are to a large extent used in the industrial sector. When the Environmental Plan was introduced in Denmark in 1987, new restrictive demands on the removal of Nitrogen, resulted in the need for implementation of nitrification and denitrification on the plants (Winther *et al.*, 1998). Since it proved hard to integrate the biofilters into the nitrogen removing plants, a drastic reduction of the number of biofilters was seen in domestic wastewater removal in Denmark.

The activated sludge system is worldwide presently the most widespread method in modern WWTPs' (Tchobanoglous and Burton, 2003). In the activated sludge system a bacterial biomass suspension, the *activated sludge*, is responsible for the removal of pollutants. Organic carbon is mainly removed by heterotrophic bacteria under addition of oxygen to the suspension. Often the aeration of the sludge also triggers autotrophic nitrifying bacteria, who turn ammonia (NH_4^+) into nitrate (NO_3^-). In WWTPs' with N-removal, denitrifying bacteria removes organic matter

under anoxic conditions with the use of NO_3^- as electron acceptor. During the denitrifying process NO_3^- is turned into atmospheric nitrogen, N_2. The biological treatment can during appropriate conditions be extended to biological removal of phosphorous. During anaerobic conditions bacteria of the type *Acinetobacter* assimilate storage of readily degradable organic matter under a simultaneous release of PO_4^{3-} (Henze *et al.*, 1987). During aerobic conditions they will however take up the PO_4^{3-} again and incorporate it into the biomass while they undergo growth. Beside the above described processes, many other processes like e.g. hydrolysis of hardly biodegradable organic matter and decay of biomass also take place.

In Denmark, and many developed countries biological removal of organic matter and nitrogen is basic technology, whereas phosphorous can be both removed by chemical precipitation or biological phosphorous removal.

With the purpose of optimization, activated sludge systems have been configured in many different ways. Different rules and regulations in different countries has had a major impact on the way WWTP have been constructed. Below, the main types of process tank configurations for activated sludge systems with biological removal of organic matter and nitrogen are roughly outlined (Winther *et al.*, 1998):

- Recirculating systems (Badenpho, 1970), (Figure 1.2 A)
- Intermittent systems (COWI, 1980), (Figure 1.2 B)
- OCO systems (Krüger, 1988), (Figure 1.2 C)
- LPD systems (COWI, 1991), (Figure 1.2 D)
- Carousel systems e(Netherlands, 1975), (Figure 1.2 E)
- SBR systems (USA, 1975), (Figure 1.2 F)
- Bio-denitro systems (Krüger, 1974), (Figure 1.2 G)

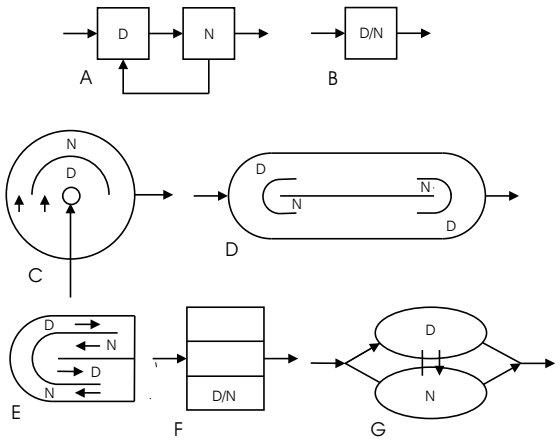

Figure 1.2 Principles of process tank configurations for wastewater treatment system with biological Nitrogen removal (Winther *et al.*, 1998). N: Nitrification, D: Denitrification.

A recirculated system, is typically a system where the sludge is recirculated from the nitrification tank to the denitrification tank (Figure 1.2A), whereas in the alternating system, the operations of the tanks are shifted between nitrification and denitrification (Figure 1.2B). The OCO system is a special case of an alternating system, where the process tanks are subdivided into an inner and an outer alternating zone, dependent of the operation of the aeration and mixing equipment (Figure 1.2C). The OCO system will in the present work be subject to further studies in terms of a case study with an OCO tank. The LPD system consists of oblong process tanks divided into an inner nitrifying part and an outer denitrifying part (Figure 1.2D). In the carousel system, the sludge alternately passes nitrification and denitrification zones on its way through the tank (Figure 1.2E). In a SBR (Sequencing batch reactor) system, the process tanks undergo all steps from aeration to settling in one sequential cycle (Figure 1.2F). The Bio-denitro system is a special case of an alternating, recirculated system undergoing a predefined cycle, where the individual tank shifts between nitrification and denitrification (Figure 1.2G).

From Figure 1.2 it is obvious that the operational principle varies significantly from system to system. Where some activated sludge systems are built upon assumptions of fully mixed reactors, others are built with basis of a system where the process tanks are highly inhomogeneous with respect to hydrodynamics and biological environment. In systems where fully mixed conditions are applicable, one could argue that detailed hydrodynamic modelling would be redundant in relation to a sufficient system description (Figure 1.3, left). In more complicated systems, like the OCO and the LPD tank systems, a complete understanding of the system performance seems impossible without a proper hydrodynamic modelling (Figure 1.3, right). As long as coupling between hydrodynamic and biological models is absent, design and optimization of such systems will to a large extent rely on experience and *rules of thumbs*. This is due to the fact that in complicated process tank systems, pollutant removal rates will be highly dependent on the density of the biomass and the available amount of electron acceptors, which again will be a function of the local hydrodynamic conditions. This linkage of hydrodynamic and biological processes is essential to a proper understanding of the process tanks performance. The importance of integrated modelling is substantiated in other branches of environmental engineering, where disciplines like groundwater modelling, modelling of estuaries and marine environments have well established integrated models.

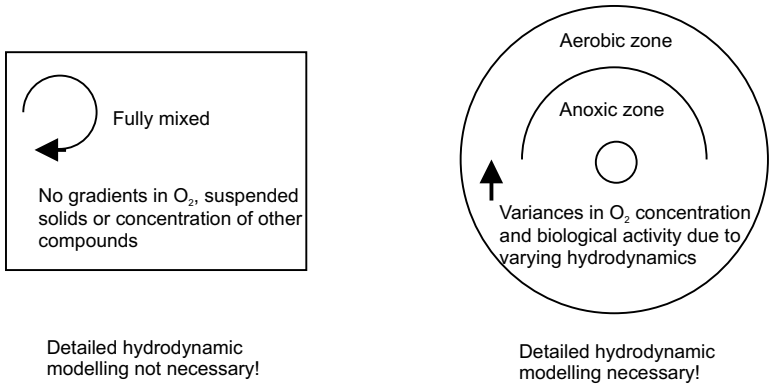

Figure 1.3 Modelling of a fully mixed versus modelling of a hydrodynamically complex process tank

Often physical unit operations are optimized independently of biological process optimization, e.g. a manufacturer of mechanical mixers is mainly interested in the energy efficiency of the device or the amount of thrust or turbulence the unit will deliver. The impact on the biological processes in the WWTP is not so important from the impeller manufacturer's isolated point of view, whereas this may be important from an operator's point of view. The linkage between physical plant setup and plant performance will only be available through an integration of hydrodynamics, biology and chemistry.

1.2 WWTP models

In general three different approaches can be undertaken when constructing or extending a wastewater treatment plant.

1. Constructing it full-scale on behalf of earlier experience with similar designs
2. Creating prior pilot-scale models before building the actual plant
3. Use numerical investigations to optimize plant design

When creating the WWTP in full-scale right away, there is either no room for mistakes with respect to the expect behaviour of the system, or otherwise large safety margins with respect to plant capacity has to be applied. If possible a pilot-scale experiment can be performed prior to the building in full-scale. Then changes of the setup and controlling of the process tanks or other devices can be tested without expensive consequences. An alternative to physical testing is numerical investigations. During numerical investigations design changes can be evaluated before actual building the plant, and this way design faults may be identified before constructing the plant.

Until recently the majority of simulation case studies have been performed on basis of mass balances and completely mixed reactor compartments (Gujer, 2006). A mass balance model of an ideal mixed reactor could be written as:

Mass balance of wastewater:

$$Q_{in} = Q_{out} + \frac{dV}{dt} \tag{1.1}$$

Mass balance substances:

$$Q_{in} \cdot C_{in} = Q_{out} \cdot C_{out} + \frac{dV\overline{C}}{dt} \tag{1.2}$$

Where Q is the flow through the reactor $[m^3 \cdot s^{-1}]$, V is the reactor volume $[m^3]$, C is the substance concentration $[kg \cdot m^{-3}]$ and $\overline{C}$ is the mean concentration $[kg \cdot m^{-3}]$:

$$\overline{C} = \frac{1}{V} \int_V C dV \tag{1.3}$$

In the last term on the right hand side of equations 1.1 and 1.2 refers to the accumulation within the tank. The accumulation term can include the removal of substances by e.g. biological or chemical processes.

The mass balance model presented above does however not take the local flow conditions or concentration variations inside the tank into account. As such the mass balance model can be considered as a *black box model approach*, which restricts the amount of information that can be withdrawn from such a model.

To the author's knowledge, no existing commercial wastewater treatment plant models include a detailed hydrodynamic description of the flow in process tanks. The mixing properties of process tanks are often modelled with simple models such as linear reservoir models, as tank-in-series, where each tank is treated as a computational node. Otherwise the hydrodynamics of the process tanks are often neglected (Coen *et al.*, 1998). Several commercial WWTP models can be grouped into a group of models where simplifying assumptions regarding the hydrodynamics of the tanks have been taken:

- AQUASIM (http://www.aquasim.eawag.ch, 2005), (Reichert, 1994)
- BioWin (http://www.envirosim.com, 2005)
- EFOR (http://www.dhisoftware.com/efor, 2005)
- GPS-X (http://www.hydromantis.com, 2005)
- SIMBA (http://www.ifak system.com, 2005)
- STOAT (http://www.wrc plc.co.uk/software, 2005)
- WEST (http://www.hemmis.com, 2005)

The above mentioned models are only an extract of the available models on the market. Common for the above listed models, is that they all represent some kind of a compartment model, where each tank or process are modelled through compartments or blocks with certain characteristics. One type of compartment could be a fully mixed reactor, and another a plug flow reactor. In this way important assumptions about the hydrodynamic conditions, needs to hold, in order to justify the use of the particular model.

Despite of the few detailed hydrodynamic WWTP models, a considerable amount of experimental work concerning the sub processes present in process tanks have been performed. Examples of such sub processes are:

- The aeration process
- The mixing process (impellers or other agitators)
- Micro biological models
- The sedimentation process

In this work, the term WWTP model will be used about the total of the hydrodynamic, biological and chemical models necessary to describe a WWTP, and especially a process tank. The WWTP model can be split up into several sub models:

- A hydrodynamic model
- A biological model
- A chemical model

The hydrodynamic model describes the flow of water and substances in the system. A complete hydrodynamic model describes the hydrodynamics of the mean flow, the turbulence and the settling, the aeration and the mixing processes in the tank. Thus, the hydrodynamic model of a process tank is very complex. The biological model describes the biological processes performed by micro organisms in the sludge. Included in the biological model are expressions describing the turnover of organic material and nutrients in the sludge. The chemical models in WWTP models are mainly concerned with the precipitation of phosphorous. Beside the mentioned hydrodynamic, biological and chemical models, also physical models for e.g. the aeration of the sludge are needed in a complete WWTP model.

If a hierarchical structure was to be applied to the three above-listed model types, the hydrodynamic model would be located on the top. The explanation for this is to be found in the nature of the hydrodynamic multiphase model, where parameters like the fraction of air bubbles and the concentration of suspended solids can be directly extracted from the model. Thus, important parameters on which the results of the biological and chemical models are dependent of, is available as a result of the hydrodynamic model. The inter-dependency is not necessarily present the other way around; the variation in ie. the concentration of ammonium, do not directly influence the outcome of the hydrodynamic model. The influence of the hydrodynamic model on the outcome of the biological model, is one important argument towards why the integration of detailed hydrodynamic and biological models is important for an accurate modelling of a process tank.

Despite the above argued necessity of detailed hydrodynamic modelling, the main part of the existing WWTP models are as mentioned in the beginning of the present section focused on a correct modelling of the biological processes, whereas only a few models include a detailed hydrodynamic description of the flow of substances in e.g. the process tanks. Often, if a hydrodynamic description is included, this part of the model is based upon rough assumptions or laboratory or field experiments. The model developed in the present work aims at closing this gap between the current available WWTP models and the need for more detailed process descriptions.

Below a brief presentation of detailed hydrodynamic models (CFD-models) and biological models will be given.

1.2.1 CFD models

(Versteeg and Malalasekera, 1995) defines Computational Fluid Dynamics (CFD) as: *The analysis of systems involving fluid flow, heat transfer and associated phenomena such as chemical reactions by means of computer-based simulation*. The term CFD model will here be defined as a numerical model, solving the hydrodynamics governed by the Navier-stokes equations. The application of a detailed CFD model for the simulation of WWTP's has several advantages:

- The ability to model full scale experiments without subsequent interpretation of results from pilot scale experiments

- The ability to model physical and biological processes in detail
- The model can give details of e.g. the flow field in places where measurements can be hard to obtain
- The possibility to test alternative tank configurations in a fast and relatively cheap way
- The possibility to identify design faults
- The ability to retrofit existing systems for obtaining increased performance

One of the main advantages of CFD modelling is the possibility to test a model of a full scale system without actually building it. Hence, modelling can save unnecessary time and money on design faults identified by the model. Also existing systems can be retrofitted in the model before taking any physical action. The application of CFD-models may take the wastewater treatment models to a higher level where e.g. the agitation by impellers or the aeration processes are modelled in detail. Since the CFD-model can deliver results with a very high resolution, a comparable resolution by measurements would often be impossible to obtain or at least very expensive. This should in general strengthen our knowledge of the overall functioning of the process tanks. In theory the resolution of the results should be unlimited, if the spatial size of the computational mesh is infinitely small. CFD modelling is however not a tool without limitations. The following drawbacks may be associated with CFD-modelling:

- The computational effort can be very demanding
- Calibration is often necessary
- Trained personnel is necessary
- Commercial CFD solvers can be expensive

If no reduction in the resolution of the CFD-model is performed, the CFD-modelling can be very demanding with respect to computational times and necessary computer hardware. Hence, often models for describing e.g. the turbulence must be applied in order to produce results within a reasonable time and resource frame. Because of the complexity of many flow problems and the models describing e.g. biological phenomena, one should be very careful when using the model results. Even strictly physical models, involving only hydrodynamic modelling of fluid flow often need some sort of calibration. One classic example of this is the application of turbulence models, where models like e.g. the $k-\epsilon$ model involves the introduction of calibration constants determined through model fitting to experimental work (Launder and Spalding, 1974), (Jones and Launder, 1972). In general, CFD models should as far as possible be accompanied with model calibration, and if necessary also a proper validation. Since CFD models are complex, only experienced specialists that know the *inside* of the model will be capable of creating trustworthy results. Moreover the commercial CFD codes can be relatively expensive. One stand-alone solver license can easily cost tens of thousands of Euros annually. The need for highly educated personnel and the expensive software in general means that until now only large companies or universities have been using CFD models in their work.

If one can overcome the drawbacks of CFD modelling, CFD-modelling does however appear to be a very promising tool for gaining better insight into the dynamics of WTTP process tanks.

1.2.2 Biological modelling

The activated sludge models (ASM) have been widely used in WWTP modelling. The ASM concept has been developed by "The International Association on Water Pollution Research and Control" (IAWPRC), now: "The International Association on Water Quality" (IAWQ) (Henze *et al.*, 1987). The purpose of the modelling concept has been analysis of domestic wastewater treatment processes. The ASM series consists of three models (ASM1, ASM2 and ASM3). The ASM models are based on deterministic descriptions of the biological turnover of organic matter and nutrients.

The ASM concept has been extensively tested for description of biological processes. Numerous experiments for testing the ASM concepts applicability for Activated Sludge systems in process tanks with both alternating and recirculation operation have been performed. (Gernaey *et al.*, 2004) gives an extensive overview of the application of the ASM models to wastewater treatment plant cases.

ASM1

ASM1 is developed with the aim of a correct modelling of heterotrophic turnover of organic matter and removal of nitrogen through nitrification- and denitrification processes (Henze *et al.*, 1987). ASM1 has in several investigations been found suitable for modelling the removal of organic matter and nitrogen. (Nowak *et al.*, 1999) do however point out that calibration of the model parameters has to be performed for the given location in order to gain acceptable results. This is especially necessary for WWTP with atypical sludge age or surplus sludge production. The main part of the experiments do however show reasonable results with respect to the prediction of outlet concentrations, active nitrifying biomass population and process kinetics (Loosdrecht and Henze, 1999), (Stamou *et al.*, 1999), (Nowak *et al.*, 1999) and (Anderson *et al.*, 2000). (Ladiges *et al.*, 1999) used ASM1 to make optimization calculations on a planned extension of the Hamburg WTTP. The commercial SIMBA model (http://www.ifak system.com, 2005) was applied, and the numerical work indicated that an extension of the existing plant with a total cost of 15 million Euro would ensure sufficient effluent quality. When compared to the originally estimated total cost of 50 million Euro, the cost of the numerical modelling seemed justified.

The ASM1 has due to its *universal appeal and practical verification* (Copp, 2002) been chosen as biological model in the *COST Simulation Benchmark*, a benchmark WWTP model developed to evaluate different activated sludge WWTP controlling strategies via simulations.

ASM2

ASM2 was made in order to account for the modelling of biological phosphorous turnover. ASM2 and later the enhanced ASM2d also introduced a more comprehensive description of the biomass, where the biomass is characterised by an inner structure, making modelling of the biomass' ability to store nutrients possible (Henze *et al.*, 1995), (Henze *et al.*, 1999).

The ASM2 have been tested for a series of WWTP. There is a general acceptance of the model concepts applicability, if the model is calibrated before use on local plants. The model contain approximately 70 model constants (Cinar *et al.*, 1998), describing stoichiometric and kinetic relations etc., troubling a proper calibration of the model. (Gujer, 2006) states that in order to predict the steady-state of a Bio-P activated sludge plant 131 independent parameters

has to be determined. Determining all these parameters is a serious task that demands a research group of experienced modelling experts and measuring know-how. Some investigations do on the other hand suggest that most of the proposed model constants in ASM2 are appropriate enough to give reasonable modelling results (Henze *et al.*, 1995). Other investigations have shown that reasonable results can be obtained by the altering of only 3 and 6 of ASM2' model constants (Brdjanovic *et al.*, 2000), (Cinar *et al.*, 1998). (Isaacs *et al.*, 1995) applied the ASM2 to model biological Phosphorous removal in a pilot-scale alternating BIODENIPHO activated sludge nutrient removal process. By including an expression to account for the denitrification of phosphate accumulating organisms (PAO), anoxic uptake of Phosphorous could be calculated with the ASM2. (Zhao *et al.*, 1999) applied the model to simulate the turnover of Nitrogen and Phosphorous in a sequencing batch reactor (SBR). When properly calibrated, the model was better suited for a detailed description of the dynamics of the SBR compared to an applied neural network model. For online process control their hybrid between the neural network model and a simplified process model was preferred over the ASM2.

ASM3

In the newest edition of the activated sludge models, ASM3, some of the deficiencies of ASM1 and ASM2 have been corrected (Gujer *et al.*, 1999). Since ASM3 is built on basis of the two former ASM models, several of the above mentioned characteristics of the ASM1 and ASM2 models are also valid for ASM3. ASM3 is made upon the same biological processes as ASM1, thus making the model applicable for the prediction of oxygen demand, sludge production and the efficiency of the nitrification and denitrification processes (Gujer *et al.*, 1999). Compared to ASM1, ASM3 do however include a description of the storage of compounds in the biomass. Compared to ASM2, ASM3 does not include a model for the biological turnover of phosphorous.

(Koch *et al.*, 2000) calibrated ASM3 to batch reactor experiments and validated the model with a pilot plant experiment. The model was also applied to four full-scale WWTP in Switzerland. The commercial AQUASIM model (http://www.aquasim.eawag.ch, 2005), (Reichert, 1994) was applied, and the sludge production and the nitrification and denitrification capacities were modelled with good agreement with the experimental findings.

1.2.3 CFD modelling of WWTP

During the last decade, experience with CFD models for modelling the processes in WWTP has started to grow. The main part of the CFD analysis' performed on WWTP have however been concerning the separation of water and sludge phases in conventional sedimentation tanks or other more sophisticated separators (Krebs, 1991), (Dahl, 1993), (Krebs *et al.*, 1996), (Rasmussen, 1997), (Brouckaert and Buckley, 1999), (Tyack and Fenner, 1999), (de Clercq, 2003).

Some CFD modelling investigations of WWTP process tanks have however been conducted:

In order to improve the conditions at the inlet of a WWTP lagoon in Australia, the hydrodynamics of the lagoon was investigated through CFD modelling by (Wood *et al.*, 1995). The hydrodynamics was modelled according to an assumption of laminar flow, and consequently the result of the investigation was considered to be subject to uncertainties.

(Janex *et al.*, 1998) used a 3D, turbulent single phase model to optimize a UV wastewater disinfection process. Since the efficiency of the UV disinfection process is highly dependent

on a homogeneous flow field, fluid short-circuiting will hinder an optimal working disinfection. With the use of CFD modelling, the authors indicated that an introduction of internal side baffles would result in a more effective heat transfer, indicating that also the UV-radiation would be more effectively distributed in the wastewater.

(Do-Quang *et al.*, 1999) made some optimisation investigations for the oxidation efficiency at different hydrodynamic conditions in an activated sludge process tank. The model was a two-dimensional two-phase model, and the results indicated that the oxygen transfer would be 30 to 40% better if the aeration tank was equipped with horizontal agitators.

(Karama *et al.*, 1999) used a single phase 3D CFD model for the prediction of dead zones in an activated sludge process tank.

(Salter *et al.*, 2000) used a three-dimensional isothermal CFD-model to investigate the hydrodynamics of a facultative lagoon in Thailand. The lagoon was suggested to be suffering from significant hydraulic short-circuiting, possible due to stratification, which was also substantiated by the numerical model. After further numerical modelling, an introduction and location of internal baffles was suggested in order to avoid further short-circuiting.

(Shilton, 2000) applied a three dimensional CFD-model to a wastewater treatment pond in New Zealand. The collected experimental data was limited, but the model indicated that the addition of an internal baffle would reduce short-circuiting and increase the removal efficiency of the pond. First order kinetics was coupled with the hydrodynamic model, and it was estimated that the outlet concentration of faecal coliform bacteria would be halved in case of the addition of the internal baffle.

(Cockx *et al.*, 2001) used a three-dimensional two-phase CFD model to simulate the gas-liquid mass-transfer of oxygen in a laboratory scale airlift reactor and a full scale oxidation ditch. They used the laboratory scale experiments to validate their model, and extended the validated model to the full scale oxidation ditch. The investigation of the full scale model, showed that gas-liquid mass-transfer was only little sensitive to the horizontal liquid flow rate, probably due to radial confinement of the gas jets. The model showed that three-dimensional hydrodynamic modelling are essential when modelling reactors with complex geometry.

(Vega *et al.*, 2003) applied a two-dimensional depth-integrated model to a full scale anaerobic pond located in southwest Colombia. The model was calibrated against measured data, and the authors claimed good correlation between modelled and measured residence time distribution. After calibration, the model was applied to alternative geometric configurations of the pond, in order to numerically indicate an optimal configuration of the location of the in- and outlet and internal walls in the pond.

On Aalborg University two M. Sc. Thesis' regarding CFD modelling of Hals Central WWTP in Northern Jutland, Denmark have been conducted (Thomsen, 2000), (Kunnerup *et al.*, 2002). The hydrodynamics, mixing properties, oxygen and suspended solids concentrations of one of the process tanks at the WWTP was modelled with differently configured single phase models.

In 2004 process tanks at Lundtofte and Aalborg East, Denmark were modelled during ATS (Aeration Tank Settling) operation (Jensen, 2004) (Jensen *et al.*, 2006). A two-phase model describing the interaction between the water and sludge phases was applied. The investigations indicated that a displacement of the inlet was necessary in order to avoid short-circuiting at the Lundtofte process tank.

Also an activated sludge process tank at Bjergmarken, Denmark was modelled during ATS operation (Laursen and Rasmussen, 2004). Again the modelling was initiated by a desire to opti-

mize the existing ATS operation of the system. The numerical analysis at Bjergmarken indicated that a combination of a larger inlet size and a slight displacement of the inlet would result in less inertia in the system, whereby the settling of the sludge during ATS would be improved.

(Glover *et al.*, 2006) integrated a multiphase CFD model with the ASM1 for the modelling of a SBR-oxidation ditch, a small perfectly mixed batch reactor and a full-scale oblong oxidation ditch. The SBR-oxidation ditch model agreed well with measured concentrations of oxygen, COD, ammonia and nitrate-nitrogen. The modelling of the perfectly mixed batch reactor showed that the simulated oxygen concentration profiles were highly dependent on the choice of mass transfer coefficient, $k_L a$, and also that due to a sufficiently high oxygen concentration, the reactor could be considered as fully mixed with respect to nutrients and COD. The modelling of the full-scale oxidation ditch revealed heterogeneities of oxygen and nitrate-nitrogen. The heterogeneities originated from insufficient aeration of the reactor.

By the application of multiphase CFD code and the ASM2d, (Oda *et al.*, 2006) optimised two denitrification tanks to achieve the maximum denitrification rate. The investigation showed that during a 90 minute cycle, the aeration should only be operational for 5 minutes. Also optimal values of aeration flow rate, aerator spacing was estimated.

1.2.4 Status on WWTP modelling

As indicated in the section above, much work has been done on both modelling the hydrodynamic and biological processes separately, whereas the amount of work on integration of the two disciplines have been sparse. Much attendance has been given towards solution of special cases where e.g. problems with short-circuiting have been solved by hydrodynamic modelling. Also extensive efforts have been given towards modelling of in-tank and effluent concentrations of pollutants on behalf of a comprehensive biological modelling. Only recently integration of detailed hydrodynamic and biological modelling has been initiated. The results from these investigations with integrated models are promising in perspective of gaining further insight into the interaction between hydrodynamic and biological processes. As the integrated models are further developed, possible optimisation advantages from achieving an optimum interplay between the physical and biological processes are likely to occur.

On the need for tedious model calibration, with resulting quite different model parameters to describe the treatment at comparable domestic wastewater at different sites, (Gujer, 2006) states: *The fact that we have accepted that site-specific calibration of biokinetic models is typically required if reliable forecasts are to be made, indicates that there is a lot of uncertainty in model parameters as well as system description (frequently the consequences of unknown transport processes are taken care of by adjusting biokinetic parameters).*

1.3 Delimitations

The physical, biological and chemical processes in a WWTP are occurring at different time scales (Table 1.1), and dependent on the time scale of modelling, some processes will be indispensable whereas others will have little influence on the results over the modelling period.

The characteristic times shown in 1.1 should be compared to the length of a couple of operational cycles of a process tank. Modelling of two operation cycles (a couple of hours) would seem reasonable with the relatively high computational demands from a 3 dimensional

Table 1.1 Typical characteristic times for parameters and processes in WWTP process tanks.

Process	*Characteristic time*
Microbial growth	15-20 days
Temperature variations	days
Flow variations	minutes - hours
Hydraulic retention time	hours - days
Sedimentation of sludge (1m lowering)	hours
One operation cycle	minutes - hours
Agitation by mixers/impellers	minutes - hours
Aeration of sludge	minutes
Turnover of oxygen after aeration	minutes
Turnover of organic matter and nutrients	minutes
Turbulence	seconds

multiphase CFD-model. Thus, since microbial growth has a characteristic time of approximately 15-20 days, it seems reasonable to assume that microbial growth would have little effect on the change of suspended solids concentration over a period of only a couple of operation cycles. Consequently, it would not be necessary to model the microbial growth in a process tank model, when viewing only over a couple of operation cycles. Due to the relatively long characteristic time for temperature variations, the same arguments as for microbial growth can be applied, and thus it can be assumed that temperature variations will have little effect on process performance over a period of the scale of operation cycles. On the other hand, the processes with characteristic times of hours and down can be expected to vary considerable during a time-scale on the order of a couple of process cycles. Hence, flow variations, hydraulic retention times, sedimentation of sludge, the structure of the process cycles in the tank, mixing by impellers, the aeration of sludge, the turnover of oxygen, organic matter and nutrients and finally turbulence, should all be accounted for when putting up a model for describing the dynamics of a process tank.

A 3D hydrodynamic numerical 3-phase model of a WWTP process tank consisting of one million elements, coupled with e.g. the ASM3 model, would involve the solution of at least 75 million discretized differential equations at every time step. If running the model over e.g. two process cycles of one hour each at a time step of 2 seconds, a total of 270 billion equations would have to be solved. For steady-state hydrodynamic problems, it could however be possible to solve the hydrodynamic model to steady-state, and then afterwards solve the transport equations for the biological components on behalf of the steady-state hydrodynamic solution, in order to save computational time. Because of the dynamic nature of a process tank, transient modelling of process tanks often have to be carried out over long real-time periods, making simulations on a very fine scale almost impossible on normal sized personal computers. Even one million elements in a process tank model would have to be regarded as a rather coarse grid with respect to modelling processes on a micro-scale level. Hence a model applicable for practical use in WWTP process tanks is doomed to be a coarse-grid model. This delimitation also applies to this project, where only macro-scale processes will be described through a coarse-grid model.

1.4 Objective of the thesis

As described above, research still has to be done regarding a complete hydrodynamic and biological modelling of process tanks at wastewater treatment plants. Because of this need of research in the future, five organizations, AIChE (American Institution of Chemical Engineers), the American Chemical Society, Chemical Manufacturers Association, Council for Chemical Research and Synthetic Organic Chemical Manufacturers Association, have published the report *Technology Vision 2020: The Chemical Industry*, where the need for a better understanding of gas-liquid-solid flows have been pointed out (Sundaresan, 2000). By integrating numerical multiphase models with advanced biological process modelling, the present work on WWTP activated-sludge process tanks are intended to close some of these gaps.

So far, the majority of commercial WWTP models contains a detailed description of the biological and chemical processes occurring at a wastewater treatment plant, whereas the solution of the hydrodynamic in the different removal steps of the plant is modelled through rough assumptions of the mean flow properties.

Compared to the many existing commercial compartment models of WWTP, where each process tank typically is described through simplifying assumptions of the hydrodynamics, the application of a detailed hydrodynamic model, can in some way be regarded as a simpler way towards describing the process tank. To the authors opinion it is easier to once for all setup a physical correct description of the hydrodynamics, rather than performing calibrations, compensating a non-physical model.

A complete process tank model taking all sub processes occurring in the tank into account, would be a very time demanding and complicated task for a single Ph.D. project. Several of the processes involved in a process tank model have been extensively investigated by other researchers. The present work aims at combining these sub models into a whole process tank model. Towards the completion of a process tank model, several of the important sub processes will be investigated in a manner useful to the cause. The process tank model is as widely as possible constructed with equally detailed process descriptions. There is no sense in modelling one sub process very detailed, if the result from such a detailed sub model disappears in a crude model for the remainder of the tank.

One important feature of a WWTP process tank model is the ability to predict the variation in concentrations of e.g. suspended solids, nutrients, biomass fractions or oxygen. A good description of mixing properties and thereby the concentration gradients is crucial for the modelling of these variations.

In order to model the mixing properties of the flow, the processes that contribute to both mixing and separation of substances needs to be accounted for in the model. Several of these processes are studied in detail in the present work:

- The aeration of the sludge, and the thereby induced mixing
- The mixing by impellers
- The sedimentation of the sludge particles

1.5 Layout of thesis

The present thesis is divided into six chapters. In chapter two, an overview of the processes occurring in a typical activated sludge process tank will be given. The purpose of the chapter is to introduce the system of the process tank to the reader. Chapter three regards the mathematical description of the processes occurring in the process tank. Special attention will be given to the governing equations for multifluid flow and the modelling of the biological processes in the tank. The outcome of the chapter is to give an overview of the framework of the applied numerical model. Since the standard framework of the hydrodynamic CFD-model do not account for some of the special sub processes occurring in the process tank, chapter four involves investigations clarifying how to include these sub processes in the model. Consequently, several important sub processes; the physical impact of bottom mounted air diffusers, the mixing by propellers and the sedimentation and rheology of the activated sludge, and finally the biology of the activated sludge are included in chapter four. The total of the model framework is tested in three case studies of WWTP process tanks in chapter five. The three cases are discussed in increasing complexity, starting with two-phase hydrodynamic modelling of a process tank undergoing a special controlling strategy applied for storm-weather conditions. The following case involves three-phase hydrodynamic and simple biological modelling of a process tank with very varying conditions in both space and time. Lastly a case combining both three phase hydrodynamic modelling and the implementation of an activated sludge model is discussed. The thesis is rounded of with a conclusion/discussion. Additionally, an appendix briefly describing the numerical solution techniques for the governing differential equations is included.

CHAPTER 2
Process description

As pointed out in chapter 1, the present work is delimitated to include investigations on activated sludge process tanks in wastewater treatment plants (WWTP). The process tank is a very complex structure, where many different physical, chemical and biological processes are occurring. The present chapter aims at introducing this diversity to the reader before going further into the investigations.

2.1 Presentation of the system

The shape and configuration of WWTP process tanks may vary significantly, depending on the manufacturer and design practices. Most of the different designs do however share similarities with respect to the components included in the tank. The present analysis regards aerated stirred process tanks. For the sake of clarity, the presentation of the process tank system will not be based on a particular tank design. Rather the system presentation will be given from a fictitious rectangular tank with inlet in the one end and outlet in the other (Figure 2.1).

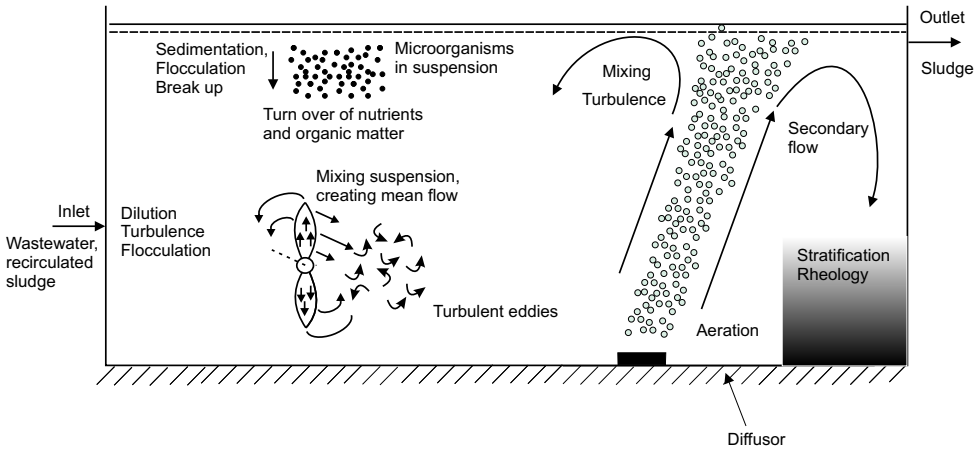

Figure 2.1 Principle outline of a WWTP activated sludge process tank.

As indicated on figure 2.1, the process tank system can be characterized as a system in which flocs of microorganisms are kept in suspension by several mechanisms. If no external energy is added to the suspension, the sludge flocs, as described below, are likely to settle out due

to the density difference relative to the wastewater carrier phase. The suspension is conveyed by a mean flow, generated by both the in and outlet of wastewater and sludge, and different kind of agitators. Mechanical mixers are ensuring mixing of the constituents meanwhile keeping the microorganisms in suspension. Dependence of the strength of the agitation, the sludge flocs will either aggregate (flocculation) or break up. The microorganisms utilize oxygen during the turnover of organic matter and the nitrification of nitrogen. The aeration equipment, on figure 2.1 indicated by a bottom mounted diffuser, is responsible for delivering the oxygen to the microorganisms, meanwhile they also contribute to additional mixing due to the additional flow generated by the resulting density variations and additional bubble generated turbulence. While the microorganisms have higher density than their carrier phase they will have a tendency to settle out. The sedimentation of the particles is exploited in the succeeding separation process, where the microorganisms are separated from the cleaned water, whereas sedimentation in general is unwanted during normal operation of process tanks. Due to the rheology of the suspension, Newtonian fluid viscosity assumptions are often incorrect, making the description of the flow of the suspension complex.

In the following sections, the different physical and biological processes indicated on figure 2.1 will be discussed. At first the constituents of the above-mentioned suspension of microorganisms will be further categorized.

2.2 Definition of phases

The suspension in an activated sludge system consist of a large diversity of matter, including water, air bubbles, different fractions of inorganic and organic matter, different kinds of biomass and everything else what could be expected to come with the wastewater from domestic and industrial sewage. Modelling every little part of this large diversity of matter would be a very challenging task. Hence in order to have a reasonable manageable system for a numerical model, a system reduction compared to reality, representing the bulk of the different fractions of matter, is necessary. In the present work, the activated sludge system will be regarded as a system of three main components/phases; Water, sludge flocs and air bubbles (Figure 2.2). Figure 2.2 shows an outline of the three phases occurring in an activated sludge process tank, as they will be defined in the present work.

During the numerical modelling, the process tank will be sub-divided into a system of interconnected cells, where each cell contains information about e.g. the properties of the flow and the biology. True to the above-mentioned phase definitions, each cell is consistent of the three phases water, sludge flocs and air bubbles in the following relationship:

$$r_{water} + r_{sludge} + r_{air} = 1 \tag{2.1}$$

I.e. the volume fraction of water, sludge flocs and air bubbles $[-]$ sum up to unity in each computational cell. The water phase is regarded as a continuous phase, whereas the sludge flocs and the air bubbles are disperse phases transported with continuous carrier phase. The water and air phases are of a nature not necessary to elaborate here. The definition of the sludge floc might however need a further description.

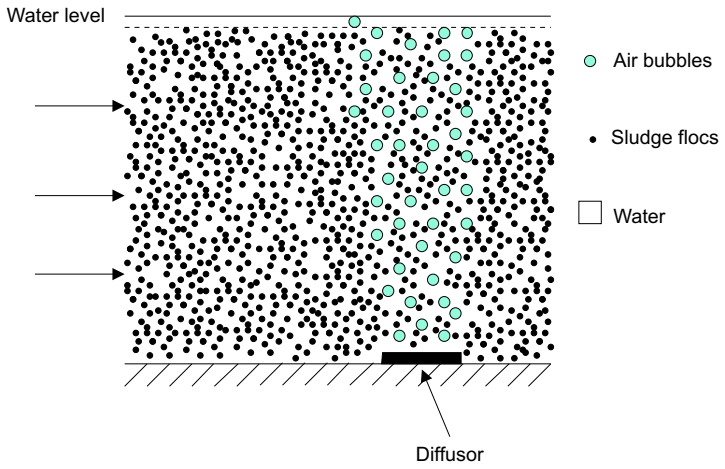

Figure 2.2 The components of the activated sludge system.

2.2.1 The activated sludge floc

The constituent responsible for the removal of pollutants in an activated sludge process tank is the suspension of bacteria, taking care of the microbiological removal of pollutants. The number of bacteria in activated sludge is typical in the range of $1 - 10 \cdot 10^{12} gVSS^{-1}$ (Nielsen, 2002), where approximately 80% are alive and active. The normal concentration of activated sludge in Danish wastewater treatment plants is in the range of approximately $4 - 6[kgSSm^{-3}]$. If an activated sludge system is working correctly, only a little part of the active biomass will be suspended as single bacteria. Instead, the bacteria are organized into flocs of relatively large populations (Figure 2.3).

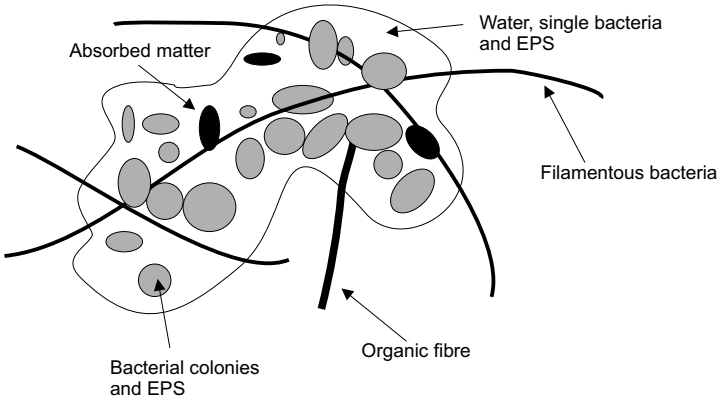

Figure 2.3 Composition of a typical sludge floc (Nielsen *et al.*, 2004).

As indicated on figure 2.3, the bacteria in the sludge suspension are grouped into aggregates consisting of biomass, water, extracellular polymeric substances (EPS) and inert material. The

EPS works as a gluing mechanism, holding the floc together. The EPS is mainly composed of polysaccharides, proteins, lipids, humic acids, nucleic acids and heteropolymers, where proteins or polysaccharides are normally the largest fractions. EPS is produced by the bacteria. The organic fibres and pieces of inorganic material on figure 2.3 do together with present ions in the EPS add to the adhering strength of the floc.

The aggregation of sludge flocs is occurring through a flocculation process, where the bacteria are aggregated in to larger sludge flocs. The flocculation process is caused by the induced mixing of the suspension, where the generated velocity gradients makes particles of biomass and other matter collide into larger aggregates. When the floc size is increased, the biomass is more easily separated from the water phase. The flocculation can be enhanced by adding gentle movements to the suspension by agitation. The opposite to flocculation is the deflocculation, where the flocs are broken into smaller particles.

Due to the limitations in floc strength, the size of the floc will be dependent on the shear of the suspension. Hence, the floc size is dependent on the amount of energy put into the system by mixing devices. The sludge floc will in a normally configured activated sludge tank have a mean diameter of approximately $80\mu m$ (Nielsen, 1994). Because the sludge flocs are heavier than the water phase, they will settle out, and a distinct phase discrimination between the water phase and the sludge flocs will develop, if no external mixing is applied to the system. This principle is exploited in the settling tanks, where the sludge flocs are settled out before the cleaned water is surged out in the recipient. Since larger sludge flocs in general have a larger settling velocity than smaller ones, and the settling velocity is dependent on the sludge characteristics, good sludge characteristics are very important for a high removal rate in an activated sludge wastewater treatment plant. If the sludge characteristics are poor, there will be a risk of washing out sludge into the receiving waters.

In the current work flocculation and deflocculation is not included directly in the model. As mentioned above, the sedimentation velocity of the sludge flocs is however dependent on the sludge size, making the flocculation and deflocculation processes very important for the sedimentation properties of the sludge. In the chosen sedimentation model (discussed later), the sedimentation velocity of the sludge flocs is dependent on the level of the shear, which influences the flocculation/deflocculation balance in the tank.

2.3 Physical processes

The present section will mainly deal with the physical processes occurring in an activated sludge tank. The following processes are included in the description:

- Mixing
- The aeration process
- Sedimentation of sludge
- Sludge rheology
- Density currents

2.3.1 Mixing

Several types of mixing are relevant for the system of an activated sludge tank:

- Mixing by turbulence
- Mechanical mixing by agitators/impellers
- Mechanical mixing by aeration equipment

The latter two items listed above might be considered as special cases of turbulent mixing devices, and as such they could be ranked as subsections to a general description of mixing by turbulence. Here, a short theoretical description of turbulence will be performed, after which a more practical point of view on the functionality of the two listed mechanical mixing processes will be given.

Mixing by turbulence

When the viscous forces of a fluid no longer can withstand the inertial forces of the fluid flow, the flow will enter a state of instability often referred to as turbulence. A turbulent flow is characterized by turbulent eddies appearing on a range of scales from the Kolmogorov scale up to a length scale on the order of the largest physical length scales of the geometry in which the flow is occurring, where the Kolmogorov length scale is defined as (Wilcox, 2000):

$$L_K \equiv \left(\frac{\nu^3}{\epsilon}\right)^{1/4} \tag{2.2}$$

where L_K is the Kolmogorov length scale $[m]$, ν is the kinematic viscosity $[m^2 \cdot s^{-1}]$ and ϵ is the dissipation of turbulent kinetic energy $[m^2 \cdot s^{-3}]$.

A turbulent flow is dissipative of nature, i.e. kinetic energy in the smallest eddies are converted into internal energy, resulting in a dissipation into heat. The kinetic energy is delivered to the smallest eddies from slightly larger eddies, who receive their energy from even larger eddies. This goes on until the presence of the largest eddies, where the energy is extracted from the mean flow. The process of energy transfer is often referred to as the energy cascade (Wilcox, 2000), (Davidson, 2003). One way of characterizing the energy within a turbulent flow is to apply a view of the wave number spectrum, where the wave number is proportional to the eddy size:

$$\kappa \propto 1/r_{eddy} \tag{2.3}$$

Where κ is the wave number $[m^{-1}]$ and r_{eddy} is the radius of the turbulent eddies $[m]$. In a wave number spectrum the energy contained in the eddies with wave number from κ to $\kappa + d\kappa$ can be calculated as (Davidson, 2003):

$$k_{\kappa \longrightarrow \kappa+d\kappa} = \int_{\kappa}^{\kappa+d\kappa} E(\kappa) d\kappa \tag{2.4}$$

In equation 2.4, the contribution to the turbulent kinetic energy k $[m^2 \cdot s^{-2}]$ is calculated for the eddies with length scales ranging from κ to $\kappa + d\kappa$. By integrating over the complete wave number spectrum, the total turbulent energy, k, can be obtained (Wilcox, 2000):

$$k = \int_0^\infty E(\kappa) d\kappa \tag{2.5}$$

Where k is the turbulent kinetic energy $[m^2 \cdot s^{-2}]$. A spectrum of the turbulence kinetic energy, E $[m^3 \cdot s^{-2}]$, as a function of wave number can be viewed in figure 2.4.

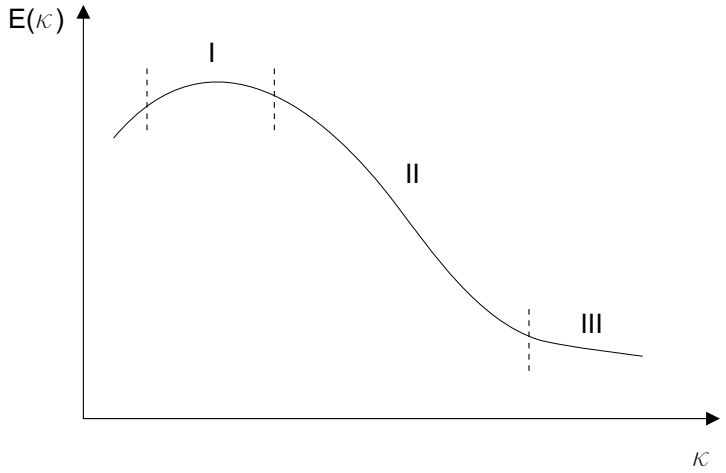

Figure 2.4 energy spectrum containing E $[m^3 \cdot s^{-2}]$ as a function of the wave number κ. I: Range for large energy containing eddies, II: Inertial subrange, III: Dissipation range, containing small isotropic eddies (From (Davidson, 2003))

In region I on figure 2.4, the largest eddies, also containing the largest amount of energy are located. The energy of the large eddies are passed on to eddies of slightly smaller length scales. The inertial subrange in region II on figure 2.4 represents the transport region of the cascade process. Again, energy is delivered from the larger eddies in the lower part of the spectrum to the smaller eddies at higher wave numbers. In the inertial subrange, a large range of wave numbers are apparent, in which the energy transferred by inertial effects dominate. On behalf of dimensional analysis Kolmogorov derived the Spectrum Law for this region (Wilcox, 2000):

$$E(\kappa) = C_{Kol} \epsilon^{\frac{2}{3}} \kappa^{-\frac{5}{3}} \tag{2.6}$$

here, C_{kol} is a constant $[-]$, ϵ is the turbulence energy dissipated at the small scales $[m^2 \cdot s^{-3}]$ and κ is the wave number $[m^{-1}]$.

In region III, where the length scales of the eddies can be approximated by the Kolmogorov scale (Equation 2.2), dissipation of energy due to the action of viscosity is appearing.

Even though the smallest eddies appear to contain the least energy in figure 2.4, these eddies continuously obtain their energy from the larger energy containing eddies, resulting in a continuous contribution to mixing from also the smallest length scales of eddies. For practical

problems it is however not feasible to resolve the smallest eddies numerically. Hence, a vertical line has to be drawn on figure 2.4, determining to what extent the eddies will be resolved. Eddies larger than the chosen level of resolution are typically resolved, whereas eddies smaller than the chosen level are modelled through a turbulence model, taking the effect of the turbulent eddies into account. Later, turbulence models will be briefly reviewed, and the chosen level of detail with respect to turbulence will be discussed.

System reduction - Reynolds averaging When measuring flow velocities in a turbulent flow, the velocities will fluctuate in a random matter due to the presence of the turbulent eddies (Figure 2.5). If one was dosing a tracer into a turbulent flow, the tracer would quickly be blurred out due to the mixing of the eddies.

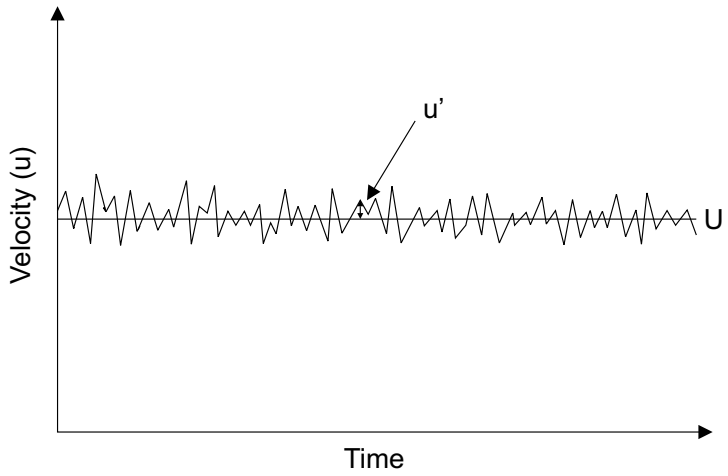

Figure 2.5 Time series of the u velocity in a turbulent flow. The definition of u' and U will be discussed below.

Because of its complexity, turbulent flow is very hard to predict or describe theoretically. The turbulent eddies, and thus fluctuant turbulent motions are however often very important for the transport of heat, mass and momentum, making the velocity field and the transport of substances dependent on the turbulent properties of the flow. In principle the Navier-Stokes equations (Chapter 3) are believed to govern any turbulent flow, and if sufficiently computing power is available it should at least in theory be possible to compute the eddies down to the smallest length and timescales. In practise the computing power available at the present time, do however only allow for the solution of flow at relatively low Reynolds number and only for a limited range of flow problems.

Since it is not feasible to consider all of the small-scale fluctuations in detail, an averaging of the flow field is often constructed. Reynolds averaging is a type of time-averaging, splitting the instantaneous velocity into a mean and a fluctuating part (Figure 2.5).

$$u = U + u' \tag{2.7}$$

where u is the instantaneous, U is the mean and u' is the fluctuating velocity, all in $[m \cdot s^{-1}]$.

With the use of this analogy, the turbulent kinetic energy (equation 2.5), can be expressed in terms of the turbulent fluctuating velocity components (Wilcox, 2000):

$$k \equiv \frac{1}{2}\overline{u'^2 v'^2 w'^2} = \frac{1}{2}\overline{u_i' u_i'} \tag{2.8}$$

where u, v and w are the fluctuating velocity components in the x, y and z directions $[m \cdot s^{-1}]$ and $\overline{u_i' u_i'}$ are the normal Reynolds' stresses $[m^2 \cdot s^{-2}]$.

By doing a time-averaging of the flow field, the velocity fluctuations are no longer described directly. Instead only the effect of the fluctuations on the flow field is described as Reynolds' stresses. The concept of Reynolds' stresses will be further described in the next chapter.

Turbulence is very important for the mixing of process tanks. Since the presence of fluctuations also will enhance the movement of individual sludge flocs, turbulence is also very important for the flocculation of sludge flocs. On the other hand, if the turbulence level is too high, it can have a negative effect, since the shearing effect of the turbulence can also result in a deflocculation of the sludge flocs.

As described above, it can be concluded that turbulence occurs at a variety of length scales, contributing to the mixing in the process tank. It is however not feasible to resolve the turbulent eddies down to the smallest length scales, which is why a system reduction has to be conducted. The Reynolds averaging is a result of the system reduction, in which the effect of the turbulent eddies are modelled through Reynolds stresses rather than modelling the eddies directly.

Mechanical mixing by agitators/impellers

The flow in many process tanks is to a large degree determined by the action of mechanical mixing. The mechanical mixing is typically performed by rotating equipment like impellers and pumps. The main role of the mechanical mixing is to maintain complete mixing of substances within each other, keep the sludge flocs in the process tank in suspension through constant mixing and to keep sludge particles flocculated.

The propeller motion originates from the application of an outer force in form of a torque resulting from the work done by a motor. When the propeller rotates it delivers a push to the body of water in the near vicinity of the impeller blades. Due to the presence of molecular and turbulent eddy viscosity, one parcel of water pushed forward by the propeller, will also drag neighbour parcels along with it, making a larger body of the water flow. Furthermore, since the flow induced by the propeller normally is not uniform, neighbouring parcels might not necessarily possess equal sized velocities, resulting in a produced torque, inducing a rotational flow.

The propeller induced velocities and turbulence are outlined in figure 2.6.

As indicated on figure 2.6, the velocities generated by the propeller can be divided into three components: An axial component, a tangential component and a radial component. In order to quantify the flow generated by the propeller.

Mechanical mixing by aeration equipment

The main purpose of the aeration equipment is primary to deliver a sufficient amount of oxygen to the microbial sludge, to ensure the wanted level of removal of organic matter and nitrogen. A positive side effect of the aeration process is however an increased level of mixing induced by

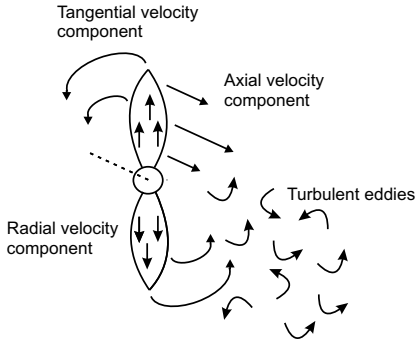

Figure 2.6 Outline of the flow and turbulence generated by a propeller.

secondary flow effects. The left hand side of figure 2.7 shows an outline of the flow generated by a bottom mounted air diffuser. A thorough description of the function and operational principle of the bottom mounted air diffuser can be found in chapter 4.

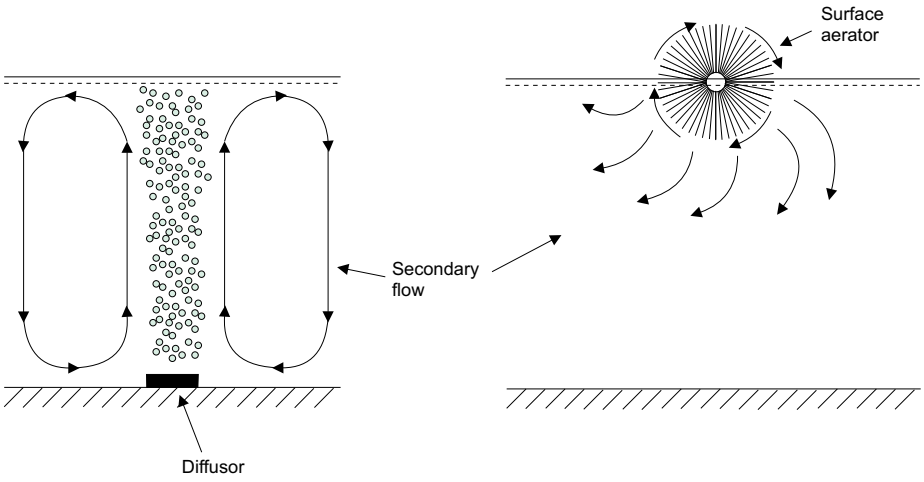

Figure 2.7 Outline of secondary flow generated by aeration equipment. Left: Bottom mounted diffuser. Right: Top mounted surface aerator.

Often another type of aeration device is however applied to activated sludge tanks; the top mounted surface aerator (Figure 2.7, right). As indicated on the right side of figure 2.7, the rotating surface aerator aerates the sludge by making a whipping of the sludge at the surface. The method locally creates a rather excessive secondary flow. This type of aerator can result in some unwanted hygienic side effects due to increased odour and increased escape of micro droplets. Generated aerosols may be problematic for especially the employees working at the WWTP. Furthermore the surface aerator may result in increased foaming due to the heavy whipping of the sludge. Aside the hygienic problems, practical problems regarding the surface aerators' efficiencies dependency's upon the water level in the tanks might also arise.

The top mounted surface aerator will not be subject to further investigations in the present work.

2.3.2 The aeration process

In order to ensure sufficient oxygen levels for the wanted biological turnover of organic matter and the nitrification of ammonium, the water in which the flocs are suspended is aerated through a reoxygenation process. Often the concentration of oxygen is held at 1-3 mg/l], and the microorganisms use it as rapidly as it is available (Tchobanoglous and Burton, 2003). The reoxygenation process is responsible for the dissolution of oxygen in the water phase. When the water is in contact with air, the oxygen concentration gradient across the interface will govern a diffusive transport of oxygen into the water phase. In the systems subject to investigation in the current work, injected air bubbles are responsible for the reoxygenation. The finer the bubbles are, the larger the relative surface area available for diffusion will be. Ideally, the diffusion process for each bubble should be described in order to model the reoxygenation process in detail. Instead, a simple equation, expressing the reoxygenation rate has been applied (Lankford, 1974), (Tchobanoglous and Burton, 2003):

$$r_{reoxygenation} = K_L a \left(C_s - C\right) \tag{2.9}$$

Where $r_{reoxygenation}$ is the reoxygenation rate $[mgO_2 \cdot L^{-1} \cdot s^{-1}]$, C is the concentration of dissolved oxygen $[mg\ O_2 \cdot L^{-1}]$, t is the time $[s]$, $K_L a$ is the overall mass transfer coefficient $[s^{-1}]$ and C_s is the saturated concentration of oxygen in water $[mg\ O_2 \cdot L^{-1}]$.

C_s is highly dependent on the temperature, where water can saturate more oxygen at lower temperatures (Frier, 1998):

$$C_s = \left(14.652 - 0.412022 \cdot T - 7.991E-3 \cdot T^2 - 7.773E-5 \cdot T^3\right) \cdot \frac{P - p}{760mm\ Hg - P} \tag{2.10}$$

here, T is the temperature $[^\circ C]$, P is the pressure $[mm\ Hg]$ and p is the saturated water vapour pressure $[mm\ Hg]$. In the current model implementation, C_s has been calculated from equation 2.10, on behalf of the temperature of the suspension.

$K_L a$ is dependent on the type of aeration device, the level of mixing, the temperature and the general composition of the sludge. The dependency of temperature, can be described by the van't Hoff-Arrhenius relation:

$$K_L a_{(T)} = K_L a_{(20^\circ C)} \theta^{T-20} \tag{2.11}$$

here, $K_L a_{(T)}$ is the oxygen mass transfer coefficient at the temperature T (in Celsius degrees) $[s^{-1}]$, $K_L a_{(20^\circ C)}$ is the mass transfer coefficient at $20^\circ C$ and θ is a coefficient dependent on the test system. A θ value of 1.024 is typical for both diffused and mechanical systems (Tchobanoglous and Burton, 2003)

2.3.3 Sedimentation of sludge

As mentioned above, the sludge flocs will in a properly working activated sludge process inherently settle out due to their higher density than the carrier phase, if no external energy is put into the system. Since the density difference between the wastewater and the suspended sludge particles is the driving parameter for the settling process, the density definitions are very important for the numerical modelling of the process tank.

Density definitions

Defining the density of sludge is not completely straight forward. It is not clear where to draw the line between sludge and wastewater; should the sludge be defined as the dry particles of biomass or should it be defined as a larger body of bacteria, water and EPS glued together in a floc? Depending on the choice of definition for the sludge as a media, the definitions of sludge density will vary correspondingly.

In the present work, the following densities will be used in the numerical model: the dry density of the sludge, ρ_s, the density of the raw wastewater, ρ_w, and the bulk density of the sludge, ρ_b. It is assumed that the density of the wastewater will be approximately the same as clean fresh water ρ_w. The correct value of ρ_w could be found by measuring the density of water from the effluent of the settling tanks. The value of 1450 kg/m^3 found by (Larsen, 1977) is used for ρ_s. ρ_s is a crucial model parameter determining the maximum obtainable suspended solids concentration and how much space the sludge will take up at a given concentration. Since both ρ_w and ρ_s are treated as constants in the present model, any deformations of the sludge flocs and the thereby induced change in density can not be handled in the present configuration. Consequently, choosing ρ_s too high would allow non-physically high sludge concentrations at e.g. the bottom of a tank, whereas a too small value would result in a very large volume taken up by the sludge a even very low suspended solids concentrations. This deficiency in the model is believed to be of minor importance when dealing with a heavily mixed process tank with small density gradients. Whereas in a settling tank where compression of the sludge is appearing at the bottom of the tank, a model including variations of ρ_w and ρ_s would be preferable.

By performing a weighted average of the fraction of wastewater and suspended sludge solids, the bulk density can be calculated:

$$\rho_b = r_w \rho_w + r_s \rho_s \tag{2.12}$$

where r_w and r_s are the volume fractions of wastewater and suspended solids $[m^3 \cdot m^{-3}]$. The problem with equation 2.12 is that it contains two unknowns; r_w and r_s. The values of these two variables are input values for the numerical model, and hence they need to be quantified. By substituting r_w with $(1 - r_s)$, the volume fraction of sludge, r_s can be calculated by equation 2.12:

$$r_s = \frac{\rho_b - \rho_w}{\rho_s - \rho_w} \tag{2.13}$$

Now the only unknown is the bulk density of the suspension, ρ_b. (Rasmussen, 1997) found that the bulk density of sludge from Aalborg East WWTP was highly dependent on the concentration of suspended solids:

$$\rho_b = 999.76 + 0.42 \cdot X_{SS}[kg \cdot m^{-3}] \tag{2.14}$$

where X_{SS} is the concentration of suspended solids $[kg\ SS \cdot m^{-3}]$. As an example, one of the process tanks at Hals WWTP had a C_{SS} concentration of 5.3 $kgSS/m^3$ during one particular measurement campaign. By using equation 2.14, the resulting bulk density is 1002 kg/m^3. The system is now closed, and the volume fractions of sludge and water can be determined.

Settling velocity

Due to the density difference between the sludge flocs and the carrier fluid, the sludge flocs will tend to settle out in a well functioning process tanks. The rate of settling is described by the settling velocity, which is determined as the velocity difference between the carrier phase and the floc.

If sludge was consisting of single homogeneous non-porous spherical shaped particles unaffected by each other, and these particles could settle freely in a quiescent fluid, the settling velocity is a function of the acceleration of gravity, the particle diameter and the buoyancy and drag on the particle:

$$W_s = \sqrt{\frac{4 \cdot g \cdot (\rho_p - \rho) \cdot d}{3 \cdot \rho \cdot C_D}} \tag{2.15}$$

where W_s is the settling velocity $[m \cdot s^{-1}]$, ρ_p and ρ are the particle and carrier fluid densities, respectively $[kg \cdot m^{-3}]$, d is the particle diameter $[m]$ and C_D is the drag coefficient $[-]$. The drag coefficient appearing in equation 2.15 is dependent on the particle Reynolds' number:

$$Re_p = \frac{\rho \cdot \mid v_r \mid \cdot d}{\mu} \tag{2.16}$$

where v_r is the relative velocity between particle and carrier fluid $[m \cdot s^{-1}]$, identical with W_S and μ is the dynamic viscosity of the carrier fluid $[kg \cdot m^{-1} \cdot s^{-1}]$. For Reynolds numbers lower than 0.2, equation 2.15 is identical with Stokes' law. For particle Reynolds' numbers higher than approximately 500 - 1000, C_D becomes constant at a value of 0.44. In the range between the Stokes' regime and particle Reynolds' numbers in the order of 500 - 1000, the drag coefficient needs to be determined empirically.

A number of properties of the particle sedimentation in activated sludge systems do conflict with the assumptions for using equation 2.15:

- Non-spherical, inhomogenous, porous particles
- Particles do not settle freely
- Highly turbulent flow in carrier fluid

Due to the aggregation of bacteria into sludge flocs (Figure 2.3), the sludge particles are in most cases non-spherical and porous of nature. Furthermore, the spacing between the sludge flocs is often too little for free settling conditions to appear in an activated sludge tank. In general several types of settling can occur in an activated sludge system dependent on the sludge concentration. In dilute parts of an activated sludge system, *flocculent particle settling* occur, where particles are flocculated as they settle through the water column (Takacs *et al.*, 1991). Although the particles due to the diluted conditions might be regarded as free settling individuals, the settling velocity might be very low due to the limited size of the particles. As the concentration of sludge flocs increase, *hindered settling* will start to dominate. In *hindered settling* inter-particle forces and upward flowing water due to continuity requirements, hinders the settling process in the suspension of sludge flocs. For high sludge floc concentrations, *compression settling* will take over, where the settling is a result of the compression of particles due to the weight of over-laying particles.

The effect of hindered settling and compression settling can be illustrated by observing a common sedimentation test in a large cylinder glass (Figure 2.8).

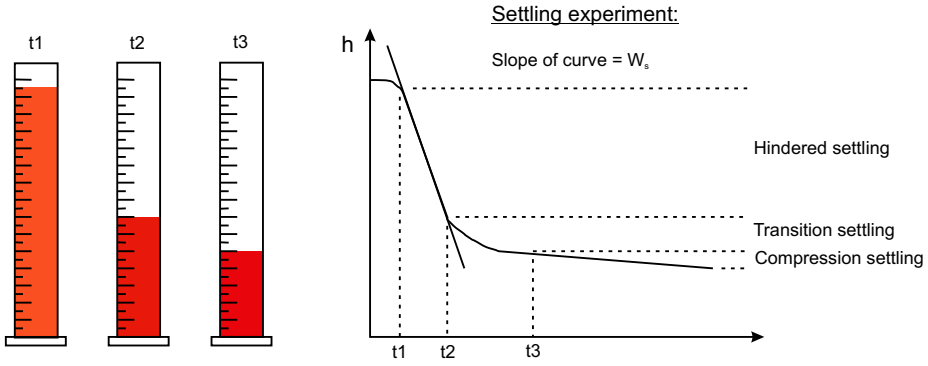

Figure 2.8 Outline of a settling test performed in a cylindrical shaped glass flask.

The test can be performed on activated sludge from settling or process tanks to quantify the settling velocity of the activated sludge. Due to the normal range of suspended solids concentrations in activated activated sludge on municipal WWTP's, the activated sludge will after an initial period of flocculation start to settle out as a whole with a clearly defined interface (The *sludge blanket*) between the activated sludge and the supernatant (Figure 2.8). The corresponding linear part of the h(t) curve on figure 2.8 represents hindered settling. At the bottom of the glass, activated sludge will deposit as it settles out. As long as the deposited activated sludge cake is not interfering with the settling sludge at the interface, the interface will sink with a linear rate. When the deposited sludge and the settling sludge starts to influence each other, a transition phase will occur after which compression will be dominating (Figure 2.8).

The above described settling test does however have a couple of shortcomings. The accuracy of the experiment is highly dependable of a clear interface between supernatant and sludge. Consequently, this method is not applicable to sludge concentrations below approximately 2 $kgSS \cdot m^{-3}$. Also at high sludge concentrations where the settling velocity is very low, the method is not longer applicable due to the very low settling velocity. Furthermore, it is not possible to introduce turbulence into the experiment without destroying the sludge/supernatant

interface. Due to the absence of mixing and aeration and the high influence from the boundaries of the glass, the method deviates from the actual settling conditions in a process tank. I.e. other methods have to be applied in order to investigate the effects of turbulence on the transport and flocculation of sludge flocs.

The local level of turbulence will highly affect the settling velocity in such way, that the sludge flocs during high levels of turbulence virtually will be kept in suspension due to a decreased effective settling velocity. The reason for this is to be found in the higher levels of shear during turbulent flow, breaking the sludge flocs into smaller flocs with a lower settling velocity.

In order to obtain an adequate expression for the settling velocity of sludge flocs in an activated sludge suspension, the above described shortcomings of applying equation 2.15 should be ruled out. An often applied expression for describing the hindered settling velocity in activated sludge suspensions (Vanderhasselt and Vanrolleghem, 2000), is the exponential function derived by (Vesilind, 1968):

$$W_s = W_0 \cdot e^{k \cdot X_{SS}} \tag{2.17}$$

Here, W_0 is the initial settling velocity $[m \cdot s^{-1}]$, k is a constant $[-]$ and X_{SS} is the concentration of suspended solids $[kg\ SS \cdot m^{-3}]$, used as a measure of the sludge concentration. Equation 2.17 expresses that the settling velocity exponentially decreases towards zero as the sludge concentration goes towards infinity. Also double exponential expressions have been evolved for modelling the settling velocity. (Takacs *et al.*, 1991) applied a double exponential model to a multi-layer settler model, with one exponential expression describing the flocculent particle settling in the upper part of a settler and the other expression describing hindered settling. Taking the exponential part for the modelling of flocculent particle settling in the upper layer out of the model, would make a model equal to the model of Vesilind.

However, the above mentioned expressions of Vesilind and Takacs are mainly constructed for the use in settling tanks and they do not take the local effect of turbulence into account when calculating the settling velocity. Since, especially in an aerated tank the turbulence level, as well as the local variation of the same property is believed to be of significant importance, an expression taking the effect of turbulence into account has been chosen for the present work (Rasmussen and Larsen, 1996). The settling model of (Rasmussen and Larsen, 1996) will be discussed in detail in chapter 4.

2.3.4 Sludge rheology

According to (Barnes, 2000), Rheology is: *The study of the flow and deformation of materials*. In this section, equations describing the rheology of the suspension in a process tanks will be outlined.

The continuous phase carrying the disperse phase in the suspension in the process tank is essentially the Newtonian Fluid, Water. All Newtonian fluids obey Newton's law of viscosity (Newton, 1687):

$$\tau = \mu \frac{\partial U_i}{\partial x_j} \tag{2.18}$$

where τ is the shear stress $[N \cdot m^{-2}]$ and μ is the dynamic viscosity $[kg \cdot m^{-1} \cdot s^{-1}]$. Newton's law of viscosity states a linear relationship between shear rates and shear stresses, where μ does not vary with the deformation rate or time.

Many fluids do however not follow equation 2.18 and are thus non-Newtonian.

Non-Newtonian fluids

In some non-Newtonian fluids such as pastes and sludges, the fluids needs to be subject to a certain amount of force before any deformation of the fluid will appear. Theoretically the yield stress is the stress below which no actual flow takes place. Initial measurements on sludges from Aalborg East WWTP (Section 4.4.1), indicated that activated sludge in WWTPt's might be yield stress fluids. The shear stress of a non-Newtonian fluid with a yield stress, can be described through one of several expressions:

The Bingham model (Bingham, 1916):

$$\tau_i = \tau_y + K \left(\frac{\partial U_i}{\partial x_j} \right) \tag{2.19}$$

the Casson model (Casson, 1957):

$$\sqrt{\tau_i} = \sqrt{\tau_y} + \sqrt{K \left(\frac{\partial U_i}{\partial x_j} \right)} \tag{2.20}$$

and The Herschel-Bulkley model (Herschel and Bulkley, 1926):

$$\tau_i = \tau_y + K \left(\frac{\partial U_i}{\partial x_j} \right)^n \tag{2.21}$$

where τ_i is the shear stress in the i'th direction $[N \cdot m^{-2}]$, τ_y is the yield stress $[N \cdot m^{-2}]$, K is the apparent viscosity $[N \cdot s^n \cdot m^{-2}]$ and n is a dimensionless constant $[-]$.

The Herschel-Bulkley model (equation 2.21) is a general model, where the choice of model parameters determines which model type the model covers. Setting $(\tau_y = 0, n = 0)$ results in a Newtonian fluid, and choosing $(\tau_y > 0, n = 1)$ yields the Bingham model (equation 2.19). If $(\tau_y = 0, n < 1)$, the fluid is pseudoplastic, whereas a dilatant fluid, where the viscosity increases with rate of shear, has the characteristics of $(\tau_y = 0, n > 1)$.

Experiments performed by (Frost, 1981) indicated that the Bingham plastic model was easy to implement, but that the model was not applicable to sludge concentrations above 4% by weight. Furthermore the pseudoplastic model did not perform well for activated or digested sludge. (Frost, 1981) did however find that the Herschel-Bulkley model was best suited to describe a wide range of sewage sludges. The drawback of the model was that fitting the model was more tedious than the more simple models.

Some non-Newtonian fluids will also undergo a decrease in viscosity with time when they are subject to a constant shear rate. A fluid with such characteristics is termed as a thixotropic fluid. Some thixotropic fluids might regain their strength if they are no longer subject to a stress.

For the case of activated sludge, the suspension might be thixotropic, since it is likely that a certain amount of stress will destroy the structure of the flocs in the mixture. If the flocs are reflocculated, the thixotropy could however be considered as reversible, since the suspension then after a while of favourable mixing conditions would have returned to the previous physical state.

2.3.5 Density currents

Due to different hydraulic properties, and thereby different conditions for settling in different part of the activated sludge tank, the bulk density might vary from one part of the tank to another. This variation might appear in both horizontal and vertical direction. Since a fluid with density differences under the action of gravity will try to find an equilibrium where the density differences are levelled out, a flow of fluid will occur from zones with high density towards zones with lower density. If the activated sludge process tank is heavily agitated, the density currents might not be a very important process compared to other flow generating processes. In settling tanks (Rasmussen, 1997), or aeration tanks that are occasionally free of agitation (e.g. if they are configured for rain weather controlling), the density currents might be very important for the overall flow in the tank. Figure 2.9 shows the principle of density currents. The figure shows the principle of an interlock experiment for estimating the bulk density of activated sludge, as performed by (Larsen, 1977).

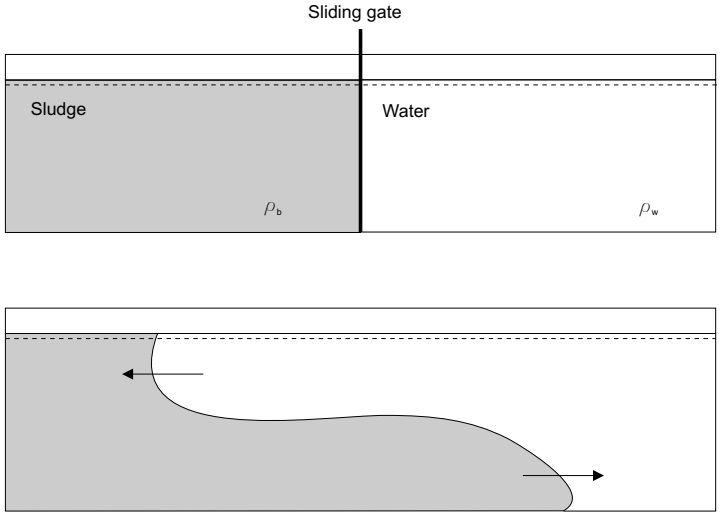

Figure 2.9 Example of density current in an interlock experiment.

The velocity of the front of the density current can be calculated from the expression found by (Keulegan, 1957):

$$u = k \cdot \sqrt{g \cdot H \cdot \frac{\triangle \rho}{\rho_w}} \tag{2.22}$$

Where k is a constant $[-]$, experimentally found to be 0.45 - 0.47, g is the gravitational acceleration $[m \cdot s^{-2}]$, H is the water depth $[m]$ and $\triangle\rho$ is the difference between the bulk density, ρ_b and the density of the wastewater supernatant, ρ_w.

From equation 2.22 it is obvious that the velocity of the density current is largely dependent on the density gradient. Large density gradients will consequently result in strong density currents. Hence, a $5m$ deep stratified tank with a density deficiency of $1kg \cdot m^{-3}$, would according to equation 2.22 generate a velocity of the density current of approximately $0.1m \cdot s^{-1}$. From this example it can be concluded that density currents may be important in tanks with little agitation and resulting stratification, whereas the effect of density currents is negligible compared to the effect of mixers in heavily agitated tanks.

2.4 Biological processes

As mentioned in chapter 1, common models for simulating the microbial processes in activated sludge systems are the Activated Sludge Models (ASM1 - ASM3) as proposed by the International Association of Water Quality (IAWQ). In the present work, the ASM3 has been integrated into the CFD-model, in order to be able to simulate the biological turnover of nitrogen compounds and organic matter.

2.4.1 ASM3

In ASM3, several soluble and particulate components are modelled (Gujer *et al.*, 1999):

Soluble components:

- Dissolved oxygen, S_O, $[mg\ O_2 \cdot L^{-1}]$
- Readily biodegradable organic substrates, S_S, $[mg\ COD \cdot L^{-1}]$
- Inert soluble organic material, S_I, $[mg\ COD \cdot L^{-1}]$
- Ammonium and ammonia nitrogen ($NH_4^+ - N\ and\ NH_3 - N$), S_{NH}, $[mg\ N \cdot L^{-1}]$
- Nitrate and nitrite nitrogen ($NO_3^- - N\ and\ NO_2^- - N$), S_{NO}, $[mg\ N \cdot L^{-1}]$
- Dinitrogen (N_2), S_{N_2}, $[mg\ N \cdot L^{-1}]$
- Alkalinity of the wastewater (HCO_3^-), S_{Alk}, $[mole\ HCO_3^- \cdot L^{-1}]$

Particulate components:

- Slowly biodegradable substrates, X_S, $[mg\ COD \cdot L^{-1}]$
- Inert particulate material, X_I, $[mg\ COD \cdot L^{-1}]$
- Heterotrophic biomass, X_H, $[mg\ COD \cdot L^{-1}]$
- Internal storage in heterotrophic biomass, X_{STO}, $[mg\ COD \cdot L^{-1}]$
- Autotrophic biomass, X_A, $[mg\ COD \cdot L^{-1}]$

- Total suspended solids, X_{SS}, $[mg\ S_S \cdot L^{-1}]$

The concentrations of the above listed components are dependent on a series of processes describing e.g. growth or respiration of different bacterial groups (Figure 2.10).

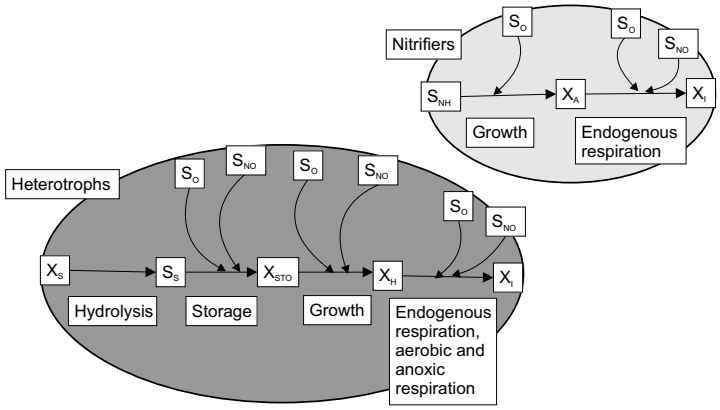

Figure 2.10 Principle layout of the flow of processes in ASM3.

As indicated in figure 2.10, the biomass is in the model is divided into two subgroups; heterotrophic organisms responsible for the turnover of organic matter and denitrification and autotrophic nitrifiers responsible for the nitrification.

When the particulate organic matter is hydrolyzed into readily biodegradable organic matter, the heterotrophs can store the organic matter internally in their biomass during either aerobic or anoxic respiration, dependent on the actual conditions in the sludge. In the model it is assumed that growth occurs entirely on the storage products. The growth of heterotrophs can occur through either aerobic respiration or denitrification. Finally, the heterotrophic biomass can be converted into inert matter through either aerobic or anoxic endogenous respiration. The endogenous respiration is responsible for all kinds of biomass loss and energy consumptions not related to growth by; decay, maintenance, lysis, predation, motility, death etc.

The autotrophic nitrifiers aerate the ammonium to nitrate with the usage of soluble oxygen (Figure 2.10). Also the nitrifiers can be converted into inert matter by both aerobic and anoxic endogenous respiration.

In figure 2.10 some of the components of ASM3 are omitted. The soluble inert material, S_I, can be produced by hydrolysis of X_S, but the inert material can not be further degraded in the treatment plants dealt with in ASM3, and as such S_I does not have influence on the remainder of the processes. Also dinitrogen, N_2, produced during denitrification is in principle a dormant component since it does not affect the remainder of the processes. Alkalinity, S_{Alk}, is both produced and used during several of the processes accounted for in ASM3. S_{Alk} is not shown in figure 2.10, but it affects several of the processes through Monod-like expressions. Modelling of the alkalinity can be used to estimate low pH conditions, an inhibitor for many biological processes. Due to the relatively long time-scale of the built-up and use of alkalinity, it can be rejected from the model during modelling of short real-time periods.

The kinetics of the processes is in ASM3 evaluated through a series of Monod expressions, e.g. for soluble components:

$$Process_i = r \cdot \frac{S_1}{K_1 + S_1} \cdot \frac{S_2}{K_2 + S_2} ... \cdot X_B \tag{2.23}$$

where r is the process rate $[d^{-1}]$, S_1 and S_2 are substrates $[mg\ substrate \cdot L^{-1}]$, K_1 and K_2 are the saturation constant for S_1 and S_2 $[mg\ substrate \cdot L^{-1}]$ and X_B is the biomass concentration $[mg\ COD \cdot L^{-1}]$. The rate, r, varies with temperature. Often the temperature dependency follows an Arrhenius like expression, where the rate within a certain temperature range increases exponentially with temperature. In this work, the rates of the biological reactions have however been set to the values from (Gujer *et al.*, 1999) as a starting point, from where all rates have been slightly and simultaneously changed during the model calibration.

In ASM3, twelve different processes are used for describing the growth and death of different types of microorganisms.

- Process 1: Hydrolysis of particulate slowly biodegradable substrate

Eight processes are involving heterotrophic microorganisms:

- Process 2: Internal aerobic storage of readily biodegradable substrates
- Process 3: Internal anoxic storage of readily biodegradable substrates
- Process 4: Aerobic growth
- Process 5: Anoxic growth by denitrification
- Process 6: Aerobic endogeneous respiration
- Process 7: Anoxic endogeneous respiration
- Process 8: Aerobic respiration of X_{STO}
- Process 9: Anoxic respiration of X_{STO}

The remaining processes are involving autotrophic microorganisms

- Process 10: Nitrification
- Process 11: Aerobic endogeneous respiration
- Process 12: Anoxic endogeneous respiration

The formulae for calculating the kinetics of the twelve processes is written out in detail in table 2.1. Beside the table of kinetics used in ASM3, one key feature of the model concept is the stoichiometric matrix, describing the correct amount of the different processes that contribute to the increase or decrease of the nutrients or biomass (Table 2.2).

In the paper by (Gujer *et al.*, 1999), a first estimate on the many kinetic and stoichiometric parameters of the ASM3 are listed (Table 2.3 and 2.4).

By the application of tables 2.1, 2.2, 2.3 and 2.4, the model has been implemented into the CFD-model. Because the inert fractions do not have any influence on any of the kinetics in

Table 2.1 Processes included in the Activated Sludge Model 3 (ASM3) (Gujer *et al.*, 1999).

Process Nr.	*Formula*
1	$k_H \cdot \frac{X_S/X_H}{K_X+X_S/X_H} \cdot X_H$
2	$k_{STO} \cdot \frac{S_O}{K_O+S_O} \cdot \frac{S_S}{K_S+S_S} \cdot X_H$
3	$k_{STO} \cdot \eta_{NO} \cdot \frac{S_O}{K_O+S_O} \cdot \frac{S_{NO}}{K_{NO}+S_{NO}} \cdot \frac{S_S}{K_S+S_S} \cdot X_H$
4	$\mu_H \cdot \frac{S_O}{K_O+S_O} \cdot \frac{S_{NH}}{K_{NH}+S_{NH}} \cdot \frac{S_{HCO}}{K_{HCO}+S_{HCO}} \cdot \frac{X_{STO}/X_H}{K_{STO}+X_{STO}/X_H} \cdot X_H$
5	$\mu_H \cdot \eta_{NO} \cdot \frac{S_O}{K_O+S_O} \cdot \frac{S_{NO}}{K_{NO}+S_{NO}} \cdot \frac{S_{NH}}{K_{NH}+S_{NH}} \cdot \frac{S_{HCO}}{K_{HCO}+S_{HCO}} \cdot \frac{X_{STO}/X_H}{K_{STO}+X_{STO}/X_H} \cdot X_H$
6	$b_{H,O2} \cdot \frac{S_O}{K_O+S_O} \cdot X_H$
7	$b_{H,NO} \cdot \frac{S_O}{K_O+S_O} \cdot \frac{S_{NO}}{K_{NO}+S_{NO}} \cdot X_H$
8	$b_{STO,O2} \cdot \frac{S_O}{K_O+S_O} \cdot X_{STO}$
9	$b_{STO,NO} \cdot \frac{S_O}{K_O+S_O} \cdot \frac{S_{NO}}{K_{NO}+S_{NO}} \cdot X_{STO}$
10	$\mu_A \cdot \frac{S_O}{K_{A,O}+S_O} \cdot \frac{S_{NH}}{K_{A,NH}+S_{NH}} \cdot \frac{S_{HCO}}{K_{A,HCO}+S_{HCO}} \cdot X_A$
11	$b_{A,O2} \cdot \frac{S_O}{K_O+S_O} \cdot X_A$
12	$b_{A,NO} \cdot \frac{S_O}{K_O+S_O} \cdot \frac{S_{NO}}{K_{NO}+S_{NO}} \cdot X_A$

Table 2.2 Stoichiometric matrix applied in the Activated Sludge Model 3 (ASM3) (Gujer *et al.*, 1999).

Nr.	S_O [O_2]	S_I [COD]	S_S [COD]	S_{NH} [N]	S_{N_2} [N]	S_{NO} [N]	S_{HCO} [mole]	X_I [COD]	X_S [COD]	X_H [COD]	X_{STO} [COD]	X_A [COD]	X_{SS} [S_S]
1		0	1	0.01			0.001		-1				-0.75
2	-0.15		-1	0.03			0.002				0.85		0.51
3			-1	0.03	0.07	-0.07	0.007				0.8		0.48
4	-0.60			-0.07			-0.005			1	-1.60		-0.06
5				-0.07	0.30	-0.30	0.016			1	-1.85		-0.21
6	-0.80			0.066			0.005	0.20		-1			-0.75
7				0.066	0.28	-0.28	0.025	0.20		-1			-0.75
8	-1										-1		-0.60
9					0.35	-0.35	0.025				-1		-0.60
10	-18.04			-4.24		4.17	-0.60					1	0.90
11	-0.80			0.066			0.005	0.20				-1	-0.75
12				0.066	0.28	-0.28	0.025	0.20				-1	-0.75

table 2.1, the models for these fractions have been ruled out of the CFD-model, in order to save computational resources.

By applying the ASM3 to the numerical model a detailed description of the biological processes occurring in the activated sludge process tank is coupled to the detailed hydrodynamic model. Since the ASM3 model can give information of the concentrations of soluble oxygen, fractions of organic matter, nitrogen and biomass as a function of the dependency of all of these components, and the hydrodynamic model can account for the physical transport of the components, a complete integrated model describing the processes in the activated sludge tank can in

Table 2.3 First estimates on the kinetic parameters applied in the Activated Sludge Model 3 (ASM3) (Gujer *et al.*, 1999).

Symbol	Characterization	Temperature 10°C	Temperature 20°C	Units
k_H	Hydrolysis rate constant	2	3	$g\ X_s\ g^{-1}\ X_H\ d^{-1}$
K_X	Hydrolysis saturation constant	1	1	$g\ X_s\ g^{-1}\ X_H$
$Heterotrophic\ organisms, denitrification, X_H$				
k_{STO}	Storage rate constant	2.5	5	$g\ S_s\ g^{-1}\ X_H\ d^{-1}$
η_{NO}	Anoxic reduction factor	0.6	0.6	-
K_O	Saturation constant for S_O	0.2	0.2	$g\ O_2\ m^{-3}$
K_{NO}	Saturation constant for S_{NO}	0.5	0.5	$g\ NO_3^- - N\ m^{-3}$
K_S	Saturation constant for S_S	2	2	$g\ COD\ m^{-3}$
K_{STO}	Saturation constant for X_{STO}	1	1	$g\ X_s\ g^{-1}\ X_H$
μ_H	Heterotrophic max. growth rate	1	2	d^{-1}
K_{NH}	Saturation constant for Ammonium, S_{NH}	0.01	0.01	$g\ N\ m^{-3}$
K_{HCO}	Bicarbonate saturation constant of X_H	0.1	0.1	$mole\ HCO_3^-\ m^{-3}$
$b_{H,O2}$	Aerobic endogenous respiration rate of X_H	0.1	0.2	d^{-1}
$b_{H,NO}$	Anoxic endogenous respiration rate of X_H	0.05	0.1	d^{-1}
$b_{STO,O2}$	Aerobic respiration rate for X_{STO}	0.1	0.2	d^{-1}
$b_{STO,NO}$	Anoxic respiration rate for X_{STO}	0.05	0.1	d^{-1}
$Autotrophic\ organisms, nitrification, X_A$				
μ_A	Autotrophic max. growth rate of X_A	0.35	1.0	d^{-1}
$K_{A,NH}$	Ammonium substrate saturation for X_A	1	1	$g\ N\ m^{-3}$
$K_{A,O}$	Oxygen saturation for nitrifiers	0.5	0.5	$g\ O_2\ m^{-3}$
$K_{A,HCO}$	Bicarbonate saturation for nitrifiers	0.5	0.5	$mole\ HCO_3^-\ m^{-3}$
$b_{A,O2}$	Aerobic endogenous respiration rate of X_A	0.05	0.15	d^{-1}
$b_{A,NO}$	Anoxic endogenous respiration rate of X_A	0.02	0.05	d^{-1}

Table 2.4 First estimates on the stoichiometric parameters applied in the Activated Sludge Model 3 (ASM3) (Gujer *et al.*, 1999).

Symbol	Characterization	Value	Units
f_{SI}	Production of S_I in hydrolysis	0	$g\ S_i\ g^{-1}\ X_S$
$Y_{STO,O2}$	Aerobic yield of stored product per S_S	0.85	$g\ X_{STO}\ g^{-1}\ S_S$
$Y_{STO,NO}$	Anoxic yield of stored product per S_S	0.80	$g\ X_{STO}\ g^{-1}\ S_S$
$Y_{H,O2}$	Aerobic yield of heterotrophic biomass	0.63	$g\ X_H\ g^{-1}\ X_{STO}$
$Y_{H,NO}$	Anoxic yield of heterotrophic biomass	0.54	$g\ X_H\ g^{-1}\ X_{STO}$
Y_A	Yield of autotrophic biomass per $NO_3^{-1} - N$	0.24	$g\ X_A\ g^{-1}\ S_{NO}$

principle be constructed.

CHAPTER 3
Hydrodynamic modelling of WWTP

In the present chapter, equations are listed for describing the hydrodynamics of WWTP process tanks. Since the mixing properties of the tank are very important for describing the distributions of the different components of the sludge, the model has to be able to describe gradients of velocities, concentrations of the different components etc. Furthermore, the sedimentation process, responsible for the separation of sludge flocs and water during quiescent conditions, is highly dependent upon the local flow conditions and the distributions of sludge itself. Also the injection of air bubbles into the suspension has an impact on the local flow conditions and the mixing properties. Thus, a rather comprehensive model framework has to be setup to include the above-mentioned hydrodynamic interactions.

Due to the nature of the flow in Wastewater Treatment Plant process tanks, special attention will be given to multiphase flow. In order to simplify things, the chapter is initiated with a quick summation of the theory of single phase flow. When the terminology of single phase flow is in its place, the theory of multiphase flow will be outlined. Also an introduction to turbulence modelling is included.

3.1 Single phase flow.

The governing equations of single phase flow are developed upon three conservation laws of physics:

- Conservation of mass in the fluid
- Newton's second law: The rate of increase of momentum of a fluid particle equals the sum of forces on the fluid particle
- The first law of thermodynamics: The rate of increase of energy of a fluid particle equals the sum of the net rate of heat added to the fluid particle and the net rate of work done on the fluid particle

On basis of the law of conservation of mass and Newton's second law, the Navier-Stokes equations were independently derived by the Frenchman Claude-Louis Navier and the Irishman George Gabriel Stokes in the nineteenth century. The Navier-Stokes equations comprise of a set of non-linear partial differential equations for describing the flow of liquids. Using tensor notation, the Reynolds' averaged (See chapter 2 for details of Reynolds' averaging) Navier-Stokes

equations for incompressible flows are listed as:

The continuity equation:

$$\frac{\partial U_j}{\partial x_j} = \frac{\partial u}{\partial x} + \frac{\partial v}{\partial y} + \frac{\partial w}{\partial z} = 0 \tag{3.1}$$

The momentum equations:

$$\rho \cdot \frac{\partial U_i}{\partial t}\rho \cdot \frac{\partial U_j U_i}{\partial x_j} = -\frac{\partial p}{\partial x_i} + \frac{\partial}{\partial x_j}\left(\mu\left(\frac{\partial U_i}{\partial x_j} + \frac{\partial U_j}{\partial x_i}\right) - \rho\overline{u_i' u_j'}\right) + S_{Mi} \tag{3.2}$$

where ρ is the density $[kg \cdot m^{-3}]$, U_i is the mean velocity in the i-direction $[m \cdot s^{-1}]$, t is the time $[s]$, p is the pressure $[kg \cdot m^{-1} \cdot s^{-2}]$, μ is the dynamic viscosity of the fluid $[kg \cdot m^{-1} s^{-1}]$ and $\rho\overline{u_i' u_j'}$ is the Reynolds' stresses $[kg \cdot m^{-1} \cdot s^{-2}]$.

The Reynolds' stresses can be described through the Boussinesq assumption, where proportionality between velocity gradients and Reynolds' stresses are assumed:

$$-\rho\overline{u_i u_j} = \mu_t\left(\frac{\partial U_i}{\partial x_j} + \frac{\partial U_j}{\partial x_i}\right) + \frac{2}{3}\rho\delta_{ij}k \tag{3.3}$$

Where δ_{ij} is the Kronecker delta $[-]$ and k is the turbulent kinetic energy $[m^2 \cdot s^{-2}]$. Along with the introduction of the Boussinesq assumption follows an assumption of constant turbulent viscosity in all directions, i.e. an assumption of isotropic turbulence. Because of this assumption, the eddy viscosity is the only unknown, resulting in a considerable reduction in unknown variables.

3.2 Multiphase flow

As discussed in chapter 2, section 2.1, the activated sludge can roughly be assumed to be consistent of three different phases; water, sludge flocs and air bubbles. Two different types of multiphase models are in general available: an Eulerian-Lagrangian and an Eulerian-Eulerian multiphase model.

In the Eulerian-Lagrangian approach, the dispersed phase is modelled with a particle tracking method, where single particles' individual trajectories are modelled by solving Newton's equations of motion for every single particle. The continuous phase is modelled with an Eulerian approach, where both temporal and spatial averaging of the fluid variables is applied. The Eulerian-Langrangian model becomes unsuitable for high particle loads like fluidized beds and other flow situations with a substantial amount of particles.

In the Eulerian-Eulerian model both the dispersed and the continuous phase's fluid variables are found by spatial and temporal averaging. The Eulerian field description method is frequently used for description of interpenetrating media situations, including gas-liquid flow situations such as bubbly flows (Lakehal, 2002). In order to get representative values for the fluid variables in the flow field, a sufficiently small size of the finite volume elements is necessary.

The Eulerian-Eulerian multiphase model can be applied as either a homogeneous model or a Multifluid Model. In the Homogenous Model, the interfacial transfer rate is considered to be

very large, with the result that all fluids share the same flow field, limiting the use of the model to only restricted cases of flow. Compared to the Multifluid Model, the model is a simplification. In the Multifluid Model each phase has its own solution field, and consequently a continuity equation and a set of momentum equations are solved for each separate phase. Each volume in the mixture of the fluids is considered to be occupied by both phases, and the local volume fractions tell how large a fraction of the volume that is occupied by each of the phases. The sum of the volume fractions of the phases occupying the volume must be unity in all volumes:

$$\sum_{\alpha=1}^{N_p} r_\alpha = 1 \tag{3.4}$$

where r_α is the volume fraction of phase α $[m^3 \cdot m^{-3}]$ and N_p is the number of phases $[-]$.

Because of the limitations of the Homogeneous Model described above, the multifluid model is chosen for the present numerical simulations. Both types of the multiphase models will be further described below.

3.2.1 Phase discrimination

In the following, thesis the term *particle* will be applied for the dispersed air bubbles and the sludge flocs. The particle will be surrounded by a fluid which due to its continuous nature will be termed as the *continuous* fluid. The α, β and γ indexes will be used for the continuous water phase and the dispersed air bubbles and sludge flocs, respectively.

3.2.2 Phase-coupling

When the phases come in contact with each other they can inter-change properties at their interfaces. This inter-phase transfer can in principle occur for both mass, momentum and energy. If inter-phase transfer between a pair of phases is important, the flow is said to be *two-way coupled*. This is true for e.g. bubbly flow, where the dispersed bubble phase will influence the flow of the water phase and vice versa. This is however not true for all types of multiphase flow. In some situations the particles may be of a size and weight that they will simply follow the flow of the continuous phase without any counteraction. In such situations the flow is termed as *one-way coupled*.

The degree of one- or two-way coupling is important for the choice of model to solve a given multiphase flow. In the present work only coupling of momentum is relevant for the flow systems, and hence only this type of coupling will be addressed in this work.

Two-way coupling - the multifluid multiphase model

In a two-way coupled system, either interphase transfer of mass, momentum or energy is of significant importance for the flow field description of both phases in e.g. a two-phase flow system (Loth, 2000). For the flow problems in the present work, mass and energy transfer will be neglected whereas momentum transfer will play an important role. Mass transfer would occur if the mass of on phase was to be transferred into the mass of another phase, like e.g. in the evaporation of water into steam. One could argue that the growing of bacteria on substrates and

e.g. oxygen is a kind of mass transfer, but in the present work these compound are regarded as either solubles in the water or sludge phase, rather than separate phases. Furthermore, the timescale of biologic growth is so large that growth can be neglected on the relative short time scale of the present simulations. Since the wastewater in the inlet in general has a temperature of approximately the same value as the suspension inside the process tank, the energy transfer has been neglected in the computations.

As the wording indicates, interphase momentum transfer is all about interchange of momentum or forces between the phases. An example is the rising of a bubble in water, where the bubble will displace the surrounding water, while the water will counteract with a resistance to the rising of the bubble.

A common multiphase model including interphase momentum transfer is the Eulerian-Eulerian multifluid model, as formulated by (Ishii, 1975). As described above, a set of Navier-Stoke's equations are solved for each phase in the multifluid model. For the incompressible phase α, the Navier-Stokes equations in three dimensions are written as:

The continuity equation:

$$\rho_\alpha \cdot \frac{\partial r_\alpha}{\partial t} + \rho_\alpha \cdot \frac{\partial (r_\alpha U_{j,\alpha})}{\partial x_j} = 0 \tag{3.5}$$

The momentum equations:

$$\rho_\alpha \cdot \frac{\partial (r_\alpha U_{i,\alpha})}{\partial t} + \rho_\alpha \cdot \frac{\partial (r_\alpha \cdot U_{j,\alpha} \cdot U_{i,\alpha})}{\partial x_j} = -r_\alpha \cdot \frac{\partial p}{\partial x_i} + r_\alpha \cdot \frac{\partial}{\partial x_j} \left(\mu_\alpha \left(\frac{\partial U_{i,\alpha}}{\partial x_j} + \frac{\partial U_{j,\alpha}}{\partial x_i} \right) + \rho \overline{u_{i,\alpha} u_{j,\alpha}} \right) + M_\alpha + S_{Mi,\alpha} \tag{3.6}$$

Where i and j are indexes ranging from 1 to 3, dependent on the coordinate direction $[-]$, α is the phase index $[-]$, ρ_α is the density of phase α $[kg \cdot m^{-3}]$, r_α is the volume fraction of phase α $[m^3 \cdot m^{-3}]$, $U_{i,\alpha}$ is the mean flow velocity of phase α in the i-direction $[m \cdot s^{-1}]$, p is the pressure $[N \cdot m^{-2}]$, $\rho \overline{u_{i,\alpha} u_{j,\alpha}}$ are the Reynolds' stresses of phase α $[N \cdot m^{-2}]$, M_α describes the interfacial forces acting on phase α due to the interaction with other phases $[kg \cdot m^{-2} \cdot s^{-2}]$, $S_{Mi,\alpha}$ is the sum of body forces acting on phase α, including the gravitational force $[kg \cdot m^{-2} \cdot s^{-2})]$ and $\mu_{eff,\alpha}$ is the effective dynamic viscosity of phase α $[kg \cdot m^{-1} \cdot s^{-1}]$:

$$\mu_{eff,\alpha} = \mu_\alpha + \mu_{t,\alpha} \tag{3.7}$$

here μ_α is fluid $\alpha' s$ dynamic viscosity $[kg \cdot m^{-1} \cdot s^{-1}]$ and $\mu_{t,\alpha}$ is the turbulent eddy viscosity $[kg \cdot m^{-1} \cdot s^{-1}]$.

The presented set of Navier-Stokes equations is written for the case where no mass exchange is present between the phases.

The interfacial forces, M_α, acting on phase α due to the presence of other phases are typically formulated into several interfacial forces. The most frequently used interfacial forces are:

$$M_\alpha = \sum_{\beta \neq \alpha} M_{\alpha\beta} = M_{\alpha\beta}^D + M_{\alpha\beta}^L + M_{\alpha\beta}^{VM} + M_{\alpha\beta}^{TD} + M_{\alpha\beta}^{HIST} + M_{\alpha\beta}^{LUB} \tag{3.8}$$

where the forces listed above, respectively represents the interphase drag force, lift force, virtual mass force, turbulent dispersion force, basset history term and lubrication force, all in the units $[kg \cdot m^{-2} \cdot s^{-2}]$. Often the interfacial drag force is by far the most dominating force of the above listed. The history and lubrication terms are mostly neglected. The remainder of the terms in equation 3.8 can be important dependent on the nature of the flow. In chapter 4, a more thorough discussion of the different force terms is included. It should be noted that the current model includes interphase momentum transfer between phase pairs, whereas a complete interaction between multiple phases in one time is not resolved. Hence, the complex interaction between e.g. wastewater, sludge flocs and air bubbles can not be accounted for in total, whereas e.g. the interaction between e.g. wastewater and air bubbles and water and sludge flocs can be resolved as pairs.

The interfacial forces between two phases are equal and of opposite direction, resulting in a zero net sum of the interfacial forces:

$$(M_{\alpha\beta} = -M_{\beta\alpha}) \Rightarrow \sum_{\alpha} M_{\alpha} = 0 \tag{3.9}$$

The interfacial transfer of momentum is directly proportional to the contact surface area between the different phases. The contact surface area between phase α and β can also be expressed as the interfacial area pr unit volume, or more useful as the interfacial area density, $A_{\alpha\beta}$. In the present model $A_{\alpha\beta}$ can be described with either a Mixture Model or a Particle Model. The Mixture Model describes the two phases symmetrically, and requires both phases to be continuous, whereas the Particle Model is applicable for interfacial transfer between a continuous and a dispersed phase. The Particle Model is applied for the present modelling with water as the continuous phase α, and either air bubbles or sludge flocs as the dispersed phase, β. The dispersed phases are assumed to be consistent of spherical shaped particles with mean diameters d_{β}. For the sludge flocs, the assumption of sphericity does not hold. This mistake is however to some extent accounted for by the introduction of a drag coefficient formula (Rasmussen, 1997) accounting for non-spherical, porous particles.

For spherical particles, the interfacial contact area can be calculated with the following expression:

$$A_{\alpha\beta} = \frac{6 r_{\beta}}{d_{\beta}} \tag{3.10}$$

Where $A_{\alpha\beta}$ is the interfacial contact area $[m^2 \cdot m^{-3}]$, r_{β} is the volume fraction of air $[m^3 \cdot m^{-3}]$ and d_{β} is the diameter of the air bubbles $[m]$.

3.3 Transport of oxygen, nutrients, organic compounds and biomass

The modelling of the transport of soluble components like e.g. soluble oxygen or ammonium is solved through the solution of an additional transport equation for these variables. The transport of soluble substances is governed by the transport-dispersion equation:

$$\frac{\partial C}{\partial t} + \frac{\partial \left(U_i \cdot C\right)}{\partial x_i} = \frac{\partial}{\partial x_i}\left(\left(\rho_\alpha \cdot D + \frac{\mu_{\alpha,t}}{Sc_t}\right)\frac{\partial}{\partial x_i}\left(\frac{C}{\rho}\right)\right) + S \tag{3.11}$$

where C is the concentration of the additional variable $[kg \cdot m^{-3}]$, D is the kinematic diffusivity of the investigated scalar $[m^2 \cdot s^{-1}]$, $\mu_{\alpha,t}$ is the turbulent dynamic viscosity of the continuous phase α $[kg \cdot m^{-1} \cdot s^{-1}]$, Sc_t is the turbulent Schmidt number (default: 0.9) and S is a source/drain term $[kg \cdot m^{-3} \cdot s^{-1}]$.

3.4 Turbulence modelling

In theory it is possible to solve any turbulent flow by solving the Navier-Stokes equations directly through Direct Numerical Simulation (DNS). It is though required that the length scale of the computational mesh and the timescale of the computation is chosen sufficiently small to resolve the smallest turbulent eddies and describe the fastest occurring processes. (Speziale, 1991) stated that a DNS of a turbulent pipe flow with Reynolds number, Re=500.000, would require a computer 10 million times faster than the Cray YMP supercomputer. The Cray YMP supercomputer had a 460 MFlop peak performance, corresponding approximately to a 2,0 GHz P4 computer. Hence, even with the available computing power today, it is only feasible to apply DNS for flows at considerable low Reynolds' numbers and small-scale flow problems. For this reason, turbulence can not be solved directly for many practical systems.

Furthermore, for most engineering applications it would not make sense to completely resolve the details of e.g. the smallest turbulent eddies. Instead various turbulence models describing the effect of turbulence on the mean flow field have been developed. In general the turbulence models are means for making closure to the system of Navier-Stokes equations, with the purpose of solving a large range of flow problems. The most important turbulence models to date can be grouped in to several types of models:

- Zero equation models
- Two-equation models
- Algebraic stress models
- Reynolds stress models
- Large eddy simulations

The turbulence models in the above mentioned list are written in order of increased complexity. The four first listed models are all applicable for the Reynolds averaged Navier-Stokes equations, whereas large eddy simulation is a model where both the mean flow and the largest eddies are resolved meanwhile the smallest eddies are modelled. The following presentation of the different turbulence models will possess the characteristics of an introduction. For further details, any turbulence textbook, e.g. (Wilcox, 2000) should be addressed.

The Zero and two-equation models are eddy viscosity models. The eddy viscosity model concept is build upon the assumption that turbulence is consisting of small eddies continuously

generated and dissipated, and that proportionality exists between Reynolds stresses and mean velocity gradients.

Beside the above-mentioned turbulence models, particle induced turbulence might also be important in many multiphase flows. Particle induced turbulence will be addressed in further details in the next chapter about the modelling of bubble generated flow systems.

In the present work the two-equation models have been applied for the description of the continuous water phase, whereas the turbulence of the disperse air bubbles and sludge flocs have been modelled through a disperse phase zero equation model. The disperse phase zero equation model relate the viscosity of the disperse phases to the continuous phase viscosity (CFX, 2005):

$$\mu_{t,\beta} = \frac{\rho_\beta}{\rho_\alpha} \cdot \frac{\mu_{t,\alpha}}{\sigma_t} \tag{3.12}$$

where $\mu_{t,\beta}$ is the turbulent dynamic viscosity of the disperse phase β $[kg \cdot m^{-1} \cdot s^{-1}]$, σ_t is the turbulent Prandtl number [-] ($\sigma_t = 1$ as default setting) and $\mu_{t,\alpha}$ is the turbulent dynamic viscosity of the continuous phase $[kg \cdot m^{-1} \cdot s^{-1}]$, determined from a two-equation turbulence model.

The somewhat special formulation, where the sludge particles (the flocs) has been assigned a finite viscosity, rather than considering the particles as pure solids, is connected to the definition of phases as described in section 2.2. The sludge floc comprise of a mixture of substances, whereby the main parts are the liquid substances water and exopolymers. The remainder of the substances in the sludge floc can be considered to be of solid like nature. In the model, the whole of the sludge floc is threaded as a fluid particle. When measuring the rheology of the activated sludge, the measurements are performed on the complete suspension of wastewater, sludge floc and other substances. Part of the observed increased viscosity of the suspension compared to the viscosity of *pure* wastewater, originates from solids-solids interactions between particles in the sludge. The solids-solids interactions between the particles are not accounted for in the model. Instead the increase of viscosity in the suspension is modelled through a corrected viscosity of both the water phase and the sludge particles. In this way the effect of solids-solids interactions are accounted for without directly dealing with interactions; the lack of a physically correct model is compensated through the application of a rheology model.

3.4.1 Two-equation models

Two-equation models are more sophisticated than zero equation models since they apply extra transport equations to account for the transport of turbulence properties. Especially the $k - \epsilon$ model has gained widespread application due to its robustness and applicability to general purpose simulations.

In the present work, two different two equation eddy viscosity models have been applied to the numerical model: the standard k-ϵ model (Jones and Launder, 1972), (Launder and Spalding, 1974) and the Shear Strain Transport (SST) model (Menter, 1996). Both turbulence models are based upon the eddy viscosity concept, as described in equation 3.7. Both models aim to determine the eddy viscosity with the use of two additional transport equations.

The standard k-epsilon model

In the standard k-ϵ model, the turbulence kinematic viscosity ν_t is calculated through the following relationship:

$$\nu_{eff} = C_\mu \frac{k^2}{\epsilon} \tag{3.13}$$

Here C_μ is the eddy diffusivity constant, equal to 0,09 $[-]$, k is the variance in the turbulent fluctuations, termed the turbulent kinetic energy $[m^2 \cdot s^{-2}]$ and ϵ is the dissipation of turbulence kinetic energy $[m^2 \cdot s^{-3}]$

k and ϵ are solved with the application of two additional transport equations (Jones and Launder, 1972), (Launder and Spalding, 1974):

Transport equation for k:

$$\underbrace{\frac{\partial k}{\partial t}}_{Rate\ of\ increase} + \underbrace{U_j \cdot \frac{\partial k}{\partial x_j}}_{Convective\ transport} = \underbrace{\frac{\partial}{\partial x_j}\left[\left(\nu + \frac{\nu_T}{\sigma_k}\right) \cdot \frac{\partial k}{\partial x_j}\right]}_{Diffusion} + \underbrace{\tau_{ij}\frac{\partial U_i}{\partial x_j}}_{Production} - \underbrace{\epsilon}_{Dissipation} \tag{3.14}$$

Transport equation for ϵ:

$$\underbrace{\frac{\partial \epsilon}{\partial t}}_{Rate\ of\ increase} + \underbrace{U_j \cdot \frac{\partial \epsilon}{\partial x_j}}_{Convective\ transport} = \underbrace{\frac{\partial}{\partial x_j}\left[\left(\nu + \frac{\nu_T}{\sigma_\epsilon}\right) \cdot \frac{\partial \epsilon}{\partial x_j}\right]}_{Diffusion} + \underbrace{C_{\epsilon 1} \cdot \frac{\epsilon}{k}\tau_{ij}\frac{\partial U_i}{\partial x_j}}_{Production} - \underbrace{C_{\epsilon 2} \cdot \frac{\epsilon^2}{k}}_{Decay} \tag{3.15}$$

Where σ_k is the Prandtl number for turbulent kinetic energy, equal to 1,0 $[-]$, σ_ϵ is the Prandtl number for the dissipation of turbulent kinetic energy, equal to 1,3 $[-]$, $\sigma_{\epsilon 1}$ and $\sigma_{\epsilon 2}$ are model constants, equal to 1,44 $[-]$ and 1,92 $[-]$ respectively and τ_{ij} is the shear stress $[N \cdot m^{-2}]$.

The shear strain transport (SST) model

The $k - \epsilon$ model does not account for the transport of turbulent shear stress, and consequently the model typically over predicts the eddy viscosity. Furthermore, the model fails to describe the extent of flow separation from smooth surfaces. This problem is solved in the SST model, where a limiter is added to the formulation of the eddy viscosity.

The SST equation is based on a blending of the Wilcox $k - \omega$ model in the sub-layer and logarithmic layer and the $k - \epsilon$ model in the wake of the boundary layer (Menter, 1996). The

$k-\epsilon$ model is rearranged in order to make two combinable equations. The Wilcox $k-\omega$ function is multiplied with a blending factor F1 and the modified $k-\epsilon$ model is multiplied by $(1-F_1)$. F_1 is equal to one in the log-layer and goes to zero in the wake region of the boundary layer.

In $k-\omega$ models, the turbulence viscosity are based upon the ratio between the turbulent kinetic energy and the turbulent frequency:

$$\nu_T = \frac{\mu_t}{\rho} = \frac{k}{\omega} \tag{3.16}$$

Where ν_t is the turbulent kinematic viscosity $[m^2 \cdot s^{-1}]$ and ω is the turbulent frequency $[s^{-1}]$

The combined $k-\omega$ and rearranged $k-\epsilon$ model results in the two following additional transport equations (Menter, 1996), (Menter *et al.*, 2003):

Transport equation for k:

$$\underbrace{\frac{\partial k}{\partial t}}_{Rate\ of\ increase} + \underbrace{U_j \cdot \frac{\partial k}{\partial x_j}}_{Convective\ transport} = \underbrace{\frac{\partial}{\partial x_j}\left[\left(\nu + \sigma_k \nu_t\right)\frac{\partial k}{\partial x_j}\right]}_{Diffusion} + \underbrace{\tilde{P}_k}_{Production} - \underbrace{-\beta^* k\omega}_{Dissipation} \tag{3.17}$$

Transport equation for ω:

$$\underbrace{\frac{\partial \omega}{\partial t}}_{Rate\ of\ increase} + \underbrace{U_j \cdot \frac{\partial \omega}{\partial x_j}}_{Convective\ transport} = \underbrace{\frac{\partial}{\partial x_j}\left[\left(\nu + \sigma_\omega \nu_t\right)\frac{\partial \omega}{\partial x_j}\right]}_{Diffusion} + \underbrace{\alpha\rho S^2}_{Production} - \underbrace{-\beta\omega^2}_{Decay} + \underbrace{2\left(1-F_1\right)\rho\sigma_{w2}\frac{1}{\omega}\frac{\partial k}{\partial x_j}\frac{\partial \omega}{\partial x_j}}_{Term\ from\ transformed\ k-\epsilon\ model} \tag{3.18}$$

Here F_1 is a blending function:

$$F_1 = \tanh\left\{\left\{\min\left[\max\left(\frac{\sqrt{k}}{\beta^*\omega y}, \frac{500\nu}{y^2\omega}\right), \frac{4\rho\sigma_{\omega 2}k}{CD_{k\omega}y^2}\right]\right\}^4\right\} \tag{3.19}$$

$$CD_{k\omega} = \max\left(2\rho\sigma_{\omega 2}\frac{1}{\omega}\frac{\partial k}{\partial x_j}\frac{\partial \omega}{\partial x_j}, 1.0\cdot 10^{-10}\right) \tag{3.20}$$

Where ν is the kinematic viscosity of the fluid $[m^2 \cdot s^{-1}]$ and y is the distance to the nearest wall $[m]$

Apart from the blending between the $k-\epsilon$ and the $k-\omega$ models, the SST model also include an altering of the eddy viscosity in order to account for the transport of the turbulent shear stress in adverse pressure gradient flows:

$$\nu_t = \frac{a_1 k}{\max\left(a_1\omega, SF_2\right)} \tag{3.21}$$

where S is the shear strain rate $[s^{-1}]$

$$F_2 = \tanh\left[\left[\max\left(\frac{2\sqrt{k}}{\beta^*\omega y}, \frac{500\nu}{y^2\omega}\right)\right]^2\right] \tag{3.22}$$

The production term in equation 3.17 is arranged with a limiter in order to prevent built-up of turbulence in areas of stagnation:

$$\tilde{P}_k = min\left(P_k, 10\cdot\beta^*\rho k\omega\right) \tag{3.23}$$

where:

$$P_k = \mu_t \frac{\partial U_i}{\partial x_j}\left(\frac{\partial U_i}{\partial x_j} + \frac{\partial U_j}{\partial x_i}\right) \tag{3.24}$$

On basis of the standard $k-\epsilon$ and the Wilcox $k-\omega$ model, the model constants for the SST model is calculated on behalf of the blending function F1:

$$\alpha = F_1\alpha_1 + \left(1 - F_1\right)\alpha_2 \tag{3.25}$$

Where α is the model constant to be transformed $[-]$, α_1 is the corresponding model constant from the original Wilcox $k-\omega$ equation $[-]$ and α_2 is the corresponding model constant from the transformed $k-\epsilon$ equation $[-]$.

The model constants used in equations 3.23 and 3.25 are listed below (Menter *et al.*, 2003): $\beta^* = 0.09$, $\alpha_1 = 5/9$, $\beta_1 = 3/40$, $\sigma_{k1} = 0.85$, $\sigma_{\omega_1} = 0.5$, $\alpha_2 = 0.44$, $\beta_2 = 0.0828$, $\sigma_{k2} = 1$, $\sigma_{\omega 2} = 0.856$.

The SST-model is superior to ϵ based models for modelling flows with adverse pressure gradients, a feature often occurring at airfoils, diffusers and heat exchangers (Carregal-Ferreira *et al.*, n.d.). The model is better at predicting the onset and amount of separation and also better at describing recirculation flow. For these reason it is believed that the SST model should be better than the standard $k-\epsilon$ model for describing the flow in process tanks, where situations of sudden geometry change an swirling flow or diffuser flow are common.

The above-described system of equations comprise of the framework of the hydrodynamic model of the present process tank model. Due to the non-linearity of the model, and the massive amount of equations needed to be solved, special solution techniques are needed in order to solve the model. In the present model, the finite volume method (FVM) forms the basis of the solution technique. The principle of the FVM technique and the general solution technique of the present model, can be viewed in Appendix A.

CHAPTER 4
Detailed analysis of sub processes

As indicated in chapter 2, a complete description of a wastewater treatment process tank involves a large amount of complicated sub processes. The sub processes are both of physical and biological nature, and often they can only be described through a combination of physics and biology. Without the ability to accurately describe these processes, the construction of an integrated process tank model seems an impossible task. Some of the physical processes like the mean and turbulent flow and density currents are automatically included in the hydrodynamic multiphase CFD-model discussed in chapter 3. Some of the other processes are however not described by a direct application of the models presented in the previous chapter. Consequently a number of sub-processes have been closely investigated in order to make sufficient closure to the integrated model of the process tank:

- The hydrodynamics of the aeration system
- The hydrodynamics of mechanical agitation equipment
- The sedimentation process
- The rheology of the suspension
- The integration of a detailed biological model

Commercially, a large diversity of aeration systems and products for creating the mechanical agitation in process tanks are available. Some of the most popular of the these products have been chosen for the analysis in the present work; a dish shaped air diffuser of the type used for bottom mounting in the tanks and a slowly moving large diameter two-bladed hydrofoil shaped propeller. These to types of products are common in many WWTP's in Denmark.

The implementation of the sludge concentration and turbulence dependent sedimentation model developed by (Rasmussen and Larsen, 1996), (Rasmussen, 1997), will be implemented and tested in the model. Furthermore, a non-Newtonian model for describing the flow of the suspension is set up based on simple experiments in a tube viscometer, constructed for on-site measurements.

Finally the implementation and validation of the ASM3 model for describing the biological processes in the activated sludge suspension is included.

4.1 Analysis of bottom mounted air diffuser

The aeration system is an important operational unit in an activated sludge process tank. The aerobic processes in the activated sludge system is highly dependent on the availability of sufficient quantities of oxygen (Tchobanoglous and Burton, 2003). In general the aeration system is responsible for:

- Supply of sufficient amounts of oxygen for the biological turnover of biologically degradable organic material, the endogenous respiration of the biomass and the nitrification process
- Adequate mixing of the suspension

The aeration system can either be a diffused-air system or a mechanical system. The two types of systems have the same function, but hydrodynamically they work very different (Chapter 2). In the diffuser, air is compressed to the hydrostatic pressure and released to the surrounding water in the form of small air bubbles, while the mechanical aeration usually aerate the water by whipping air bubbles into the water phase through the top mounted surface aerator. The present experiments and modelling deals with the diffused-air system, whereas mechanical treatment not will be subject to any further investigations.

Because of the importance of a well functioning aeration system, it is consequently important to have a comprehensive knowledge of the hydrodynamics of the aeration system. For that reason experiments regarding the local flow conditions around a diffuser have been performed at the Hydraulics and Costal Engineering Laboratory at the Department of Civil Engineering, Aalborg University.

Beside the experimental analysis, a numerical model complimenting the experimental data has been constructed.

4.1.1 Experimental methods for investigating two-phase bubbly flow

Gas-liquid flow is a very important process in many bioreactor systems throughout the industrial sectors. Examples where gas-liquid flow plays an important role are: bioreactors used in biotechnology and process tanks on wastewater treatment plants. Because gas-liquid flows play such a major role in many processes, much work have been done on describing this kind of flow properly through experiments and numerical simulations. Some of the most important experimental techniques and experimental work done by other authors will be discussed in the present section.

Proper model verification is an important task in creating trustworthy CFD models. The verification is however highly dependent on good quality data for comparisons between model and reality. Since multiphase systems generally are complex involving several phases, and the visibility through the different phases can be scarce, measuring is not an easy task. Considering these needs and challenges, good measurement techniques have been a scientific topic for many years. Some of the techniques have been transferred from single phase measurements with varying success. Among the most common used techniques are:

- Hot Film Anemometry (HFA)
- Laser Doppler Anemometry (LDA)
- Phase Doppler Anemometry (PDA)

- Particle Image Velocimetry (PIV)
- Doppler Ultrasound Velocimetry (DUV)
- Electric Conductivity Probes (ECP)

The above listed techniques can not necessarily be applied to measure the same quantities. Some are best suited for measuring void fractions, whereas others are for measuring velocity components. Below the techniques are grouped into techniques for measuring void fraction and techniques for measuring velocity components. In this connection other authors' experiences with the different techniques are discussed.

Void fraction measurements

Void fractions or solids concentrations are important measures in almost any kind of multiphase system. For global gas void fraction or hold-up in a bubble column, a simple calculation applying knowledge of the aerated column and non-aerated suspension volumes, can be performed (Chaouki *et al.*, 1997):

$$r_{\alpha,global} = (H_g - H_0)/H_g \tag{4.1}$$

where $r_{\alpha,global}$ is the global volume fraction of air $[m^3 \cdot m^{-3}]$, H_0 is the pressure level of the liquid in the bubble plume without bubble injection [Pa] and H_q is the pressure level of the liquid in the bubble column with air injection [Pa]. The simple relation described in equation 4.1 has, as will be described later, been successfully applied for the calibration process of an ultrasonic probe used for local measurements of the mean volume fractions of air.

Other simple methods for measuring the global void fraction are pressure drop measurements along the bubble column and the use of quick closing valves. Also impedance void meters can be applied. Impedance void meters take advantage of the liquid and disperse phases different conductivity when the void fraction is calculated. (Chaouki *et al.*, 1997)

If one wishes to measure local void fractions, other somewhat more sophisticated methods must be employed. Radiation techniques are accurate and non-intrusive, but are expensive and health and security issues might also be a problem. Ultrasound probes exploits that water attenuates the ultrasound more than air and can be applied to systems with void fractions less than 10-15%. Electrical probes takes advantage of the different conductance, resistance or capacitance in the continuous and disperse phase to calculate the local void fraction. A conductivity probe connected to a wall in a gas-liquid flow system would act as an on/off switch delivering binary signal dependent on what material get in contact with the probe. (Chaouki *et al.*, 1997)

(Pfleger and Becker, 2001) measured the local void fraction with an electrical conductivity probe in a cylindrical bubble column. The authors reported the method to be fairly unidirectional. Hence, the method worked well for straight upward rising bubbles, whereas the void fraction was believed to be underestimated in zones with horizontal or downward flowing bubbles.

From an accuracy point of view it would seem most attractive to acquire a non-intrusive method for measuring the local void fraction in the bubbly flow. Due to the health issues with the radiation technique, this has however been ruled out. From the above-listed intrusive methods it is hard to say that one should be better than the other. For this reason it has been chosen to construct a local void fraction meter on the basis of some of the existing equipment in the

laboratory. Consequently, an ultrasonic probe has been applied for the measuring of mean local volume fractions of air in the present investigation (Subsection 4.1.4).

Velocity measurements

When it comes to measuring bubble size and velocity in gas-liquid systems the amount of available measuring methods narrow down. Several practical difficulties are associated with experimental measurements of the flow field in bubble columns. Special attention needs to be taken in order to discriminate between the liquid and gas phase.

LDA measurements The LDA technique is a well established non-intrusive measurement technique in single phase flow. However, multiphase flow systems introduce complications that affect the performance of the LDA technique:

- High volume fractions of bubbles reduce the penetration of the laser beam
- The LDA technique can only give point wise information of the velocities, making whole-field visualization cumbersome
- Refraction at the walls of the bubble columns
- Advanced signal processing necessary to separate phase velocities

Because the presence of bubbles will reduce the penetration length of the laser beams, LDA measurements are in general not possible in many practical multiphase flow situations. Since the LDA technique only give point wise information in space at a particular time, it is very hard to capture the dynamics of the whole flow field. Time-averaged LDA measurements would give a steady-state solution of the flow field.

A major drawback of the LDA technique is the difficulty to relate the measured signals to the correct phase/phases. Since the LDA does not provide certain phase discrimination between the two phases, it is often necessary to apply a phase detector in order to distinguish the part of the signal that belongs to the continuous phase.

Often LDA measurements are performed outside the fluid media itself. In such situations refraction from the surface of the fluid container can give rise to complications, making measuring through curved surfaces problematic.

In order to overcome these practical problems, bubble columns in the laboratory are often relatively small in dimension. With good measurements through the whole depth of the bubble column in mind, flat bubble columns with a depth of only a few cm are often preferred. This is in contrast to the present study, where a large scale bubble plume is studied, given raise to multiple of the previous described issues. Despite of the above-mentioned drawbacks, several investigations have been performed successfully on especially small scale bubble columns:

(Suzanne *et al.*, 1998) performed simultaneous LDA and HFA measurements of liquid velocities in a bubbly flow. When proper noise filtering where applied to the LDA measurements and the velocity drop due to bubble passages of the HFA where taken out of the data, the two methods showed very similar results. With proper filtering of the measured signal the LDA technique performed well for void fractions below 2%. For void fractions above 2% the LDA technique was no longer suitable.

(Groen *et al.*, 1999) gave a detailed description of the experience with their application of the LDA technique in bubbly flows. Both the forward and back scatter installations were applied and compared. The measurements were conducted on single bubbles and compared to photos taken with a high-speed camera. The authors found that almost all of their measured signals were related to velocities of the liquid phase, whereas the possibility of measuring the velocity of a bubble was relatively small. The authors did however measure an increase in the measured liquid velocity in the areas closely following and preceding a bubble. A bubble itself would only give rise to a measured velocity if the laser beams were intersecting the bubble surface almost perpendicularly. If back scatter mode was applied the use of seeding particles was recommended in order to get a reasonable data rate.

(Vassallo and Kumar, 1999) Used LDA to measure simultaneous gas and liquid velocities in a thin vertical rectangular bubble plume. Discrimination of the phase velocities were obtained through the use of amplitude discrimination. 5 μm latex seeding particles were used as liquid phase tracers. The LDA measurements showed good agreement with concurrent high speed photographs and HFA measurements.

(Pfleger and Becker, 2001) used a backscatter arrangement to measure liquid velocities in a large cylindrical bubble column. The authors reported a maximum measuring depth of 15 cm. With the use of seeding particles a data rate of 100 Hz could be obtained near the column walls, whereas the data rate was as low as 1 Hz in the centre of the column. Local gas hold-up was measured with a electric conductivity probe. Also (Becker *et al.*, 1999) applied the LDA technique to bubble plume experiments. They used a backscatter arrangement and metal coated 12 μm glass particles as tracers for the liquid phase. Characteristics of the dynamic movement of the bubble plume were captured through fast fourier transformation, and characteristic frequencies of the lateral movement of the plume could be calculated. The authors found a characteristic low frequency of the whole column in a flat rectangular bubble column, whereas no characteristic frequency valid for the whole column could be found for a cylindrical bubble column.

(So *et al.*, 2003) used a combination of LDA technique and high-speed digital cameras to measure liquid velocities and gas hold-up in a vertical circulating water tunnel with liquid-gas flow. The velocity components of the water were measured with LDA and the gas hold-up was measured with the high-speed cameras.

PDA measurements Phase Doppler anemometry (PDA) is a further development of the LDA technique, where two receiving lenses and photo detectors are applied instead of one. It is possible to measure both the liquid and particle velocities, but also the particle sizes can be determined by comparing the phase shift from the two detectors (http://www.dantecdynamics.com, 2005).

Since the technique is an extension of the LDA technique, the problems associated with the LDA technique also apply to the PDA technique. The use of an extra receiving sensor can however to some extent exclude phase discrimination problems.

(Bröder and Sommerfeld, 1998) applied PDA to obtain liquid phase velocities and bubble phase properties. Seeding particles were applied to improve the measuring of liquid velocities and an optical filter was applied to separate the signal from the two phases.

(Brenn *et al.*, 2002) used the PDA technique to perform measurements of the liquid and the bubble velocities and the bubble size distribution in a small model bubble column. They found that large bubbles were generally located at the centre of the column, whereas the smaller bubbles to some extent were entrained into the recirculation zones. In the lower parts of the

bubble column the flow field was highly unsteady and the possibility density functions of the liquid and the bubble velocities were bimodal. In the upper part of the column the velocities were unimodal and the flow field possessed a quasi-stationary condition.

HFA measurements The Hot-Film Anemometry (HFA) method is a well proved technique in single phase flow (Bruun, 1996). Since the HFA probe needs to be in contact with the fluid during measurements, the method is intrusive. The method's advantage over LDA is that it can also work for dense bubbly flows. Since the HFA voltage signal is both fluid and temperature dependent, one disadvantage of the HFA technique is the need for calibration. For bubbly flow, significant drops in the liquid velocity signal appears when bubbles pass the probe. This is due to the change in heat transfer coefficient.

As described in the paragraph about LDA measurements (Suzanne *et al.*, 1998) performed simultaneous HFA and LDA measurement of the liquid velocity in bubbly flow.

Also (Sun *et al.*, 2002) performed simultaneous HFA and LDA measurements of the liquid velocity. A threshold scheme based on information of the local void fraction measured by a conductivity probe and the velocity distribution in single phase flow was constructed for the LDA measurements. For the HFA an amplitude threshold scheme was applied. The drawback of the LDA method was the necessity of accurate void fraction measurements, whereas a drawback of the HFA measurement method is the dependency upon local temperature measurements.

PLV/PIV measurements The Pulsed-Light Velocimetry (PLV) or Particle Image Velocimetry (PIV) technique can be utilized to make instantaneous flow field measurements in slice planes in various multiphase flow situations. Typically a pulsed light sheet is emitted into the bubble column by a laser. One or two digital CCD cameras are used to capture the flow fields of the liquid and the bubbles. In order to discriminate the two phases, tracer particles are applied to the liquid phase and different optical band-pass filters are applied to the cameras. By using a frame grabber on a pc, the data can be collected and transformed into vector plots showing velocities and fluctuating velocities. The vector plots are achieved by measuring the movement of particles between light pulses.

(Delnoij *et al.*, 1999*a*) applied the PIV technique to measure liquid and bubble velocities in a 1.0m high bubble column. They used one CCD camera in a double exposure mode with an image shift. The technique revealed the complexity of the liquid flow field in the bubble column. By subtracting mean bubble and liquid velocities, a slip velocity of $0.22m \cdot s^{-1}$ was obtained, corresponding well to the steady rise velocity of a $2mm$ air bubble in a quiescent bubble column (Clift *et al.*, 1978).

(Bröder and Sommerfeld, 2002) applied this technique to a small-scale bubble column, and deduced both liquid and bubble mean velocities and fluctuating velocities. The method was compared to PDA measurements and showed good accordance with these measurements. For measurements on the liquid phase, the method was due to the reduced optical access caused by the bubbles only applicable at distances halfway through the bubble column ($7cm$). When measuring on the bubble phase, the method was applicable all the way through the column with a diameter of $14cm$.

(Deen and Hjertager, 2002) used PIV for measuring the liquid velocities in a stirred and aerated reactor. The reactor was stirred with a six-blade Rushton turbine. Both mean and fluctuating velocities were compared to measurements performed by other workers. Compared to single phase flow, trailing vortices from the blade diminished during aeration and the flow was

shifted from axial in single phase flow to a more radial character in the two-phase flow. Also the flow field seemed to be less periodic and the measured velocities lower.

DUV measurements In Doppler Ultrasonic Velocimetry (DUV), ultrasonic pulses are emitted from a probe into the fluid stream. When the ultrasonic pulses are reflected by small particles in the fluid, these ultrasonic echoes will due to the Doppler effect be registered with a phase shift in a receiver. Like in the LDA method, the fluid velocity is calculated on behalf of this phase shift.

(Wang *et al.*, 2003) applied Doppler ultrasonic velocimetry (DUV) to liquid-solid and liquid-gas systems. For low void fractions, the method was applicable for measuring both liquid and bubble mean velocities. A slip velocity of approximately 0.2m/s was obtained from the measurements in the recirculated bubble plume. The method was intrusive since the ultrasonic probe had to be placed in the flow field with the transmitter/receiver placed with the front to the flow direction in order to obtain a known Doppler angle.

Concluding on the multiphase measurements review, no technique for proper determination of flow characteristics and bubble size distributions are available for practical large-scale bubble flow system. This is mainly due to the low visibility of the system, where bubbles reflect and cover for the light of laser beams. As a consequence of this limit in possible measurement distance, nearly all measurements performed on bubble plumes are originating from small-scale bubble plumes. An intrusive method involving a small measurement impeller normally used for measuring in single phase flows has thus been applied and corrected for the current bubble flow system (Subsection 4.1.4).

4.1.2 Numerical methods for investigating two-phase bubbly flow

Several investigations involving numerical computations and experiments have been conducted on bubble columns during especially the last decade. An overview of some of this work is listed in the following subsections.

(Devanathan *et al.*, 1995) performed three dimensional Two-phase Euler-Lagrange modelling on a 25 liter bubble column. They found the flow to be highly chaotic with flow structures up to a length scale of approximately one column diameter. Since the circulating flow structures had a tendency to capture air bubbles, the flow structures would eventually move upwards in the column due to a decreased local density. The authors compared their model to rough experimental data where a neutrally buoyant tiny particle was tracked with a particle tracking method.

(Sokolichin *et al.*, 1997) compared 2D Eulerian/Eulerian and Eulerian/Langrangian two-phase models on a flat bubble column of 1.5m height in the case of both local and uniform aeration. The effective viscosity of the mixture of air and water was assumed to be equal to the viscosity of water. For the Eulerian/Eulerian case, both the first order UPWIND scheme and a second order accurate Total Variation Diminishing (TVD) scheme was applied for discretizing the convective fluxes. I.e. a limiter was multiplied to the second order flux in areas of large discontinuities, making the scheme go towards UPWIND discretization in such cases. Due to numerical diffusion effects the UPWIND scheme proved to give considerably different results compared to the remainder of the results, whereas the Eulerian-Lagrangian and the second order discretized Eulerian-Eulerian model proved to be quite similar. When properly discretized the

authors could not separate the results of the Eulerian-Eulerian model from the results of the Eulerian-Lagrangian model.

(Solbakken and Hjertager, 1998) investigated the flow pattern in a pilot and a full scale bubble column both experimentally and numerically. They used a two-fluid Euler-Euler model and applied 2 different drag models. Both drag models seemed to perform well. The inclusion of a bubble size dependent lift force was implemented in order to model a correct void distribution. The numerical model was substantiated through concurrent Laser Doppler Anemometer (LDA) experiments.

(Lain *et al.*, 1999) applied an Euler-Lagrange scheme to the simulation of the experimental results obtained by (Bröder and Sommerfeld, 1998). The simulations showed that drag curves applicable for fluid particles performed significantly better than drag curves for rigid particles. Also the inclusions of bubble size distributions seemed to improve the accuracy of the simulation of the correct bubble-rise velocities. Moreover, the application of additional sources to the standard $k-\epsilon$ turbulence equation had a drastic effect on the modelling results. The authors found that the drag in bubble swarms seemed to be reduced comparing their data with terminal velocities for single bubbles. The investigations were resumed in (Lain *et al.*, 2001), where new formulations of the $k-\epsilon$ source terms were tried out through modelling on the data from the same bubble column. They did however not find a sufficiently adequate way of modelling the influence of the bubble phase on the fluctuating turbulent kinetic energy of the liquid phase. A further investigation into the subject was suggested for future research.

In (Sokolichin and Eigenberger, 1999), comparisons of 2D and 3D two-phase models of a 1.5m high flat bubble column were conducted. For the 2D model both laminar and $k-\epsilon$ turbulence modelling was tried out. The 2D model proved to be highly dependent on the grid refinement, with the number of vortices increasing as the grid was refined. Moreover, the 2D model with the $k-\epsilon$ dampened out the dynamic of the bubble plume because of an overestimated effective viscosity. Moving to 3D modelling of the plume, the low frequency movement of the plume could be resolved due to a more correct modelling of the effective viscosity.

(Borchers *et al.*, 1999) applied a 3D Euler-Euler two-phase model with constant slip velocity between the two phases to a small-scale bubble column. The work was an extension of the work described in the article by (Sokolichin and Eigenberger, 1999). The standard $k-\epsilon$ turbulence model was applied and quantitatively the model showed good agreement with long time averaged liquid velocities. Qualitatively the model also was in compliance with video images showing the shape and the spreading of the bubble swarm and the shape of the liquid vortices.

(Delnoij *et al.*, 1999*b*) used a 3D Euler-Lagrange two-phase flow model to calculate the effect of bubble column aspect ratio on the overall liquid recirculation pattern. The model included drag, lift and virtual mass forces. The results were not compared to experimental work, but the model showed that low aspect ratios resulted in a distinct *cooling tower* effect with upflow at the centre of the column and downflow at the sidewalls. At higher aspect ratios dynamic modelling showed that the flow shifted to a more dynamic behaviour with multiple staggered vortices, whereas the bubble column still resembled the *cooling tower* effect during steady-state computations.

Also (Friberg and Hjertager, 2000*a*) performed numerical analysis of the flow pattern in bubble columns. A two-fluid Euler-Euler model was again applied, and different models with various interfacial force terms were compared. Again the inclusion of the lift force seemed to be important. Also the choice of drag model would give different results, especially with respect to modelling the correct void fraction, but none of the models predicted the gas fraction precisely.

The choice of lift force did show a drastic effect on the predicted radial profiles of velocities and void fractions.

(Deen *et al.*, 2000) applied a 3-dimensional two-fluid Euler-Euler scheme for the modelling of both a flat and a squared bubble plume. The drag force was the only interfacial force included in the model. Bubble induced turbulence were taken into account in the k-ϵ model. The simulations where transient and in case of the flat bubble column a pseudo periodic movement was found that corresponded well with experiments. The oscillation period was 20 seconds overestimated. Velocities and velocity fluctuations were well correlated with experiments. The squared bubble column showed too little time dependency compared with experiments. These shortcomings were sorted out later (Deen *et al.*, 2001), and the authors extended their model to include Large-Eddy simulation (LES). Also lift force and virtual mass force terms were included in the model. The lift force proved to have a great impact on the spreading of the bubble plume, whereas inclusion of virtual mass force only had little effect. Compared to the earlier modelling with the k-ϵ model in (Deen *et al.*, 2000), the LES simulation resolved much more of the measured details of the flow, and also the transient movement of the bubble plume was captured.

A single phase model describing the steady-state hydrodynamics of a bubble plume was developed by (Bernard *et al.*, 2000). The buoyancy force in the bubble plume was modelled through a simple approximation, making the buoyancy force proportional to the acceleration of gravity, g, and the local volume fraction of air bubbles r_β. The bubble plume was assumed to be cylindrical of shape, and a constant slip velocity between water and air bubbles was assumed. Comparisons to experiments proved the model to be sufficiently accurate for reproducing time-averaged far field mixing, whereas the model due to its limitations had reduced accuracy within the plume itself.

(Pfleger and Becker, 2001) employed a 3-dimensional two-phase model to a $2.6m$ high bubble column. The interfacial drag force was applied with basis in a constant slip velocity of $0.2m/s$. No other interfacial forces were modelled. Turbulence was modelled through the standard $k-\epsilon$ model, but additional production terms were added to the transport equations for k and ϵ. The extra production terms accounted for additional stresses caused by the wakes behind the rising bubbles. Both long time averaged profiles of the velocities and the void fraction were in good agreement with the measurements. Also the large scale fluctuations of the bubble plume could be captured. Both the application of bubble induced turbulence and grid refinements had a positive effect. The authors did however conclude that the accuracy of the numerical investigations had to be a compromise between grid density and computational efforts.

(Buscaglia *et al.*, 2002) compared CFD modelling with 1D integral modelling for a single bubble plume in a deep biochemically active reservoir. The hydrodynamic 2-phase mixture model was coupled with a mass-transfer model, accounting for the transfer of oxygen from the gas to the liquid phase. The standard k-ϵ model was applied and no additional bubble induced turbulence was formulated. The model assumed a bubble slip velocity that only depended on the bubble radius. Comparisons between the 1D integral model and the 3D CFD models showed good agreement with respect to gas hold ups, bubble diameter, liquid velocity and gas dissolution rates. The entrainment coefficient correlated well with experimental observations.

(Lain *et al.*, 2002) extended their earlier investigations (Lain *et al.*, 1999) to a more detailed examination of the source terms due to bubbles in the $k-\epsilon$ equation. Again the Euler-Lagrange formulation was used on the data from (Bröder and Sommerfeld, 1998), and their findings indicated that the modelling of the source term induced by bubbles in the $k-\epsilon$ equation was important in order to model the hydrodynamic behaviour of a bubble column.

A large-scale bubble plume was investigated numerically by (Zboray and de Cachard, 2005) and the simulations were compared to measurements performed by (Simiano *et al.*, 2004). A two-phase scheme in both two and three dimensions was applied, as well as different interfacial transfer and turbulence models were tried out. The simulation results proved the importance of including the appropriate models for the lateral forces on the bubbles. They found that especially the right turbulent dispersion model had great influence on the modelling results.

From the literature review it appears that both Eulerian-Eulerian and Eulerian-Lagrangian multiphase schemes can be applied to bubble flow systems with success. In some cases where concurrent numerical investigations have been done with both models, the results have been equally good. Due to the nature of the Eulerian-Lagrangian scheme, this type of model is however not feasible for large systems with millions of particles, like in e.g. large process tanks. For that reason, it is chosen to use an Eulerian-Eulerian scheme for the remainder of this thesis.

With respect to the inclusion of interfacial momentum transfer terms, the tendency is not perfectly clear, although most authors state the importance of the inclusion of interfacial force terms for the modelling of the lateral spreading of the plume. Several of the interfacial force terms have been included and excluded with success in the simulations performed by different authors. Hence, no clear picture are available for setting up the perfect model for a given bubble flow system. The choice of appropriate interfacial force terms seems to be highly dependable on the specific characteristics like bubble and fluid domain size and superficial gas velocities etc. Since the present investigation is different to most of the above discussed investigations due to especially the large scale of the geometry of the model, it does not seem justified to strictly transfer setup from experiments performed by other investigators to the present experiment.

The choice of detail with respect to turbulence modelling, seem to have a drastic effect on the modelling results, and especially on the nature of the available information coming out of the model. The transient movement of a swirling bubble plume is hardly to be captured right with the eddy viscosity models like the $k - \epsilon$ model, whereas the steady-state profiles of volume fractions and velocities can be sufficiently captured. Since the measurements in the present work are steady-state of nature, available data justifying a more rigorous turbulence model is not available; Consequently, the choice of an eddy viscosity model seems plausible for the present investigation. The choice of eddy viscosity model for many of the investigations represented in the literature review has been the standard $k - \epsilon$ model, modified through especially additional source terms, accounting for the altering of the turbulence induced by the presence of the bubbles. This is perhaps not surprising, since the standard $k - \epsilon$ model has been the most popular turbulence model for many practical single phase flow systems.

Should the need for a correct modelling of the transient movement of the plume however be present, more deterministic turbulence models seems to be a means for modelling the very transient and complex nature of the flow within a bubble plume.

4.1.3 Plume theory

Before going further into the present measurements and numerical modelling, a brief introduction to plume theory is appropriate.

Numerical integration of point source air-bubble plume in stagnant water

For limited cases with straight-forward stationary boundary conditions and quiescent background media, bubble plume hydrodynamics can be solved by numerical integration.

(Ditmars and Cederwall, 1974) developed models for describing the velocities, plume width and induced flow rates in bubble plumes derived form either point- or line-sources. The models were applicable for the part of the plume beneath the zone influenced by horizontal flow. Hence the flow in the upper part of the bubble plumes, near the surfaces, can not be calculated with this type of model. Furthermore the models developed by (Ditmars and Cederwall, 1974) are only applicable for media without density layers. For cases with air injection in media with stratification, (McDougall, 1978) later developed an applicable model.

(Brevik and Killie, 1996) took a slightly different approach than (Ditmars and Cederwall, 1974), where the behaviour of an axisymmetric air-bubble plume was solved by the use of a continuity equation and balance equations for momentum and kinetic energy. Differently from the work in (Ditmars and Cederwall, 1974), where an assumption of proportionality between the rate of entrainment and the centreline velocity was applied, this assumption was neglected and an assumption of self-preservation of the dominant Reynolds-stress component was applied (Brevik and Killie, 1996). Below the model of (Ditmars and Cederwall, 1974) is presented.

When air is discharged into a body of water, a vertical rising turbulent plume will develop (Figure 4.1). This upward rising plume is a direct consequence of the reduced density of the mixture of air and water in the centre of the column. As the plume rises towards the water surface, ambient water is entrained in to the plume, making the plume wider as the distance to the source is increased.

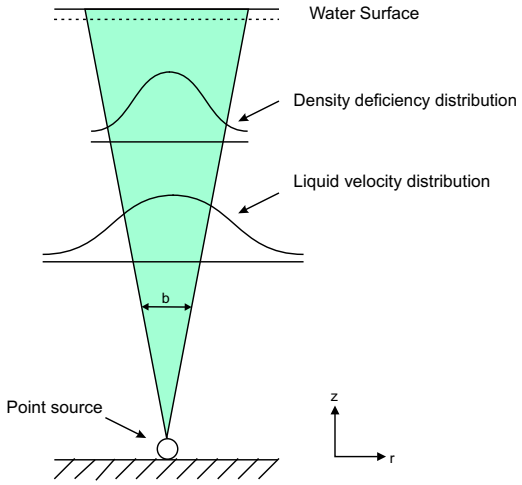

Figure 4.1 Outline of ideal bubble plume originating from a point source.

As outlined on figure 4.1, the distributions of the velocity of the rising plume and density deficiency between the plume and the surrounding water are Gaussian of nature:

$$w(z,r) = w_m(z)e^{-r^2/b^2} \tag{4.2}$$

$$(\rho_\alpha - \rho_{\alpha\beta})(z,r) = \triangle\rho_m(z)e^{-r^2/(\lambda b)^2} \tag{4.3}$$

where $w(z,r)$ is the axial liquid velocity in the plume as a function of the axial coordinate z and the radial coordinate r $[m \cdot s^{-1}]$, $w_m(z)$ is the centerline liquid velocity as a function of z $[m \cdot s^{-1}]$, ρ_α is the density of the ambient water $[kg \cdot m^{-3}]$, $\rho_{\alpha\beta}$ is the density of the mixture of air and water in the bubble plume $[kg \cdot m^{-3}]$, $\triangle\rho_m(z)$ is the density deficiency at the center of the bubble plume as a function of the axial coordinate $[kg \cdot m^{-3}]$, λ is the lateral spreading ratio $[-]$ and b is the characteristic lateral dimension of the plume $[m]$. The characteristic lateral dimension of the plume, $b(z)$, is defined upon the standard deviation, σ, of the lateral velocity distribution:

$$\sigma = b \cdot \sqrt{2} \tag{4.4}$$

Later, equation 4.2 and 4.3 will be related to the measurements performed on a bubble plume generated by a bottom mounted air diffuser used for aeration of sludge in an activated sludge process tank.

By solving the buoyancy-flux and the momentum equation for the bubble plume by numerical integration, the centreline velocity, w_m, and the lateral dimension b, the volume flux and the width of the bubble plume can be determined. Beside the rate of gas injection at the source, the only parameter needed to solve the equations is the slip velocity between the water phase and the air bubbles, a parameter that can be estimated by e.g. the use of (Clift *et al.*, 1978).

4.1.4 Description of laboratory experiments

The laboratory experiments were performed in a pit, placed in the middle of a larger shallow watered basin. In order to get as developed a bubble plume as possible, the diffuser was positioned at the bottom of the pit.

Experimental setup

Figure 4.2 shows an outline of the geometry of the basin and pit used for the experiments.

The depth, width and length of the pit were 1.5, 2.10 and 2.1m, respectively. The top of the pit was only open in one end. The water level above the pit was 0.5m, and the total water depth 2,0m. The pit was positioned at the bottom of a larger basin, normally used for generation of offshore waves.

Air was injected through a circular disc diffuser from a wastewater treatment plant process tank. The diffuser material was fine pored flexible rubber, where the size of the pores depends on the applied air flow rate. The inflow of air was monitored with a Cole Parmer correlated flow meter and kept constant at the inflow rate of 0,028 $[m^3 \cdot min^{-1}]$. On figure 4.3 the diffuser is located at the circular ring at the pit floor, indicating the inlet of air. The left side of figure 4.3 shows the position of the diffuser, seen from the top of the pit.

As indicated on figure 4.3, the active diffuser area of the disc, is an approximately 2 cm wide band, consisting of a membrane perforated with small holes. Figure 4.4 shows a picture of the diffuser, taken during one of the measurements in the laboratory.

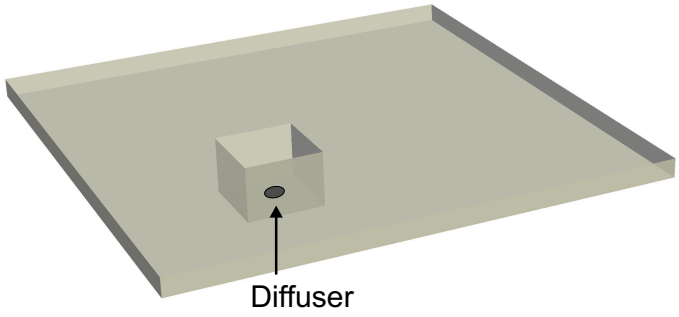

Figure 4.2 Outline of the geometry of the basin and pit.

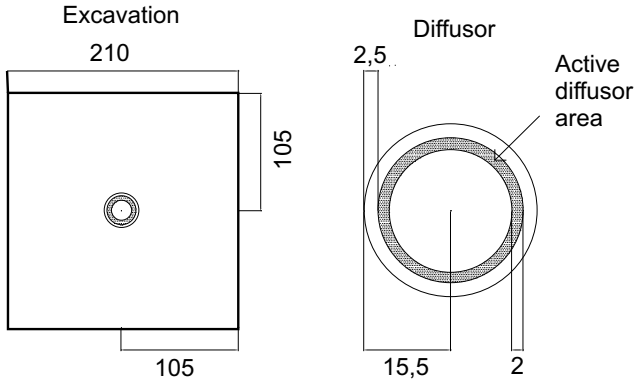

Figure 4.3 Left: Location of diffuser in basin pit. Right: Visualisation of active diffuser area. The shown distances are in cm.

Immediately after the bubbles escape the diffuser, they tend to have an inward motion. This is possibly a result of a combination of the geometry of the inlet and the secondary flow generated by the bubble plume. The diffuser applied for the present experiments was perforated all the way from the edge to the centre of the disc. Because of limitations due to low flow capacity in the diffusers inlet hoses, it was not possible to get the entire diffuser area active, and consequently only a ring of approximately 2 cm was active.

Method of measuring

The mean volume fractions of air bubbles and the mean velocities of the liquid phase inside the bubble plume were measured in the bubble plume. The details of the measurement techniques are described in the subsections below.

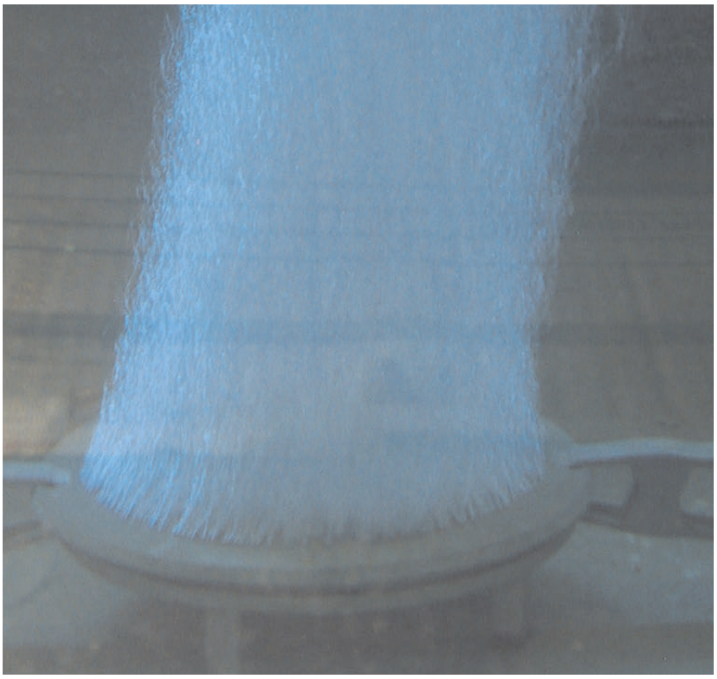

Figure 4.4 Close-up on the diffuser during the measurements.

Measurements of bubble volume fractions Measurements of the local point-wise volume fractions of the dispersed air bubbles in the bubble plume were conducted with an Ultrasonic High Concentration Meter (UHCM) (http://www.wldelft.nl/inst/sed/uhcm/index.html, 2004). The UHCM was originally constructed for measuring high particle concentrations in sediments, but as shown in the present experiments, the UHCM proved useful for measuring volume fractions of air as well. The UHCM system basically consists of:

- An acoustic probe with adjustable transmitter and receiver elements (Figure 4.5)
- A power supply
- A control unit

The measurements are based on the attenuation or augmentation of sound by particles. When air bubbles pass the two transmitter and receiver elements, the transmitted sound waves are augmented, resulting in an altered signal to the control unit. The signal is converted into a voltage signal in the control unit. From the control unit it is possible to output the voltage signal to data acquisition on a computer.

As mentioned earlier, the flow of air injected through the diffuser was monitored with a manually read Cole Parmer correlated flow meter. Since an air compressor was delivering the air supply, the inflow could consequently be subject to some instability in flow rate, because of small pressure differences in the compressor. These instabilities were monitored with measurements of the pressure difference over a part of the air tubes.

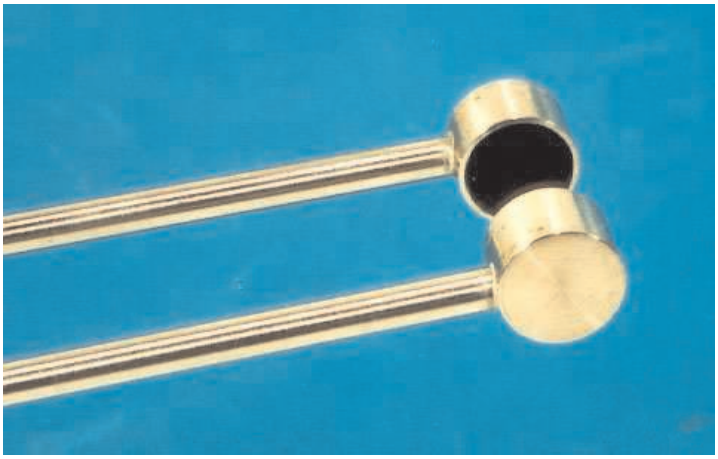

Figure 4.5 Acoustic probe. (http://www.wldelft.nl/inst/sed/uhcm/index.html, 2004)

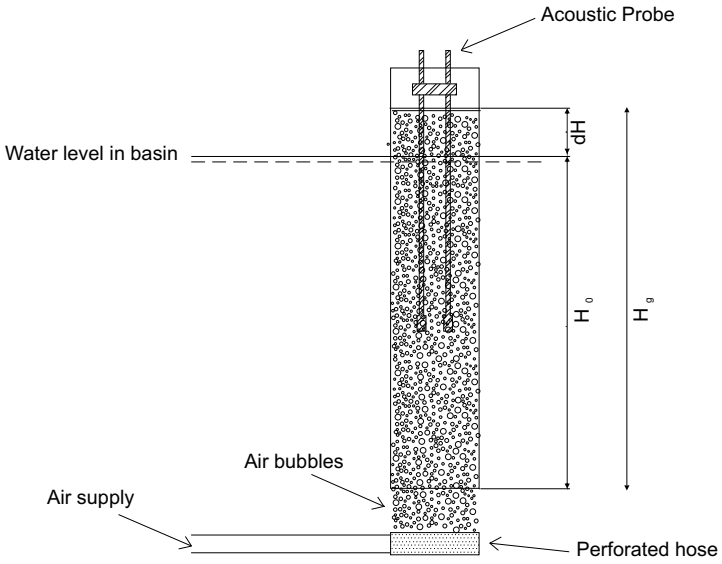

Figure 4.6 Experimental setup for calibration of the acoustic probe

Since the measurements are based on the attenuation of sound by particles, the signal is dependent on the actual fluid and particle materials. Consequently, calibration of the UHCM is necessary when measurements are performed on new materials. The calibration has been performed with the use of a transparent plastic tube, where air was blown in from the bottom (Figure 4.6).

During the calibration, air was injected to the tube through two perforated hoses. The injection of air resulted in a rise in the level of the water table inside the tube. The difference

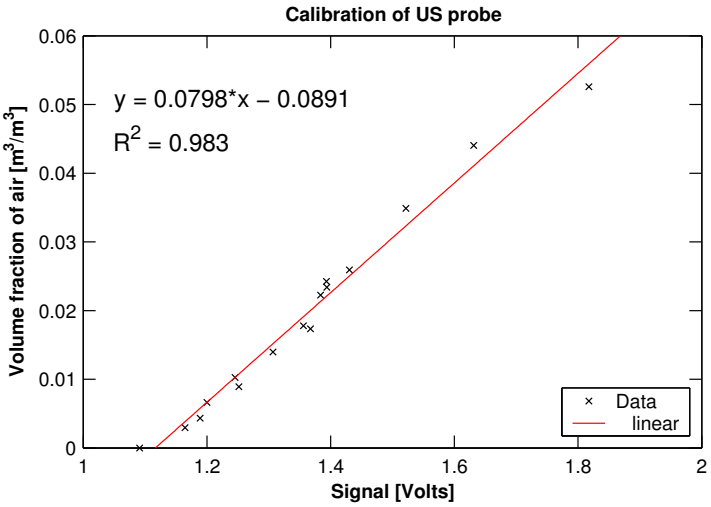

Figure 4.7 Probe Calibration

in water level between the water inside the tube and the water in the basin surrounding the tube, termed as dH on figure 4.6, was in accordance with equation 4.1 assumed to be proportional to the change in the volume fraction of air inside the tube.

The calculated volume fractions and the corresponding voltage signals from the UHCM output proved to be linearly correlated, and an expression for calculating volume fractions of air as a function of the UHCM voltage signal was developed (Figure 4.7).

Measurements of liquid velocities As described in subsection 4.1.1, most methods for measuring velocities in single phase flow suffer from serious drawbacks when they are transferred to multiphase flows; especially large scale multiphase flows where the visibility is low.

Due to these unavoidable complications, measurements of the liquid velocities were performed with a small impeller in the bubble column. The method is well-known in single phase flow, but modifications have to be made in order to transform the method to bubbly flows. Questions like how the bubbles interfere with the readout of the impeller arise, making it hard to determine what the impeller is actually measuring. In the present study, one of the tasks in the velocity measurements performed with the impeller has been to translate the signal from the impeller into a corresponding liquid velocity. Hence, the measurements performed in the bubble column needed to be corrected in order to describe the liquid velocity in the plume.

In order to find the interrelationship between the signal from the impeller and the liquid velocities in the bubbly flow, a special case of an air-lift pump was constructed (Figure 4.8. By applying the measurement impeller in both the right bubble filled tube and the left reference tube without air bubbles, but with identical flow of water, the signal of the measurement impeller could be corrected for the application into bubbly flows.

The main part of the experimental layout was a system of connected plastic pipes in which the water could circulate (Figure 4.8). The circulation of the water was generated by the action of an air-lift pump like system, where bubbles of approximately 3mm diameter were injected into

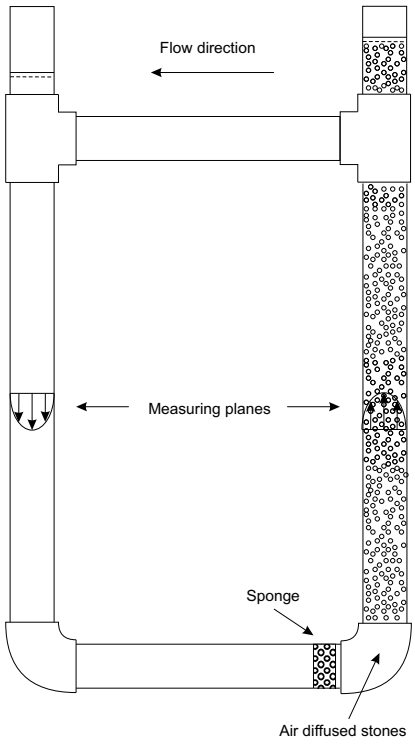

Figure 4.8 Circulated pipe system applied for calibration of the impeller

the right vertical tube through five porous stones normally used for aeration in aquariums. The injection of air bubbles resulted in a lowering of the specific gravity of the mixture of water and air bubbles, resulting in a air-lift pump like system, where denser surrounding water was lifted upwards by lighter mixture of water and air bubbles. Due to the system of interconnected pipes, the air-lift pumped water started a circulating pipe flow. In order to prevent too high flow in the system during high flow rates of air in the injection, a sponge inserted in the lower horizontal tube was working as flow resistor. During the measurements the liquid velocity was measured in the undisturbed tube by cross measuring with the impeller across the tube. The measurement profile was located downstream in the tube, but far enough from the downstream bending of the tube to avoid too large effects from the sideways acceleration of the water.

Measurements of the volume fractions of air during the experiments showed that the column at the measurement position in the right tube could be regarded as fully mixed with respect to air volume fractions. If only one porous stone where applied to the bubble column, the assumption of fully mixed column at the measurement position did not hold. Hence, it was necessary to use five stones arranged in a cross to get a uniform distribution of air bubbles at the measurement position. By controlling a valve and measuring the flow, the inflow of air was kept constant throughout the measurements. Since both of the vertical tubes were running through T-shaped connections with a free water surface, the bubbles could freely be degassed to the surroundings in the laboratory. Thus, no air bubbles could survive into the left vertical tube.

The flows in the two tubes were determined by integrating the velocities over the cross sections of the tubes:

$$Q = \int_A U \, dA \tag{4.5}$$

where Q is the flow in the tube $[m^3 \cdot s^{-1}]$, A is the cross sectional area of the tube and U is the axial velocity in the tube $[m \cdot s^{-1}]$.

The impeller used for the measurements integrates the flow over the impeller radius of approximately $1.25cm$, and the measurements are made so that the impeller overlaps almost all the distance from the centre to the periphery of the tube, in the four profiles conducted in the tube. Quadratic polynomial equations have been fitted to the measurements to describe the velocity distributions of the profiles.

In the right tube both liquid velocities and air volume fractions were measured at the same positions and at the same flow. Due to velocity and volume fraction fluctuations each measurement was performed for at least 10 minutes.

Compared to the values obtained in the left tube where no air bubbles are present, the measured velocities were higher in the right tube where air bubbles are injected. This was visualized through a higher measured flow in the air filled right tube compared to the left tube. This is expected, since the air bubbles due to buoyancy forces in general have a larger vertical rise velocity than the surrounding water in the right water tube. The higher velocities of the air bubbles are possibly transferred to the impeller due to both frictional and pressure forces occurring when the air bubbles hit the impeller. Beside the force influence originating from the interaction between bubbles and impeller, another straight-forward reason for measuring higher velocities in the right tube is found in a smaller effective flow area. The air bubbles take up space in the tube, resulting in a reduced flow-through area for the water. Hence, the water can be thought of as flowing at a Darcy-like filter velocity.

The difference in flow between the two vertical tubes turned out to be dependent on the injected amount of air in the right tube. Consequently, the velocity measurements were performed at different flow rates of air and the volume fractions of air were monitored. As an outcome of the measurements, an expression describing the liquid velocity correction as a function of air volume fractions was constructed (Figure 4.9)

As viewed on figure 4.9, a quadratic expression was fitted to the relation between impeller correction factor and the volume fraction of air in the bubble plume ($R^2 = 0.94$). The quadratic fit is due to the scarce amount of data points a rather crude assumption, and other expression types like e.g. a linear fit might have been applied instead. When evaluating the total uncertainty on the measurements, both the uncertainty on the volume fraction measurement and the assumption of equal volume fraction distribution in the measurement cross section affects the obtained correction factor. Also the impeller measurements them selves are connected with a uncertainties, adding up to the total uncertainty.

After the determination of the correction factors the measurements on the diffuser could be initiated.

Measuring programme for full-scale diffusor

Five measured profiles of the volume fractions of air and the liquid velocities in the bubble plume were performed 35, 60, 110, 160 and 185cm above the pit floor in the direction parallel to the

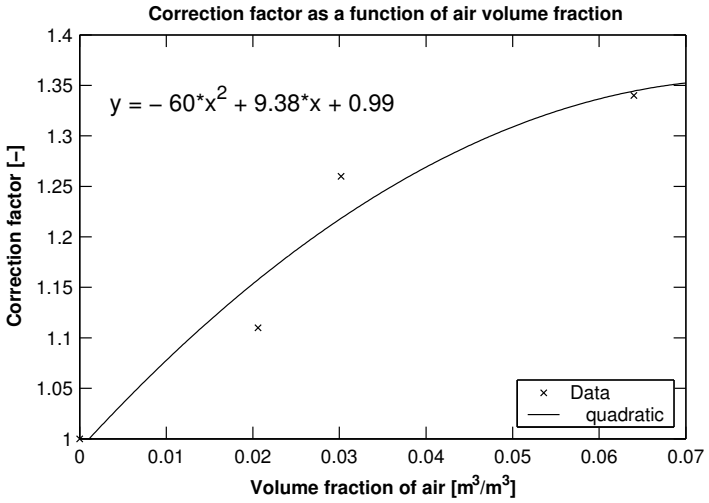

Figure 4.9 Correction factor for liquid velocities measured with a small impeller in a bubble plume.

length of the pit. Since the surface of the diffuser was located above the floor, these positions correspond to 25, 50, 100, 150 and 175cm above the diffuser surface. When the measurements were performed in the direction parallel to the pit, a bridge above the basin could be used for traversing the measurement equipment along the line of measurement direction. In order to perform simultaneous measurements of liquid velocities and volume fractions of air, the ultrasonic meter and the measurement impeller were located on the same rod (Figure 4.10).

The measurement impeller and the ultrasonic meter were located $5cm$ apart in the direction of traversing. When traversing the measuring probes, displacements of 2.5 or $5cm$ were applied, ensuring both velocities and volume fractions were measured at the same positions. In order to avoid effects from volume fraction fluctuations due to the presence of eddies continuous measurements were performed for 5 minutes duration at every measurement point.

Photographs of the bubble plume were during the experiments captured through a window in one of the sidewalls of the pit (Figure 4.11). As indicated on the figure, the plume was fluctuating from side to side during the experiments.

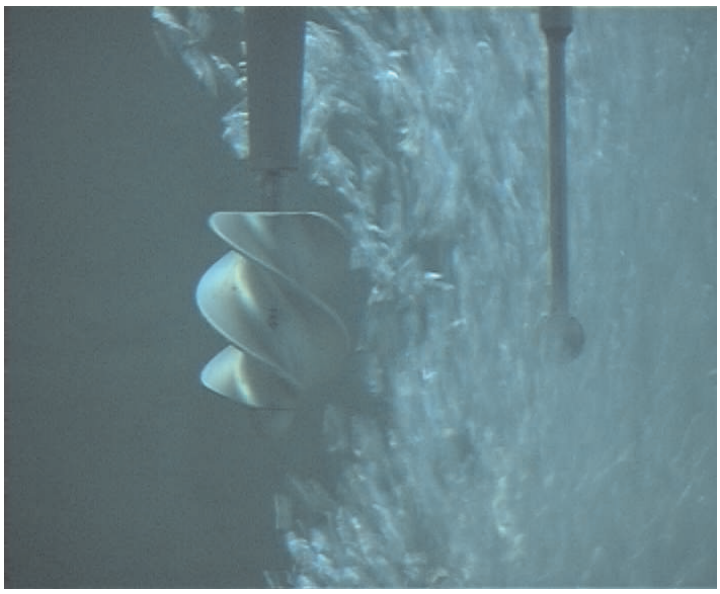

Figure 4.10 Measurements in the bubble plume. The USM transmitter and receiver is located on the right of the picture.

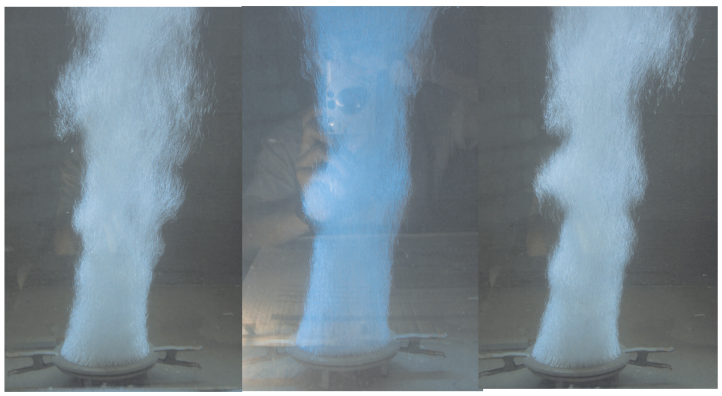

Figure 4.11 Snapshot of the bubble plume during the experiment.

4.1.5 Results from measurements

Volume fraction of air

The 5 measured profiles of the volume fractions are illustrated together with a fit to the theoretical distribution as described in equation 4.3 (Figure 4.12). As indicated on the figure, the peak values decrease and the width of the plume increase as the vertical distance to the diffuser increase. For the theoretical fit, a λ value of 0.5 was applied for the lateral spreading ratio, and the characteristic lateral dimension of the plume, σ, was calculated from equation 4.4. In (Ditmars and Cederwall, 1974) a reference to the measurements of (Kobus, 1968) indicated values of λ of approximately 0.2 for large-scale laboratory experiments with air-bubble plumes, which corresponds to a higher lateral spreading in the present experiments compared to the results of (Kobus, 1968). As indicated, good agreement between the theoretical bell-shaped Gaussian distribution and the measurements has been obtained.

The measured profile, 35 cm above the pit floor, appears to be fairly distorted. The volume fraction profile at this height has a local minimum just to the right of the centre of the diffuser. Since the active area of the diffuser is formed as a closed ring, the local minimum at this profile is a direct consequence of the geometry of the inlet. Additional measurements at this height in the bubble plume did however indicate large volume fraction fluctuations. It turned out that the measurement period of 5 minutes could be insufficient to get reproducible results. When measuring higher above the pit floor, the fluctuations were smaller and the measurement period was sufficient to get reproducible volume fraction profiles.

Apart from the lowest profile where large fluctuations were present, the measured profiles seemed to be fairly Gaussian shaped, with a wider and wider volume fraction distribution as the vertical distance to the diffuser was increased (Figure 4.12).

From visual observations in the laboratory, the equivalent bubble size has been estimated to approximately 3mm.

Velocities of the liquid phase

The velocities of the liquid phase were measured in the same five depths as was the case for the air volume fraction (Figure 4.13). From the figure it appears that the peak velocities of the profiles seems to be fairly constant for the 5 depths, whereas the distribution due to entrainment of ambient water becomes wider at larger distances from the diffuser. From the profiles 60 cm above the pit floor, it is evident that the bubble plume is symmetric around its main axis with respect to liquid velocities. The velocity measurements do, like in the case of the volume fraction measurements, fit the plume theory fairly well.

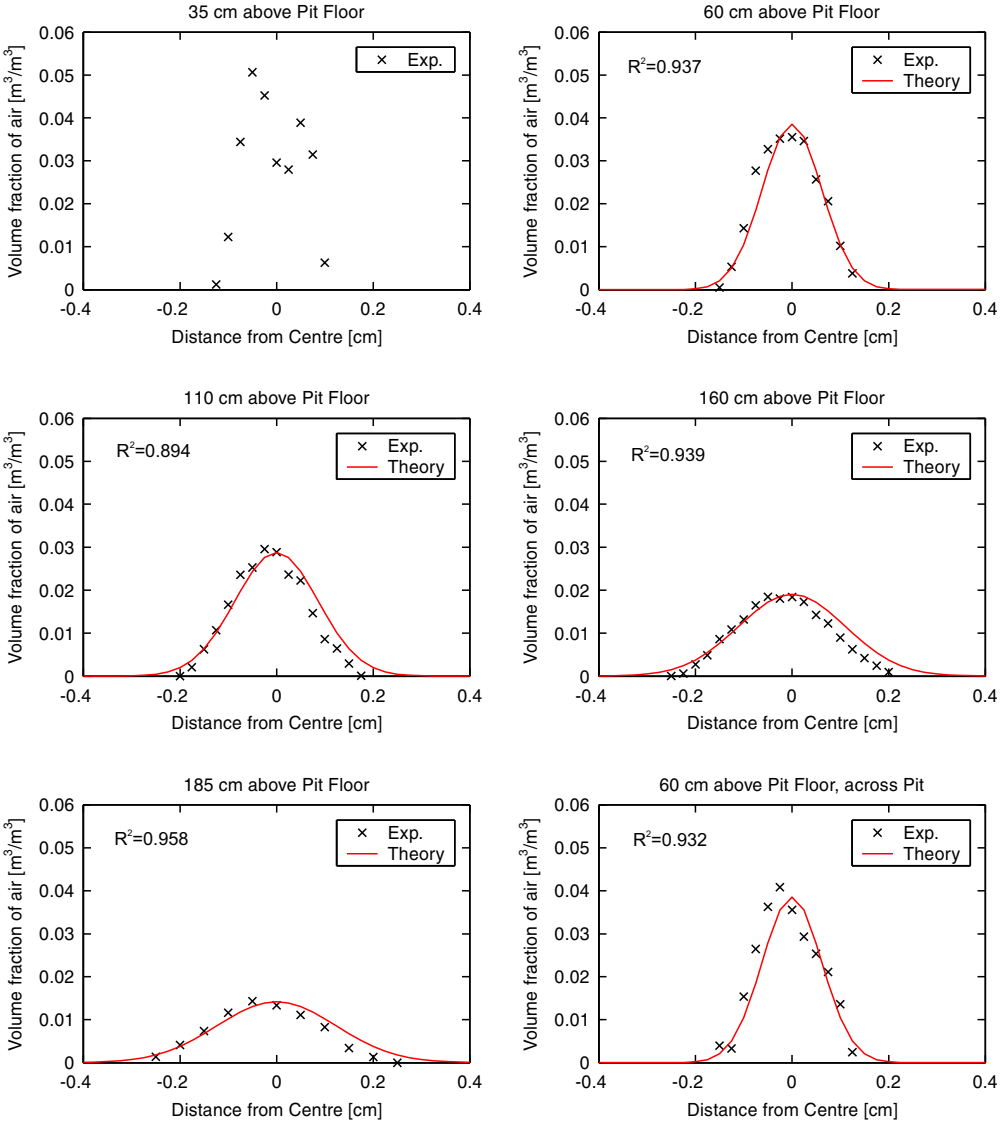

Figure 4.12 Measured profiles of the volume fraction of air in the bubble plume. The distance indicated on the x-axis, is equal to the horizontal distance from the centre of the diffuser. The profile in lower right corner is a reference profile measured across the pit: orthogonal to the remainder of the profiles.

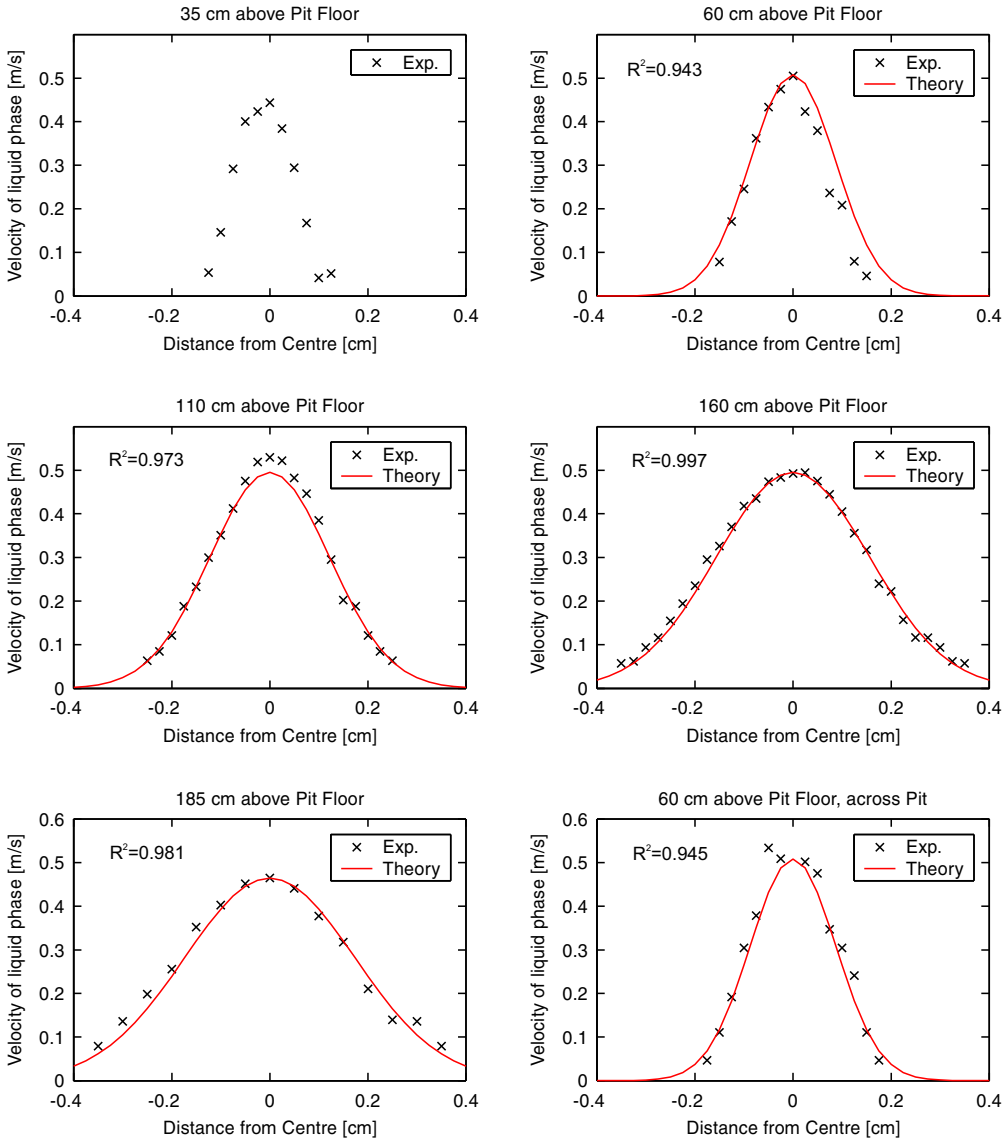

Figure 4.13 Measured profiles of the mean velocities of the liquid inside the bubble plume. The distance indicated on the x-axis, is equal to the horizontal distance from the centre of the diffuser. The profile in lower right corner is a reference profile measured across the pit: orthogonal to the remainder of the profiles.

4.1.6 Numerical modelling

A numerical model was developed with the use of the commercial CFD software packages in the ANSYS CFX-5 family (CFX, 2005). Because of the complex geometry of the experimental setup, a three dimensional model was applied. The multifluid model was used (Section 3.2.2), thus a set of Navier-Stokes equations were solved for both the continuous water phase and the dispersed air bubbles. Because of the fixed and steady boundary conditions in the experimental setup and the stationary nature of the measurements, a steady state model was applied.

Interfacial momentum transfer

The motion of fluid and particles in a flow system will be determined by forces acting on both the fluid and the particles. Several types of forces are relevant for the flow systems regarded in the present work:

- Pressure forces, F_P
- Inertial forces, F_I
- Viscous forces, F_V
- Gravitational forces, F_G
- Buoyancy forces, F_B
- Surface tension forces, F_S

A bubble in force equilibrium, is said to travel at its terminal velocity, V_T. The force balance of a bubble travelling at its terminal velocity is outlined in figure 4.14.

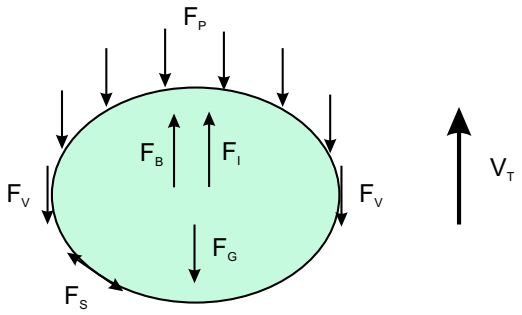

Figure 4.14 Outline of the forces acting on a single bubble in force equilibrium, rising at its terminal velocity. The forces are only roughly sketched in their main direction or point of action (Further explanation is included in the text below).

On figure 4.14, the forces are presented at their main approximate position and their principle point of action. The pressure force, F_P is a surface force working on the complete surface of the bubble. In order to simplify figure 4.14, only the resulting contribution to F_P is shown. For at rising bubble, pressure forces will act on all sides of the bubble, but the resulting pressure forces F_P will be located on the front side of the bubble as indicated on the sketch. The viscous force,

F_V is also a surface force, working as a friction force on the interface between the water and air phases. Again, this force works on the whole surface of the bubble, but for viewing purposes it is only shown in the vertical direction. The gravitational force, F_G, the buoyancy force, F_B and the inertial forces are all volume forces that can be assigned to the centre of gravity of the bubble, hence correctly the force vectors of these forces should all be originating from the centre of gravity on the bubble on figure 4.14. The surface tension force is working on the surface of the bubble, counteracting the deformation originating from the action of especially the viscous and the pressure forces. In order to determine which of the forces described above that is dominant in the present bubble flow, an analysis applying dimensionless groups is included in the following.

Analysis using dimensionless groups

Before going into further detail with the individual interfacial momentum transfer forces, an analysis of the importance of each of these forces will be performed. This way a prior indication of the magnitude of the different forces will be made and forces that may be neglected can be identified.

For this purpose, a number of dimensionless groups expressing the ratio between the different forces can be calculated (Wörner, 2003). The dimensionless groups will initially be set up in their general form. Later the dimensionless groups will be related to bubbles and their actual values will be estimated.

First the $Reynolds'$ number, expressing the ratio between inertial and viscous forces can be evaluated:

$$Re = \frac{F_I}{F_V} = \frac{\rho L_{ch} U_{ch}}{\mu} \tag{4.6}$$

where L_{ch} is a characteristic length $[m]$ and U_{ch} is a characteristic velocity $[m \cdot s^{-1}]$. The $Froude$ number describes the ratio between inertial and gravitational forces:

$$Fr = \frac{F_I}{F_G} = \frac{U_{ch}^2}{g L_{ch}} \tag{4.7}$$

The $Euler$ number describes the ratio between the pressure gradient and the inertial forces:

$$Eu = \frac{F_P}{F_I} = \frac{\triangle p}{\rho U_{ch}^2} = \frac{F_d}{A_p \rho U_{ch}^2} \tag{4.8}$$

where it is exploited that the pressure loss associated with the change of the flow field due to the presence of bubbles can be expressed in terms of the drag force on the bubble. $\triangle p$ is the pressure loss due to the modification of the flow field caused by the presence of bubbles $[N \cdot m^{-2}]$, F_d is the drag force exerted on the bubble $[N]$ and A_p is the projected cross sectional area of the bubble perpendicular to the flow direction $[m^2]$.

Beside these general dimensionless groups, additional groups involving the surface tension force can be set up for liquid-liquid and gas-liquid multiphase flows. The ratio between inertial and surface tension forces is described through the $Weber$ number:

$$We = \frac{F_I}{F_S} = \frac{\rho L_{ch} U_{ch}^2}{\sigma} \tag{4.9}$$

where σ is the coefficient of surface tension $[N \cdot m^{-1}]$. Furthermore the ratio between buoyancy and surface tension forces can be expressed via the $Eötvös$ number:

$$Eo = \frac{F_B}{F_S} = \frac{\triangle \rho g L_{ch}^2}{\sigma} \tag{4.10}$$

A high $Eötvös$ number indicates highly distorted bubbles, while a low $Eötvös$ number indicates nearly spherical shaped bubbles. (Clift *et al.*, 1978) constructed a figure showing the bubble shape regimes as a function of $Eötvös$ number for air bubbles in water (Figure 4.15).

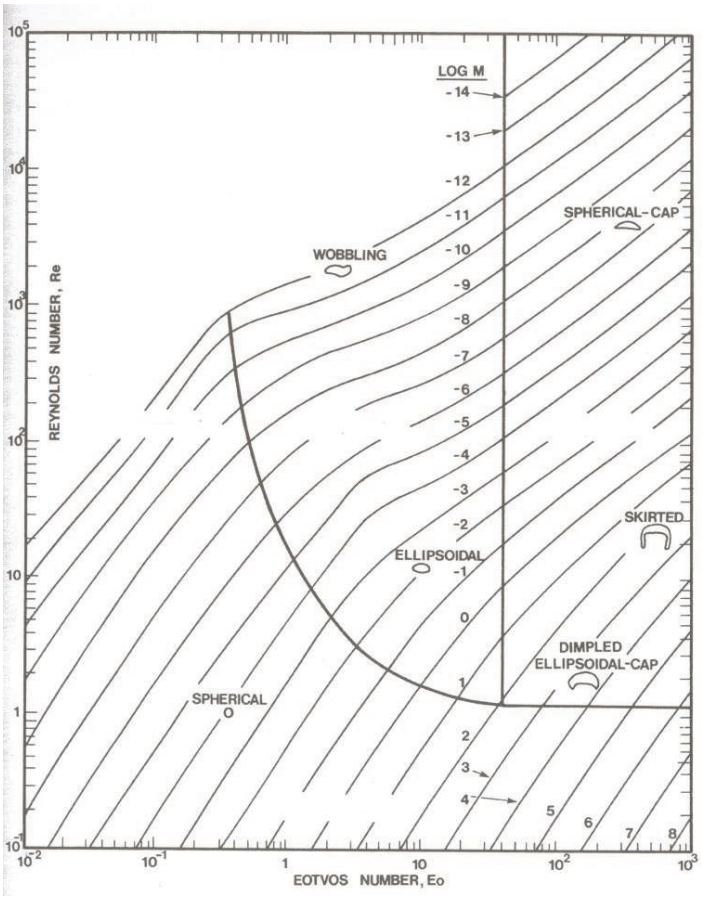

Figure 4.15 Shape regimes for bubbles and drops in unhindered gravitational motion through liquids (Clift *et al.*, 1978).

From figure 4.15 it appears that the combination of the $Reynolds'$, the $Eötvös$ and the $Morton$ number (Defined in the text below) determines the shape of the bubbles.

The ratio between some of the above-mentioned dimensionless groups can be used to create other valuable dimensionless groups. The $Morton$ number involving only fluid properties can thus be created with background in the $Eötvös$, $Weber$ and $Reynolds'$ number:

$$Mo = \frac{F_B F_V^4}{F_I^2 F_S^3} = \frac{g \triangle \rho \mu_\alpha^4}{\rho_\alpha^2 \sigma^3} = \frac{EoWe^2}{Re^4} \tag{4.11}$$

where μ_α is the dynamic viscosity of phase α $[kg \cdot m^{-1} \cdot s^{-1}]$ and ρ_α is the density of phase α $[kg \cdot m^{-3}]$.

Knowledge of the $Morton$ number can combined with the bubble $Reynolds'$ number and the $Eötvös$ number give valuable information about the expected shape and behaviour of the bubbles. (Clift *et al.*, 1978) constructed diagrams for this purpose (Figure 4.16).

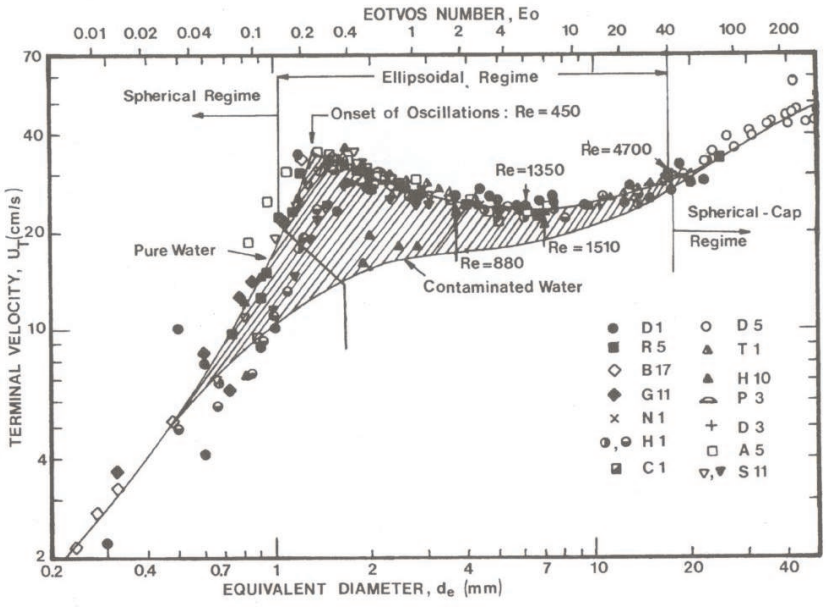

Figure 4.16 Terminal velocity for air bubble in water at $20°C$ (Clift *et al.*, 1978).

From the work of (Clift *et al.*, 1978) it is evident that larger bubble tends to rise faster than smaller ones. In pure water a local maximum do however appear at a diameter of approximately $1.5mm$. The local maximum is not apparent for bubbles in contaminated water.

Also the $capillary$ number, describing the ratio between viscous and surface tension forces can be set up:

$$Ca = \frac{F_V}{F_S} = \frac{\mu U_{ch}}{\sigma} = \frac{We}{Re} \tag{4.12}$$

Since the viscous forces will try to deform the bubble shapes and the surface tension forces works as a resistance to this deformation, low capillary number bubble flow, indicate nearly

spherical non-deformed bubbles, whereas high capillary numbers indicate highly distorted bubbles. (Manga *et al.*, 1998) states that bubbles at high capillary numbers contribute less to increased shear than bubbles at low capillary numbers. The reason for this is that the bubbles becomes aligned in flow direction at high capillary numbers.

In order to calculate representative dimensionless groups for the given flow system, the characteristic length scale, L_{ch}, and velocity scale, U_{ch} has to be defined in a meaningful way. For the air bubbles regarded in this work, the terminal rise velocity V_T and the bubble diameter, d_β, are chosen as representatives of U_{ch} and L_{ch}. d_β is set to 3mm, the value estimated from the laboratory experiments, and V_T is determined by the application of figure 4.16. Besides these two characteristic numbers, all other properties of the fluid can be viewed in table 4.1, where also the representative values of the dimensionless groups are listed.

Table 4.1 Relevant fluid properties and values of dimensionless groups for the present bubble flow.

Property	$Value$	$Unit$
Bubble diameter	0.003	$[m]$
Density, water	997.1	$[kg \cdot m^{-3}]$
Density, air	1.185	$[kg \cdot m^{-3}]$
Acceleration of gravity	9.82	$[m \cdot s^{-2}]$
Surface tension coefficient	0.072	$[N \cdot m^{-1}]$
Dynamic viscosity, water	1.0E-3	$[kg \cdot m^{-1} s^{-1}]$
C_d in equilibrium	0.98	$[-]$
Terminal velocity	0.2	$[m \cdot s^{-1}]$
Bubble Reynolds' number, Re	599	$[-]$
Euler number, Eu	0.49	$[-]$
Froude number, Fr	1.36	$[-]$
Weber number, We	1.66	$[-]$
Eotvos number, Eo	1.22	$[-]$
Capillary number, Ca	2.8E-3	$[-]$
Morton number, Mo	2.6E-11	$[-]$

Table 4.1 gives valuable information about the expected bubble flow system.

In agreement with (Clift *et al.*, 1978) bubbles in water with a diameter of 3mm, corresponding to the conditions in the present experiment, have an $Eötvös$ number of approximately 1.2, indicating the bubbles to be close to spherical shaped.

A particle $Reynolds'$ number of approximately 600 indicates that inertial forces dominate over viscous forces. It does however also indicate that the bubbles are located somewhat in between the Stokes and the inertial regime, making the drag-coefficient highly dependent on the bubble $Reynolds'$ number, and hence emphasizing the importance of the choice of drag model.

Comparing the $Eötvös$, $Reynolds'$ and $Morton$ numbers against the plot constructed by (Clift *et al.*, 1978) (Figure 4.15), the bubbles are again expected to be of spherical shape. This combination of dimensionless groups also indicate that some *wobbling* of the air bubbles could be present. *Wobbling* is characterized by fluctuating lateral movements of the air bubbles. The presence of wobbling bubbles is furthermore expected to locally increase turbulence in the presence of the bubbles.

As expected, the $Froude$ number states that both inertial and gravitational forces are significantly governing the flow. The Euler number states that also the pressure force, i.e. the drag

contributed by form drag will be important for the particular flow.

Like the $Eötvös$ number, the low $capillary$ number also indicates that the bubbles are close to spherical shaped. The size of the $Weber$ number furthermore indicate the surface tension forces to be of the same order of magnitude as the inertial forces, again backing up that deformation of the bubbles will not be dominant.

In the present model, the effect of some of the forces described above are formulated into interfacial forces, where the different phases in a multiphase flow can influence each other through force exchanges at the phase interfaces (Subsection 3.2.2). The interfacial force terms relevant for the current bubble flow are listed below:

- Drag forces
- Lift forces
- Virtual mass forces
- Turbulent dispersion forces
- Wall lubrication forces
- Basset forces

Further explanation of the above mentioned forces will be given below.

Drag force

Together with the gravity force, the drag force is in general the main interfacial force acting in a particulate flow (Loth, 2000). The drag force exerted on a bubble by the surrounding water, arise from both skin friction and form drag, where the former is due to the viscous surface shear stress and the latter is due to the pressure distribution around the bubble. Thus, with reference to the previous force analysis, the drag force is composed of contributions of the pressure force, F_P, and the viscous force, F_V. At low bubble $Reynolds'$ numbers, skin friction dominate over form drag, whereas the opposite is occurring at high bubble $Reynolds'$ numbers.

The interfacial drag force acting on phase α due to the presence of phase β is assumed to be proportional to the relative speed between the two phases:

$$\mathbf{M}^D_{\alpha\beta} = c^D_{\alpha\beta}\left(\mathbf{U}_\beta - \mathbf{U}_\alpha\right) \tag{4.13}$$

Where $c^D_{\alpha\beta}$ is the interfacial drag coefficient $[kg \cdot m^{-3}s^{-1}]$ and $(U_{i,\beta} - U_{i,\alpha})$ is the relative velocity component in the i direction between phase α and β $[m \cdot s^{-1}]$. $c^D_{\alpha\beta}$ is calculated as follows:

$$c^D_{\alpha\beta} = \frac{C_d}{8} A_{\alpha\beta}\rho_\alpha|\mathbf{U}_\beta - \mathbf{U}_\alpha| \tag{4.14}$$

Where C_D is the dimensionless drag coefficient $[-]$ and $|\mathbf{U}_\beta - \mathbf{U}_\alpha|$ is the relative speed between phase α and β. For spherical shaped bubbles, $c^D_{\alpha\beta}$ is calculated as:

$$c^D_{\alpha\beta} = \frac{3}{4}\frac{C_d}{d_\beta} r_\beta \rho_\alpha |\mathbf{U}_\beta - \mathbf{U}_\alpha| \tag{4.15}$$

C_D is dependent on the morphology of the particles and the flow situation. Bubbles are known to possess different forms dependent on the flow situations (Figure 4.17).

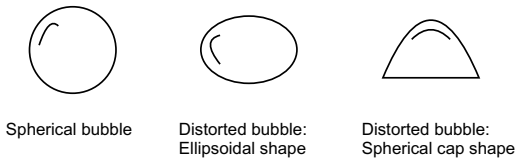

Figure 4.17 Outline of bubble shapes corresponding to different flow regimes.

In the present experiments the particles are air bubbles, termed as fluid particles. Compared to solid particles, the drag coefficient correlations are more complicated, since the drag coefficient will vary with the shape of the fluid particles. The shape of the bubbles is highly dependent on the nature of the flow regime surrounding them. Again, the particle $Reynolds'$ number can be written:

$$Re_{\alpha\beta} = \frac{\rho_\alpha |\mathbf{U}_\beta - \mathbf{U}_\alpha| d_\beta}{\mu_\alpha} \tag{4.16}$$

This equation is equal to equation 4.6, except that it in this version is written in terms of the magnitude of the relative speed between the two phases.

At low bubble $Reynolds'$ numbers, in the viscous regime, the flow of a particle moving through a quiescent liquid can be solved analytically, resulting in Stokes drag law, where C_D is calculated as (Clift *et al.*, 1978):

$$C_D = \frac{24}{Re_{\alpha\beta}} \tag{4.17}$$

As seen in equation 4.17, C_D is only dependent upon the bubble Reynolds number in the viscous regime.

The high value of the drag coefficient in the Stokes' (viscous) regime is probably not relevant for practical bubble flows, since the bubble $Reynolds'$ number typically is high enough to make the flow far from being purely dominated by viscous drag (Section 4.1.6).

In the viscous Stokes regime, the viscous drag and the form drag are of the same order of magnitude. Consequently, the shape of the bubbles will be nearly spherical. As the bubble $Reynolds'$ number increase the form drag originating from the fluids inertia will start to dominate over the viscous drag. For bubble $Reynolds'$ higher than unity, the drag coefficient relation in general has to be determined by experiments.

In the inertial or Newton's regime, at higher $Re_{\alpha\beta}$ numbers, air bubbles differ from their spherical shape due to surface tension effects. The bubbles first become ellipsoidal in shape, after which they at high $Re_{\alpha\beta}$ become spherical cap shaped.

At sufficiently high bubble $Reynolds'$ numbers, the bubbles are highly dominated by form drag. This flow regime is termed as the spherical cap regime, due to the distinct shape of the bubbles (Figure 4.17). In the spherical cap regime the drag force becomes constant (Clift *et al.*, 1978):

$$C_D = \frac{8}{3} \tag{4.18}$$

For moderate $Re_{\alpha\beta}$, both viscous and inertial effects have influence. As indicated earlier, bubbles can be regarded as spherical when the surface tension is considerably larger than the inertial or viscous forces (Section 4.1.6) (Clift *et al.*, 1978). (Clift *et al.*, 1978) states that significant deformation occur at approximately $Re_{\alpha\beta} > 600$ for freely rising bubbles in practical systems. Hence a drastic shift in bubble shape is expected to occur in this transitional regime, resulting in a drag coefficient highly dependable on the bubble $Reynolds'$ number. The drag coefficient correlation can not be determined analytically in the transitional regime, thus an experimentally determined drag correlation has to be applied.

As long as the surface tension forces of the bubbles are strong enough to maintain sphericity of the bubbles, drag correlations for solid spherical particles can be regarded as applicable for bubbly flows. In the transitional region between the viscous and inertial regime, the drag coefficient is a complex function of the particle $Reynolds'$ number (Equation 4.16). One such correlation describing this relationship is the Schiller-Naumann (Schiller and Naumann, 1933) drag correlation for solid spherical particles applicable for $0.1 < Re_{\alpha\beta} < 1000$:

$$C_{D,spherical} = \frac{24}{Re_{\alpha\beta}} \left(1 + 0.15 Re_{\alpha\beta}^{0.687}\right) \tag{4.19}$$

Note that for a particle $Re_{\alpha\beta}$ approaching 1000, the outcome of equation 4.19 produces a value of 0.44, corresponding to the constant value of C_D in the inertial regime ($1000 < Re_{\alpha\beta} < 1 - 2 \cdot 10^5$).

Since the estimated particle $Reynolds'$ number of 600 (Table 4.1) is right in the transitional region where significant bubble deformation is likely to occur, drag correlations for spherical particles should be replaced by drag correlations for bubbles with distorted shapes. Several of such drag coefficient relations estimated by other authors will briefly be presented in the following. Because either Stokes regime or spherical cap regime flows are likely to be present in the present investigations, the brief presentations will primarily involve the drag correlations for the transitional region between the viscous and the inertial regime at moderate bubble $Reynolds'$ numbers. The tested drag correlations listed below are an extract of the many drag models described in the literature, and the represent a choice of the models believed to be most appropriate for the purpose of modelling bubbly flows:

- The Ishii-Zuber drag correlation
- The Grace drag correlation
- A drag correlation applied in (Lain *et al.*, 1999)
- A drag correlation for wobbling bubbles
- A drag correlation for contaminated systems

Ishii-Zuber drag correlation (Ishii and Zuber, 1979) constructed a general drag model applicable for any pair of fluid phases. The model takes dense particle effects into account, and is thus applicable for flow at high air volume fractions. The dense particle effects are regarded in the model by calculating a mixture density, dependent on the actual volume fraction of particles.

In the viscous regime, the drag model for spherical shaped bubbles takes the form of a modified version of the Schiller-Naumann (Schiller and Naumann, 1933) equation for solid spherical particles (Equation 4.19):

$$C_{D,spherical} = \frac{24}{Re_m}\left(1 + 0.15Re_m^{0.687}\right) \tag{4.20}$$

where Re_m is the mixture bubble $Reynolds'$ number $[-]$:

$$Re_m = \frac{\rho_\alpha |\mathbf{U}_\beta - \mathbf{U}_\alpha| d_\beta}{\mu_m} \tag{4.21}$$

here, μ_m is the dynamic mixture viscosity $[kg \cdot m^{-1} \cdot s^{-1}]$, calculated from:

$$\frac{\mu_m}{\mu_\alpha} = \left(1 - \frac{r_\beta}{r_{\beta max}}\right)^{-2.5 r_\beta \mu_*}, \quad \mu_* = \frac{\mu_\beta + 0.4\mu_\alpha}{\mu_\beta + \mu_\alpha} \tag{4.22}$$

where $r_{\beta max}$ is the maximum packing value of phase β $[-]$.

The reason for using a mixture viscosity is to be found in the imparted motion on the continuous phase due to the movement of the bubbles. A bubbles movement through a bubble and water mixture will generate a motion in the continuous phase. The deformation of the continuous fluid will further cause extra movements of bubbles. The bubbles resistance to deformation will create a system of forces reacting on the continuous phase, resulting in additional stresses, which by the bubbles will be felt as an extra resistance to their movement. This additional bubble induced resistance to movement can be regarded as an increased viscosity in the bubble flow (Ishii and Zuber, 1979).

In the distorted regime the Ishii-Zuber drag correlation includes a multiplying factor to the drag correlation of a single bubble:

$$C_{D,ellipsoidal} = E(r_\beta) C_{D\infty}, \quad C_{D\infty} = \frac{2}{3} E_o^{1/2} \tag{4.23}$$

where the correction factor $E(r_\beta)$ is calculated from:

$$E(r_\beta) = \frac{1 + 17.67[f(r_\beta)]^{6/7}}{18.67 f(r_\beta)}, \quad f(r_\beta) = \frac{\mu_\alpha}{\mu_m}\left(1 - r_\beta\right)^{1/2} \tag{4.24}$$

Likewise, the drag coefficient for single bubbles in the spherical cap regime is corrected to account for the entrainment of bubbles in the wakes of other bubbles (Ishii and Zuber, 1979), decreasing the effective drag coefficient of the bubbles:

$$C_{D,sphericalcap} = (1 - r_\beta)^2 C_{D\infty}, \quad C_{D\infty} = \frac{8}{3} \tag{4.25}$$

In the present model, an automatic selection of bubble regimes is in function, based on a simple selector:

$$C_D = \begin{cases} C_{D,spherical} & if \quad C_{D,spherical} \geq C_{D,ellipsoidal} \\ min\left(C_{D,ellipsoidal}, C_{D,sphericalcap}\right) & if \quad C_{D,spherical} < C_{D,ellipsoidal} \end{cases} \tag{4.26}$$

Grace drag correlation The Grace Drag Model, developed upon air-water data, is a specialized model suited for the physical conditions of the present experiments (CFX, 2003), (Clift *et al.*, 1978). In the Stokes regime, the drag coefficient is calculated from equation 4.17. Again, as long as the bubbles are spherical of shape, the Schiller-Naumann equation (Equation 4.19) applicable for spherical solid particles is applied. In the distorted regime, the Grace drag model defines the drag coefficients for ellipsoidal bubbles as follows:

$$C_{D,ellipsoidal} = \frac{4}{3} \frac{g d_\beta}{U_T^2} \frac{\triangle \rho}{\rho_\alpha} \tag{4.27}$$

where U_T is the terminal velocity $[m \cdot s^{-1}]$, ρ_α is the density of the continuous phase $[kg \cdot m^{-3}]$ and $\triangle\rho$ is the density difference between phase α and phase β $[kg \cdot m^{-3}]$

The terminal velocity is dependent upon the Morton number (equation 4.11):

$$U_T = \frac{\mu_\alpha}{\rho_\alpha d_\beta} Mo^{-0.149} \left(J - 0.857\right) \tag{4.28}$$

With J defined as:

$$J = \begin{cases} 0.94 H^{0.751} & 2 < H \leq 59,3 \\ 3.42 H^{0.441} & H > 59.3 \end{cases} \qquad H = \frac{4}{3} EoMo^{-0.149} \left(\frac{\mu_\alpha}{\mu_{ref}}\right)^{-0.14} \tag{4.29}$$

here μ_{ref} is the dynamic viscosity of water at 25 $°C[kg \cdot m^{-1} \cdot s^{-1}]$ and Eo is the $Etvs$ number calculated from equation 4.10

In the spherical cap regime, C_D is calculated from equation 4.18.

An automatic regime selector selects the appropriate C_D formula on behalf of the output the different C_D correlations:

$$\begin{aligned} C_{D,ellipsoidal} &= min\left(C_{D,ellipsoidal}, C_{D,sphericalcap}\right) \\ C_D &= max\left(C_{D,spherical}, C_{D,ellipsoidal}\right) \end{aligned} \tag{4.30}$$

The Lain drag model for fluid particles The following drag correlation is identical with the one used in (Lain *et al.*, 1999) for their bubble column model. At low bubbles $Reynolds'$ numbers, in the Stokes regime, the drag coefficient is only two third the size of the drag coefficient presented in equation 4.17:

$$C_D = \frac{16}{Re_{\alpha\beta}}, \quad Re < 1.5 \tag{4.31}$$

For spherical bubbles, the drag coefficient is calculated as in the model proposed by (Haas *et al.*, 1972):

$$C_{D,spherical} = 14.9 \cdot Re_{\alpha\beta}^{-0.78}, \quad 1.5 < Re_{\alpha\beta} < 80 \tag{4.32}$$

At higher bubble $Reynolds'$ numbers, the drag coefficient is defined as:

$$C_{D,ellipsoidal} = \frac{48}{Re_{\alpha\beta}} \left(1.0 - 2.21 \cdot Re_{\alpha\beta}^{-0.5}\right), \quad 80 < Re_{\alpha\beta} < 700 \tag{4.33}$$

Drag correlation for wobbling bubbles When the bubble shapes are distorted, the bubbles will have a tendency to elongate in the vertical direction and often also show a wobbling nature. When the distorted bubbles rise, a significant wake can occur behind the bubbles. Other bubbles will be dragged into these wakes, making the bubbles rise in an elongated motion. (Zboray and de Cachard, 2005) applied an expression for wobbling bubbles adopted from a lecture by Professor M. Ishii of Purdue University, USA, in 2003:

$$C_{D,wobbling} = \frac{\sqrt{2}}{3} N_\mu Re_{\alpha\beta}, \quad N_\mu = \frac{\mu_\alpha}{\sqrt{\rho_\alpha \sigma \sqrt{\sigma / g \left(\rho_{\alpha - \rho_\beta}\right)}}} \tag{4.34}$$

Drag correlation for contaminated system Since the drag coefficient of a fluid particle is very dependent on the deformation of the particle, the degree of surfactants or other impurities in the water can affect the drag coefficient drastically. A media without impurities is said to be a pure system, whereas the opposite is defined as a contaminated system. Because of the problems arising with keeping a system completely pure, surface-active contaminants are of importance in most systems (Clift *et al.*, 1978). A rough definition of *contaminated*, corresponds to surfactant volumetric concentrations in the order of $10^{-8} - 10^{-6}$ (Loth, 2000). In contaminated systems, the bubbles will due to a decrease in internal fluid recirculation be subject to a higher drag. Since nothing has been done to purify the system in which the present experiments have been taking place, it is likely that the basin in the laboratory will be contaminated. Furthermore, an activated sludge system must to a large degree be regarded as contaminated, justifying for the test of a drag model for contaminated systems. In order to quantify the effect of a contamination on the modelled drag, and thus the effect on the modelled volume fraction and velocity profiles, a drag correlation applicable for grossly contaminated systems have been adopted from (Clift *et al.*, 1978). In the Stokes regime:

$$C_{D,Stokes} = \frac{24}{Re_{\alpha\beta}} \left(1 + (3/16)\, Re_{\alpha\beta}\right), \quad Re < 1 \tag{4.35}$$

In the viscous regime, where the bubbles are mainly spherical, the drag correlation takes the following form:

$$C_{D,spherical} = \frac{24}{Re_{\alpha\beta}} \left(1 + 0.1935 Re_{\alpha\beta}^{0.6305}\right), \quad 1 < Re < 78 \tag{4.36}$$

Finally, in the distorted regime:

$$C_{D,distorted} = \frac{24}{Re_{\alpha\beta}} \left(1 + 0.03875 Re_{\alpha\beta}\right), \quad 78 < Re < 300 \tag{4.37}$$

Lift force

A bubble rising in a rotational fluid will be subject to a horizontal lift force. In the present work the lift force is implemented through the following expression (Zboray and de Cachard, 2005), (CFX, 2005):

$$\mathbf{M}_{\alpha}^{L} = -\mathbf{M}_{\beta}^{L} = C_L r_\beta \rho_\alpha \left(\mathbf{U}_\beta - \mathbf{U}_\alpha\right) \times \left(\nabla \times \mathbf{U}_\alpha\right) \tag{4.38}$$

where C_L is the lift coefficient $[-]$, typically having values between 0.01 and 0.5 (Zboray and de Cachard, 2005), (CFX, 2005) and $\nabla \times \mathbf{u}_\alpha$ is the curl of $\mathbf{u}_\alpha$ $[s^{-1}]$.

Virtual mass force

When a bubble is accelerated through a liquid, the liquid in the nearby vicinity of the bubble is displaced. The virtual mass force is a result of this displacement, and it causes a resistance to the bubble acceleration (CFX, 2005).

$$\mathbf{M}_{\alpha}^{VM} = -\mathbf{M}_{\beta}^{VM} = C_{VM} r_\beta \rho_\alpha \left(\frac{\partial \mathbf{U}_\beta}{\partial t} - \frac{\partial \mathbf{U}_\alpha}{\partial t}\right) \tag{4.39}$$

where C_{VM} is the virtual mass coefficient $[-]$. For a single bubble in an unbounded fluid, the value of the virtual mass coefficient is 0.5 (Clift *et al.*, 1978). For systems with larger void fractions, C_{VM} is believed to increase with the value of the void fraction (Laurien and Niemann, 2004). The increase in C_{VM} was explained by an increase in pressure difference between up- and downstream side of the bubble interface, resulting in an increased virtual mass force.

The addition of the virtual mass force has been problematic, since modelling experience in the present work quickly showed that the model was less robust with this force included. Often initial modelling without the virtual mass force was necessary before switching the virtual mass on during computations in order to maintain a stable converged solution.

Turbulent dispersion force

The turbulent dispersion of bubbles is occurring due to the random turbulent eddies in the water phase. The force is proportional to the local gradient of the volume fraction of the continuous liquid phase. Since the distribution of the bubble volume fraction in radial directions in the bubble plume ideally is Gaussian, the turbulent dispersion force results in bubble spreading in radial directions, away from the centre axis of the plume.

In the present work, a Favre averaged turbulence dispersion force has been applied (Burns *et al.*, 2004):

$$\mathbf{M}_{\alpha}^{TD} = -\mathbf{M}_{\beta}^{TD} = C_{TD} C_{\alpha\beta}^{D} \frac{\nu_{t,\alpha}}{\sigma_{t,\alpha}} \left(\frac{\nabla r_{\beta}}{r_{\beta}} - \frac{\nabla r_{\alpha}}{r_{\alpha}} \right) \tag{4.40}$$

here, M_{α}^{TD} is the interfacial turbulent dispersion force $[kg \cdot m^{-2} \cdot s^{-2}]$ exerted on phase α, C_{TD} is the turbulent dispersion coefficient $[-]$, $c_{\alpha\beta}^{D}$ is the momentum transfer coefficient for the interface drag force between phase α and β $[kg \cdot m^{-3} \cdot s^{-1}]$, $\nu_{t,\alpha}$ is the turbulent kinematic viscosity of phase α $[m^2 \cdot s^{-1}]$, $\sigma_{t,\alpha}$ is the turbulent Schmidt number for the continuous volume fraction (the value is taken to 0.9) $[-]$ and r_{α} and r_{β} is the volume fractions of phase α and β, respectively $[m^3 \cdot m^{-3}]$.

Wall lubrication force

The wall lubrication force is a force that tends to force the bubbles away from walls. The force acts in the direction normal to the wall. Common lift force models results in forces directed against the wall in regions even very close to the walls, resulting in nonphysical model flows where the bubble concentration is largest at the walls. The wall lubrication force is made to counteract the nonphysical lift force in the vicinity of walls, and it is thus more a numerical tool than a force term based on physical relationships. (Antal *et al.*, 1991) derived an expression for describing this type of force:

$$\mathbf{M}_{\alpha}^{W} = -\mathbf{M}_{\beta}^{W} = -r_{\beta} \cdot \rho_{\alpha} \frac{\left(\left(\left(\mathbf{U}_{\alpha} - \mathbf{U}_{\beta} \right) - \left(\left(\mathbf{U}_{\alpha} - \mathbf{U}_{\beta} \right) \cdot \mathbf{n}_{\mathbf{w}} \right) \cdot \mathbf{n}_{\mathbf{w}} \right) \right)^2}{d_{\beta}} \cdot max \left(C_1 + C_2 \frac{d_{\beta}}{y_w}, 0 \right) \mathbf{n}_{\mathbf{w}} \tag{4.41}$$

where $\mathbf{M}_{\alpha}^{W}$ is the interfacial wall lubrication force acting on phase α $[kg \cdot m^{-2} \cdot s^{-2}]$, $\mathbf{n_W}$ is the unit vector normal to the wall $[m, m, m]$, y_W is the distance to the nearest wall $[m]$ and C_1 and C_2 is coefficients with the values -0.01 and 0.05 $[-]$, respectively.

The diffuser experiment covered in the present work is set up in a manner where the air bubble are unlikely to get in contact with the walls, making the inclusion of wall lubrication forces unnecessary.

Basset history term

The Basset history force is an unsteady force arising from the lagging boundary layer development with changing relative velocity. The Basset force includes the effect of past accelerations,

and it works as an increased viscous drag on the bubble. The Basset forces can be calculated from:

$$\mathbf{M}^H = \frac{9r_\beta}{\pi d_\beta}\sqrt{\pi\rho_\alpha\mu_\alpha} \times \int_{t_{p0}}^{t_p} \frac{(d/d\tau)(\mathbf{U}_\alpha - \mathbf{U}_\beta)}{\sqrt{t_p - \tau}} d\tau \tag{4.42}$$

where $t_p - \tau$ is the time lag since the past acceleration $[s]$.

For spheroidal bubbles at high $Reynolds'$ numbers, history effects are believed to be small (Magnaudet and Eames, 2000), neglecting the necessity for inclusion of the Basset history term.

Bubble induced turbulence

As disperse bubbles move through a continuous liquid they will have an impact on the turbulence of that liquid. This impact on the continuous liquid results in a turbulence modulation. The modulation is believed to be originating from several phenomena (Crowe, 2000):

- Streamline distortion due to the presence of particles
- Wakes created by the particles
- Modification of velocity gradients in the continuous carrier phase
- Damping of turbulence motion by the particle induced drag force

Presently, a complete model that can describe all of the above mentioned phenomena is yet to be found. In general large particles are believed to enhance the turbulence in the liquid phase, whereas smaller particles will have a tendency to dampen turbulence (Gore and Crowe, 1989). The shift from turbulence attenuation to augmentation happens at a ratio of particle diameter to turbulent length scale of approximately 0.1.

Beside the turbulence modulation described through an additional turbulent dispersion interfacial force term (4.1.6), a common way of introducing particle induced turbulence modulation is to add extra source terms to the $k-$ and ϵ transport equations 3.14 and 3.15. In the present computations extra source terms are added based on the formulations from (Simonin and Viollet, 1988):

Source of turbulent kinetic energy, k:

$$S_k = C_{k2}C^D_{\alpha\beta}r_\alpha k_l \tag{4.43}$$

Source of turbulent eddy dissipation, ϵ:

$$S_\epsilon = C_{\epsilon 2}C^D_{\alpha\beta}r_\alpha \epsilon_l \tag{4.44}$$

where C_{k2} and $C_{\epsilon 2}$ are source coefficients $[-]$, with values of 0.75 and 0.6. $C^D_{\alpha\beta}$ is again he momentum transfer coefficient for the interface drag force between phase α and β $[kg{\cdot}m^{-3}{\cdot}s^{-1}]$ (Equation 4.15).

Equation 4.43 and 4.44 were successfully applied to the modelling of a large-scale bubble column by (Zboray and de Cachard, 2005).

In the present investigation a constant drag coefficient, C_D, corresponding to bubbles in the inertial regime is applied in formula (4.43 and 4.44), making the formula independent of the actual drag coefficient in the flow.

(Sato and Sekoguchi, 1975) constructed an expression directly describing the additional particle induced turbulence viscosity, $\mu_{t\beta}$:

$$\mu_{t\beta} = C_{\mu\beta}\rho_\alpha r_\beta d_\beta |\mathbf{U}_\beta - \mathbf{U}_\alpha| \tag{4.45}$$

where $C_{\mu\beta}$ is a constant of value 0.6 $[-]$. Both the turbulence modulation of (Simonin and Viollet, 1988) and (Sato and Sekoguchi, 1975) has been tested in the present study.

4.1.7 Setup of numerical model

A grid with a relatively high density in the pit and especially in the area above the diffuser was constructed. The dense grid above the diffuser was created along a vertical line going from the centre of the diffuser to the water surface. An outline of the surface mesh is illustrated in figure 4.18.

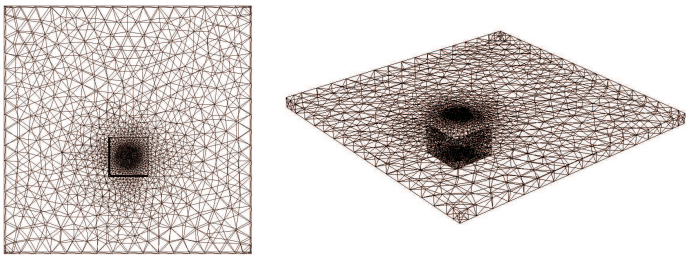

Figure 4.18 Surface mesh on the diffuser model.

The mesh on figure 4.18 consists of approximately 255,000 tetrahedron and prismatic shaped cells. The SST-model is recommended for accurate boundary layer modelling, but in order to benefit from the model the resolution in the boundary layer has to be at least 10 nodes (CFX, 2003). This demand is managed by shifting the grid on the wall boundaries to an inflated boundary, consistent of a layer of 10 prisms with increasing thickness in directions away from the walls. An extract from the inflated boundary is shown in figure 4.19.

4.1.8 Modelling results

The present subsection includes the numerical simulations of the bubble diffuser flow. The modelling is performed with the application of several of the relevant interfacial forces described in section 4.1.6. Furthermore, different turbulence models for the continuous phase and the bubble induced turbulence is applied in the model. This way the sensitivity to the different interfacial force models and turbulence models are evaluated through the modelling. Initially five different

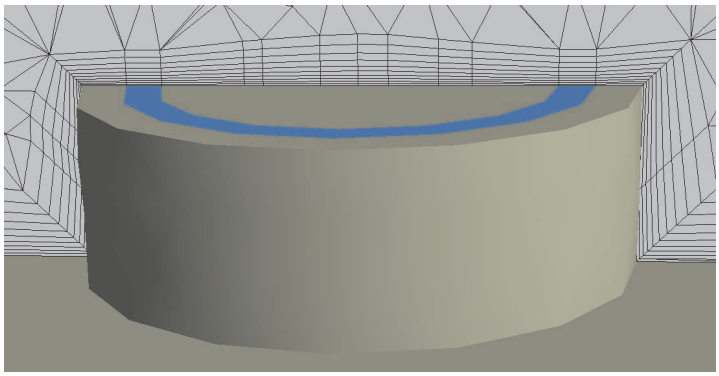

Figure 4.19 Prismatic layer around the diffuser.

drag models are tested, after which the most appropriate model is chosen for further combination with additional interfacial forces and versions of the turbulence modelling. It should here be mentioned that not all combinations of the different interfacial force models and turbulence models are tested, and hence the most optimal combination of models might not be found from the present investigation.

Drag model dependency

As stated above, the drag forces are the most important interfacial forces in a typical bubble flow. In order to investigate the dependency on the chosen drag model, the drag models presented previously in this chapter have been tested:

- The Grace drag model (Equation 4.27)
- The Ishii-Zuber drag model (Equation 4.19 and 4.23)
- The Lain drag model for fluid particles (Equation 4.31, 4.32 and 4.33)
- The Ishii 2003 drag model (Equation 4.34)
- A drag model for highly contaminated water (Equation 4.35, 4.36 and 4.37)

The models are evaluated against the measured mean volume fractions of air and the mean axial liquid velocities inside the bubble plume (Figure 4.20 and 4.21).

As indicated on figure 4.20, the air volume fraction distributions are slightly dependent on the chosen drag model. The drag model for air bubbles in *contaminated* water does however appear to result in the largest volume fractions of air. This agrees well with the fact that the drag coefficient in general is higher in *contaminated* water. On the other hand the Grace drag model seems to produce slightly lower air volume fractions than the remainder of the models. In general, good agreement between the measurements and the models are achieved. Close to the diffuser the volume fractions are underestimated by the model, whereas the opposite is the case for the profiles farthest away from the diffuser. Furthermore, the high peak values at the diffuser are not captured by the models. This is possibly due to uncertainties about the arrangement of a

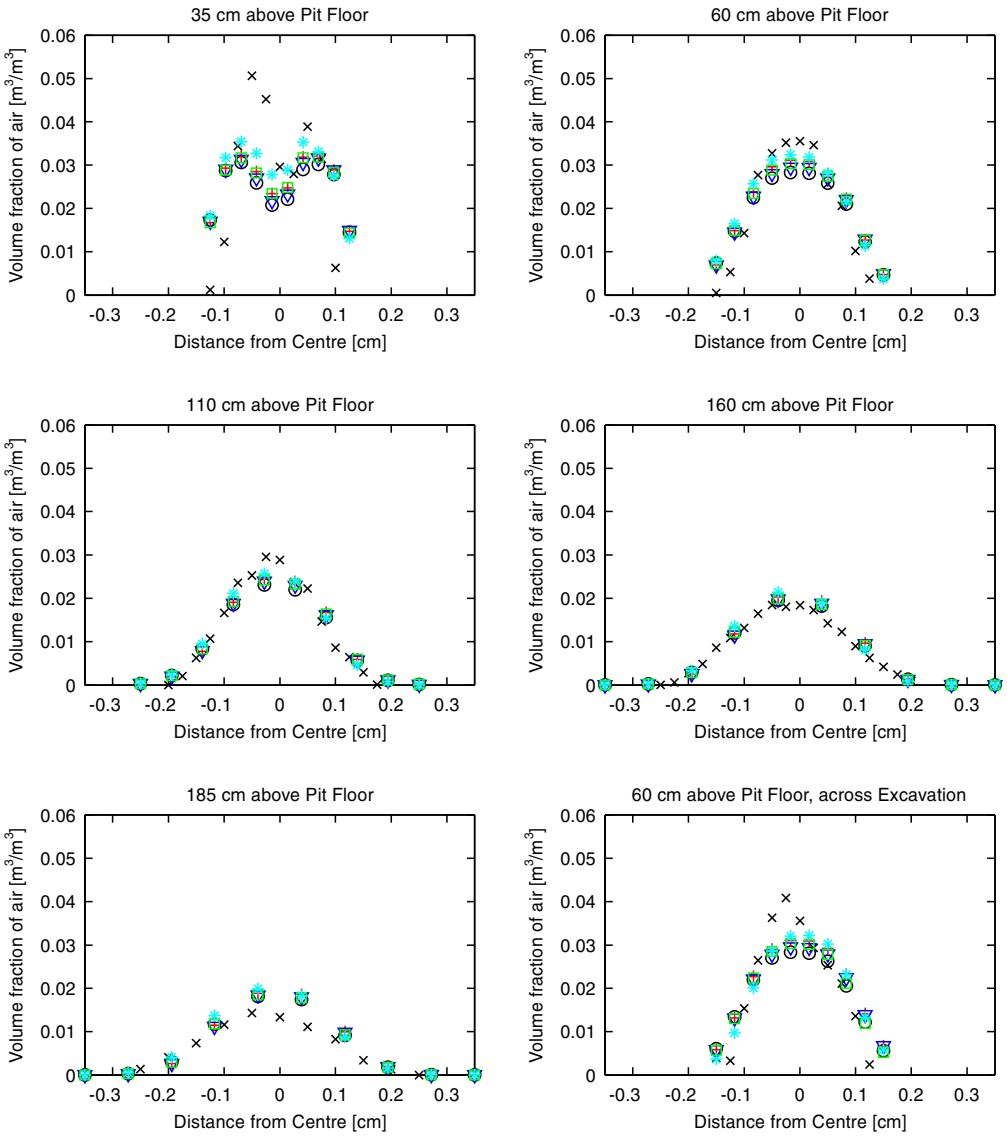

Figure 4.20 Modelled versus measured mean volume fractions of air for different drag models; ×: Measurements, ○: The Grace Drag model, +: Lain model for fluid particles, ▽: Ishii2003 model, □: Ishii-Zuber drag model and ✳: The drag model for contaminated water.

correct inlet boundary condition and measurement uncertainties connected to the very dynamic flow conditions close to the diffuser.

Except for the drag model for air bubbles in contaminated water, the measured liquid velocities are nearly identical for the chosen drag models. The drag model for air bubbles in con-

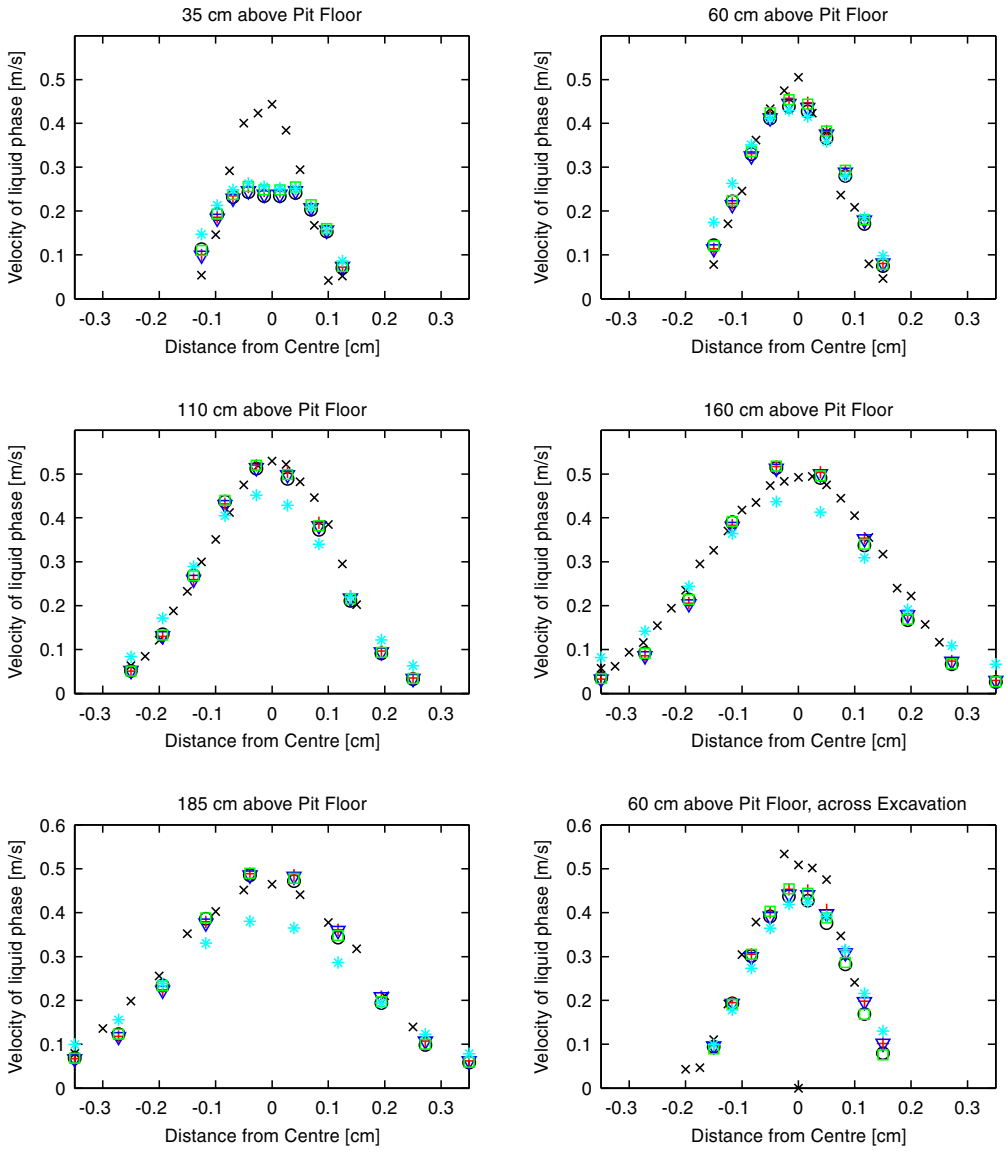

Figure 4.21 Modelled versus measured mean liquid velocities inside the bubble plume for different drag models; ×: Measurements, ○: The Grace Drag model, +: Lain model for fluid particles, ▽: Ishii2003 model, □: Ishii-Zuber drag model and ✳: The drag model for contaminated water.

taminated water seems to under predict the liquid velocities at the profiles farthest away from the diffuser. All the models under predict the liquid velocities at the profile just above the diffuser. Again this could be a boundary definition problem.

With reference to figure 4.20 and 4.21, any of the models except for the model for contaminated conditions can adequately describe the present diffuser induced bubble flow. Since the Grace drag model is especially constructed on the basis of bubble flows, this model is in general expected to give the most reliable results and for that reason it is chosen for further investigations involving contributions from lift, virtual mass and turbulence dispersion forces.

Interfacial force dependency

In accordance with the analysis in section 4.1.6, the following interfacial forces are combined with the Grace drag model in order to capture any possible positive synergical effects:

- The lift force (Equation 4.38)
- The virtual mass force (Equation 4.39)
- Favre averaged turbulence dispersion force (Equation 4.40)

The resulting modelled profiles of mean air volume fractions and mean liquid velocities in the centre of the plume is shown in figure 4.22 and 4.23.

As expected the inclusion of the virtual mass force increases the retention of air bubbles in the system. This can be seen as higher modelled gas hold ups in the plume (Figure 4.22). This is expected since the virtual mass force introduces an extra resistance to the bubbles as they accelerate additional liquid when they rise through the water column. Oppositely, the addition of a turbulence dispersion force or lift force, enhances the lateral spreading of the plume as anticipated (Figure 4.22). Close to the diffuser the lift force induces the highest degree of lateral spreading, whereas the turbulent dispersion force result in the highest spreading in the profiles farthest away from the diffuser.

Except from the profile closest to the diffuser, good agreement is obtained between the modelled and measured liquid velocities (Figure 4.23). Since the inclusion of the virtual mass force induces additional acceleration of the water phase, an increment in modelled liquid velocities is observed for this model. This results in a better modelling of the liquid velocities in the profiles close to the diffuser, whereas the liquid velocities are overestimated at the profiles farthest away from the diffuser for this model. For the rest of the models, the modelled profiles are nearly identical.

From figure 4.22 and 4.23 it can be concluded that the inclusion of additional interfacial momentum transfer terms do alter the modelled profiles of mean air volume fractions and liquid velocities inside the bubble plume slightly.

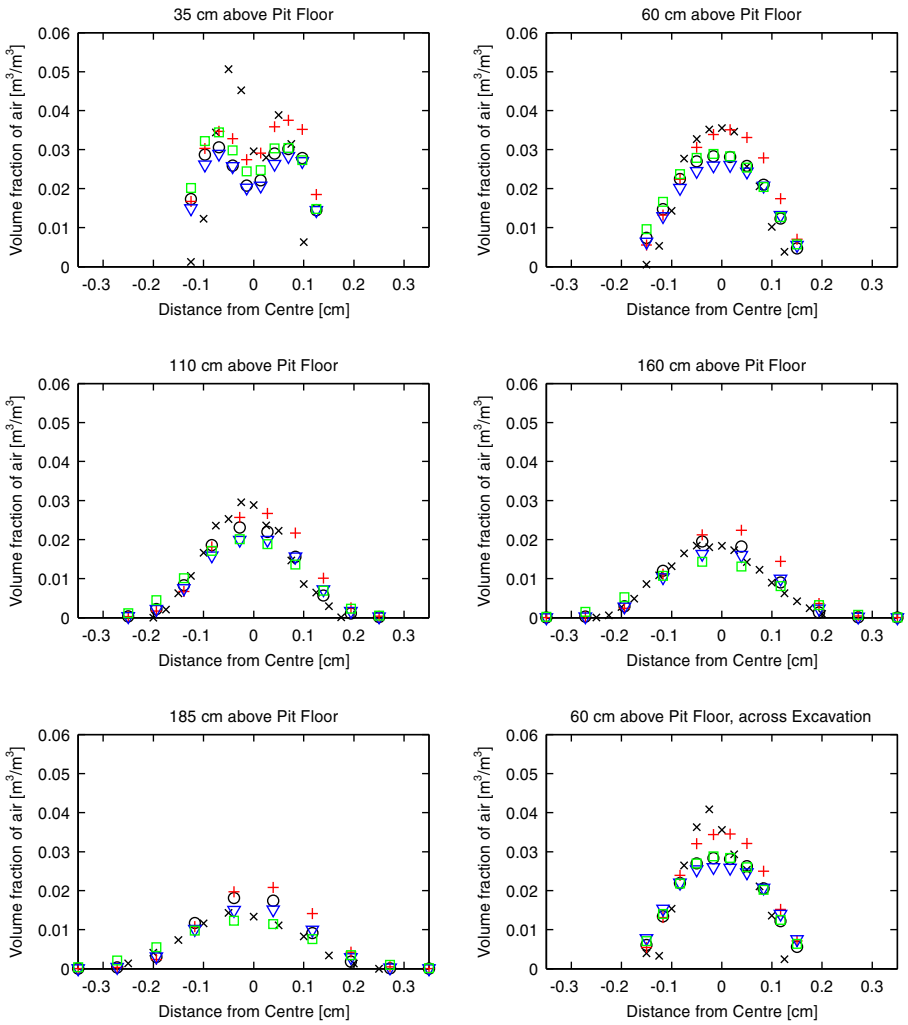

Figure 4.22 Modelled versus measured mean volume fraction of air for different drag models; ×: Measurements, ○: The Grace Drag model without additional interfacial forces, +: Virtual mass force included, ▽: Lift force included, □: Turbulent dispersion force included.

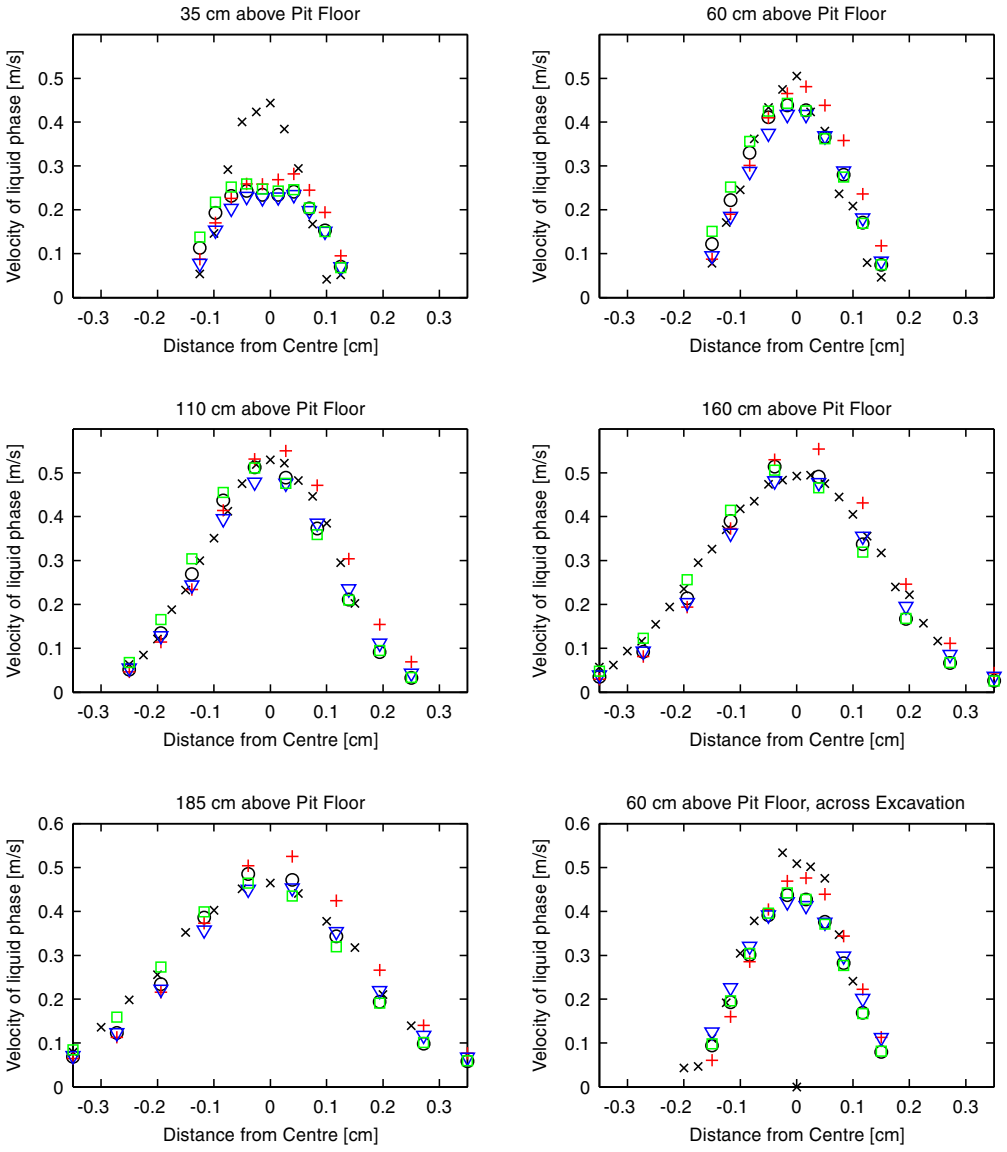

Figure 4.23 Modelled versus measured mean liquid velocities inside the bubble plume for different interfacial force models; ×: Measurements, ○: The Grace Drag model without additional interfacial forces, +: Virtual mass force included, ▽: Lift force included, □: Turbulent dispersion force included.

In order to quantify this trend in a more physical manner, a hand calculation of the size of the different interfacial momentum terms have been performed in a point displaced $0.15m$ in the x-direction, $1m$ above the diffuser (Figure 4.24), (Table 4.2). All incoming parameters to the hand calculations have been directly extracted from the CFD model at the above mentioned point.

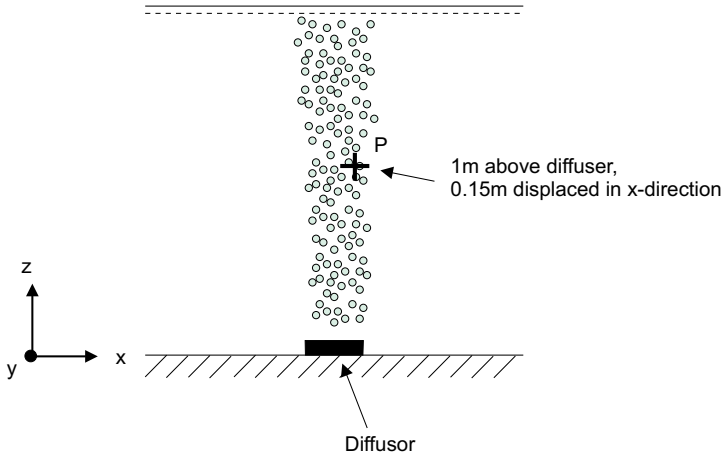

Figure 4.24 Calculation point where the comparison of the size of the different interfacial force components have been performed.

Table 4.2 Hand calculation of the size of the interfacial force terms working on the continuous phase in the point P as defined in figure 4.24.

$Term$	$x-component$ $[kg \cdot m^{-2} \cdot s^{-2}]$	$y-component$ $[kg \cdot m^{-2} \cdot s^{-2}]$	$z-component$ $[kg \cdot m^{-2} \cdot s^{-2}]$
Grace drag	6.6	$0.12 \cdot 10^{-4}$	56.8
Lift	-1.6	$-8.1 \cdot 10^{-2}$	0.2
Virtual mass	$4.8 \cdot 10^{-5}$	$1.2 \cdot 10^{-4}$	0.0
Favre Turbulent dispersion	-6.7	-0.2	$-2.1 \cdot 10^{-2}$

As expected, the drag term is by far the dominating term in the vertical component. The other terms are clearly negligible in this direction. The same trend is observed for the y-direction. In the x-direction, both lift and turbulent dispersion counteracts the drag force with approximately the same order of magnitude. Since the interfacial forces on the bubbles are of opposite signs than interfacial forces on the water phase, it is as expected indicated that both the lift force and the turbulent force will have a dispersive effect on the volume fraction of bubbles. Due to the stationary nature of the model, the velocity gradients are nearly constant in time. Consequently, the virtual forces are negligible compared to the remainder of the forces.

It can be concluded that the Grace drag model without any additional interfacial momentum transfer terms seems to reproduce the measured profiles most satisfactory, even though hand calculations show that both lift and turbulent dispersion forces are likely to produce additional lateral spreading of the bubble plume. It is however chosen to neglect the additional momentum

transfer terms and only operate with interfacial momentum transfer originating from the Grace drag force in the remainder of this thesis.

Turbulence model dependency

In order to investigate the dependency on the chosen turbulence models, several turbulence models have been tested on the bubble plume:

- The $k-\epsilon$ model (Equations 3.13-3.15)
- The shear stress transport (SST) model (Equations 3.16-3.25)
- The Sato enhanced eddy viscosity model (Equation 4.45)
- The Simonin and Violet $k-\epsilon$ source model (Equation 4.43 and 4.44)

With respect to the modelling of mean volume fractions, the choice of turbulence models seems to have little effect; The four models are nearly indistinguishable from each other (Figure 4.25).

The choice of turbulence model do however prove to have a significant effect on the modelled mean liquid velocities inside the bubble plume (Figure 4.26). Close to the diffuser the four models are indistinguishable, whereas especially the model with additional $k-\epsilon$ model source terms as suggested by (Simonin and Viollet, 1988) result in a lowering of the centre velocity in the plume and an extra lateral spreading of the bubble plume. Also the model where SST turbulence modelling is applied show slightly lower velocities compared to the model including $k-\epsilon$ turbulence modelling. The enhanced eddy viscosity model as suggested by (Sato and Sekoguchi, 1975) does not seem to have significant effect compared to e.g. applying the standard $k-\epsilon$ without any turbulence altering. From figure 4.25 and 4.26 it is concluded that the modelling with standard $k-\epsilon$ model reproduce the measurements with a slightly better degree of accuracy than the remaining turbulence models.

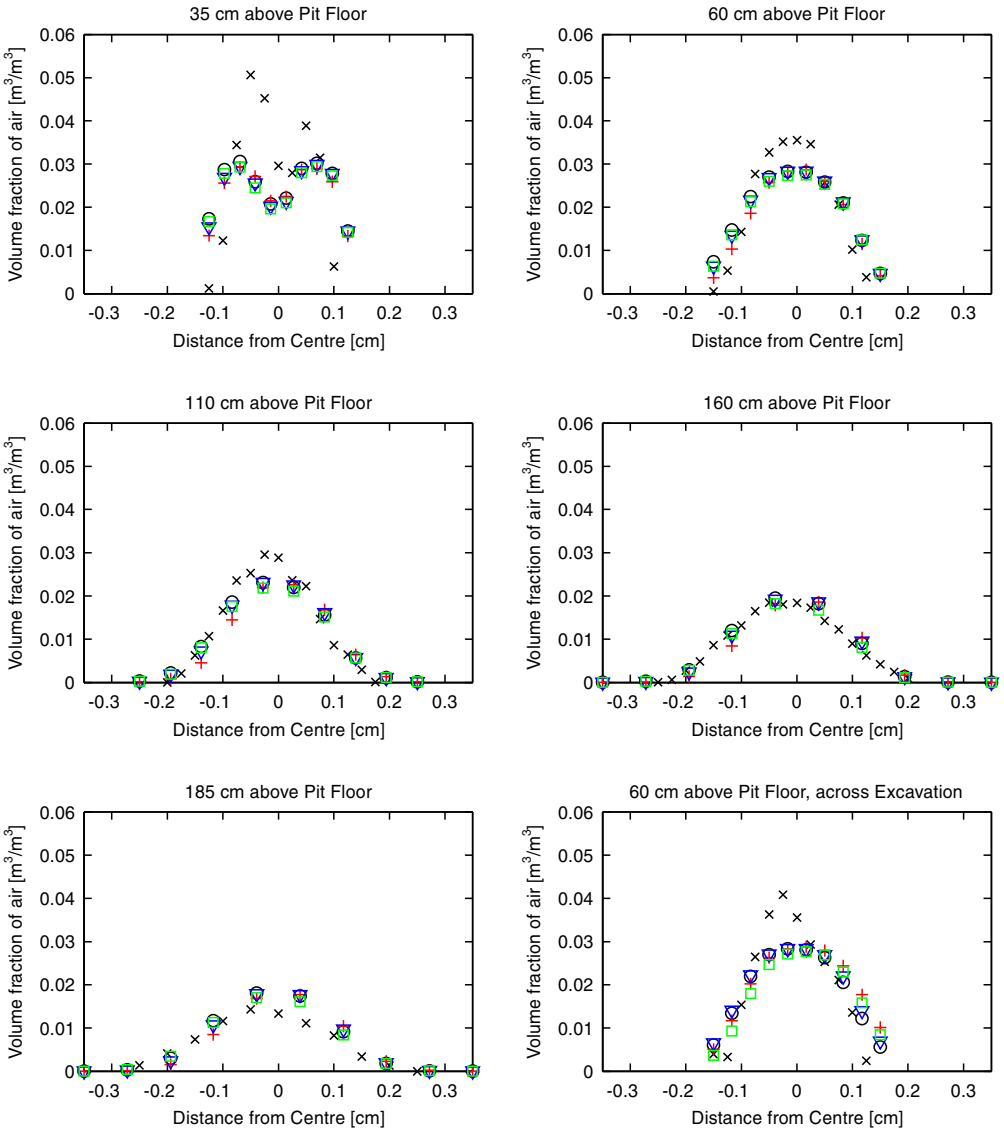

Figure 4.25 Modelled versus measured mean volume fraction of air for the Grace drag model combined with different turbulence models; ×: Measurements, ○: The $k-\epsilon$ model and +: The shear stress transport (SST) model, ▽: Sato enhanced turbulence viscosity included and □: Simonin and Violet $k-\epsilon$ source model included.

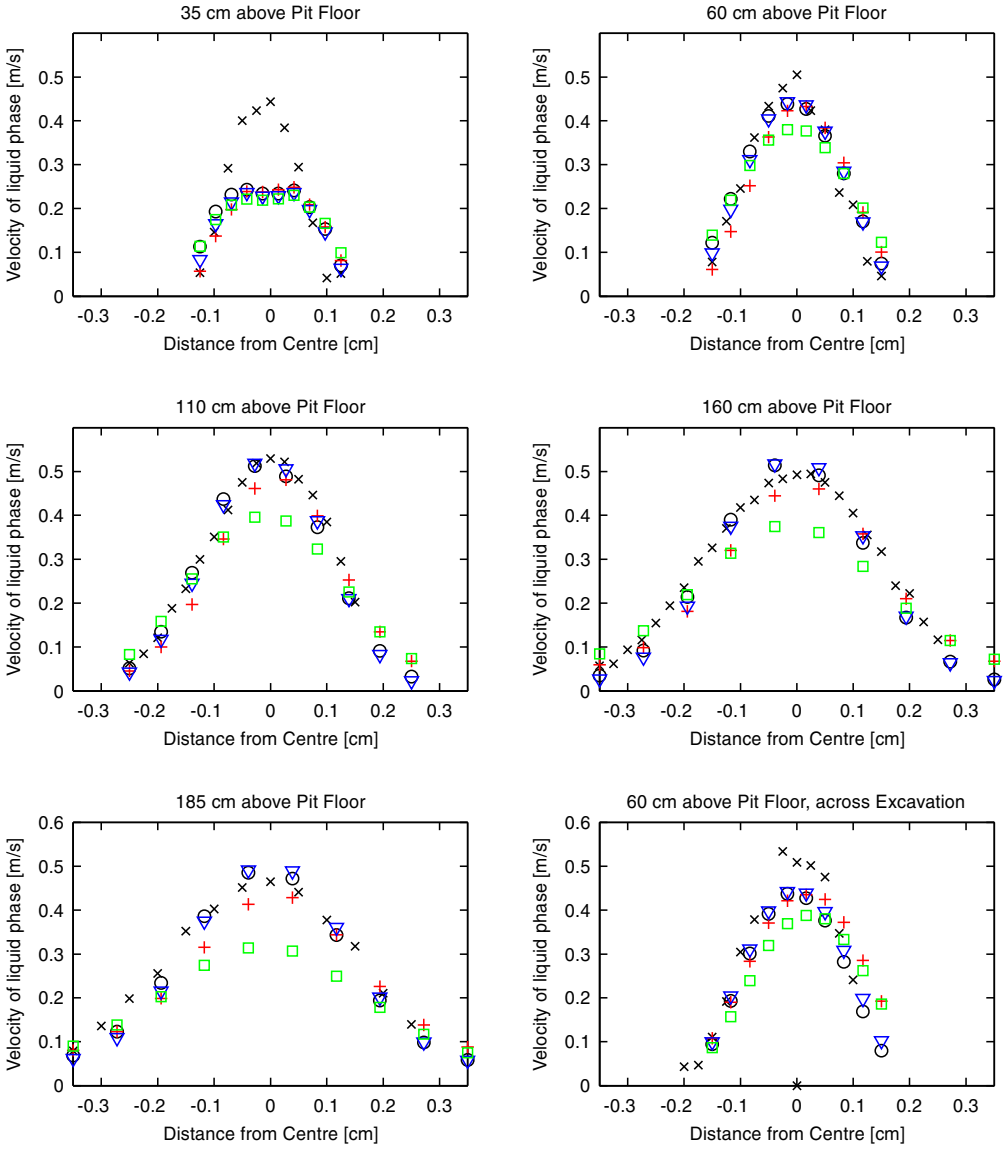

Figure 4.26 Modelled versus measured mean liquid velocities inside the bubble plume for the Grace drag model combined with different turbulence models; ×: Measurements, ○: The $k-\epsilon$ model and +: The shear stress transport (SST) model, ▽: Sato enhanced turbulence viscosity included and □: Simonin and Violet $k-\epsilon$ source model included.

4.1.9 Summary

The hydrodynamics of a bubble plume generated by a submerged air-diffuser often used in wastewater treatment plant process tanks has been investigated experimentally and numerically. The local mean volume fractions of air and the local mean liquid velocities inside the bubble plume was measured, with relatively simple measurement equipment. The measurements were successfully reproduced through a numerical two-phase multifluid model. Several interphase force terms and turbulence models were tested, and it was found that the model could give satisfactory results with the application of the Grace drag model and the SST turbulence model. Even though no significant difference can be observed between using the SST or the $k-\epsilon$ model, the former is chosen since it is recommended due to its superiority over latter with respect to modelling swirling and adverse pressure flows. No other interfacial force terms proved necessary, even though the presence of several of the terms did not result in a distinct decrease of accuracy. Furthermore, the introduction of additional bubble induced turbulence seemed to have a too large diffusive effect on the flow field, resulting in too high lateral plume spreading. The applied model is steady-state. In order to completely model the full transient behaviour of the bubble plume, more rigorous turbulence modelling has to be applied; Like e.g. Large-Eddy simulation. Due to the large-scale flow system of practical process tanks, such modelling is however not feasible. It is concluded that the two-phase plume model performs satisfactory enough for further application in a wastewater treatment plant process tank model.

4.2 Modelling of a full-scale two-bladed propeller

Previously, in the preceding section 4.1, one of the important mixing processes in many wastewater treatment plant; the injection of large amounts of air bubbles through air-diffusers, was investigated. Another very important mixing process, the mixing induced by mechanical agitation, will be investigated in the present section. The investigation mainly involves numerical modelling of a slow rotating large-scale two-bladed hydrofoil shaped propeller.

For several reasons mixing is an important unit operation in many parts of a wastewater treatment plant (Tchobanoglous and Burton, 2003):

- mixing of substances and blending of miscible liquids
- Flocculation of particles
- Maintenance of continuous mixing of the liquid suspension
- Heat transfer

In general terms, three types of mixers can be defined for use in physical-chemical treatment of water (Sincero and Sincero, 2003):

- Rotational mixers
- Pneumatic mixers
- hydraulic mixers

As indicated in the name, *rotational* mixers agitate the media by the use of a rotating element, whereas *pneumatic* mixers utilize gas bubbles to agitate and *hydraulic* mixers use mixing originating from the flow of water.

4.2.1 Rotational mixers

Various types of impellers are used in WWTP process tanks and in other unit operations at the WWTP where mixing is necessary (Figure 4.27).

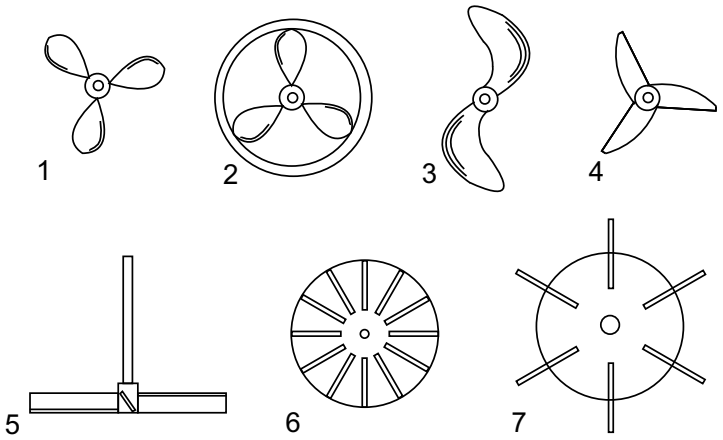

Figure 4.27 Types of mixers: (1)-(4) different propeller types; (5) paddled impeller; (6) shrouded blade turbine; (7) vaned disc (Rushton turbine).

Propellers (Figure 4.27 1-4) are impellers, where the main flow generated by the rotation is in the axial direction. The blades on the propellers can be twisted in different ways dependent on the purpose of the device.

Paddled impellers (Figure 4.27 5) are called so because of their paddle shaped rotational elements. The paddles are not twisted like the blades on the propellers. Dependent on the pitch of the paddles the flow generated can go from mainly radial and tangential to mainly axial.

Impellers with shorter paddles than paddled impellers are called *turbines* (Figure 4.27 6). Turbines rotate at higher speeds than propellers and paddled impellers and they mainly produce radial and tangential flow.

A special case, the Rushton turbine (Figure 4.27 7), where a non-pitched paddled impeller is combined with a disc, is widely used in the agitation of reactors throughout the chemical industry.

Of the above mentioned mixer types, the propellers are often used in WWTP process tanks, and the investigation in this thesis will mainly deal with propeller type mixers. The reason for their frequent application in process tank is that they are well suited for making a large amount of axial thrust, which is necessary for keeping a large body of sludge in suspension. Often large slowly rotating propellers are used, due to their gentle mixing while they still deliver enough energy to the suspension to keep the sludge well mixed and flocculated.

Characteristic numbers of the propeller

The power consumption is directly proportional to the torque on the propeller. The proportionality factor is the angular velocity, ω:

$$P = M\omega \tag{4.46}$$

here, M is the torque on the propeller $[N \cdot m]$ and ω is the angular velocity of the propeller $[rad \cdot s^{-1}]$.

When the power consumption, P, is known, the power number, N_p, proportional to the ratio between drag forces and inertial forces, can be calculated (Armenante *et al.*, 1997):

$$N_p = \frac{2\pi NM}{\rho N^3 D^5} = \frac{P}{\rho N^3 D^5} \tag{4.47}$$

where N_p is the dimensionless power number $[-]$ and N is the rotational speed of the propeller $[rotations \cdot s^{-1}]$, measured in revolutions per second and D is the diameter of the propeller $[m]$.

The pumping capacity of the propeller can be calculated by locally integrating the velocities in the impeller region (Armenante *et al.*, 1997):

$$Q = 2\pi \int_0^{D/2} U_y(r)|_{y=y_0} r dr + \pi D \int_{y_0}^{y_{+\longrightarrow -}} U_r(y)|_{r=D/2} dy \tag{4.48}$$

here, Q is the pumping capacity of the propeller $[m^3 \cdot s^{-1}]$, D is the propeller diameter $[m]$, $U_y(r)$ is the axial velocity in the radial coordinate direction $[m \cdot s^{-1}]$, $U_r(y)$ is the radial velocity as a function of the axial coordinate $[m \cdot s^{-1}]$, r is the radial distance from the centerline of the propeller $[m]$ and y is the axial coordinate $[m]$. The definition of $[y_0]$ and $[y_{+\longrightarrow -}]$ is indicated in figure 4.28.

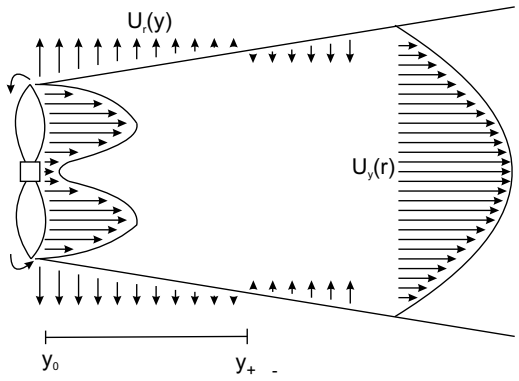

Figure 4.28 Outline of velocity profiles behind a propeller. The left axial profile show a distinct trough shape caused by the presence of the propeller hub, whereas the right axial profile show a more Gaussian shape.

Based on Q, the flow number, Fl, can be calculated:

$$Fl = \frac{Q}{ND^3} \tag{4.49}$$

here, Fl is the dimensionless flow number $[-]$.

The propeller Reynolds number can be estimated on behalf of characteristics of the propeller and the fluid:

$$Re_p = \frac{\rho N D^2}{\mu} \tag{4.50}$$

where Re_p is the Reynolds number of the propeller $[-]$, ρ is the density of the fluid $[kg{\cdot}m^{-3}]$ and μ is the dynamic viscosity of the fluid $[kg \cdot m^{-1}s^{-1}]$.

Jet characteristics

Close to the impeller, the characteristics of the jet will mainly be dependent on the impeller design, i.e. the diameter, the number of blades, the shape of the blades and the rotational speed of the impeller. In this region the flow will show periodicity in the circumferential direction as a function of the location of the blades. For a 3 bladed axial propeller this zone was found to be within 1-2 impeller diameters of the impeller (Petersson *et al.*, 1996), (Petersson *et al.*, 2000). At a downstream distance of 2D the periodicity had disappeared. Often the mean axial velocity profile will exhibit a trough shape close to the impeller (4.28). This phenomenon is mainly caused by the blocking effect of the impeller hub and the centrifugal forces in the rotating jet.

Further downstream of the impeller, in the case of the investigations of (Petersson *et al.*, 1996), (Petersson *et al.*, 2000) approximately 4D, the flow shows self-similarity with respect to mean axial velocities, hence 4D downstream of the propeller all mean axial velocity profiles can be described by scaling the same Gaussian curve:

$$\frac{U_y(y,r)}{U_m} = e^{-C_u \xi^2} \tag{4.51}$$

Where $U_y(y,r))$ is the axial velocity as a function of the axial and radial distance to the centre of the propeller $[m \cdot s^{-1}]$, U_m is the maximum axial velocity $[m \cdot s^{-1}]$, C_u is a non-dimensional coefficient $[-]$ and ξ is the similar radial coordinate: $r/(y+a)$ $[m]$. Here r is the radial coordinate $[m]$, y is the axial coordinate $[m]$ and a is the distance to the virtual origin of the jet, upstream from the propeller $[m]$.

The degree of swirl in an axisymmetric jet can be described by the dimensionless swirl number (Gupta, 1984):

$$S = \frac{G_\phi}{G_x R} \tag{4.52}$$

where S is the swirl number $[-]$, R is the impeller radius $[m]$, G_ϕ is the axial flux of angular momentum $[kg \cdot m^2 \cdot s^{-2}]$:

$$G_\phi = 2\pi\rho \int_0^\infty r^2 \overline{U_y U_t} dr \tag{4.53}$$

and G_x is the axial flux of linear momentum $[kg \cdot m \cdot s^{-2}]$:

$$G_x = 2\pi\rho \int_0^\infty r \left(\overline{U_y}^2 - \frac{\overline{U_t}^2}{2} \right) dr \tag{4.54}$$

where ρ is the fluid density $[kg \cdot m^{-3}]$ and U_t is the mean tangential velocity $[m \cdot s^{-1}]$.

4.2.2 Experimental methods for investigating propeller flow

Several experimental investigations have been made on especially smaller fast rotating impellers:

(Petersson *et al.*, 1996) applied 2D Laser Doppler Anemometry (LDA) to measure the velocity field downstream of a model impeller. The impeller model was a 1:10 model of a three-bladed axial impeller from ITT Flygt. The authors found self similarity for the mean axial velocity profile 3-4 diameters after the impeller, and a Gaussian curve could well describe the shape of the profile. No other quantities was proven to show self-similarity within 12 diameters from the impeller. At the zone of established flow, the velocity profiles could be described with Gaussian distributions, and the radial spread of the jet was linear with a spreading angle of 7.1 degrees. The authors extended their study to involve weak co- and counter-flow (Petersson *et al.*, 2000), in which the co-flow case is very relevant to situations involving mixing at WWTP process tanks constructed of ring channels. The counter flow case produced a wider jet width than the co-flow case, making a larger spreading angle. The volume flux did however show similar growth rate, indicating that the wider spreading angle observed in the counter-flow was mainly due to a lateral oscillation of the jet coursed by the interaction of the return flow.

(Wu and Pullum, 2000) made LDA measurements of the velocity distributions for different axial flow impellers in mixing tanks. Also theoretical evaluations of the impeller performances were performed based on blade-element theory. The investigated impellers were a three-bladed and a four-bladed impeller and 30° pitched-bladed turbine. A good agreement between measurements and theory was found. The method is however not applicable for impellers also generating radial flow. Furthermore a drawback of blade element theory is that knowledge about the lift and drag coefficients are needed in order to perform the calculations.

Experimental investigations of the propeller generated flow field in channels are available for model-scale fast rotation propellers and impellers used for mixing in chemical reactors. To the author's knowledge, no investigations except for any confidential measurements performed by the propeller manufacturers are available for the flow field generated by slow rotating large-scale propellers in channels. Within the field of naval science, a number of publications are however available. Since the flow generated by a propeller is highly dependent on both the specific design of the propeller and the conditions under which it is operated, the flow generated by the special slow rotating propellers used in many WWTP's can not be derived directly from such studies.

Numerical work

Apart from the above described experimental investigations, a large amount of work has been done on modelling stirred reactors used in different branches of chemical engineering. The focus has mainly been aimed at small chemical reactor with impellers turning around the vertical axis. Some of the work done by other authors is listed below.

(Morud and Hjertager, 1996) performed concurrent LDA measurements and CFD modelling of the gas-liquid flow in a stirred vessel. They applied a two-dimensional two-fluid Euler-Euler model, where the impellers and baffles were modelled through source and sink terms. The model showed qualitative agreement with the LDA measurements, but the model could due to its 2D nature not capture 3D effects of the baffles. Also the standard k-ϵ model turned out to have shortcomings with respect to modelling the swirling motion and the effect of bubble motion on liquid turbulence.

(Armenante *et al.*, 1997) investigated a 6-blade 45° pitched-bladed turbine with coherent LDV-measurements and 3D CFD computations in an eight litre mixing vessel. Velocities measured in the vessel were used as boundary conditions in the CFD model. E.g. the measured mean velocity and k and ϵ were used as impeller boundary conditions. By comparing measured and modelled velocities, dimensionless numbers and turbulent kinetic energy, it was concluded that an algebraic stress turbulence model (ASM) was superior to the k-ϵ model, except for the flow and power number.

(Friberg and Hjertager, 1998) simulated a 3-dimensional large-scale fermenter with four Rushton turbines. A 3-dimensional two-fluid model was used and turbulence was modelled through a modified k-ϵ model where bubble induced turbulence was accounted for. In order to get the axial velocity profiles right, a negative lift coefficient was applied in the lift force term. Compared to measured data, the model predicted velocities well, whereas void fractions were overestimated. Further studies of interfacial forces between the fluids, the boundary conditions at the impeller and two-phase turbulence where suggested for future work.

Also (Revstedt *et al.*, 1998) studied a stirred reactor. A large eddy turbulence model was applied. The Rushton turbine was modelled through a momentum model, adding source terms to the momentum equations at the location of the impeller blades. Good qualitative agreement between the model and LDA-measurements was obtained, whereas the model qualitatively, especially close to the impeller was lacking accuracy. This was probably due to the simplified description of the impeller. (Jenne and Reuss, 1999) investigated the same reactor. They mainly focused on the application of different versions of the $k-\epsilon$ model. They found that none of the models performed satisfactory in their original version. A modified version of the Chen-Kim $k-\epsilon$ model did however produce accurate mean flow and turbulence quantities in the outflow of the impeller and in the main part of the tank.

(Blackburn *et al.*, 2000) constructed a hybrid impeller model, where the time-mean flow in the impeller region was modelled with blade element theory and the flow in the remainder of the mixing vessel was determined through numerical CFD-modelling. The method is computationally cheaper than modelling the flow in the impeller region by e.g. the sliding mesh CFD method. The model was compared to LDA measurements of a three bladed axial impeller in a mixing vessel and good compliance between model and measurements was obtained.

(Friberg and Hjertager, 2000*c*) analyzed the flow pattern in a stirred tank equipped with a six bladed Rushton turbine. They compared three different impeller models and two different turbulence models. With respect to a correct modelling of velocities and turbulent kinetic energy, a modified $k-\epsilon$ model with an extra source term in the dissipation rate equation proved better compared to the standard $k-\epsilon$ model. The modelling of the impeller turned out to be more successful with the sliding mesh and snapshot models compared to the empirical source term model. In the snapshot method the flow field is obtained by ensemble averaging of stationary solutions obtained at different impeller positions. In (Friberg and Hjertager, 2000*b*) the authors replaced the empirical source term impeller model used in (Friberg and Hjertager, 1998) with

a sliding mesh model. (Friberg and Hjertager, 1999) combined a hydrodynamic model with a model for the fermentation of *Escherichia Coli* in a 3-dimensional baffled fermenter. Again, the hydrodynamic model was a two-fluid Euler-Euler model, a modified k-ϵ model was used and a sliding mesh technique was applied for the impeller model. Both gas fractions, velocities and biological processes were well predicted.

(Börjesson and Fahlgren, 2001) performed comprehensive CFD computations on the modelling of a propeller of the same type as the one investigated in the present work. The investigation involved both model- and full-scale modelling. The authors made comparisons between sliding mesh, multiple reference frame and momentum source models. Their findings indicated that the momentum model could adequately reproduce the overall effect of the propeller as calculated by the sliding mesh model, whereas the multiple reference frame model failed to realistically resolve the properties of the propeller jet.

To the knowledge of the author, only the investigation of (Börjesson and Fahlgren, 2001) have involved large-scale impellers effect on large-scale mixing tanks. The present investigations aim to get experience in the modelling and understanding of impeller driven flows in large-scale process tanks.

4.2.3 Investigations of a Flygt 4430 propeller.

As described in details in section 5.2, the process tanks at Hals WWTP are equipped with large slow moving two-bladed hydrofoil shaped propellers. A spare blade from one of these propellers was borrowed from the plant for analysis. This section regards both the measurements performed and the numerical modelling of the propeller.

Propeller details

The propeller subject to investigations is a FLYGT 4430, made for mixing of large volumes in e.g. process tanks. The propeller i often referred to as a *banana impeller* due to its unique shape. The propeller is two-bladed and it has a total diameter of 2.5m.

The propeller is operated at 35rpm, and it is driven by a 3.1kW electrical motor running at 1440rpm. The combination of slow propeller speed and a large diameter, ensures a high thrust with low power consumption and the swept back shape of the blades results in good self cleaning in media with fibrous materials (http://www.flygtus.com/115917.asp, 2005).

Measurements of propeller geometry

In order to get detailed measurements of the propeller geometry, the propeller blade was measured with a profiler in the laboratory. The profiler is an in house made product, utilizing a laser beam to measure the shape of the propeller surface (Figure 4.30).

By the utilization of servo motors, the laser could accurately move back and forth above the surface of the blade, and height values were logged to a file at fixed displacement intervals in the x and y directions. In this case the height displacements between logging were chosen to be 5mm. This value was chosen on a trade-of between the wanted level of resolution and the resulting measuring time. The utilized laser was a small 1 mW 670nm laser. Data acquisition was obtained by connecting a data logger to a PC. The program, EPRO, written for the data analysis was made in-house at the Department of Civil Engineering, Aalborg University (http://www.hydrosoft.civil.aau.dk/epro/index.htm, 2005).

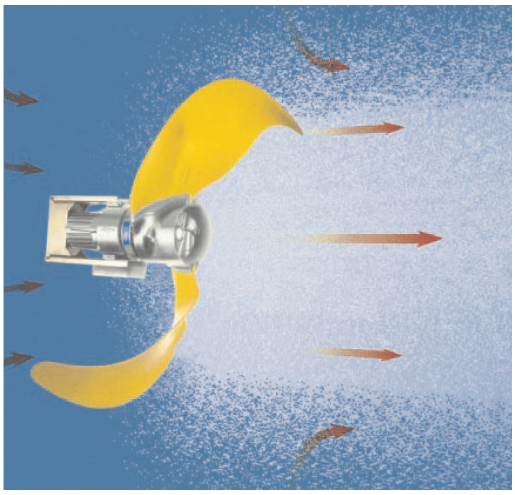

Figure 4.29 Flygt 4430 propeller. From: (http://www.flygtus.com/115917.asp, 2005).

Figure 4.30 Experimental set up for measuring the geometry of the propeller blade.

Both sides of the propeller blade were measured with the profiler, and the coordinate sets obtained from the measurements were loaded into a CAD Program. In the CAD program the

bottom and the top of the blade were "glued" together, constructing a complete propeller blade. The blade was copied and a complete propeller was constructed by "gluing" the two blades together with a hub. Also the physical shape of the motor behind the propeller was taking into account when building the appropriate geometry (Figure 4.31). To get an accurate propeller model as possible, the propeller was constructed by carefully looking at drawings in the product specifications.

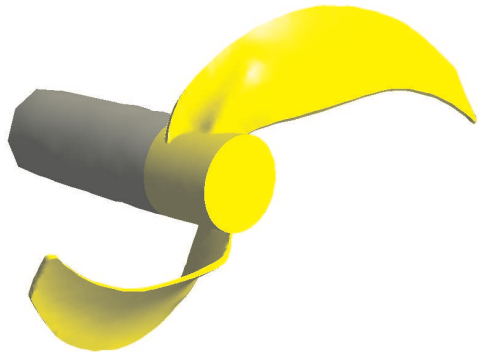

Figure 4.31 CAD model of the Flygt Propeller.

After construction of the CAD drawing, the geometry was loaded into the CFX Designmodeller interface in order to create the computational mesh.

4.2.4 Setup of numerical model

Two very different setups for the different models were tried out; a comprehensive sliding mesh model and a less computational demanding momentum source model. The two models will be more closely described below.

The reason for choosing two such different models is to be found in the purpose of the model. As described in chapter 1, one of the purposes of the model is to construct a process tank model that can accurately calculate the effect of mixing originated from different mixing equipment. For that reason the propeller is closely investigated by the use of a sliding mesh model, where the rotation of the propeller is resolved, whereby the direct impact of the propeller is modelled. Because numerical modelling of the movement of the propeller requires a resolution of several time steps per propeller revolution and the propeller in general demands a very dense grid in order to be adequately resolve the surfaces, the sliding mesh model is however computational expensive, and not very suited for longer transient runs of e.g. a duration in the order of process cycles in a WWTP process tank. For that reason a momentum source model is made for modelling the propeller. This momentum source model is calibrated to the modelling results of the sliding mesh model. The present momentum model can however not model the direct transient effects of the propeller as it rotates in the media. As will be shown later, the direct transient effects of the movement of the propeller becomes less significant when observing the flow at a distance downstream of the propeller.

Both models were constructed on a single phase scheme, with water as the fluid, and the application of the SST turbulence model. Since the sliding mesh method is computationally demanding, the single phase option is preferred over a multiphase model. Due to convergence problems experienced when using the sliding mesh model together with a non-Newtonian fluid for sludge in the process tank, the non-Newtonian fluid was abandoned for use with the sliding mesh model. Instead, water was applied as fluid. The use of a Newtonian fluid instead of a non-Newtonian one, do impose a uncertainty, since it is in general not known whether the propeller will interact with the sludge in same way as with the water. It is however believed that the same trends in imposed swirl, thrust and turbulence parameters will be applicable for sludge as for water.

Sliding mesh model

In the sliding mesh calculation, the flow problem is divided into two regions involving two domains. The inner rotating domain includes the region with the propeller, whereas the outer domain is a stationary frame including the bulk fluid and the tank. As indicated by the name of the method, the inner grid rotates with the impeller, whereas the outer grid remains stationary, hence the inner grid slides past the outer grid at a cylindrical interface. Values of flow variables are transferred across the interface through a general grid interface (GGI).

Because of the complexity of the propeller geometry, an unstructured mesh with tetrahedron elements has been applied to the inner domain (Figure 4.32).

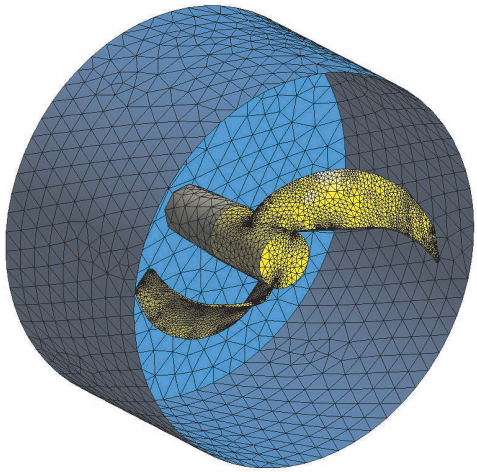

Figure 4.32 Computational mesh of inner rotating domain

The total number of tetrahedron elements is 312,000 in the inner domain, where the density is highest near the surface of the propeller. The impeller blades are made of fibreglass-reinforced polyurethane, and the blade surfaces are correspondingly modelled as hydraulic smooth surfaces.

The outer domain consists of a circular channel in which the propeller is installed (Figure 4.33).

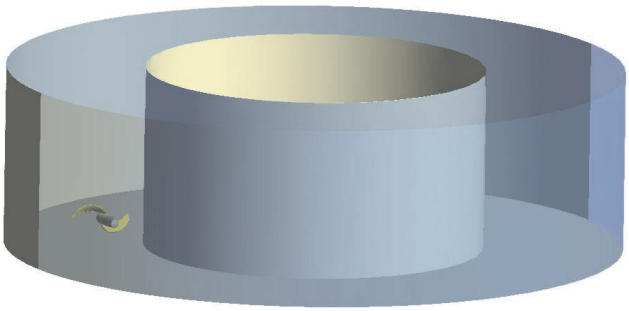

Figure 4.33 Computational mesh of inner rotating domain

The circular ring corresponds well to the typical flow situation appearing at many circular or ring shaped process tanks on wastewater treatment plants. Thus the ring channel shape is chosen in order to include the co-flow often appearing in ring-shaped process tank systems.

The outer domain consists of approximately 141,000 tetrahedron elements.

The sliding mesh model is a fully transient stator/rotor model where the rotating propellers interaction with the fluid is fully resolved. The transient simulation was used to investigate the build up of flow in the channel from a typical start up in quiescent conditions to a fully developed flow. During the transient computations the size of the time step was chosen to be 0.1 second, resulting in a resolution of approximately 17 time steps per propeller revolution.

4.2.5 Modelling results

Below, the results of the modelling with the sliding mesh model are presented. The transient model is run to a steady-state, where no further build up of channel flow is occurring. Plots of characteristic flow parameters of the impeller and the remainder of the tank have been constructed at the steady-state condition. Furthermore, based on the steady-state solution, characteristic propeller numbers are calculated at the end of the subsection. During the run, transient results files are stored to a file as the computation progresses. Consequently, the flow development in the ring channel has been plotted.

Steady-state results

After running the transient sliding mesh propeller model to steady-state, the model is stopped and the velocity distribution immediately downstream of the propeller is plotted in a plane perpendicular to the axial direction (Figure 4.34). The shown plane is intersecting the downstream part of the propeller blades and hub.

Close to the propeller the axial velocity distribution is clearly dependent on the location of the propeller blades, and it is apparent that the highest velocities are located in the close vicinity of the blades.

A more detailed view of the flow in the vicinity of the propeller can be viewed by plotting the velocity vectors in this region (Figure 4.35). The vector plot clearly shows both how the propeller

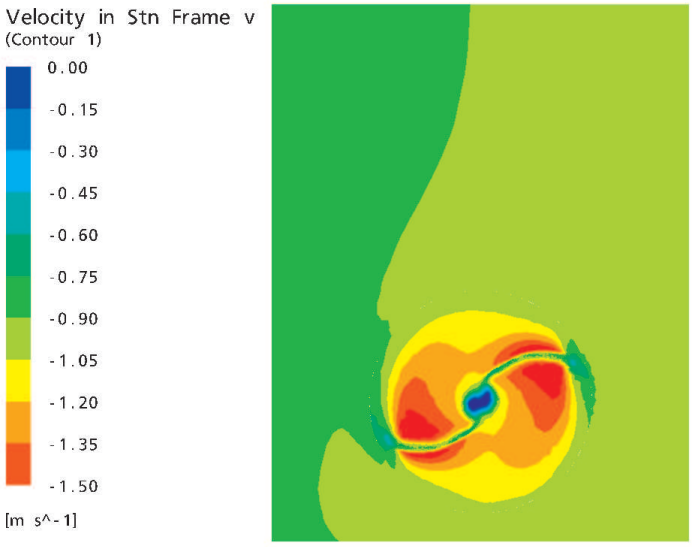

Figure 4.34 Slice plane intersection the downstream part of the propeller blades and hub. The plane is perpendicular to the axial direction and showing the axial velocity distribution.

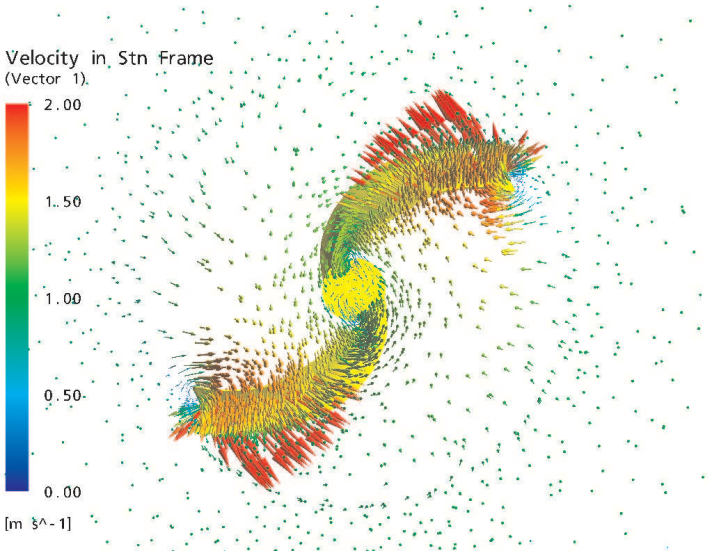

Figure 4.35 Slice plane showing the velocity vectors in a plane intersecting the downstream side of the propeller geometry. Due to the viewing purposes of the figure, the number of vectors is reduced with a factor five compared to the actual number of mesh points in the impeller region.

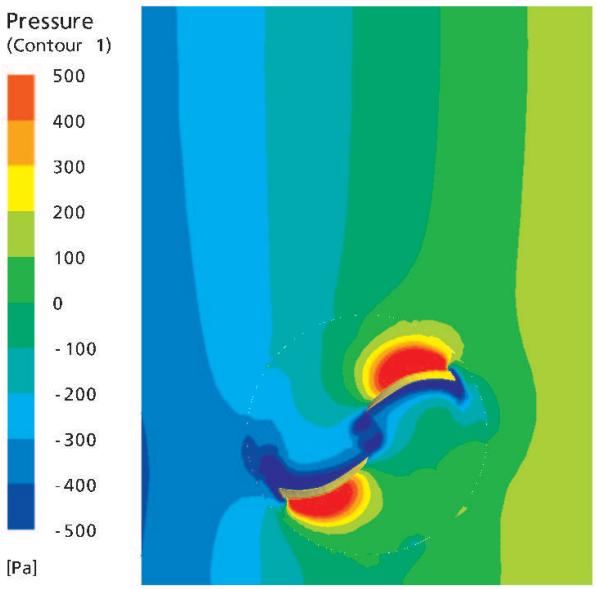

Figure 4.36 Pressure distribution in a slice plane intersecting the downstream side of the propeller.

pushes the liquid in front of the blades, but also how liquid is entrained from the surroundings by the wake of the blades (Figure 4.35).

The vector plot clearly shows both how the propeller pushes the liquid in front of the blades, but also how liquid is entrained from the surroundings by the wake of the blades (Figure 4.35).

Also when plotting the pressure distribution, the blade dependency of the flow is obvious (Figure 4.36). As expected, zones with high pressure are located on the front side of the propeller blades, whereas zones of low pressure are situated in the wake of the blades.

Further downstream of the propeller, the flow is less dependent of the exact radial position of the propeller blades. Figure 4.37 - 4.39 illustrates the flow $1m$, $2m$ and $5m$ down stream of the propeller.

1m downstream of the impeller, the flow is still highly dependent on the position of the propeller blades. 1m downstream of the propeller, the flow structure is still highly dependent on the position of the propeller blades (Figure 4.37). Further downstream, 2m away from the propeller, the blade dependency is more blurred out (Figure 4.38). Higher velocities is however still vaguely observed in areas corresponding to the location of the impeller blades. The velocity distribution is at this position starting to deform from the ideal circular jet shape.

5m downstream from the propeller, the blade dependency is completely gone, and the jet has moved out close to the outer wall due to centrifugal forces (4.39).

A more complete picture of the propeller jet can be illustrated by plotting a horizontal velocity plane in the same height as the centre of the propeller hub (1.5m above the bottom) (Figure 4.40). Again the influence of the propeller geometry on the near field flow is obvious. In the area just downstream of the propeller blades, the velocities are peaking, whereas the velocities

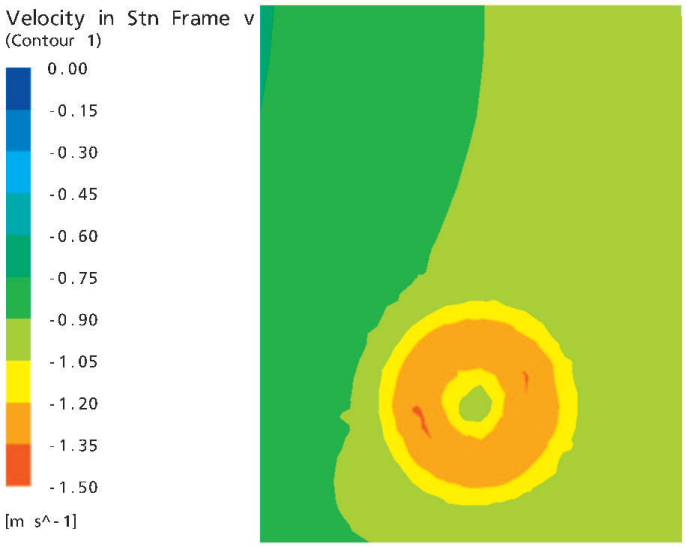

Figure 4.37 Slice plane showing velocity distribution 1m downstream of the propeller. The plane is parallel to the propeller, and the shown velocities are axial velocities

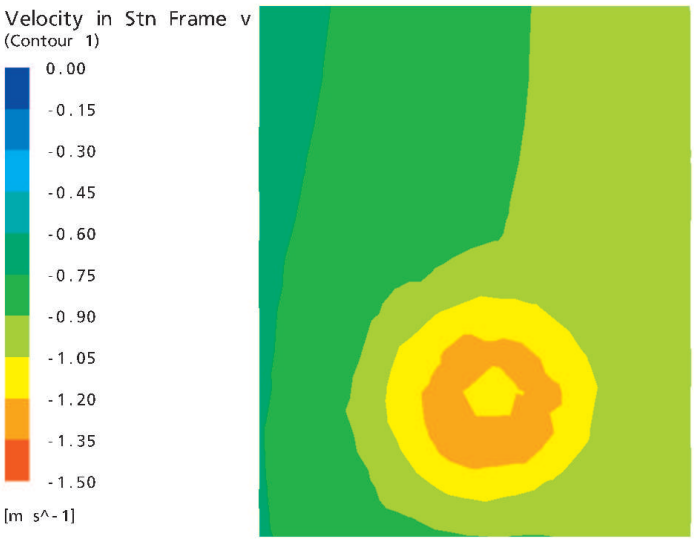

Figure 4.38 Slice plane showing velocity distribution 2m downstream of the propeller. The plane is parallel to the propeller, and the show velocities are axial velocities

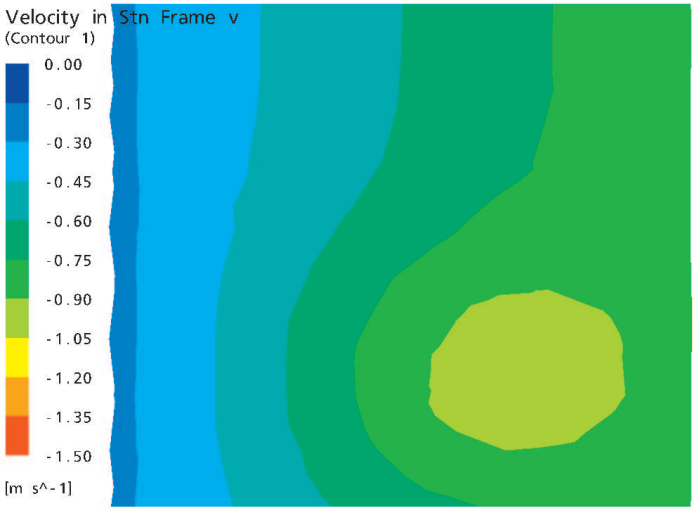

Figure 4.39 Slice plane showing velocity distribution 5m downstream of the propeller. The plane is parallel to the propeller, and the show velocities are axial velocities

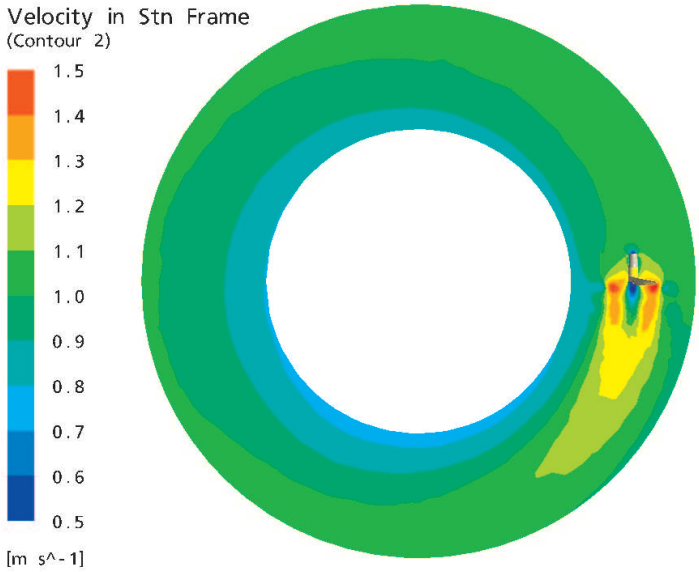

Figure 4.40 Contour plot showing the velocity in a plane 1.5 m above the tank bottom.

are lowest behind the hub 4.40). As indicated by the higher velocities at the outer wall the jet is pushed outwards by the centrifugal forces.

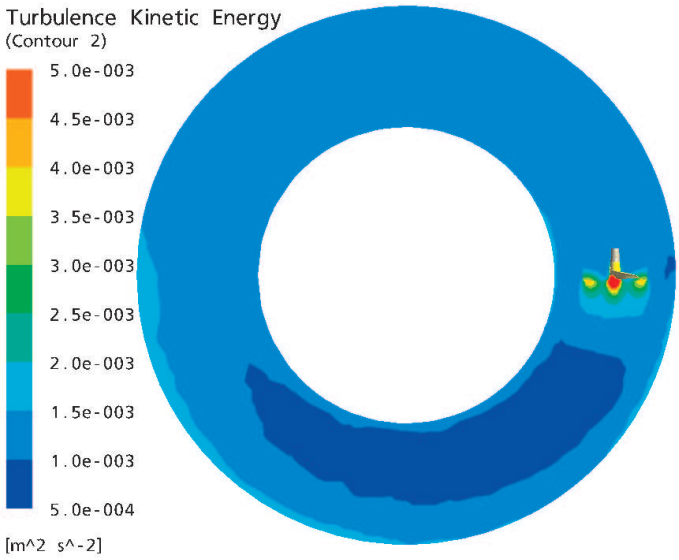

Figure 4.41 Contour plot showing the turbulent kinetic energy, k, in a plane 1.5 m above the tank bottom.

Staying in the same plane as for figure 4.40, the distribution of turbulent kinetic energy, k, is shown in a contour plot (Figure 4.41). As expected, the turbulent kinetic energy has peak values in the immediate vicinity of the impeller (Figure 4.41). The turbulent kinetic energy quickly dissipates a few propeller diameters downstream of the propeller. In the bulk of the ring channel, k is fairly constant at a value of approximately $1 \cdot 10^{-3}[m^2 \cdot s^{-2}]$.

Corresponding to the high values of k at the propeller, the turbulence eddy frequency, ω, is also high in this area (Figure 4.42). In the remainder of the ring channel the value of ω is lower than $1[s^{-1}]$.

Plotting the eddy viscosity shows a rather unexpected trend with an area of low eddy viscosity immediately behind the propeller (Figure 4.43). The present computations were performed with a rather strict convergence criteria where the mean residual values should fall beneath $1 \cdot 10E - 5$ before the solver would stop or jump to the next time step. Even though this rather strict convergence criteria was applied, both the stationary and transient models showed the same trends with respect to modelled eddy viscosity downstream of the impeller.

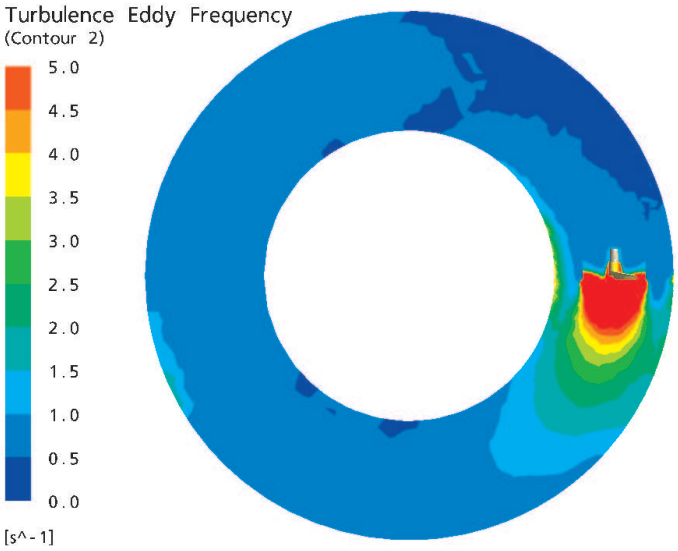

Figure 4.42 Contour plot showing the turbulence eddy frequency, ω, in a plane 1.5 m above the tank bottom.

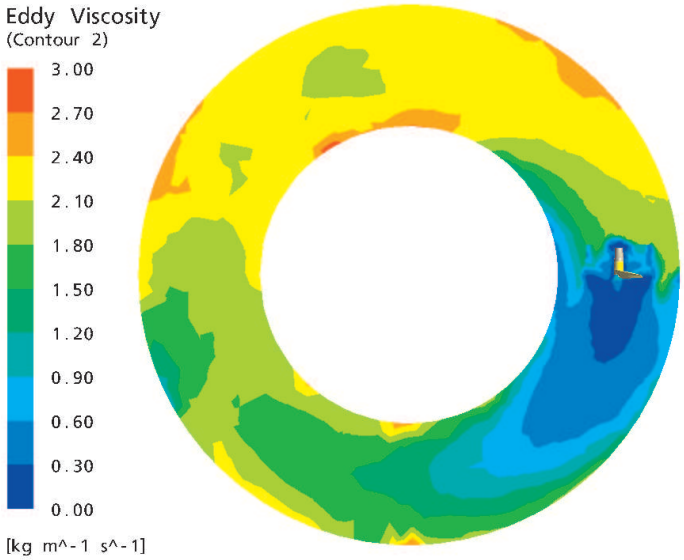

Figure 4.43 Contour plot showing the eddy viscosity, ν_t, in a plane 1.5 m above the tank bottom.

Transient results

The transient development of the flow from propeller start up to steady-state flow in the tank is illustrated by streamline plots. The streamlines are initiated at the propeller blades, and the time limit is set to maximum of 60 seconds. Hence, the streamlines are calculated on the actual flow field at a given time step, and the length of the streamlines corresponds to the distance an imaginary infinitesimally small fluid particle will travel in 60 seconds, when it is released at the propeller blades in the given flow field. The colours of the streamlines correspond to the velocity scale situated along the sides of the figures.

Since the flow field is only partly developed in the start of the simulation, the streamlines are not reaching very far in the channel (Figure 4.44). At this particular instant in the flow field, the streamline pattern is chaotic and a lot of vortices are present.

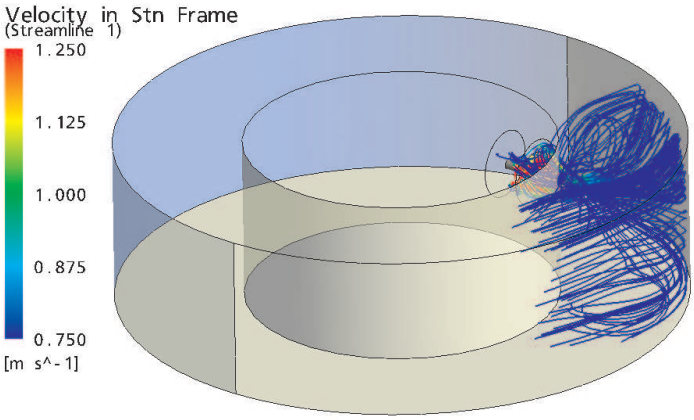

Figure 4.44 Streamline plot showing the flow 1 min. after start up of the impeller. The streamlines are initiated at the propeller blade, and the length of the lines corresponds to 60 seconds of flow.

After 8 minutes, approximately half way through the simulation, the flow field is more developed and the structure of the streamline pattern is much more organized (Figure 4.45). The flow field is however still developing with time, and plotting the streamlines at the end of the simulation (after 15 seconds of simulation) shows slightly higher velocities and correspondingly longer streamlines (Figure 4.46).

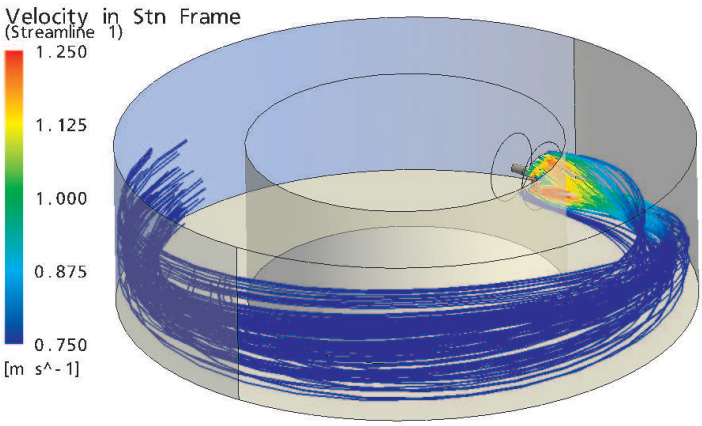

Figure 4.45 Streamline plot showing the flow 8 min. after start up of the impeller. The streamlines are initiated at the propeller blade, and the length of the lines corresponds to 60 seconds of flow.

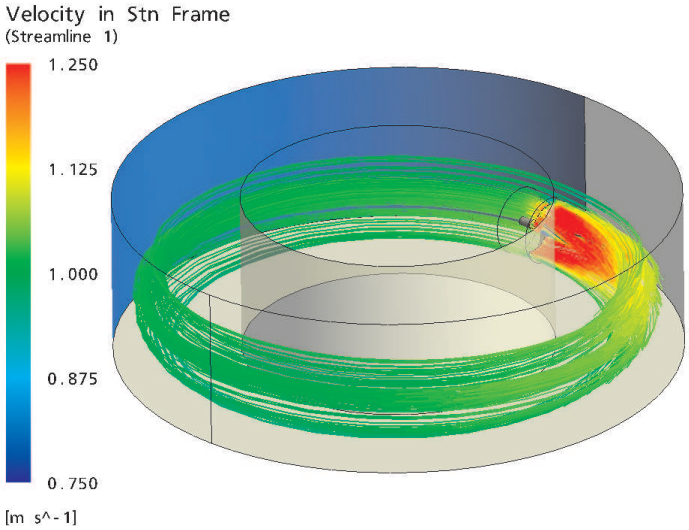

Figure 4.46 Streamline plot showing the flow 15 min. after start up of the impeller. The streamlines are initiated at the propeller blade, and the length of the lines corresponds to 60 seconds of flow.

Calculation of characteristic propeller and jet numbers

By the application of equation 4.46, the power consumption has been calculated to $2.49kW$, not far from the specified effect of $3.1kW$ of the electrical motor driving the propeller. The calculated value of the power consumption corresponds with an efficiency of 80% for the total system of electric motor and gear. Due to these considerations, it is believed that the value of P, calculated by equation 4.46 is likely to be correct, and thus the power number, N_p, is calculated on behalf of this value. By using equation 4.47, N_p has been estimated to 0.31, corresponding well to the power number of a hydrofoil impeller investigated by (Poirier, 2004). From equation 4.48, the pumping capacity of the propeller, Q, has been calculated to $5.1m^3 \cdot s^{-1}$. This number is calculated only from the flow going through the propeller swept area in the axial direction. Due to the complexity of the flow, it has not been possible to readily quantify the contribution from the radial flow. From visual observation of the numerical results it has however been estimated that the radial contribution is insignificant compared to the contribution from axial flow. On behalf of the flow capacity and the application of equation 4.49, the flow number, Fl, has been estimated to the value of 0.82. The propeller $Reynolds'$ number has been estimated to 28200 (equation 4.50). The swirl number of the jet is calculated to a value of 0.24 $[-]$ for both the transient and the steady-state case, corresponding to weakly swirling flow (Gupta, 1984).

The calculated characteristic propeller and jet numbers are summarized in table 4.3:

Table 4.3 Calculated characteristic propeller and jet numbers for the Flygt 4430 propeller.

$Parameter$	$Value$
Propeller Reynolds' number, Re_p $[-]$	28,200
Power consumption, P $[kW]$	2.49
Power number, N_P $[-]$	0.31
Pumping capacity, Q $[m^3 \cdot s^{-1}]$	5.1
Flow number, Fl $[-]$	0.82
Swirl number, S $[-]$	0.24

The above mentioned properties of the flow field are in the following attempted reproduced through a momentum source model in the area of the impellers.

Momentum source model

A momentum model has been constructed with the purpose of describing the effect of the propeller adequately through a computationally cheaper model than the sliding mesh model. The aim of the model is to describe the steady-state velocity components and the turbulence generated by the propeller shown in figure 2.6 adequately. A subdomain of the same size as the inner rotating domain in the sliding mesh method is constructed. In order to model the trough shaped velocity profile downstream of the propeller, a smaller cylinder of approximately the same size of the electrical motor and the propeller hub is cut out of the subdomain. Because the geometry of the propeller is not resolved in the momentum source model, the demand on the mesh density is much lesser than for the sliding mesh model, resulting in a coarser mesh.

Initial modelling quickly revealed that the velocity components of the propeller could be adequately described by adding momentum sources in two of the three possible dimensions; the axial and the tangential dimension:

$$M_{axial} = step(1.1 - r/1[m]]) \cdot step(r/1[m] - 0.5) \cdot (-275\ [kg \cdot m^{-2} \cdot s^{-2}]) \tag{4.55}$$

$$M_{\theta} = step(1.05 - r/1[m]]) \cdot step(r/1[m] - 0.25) \cdot (-300\ [kg \cdot m^{-2} \cdot s^{-2}]) \tag{4.56}$$

where M_{axial} and M_{θ} are the axial and tangential source components, respectively $[kg \cdot m^{-2} \cdot s^{-2}]$ and r is the radial coordinate with origin in the centre axis directed in the axial direction of the propeller $[m]$. The step-functions applied, are functions returning a value of 1.0 when the expression inside the step-function is positive, and returning a value of 0.0 for negative values. When the expression inside the step-function is zero, a value of 0.5 is returned. The step functions are mainly applied in order to model the trough shape immediately behind the propeller.

Parallel to the models for the momentum source, turbulence sources for k and ω in the SST-model have been developed:

$$S_k = step(1.1 - r/1[m]]) \cdot step(r/1[m] - 0.5) \cdot (2.5\ [W \cdot m^{-3}]) \tag{4.57}$$

$$S_{\omega} = step(1.1 - r/1[m]]) \cdot step(r/1[m] - 0.5) \cdot (16000\ [W \cdot m^{-3} \cdot s^{-1}]) \tag{4.58}$$

here, S_k and S_{ω} are the sources of k and ω, respectively $[W \cdot m^{-3}]$, $[W \cdot m^{-3} \cdot s^{-1}]$.

The high value of the ω source has been applied in order to model the eddy viscosity drop in the zone downstream of the propeller.

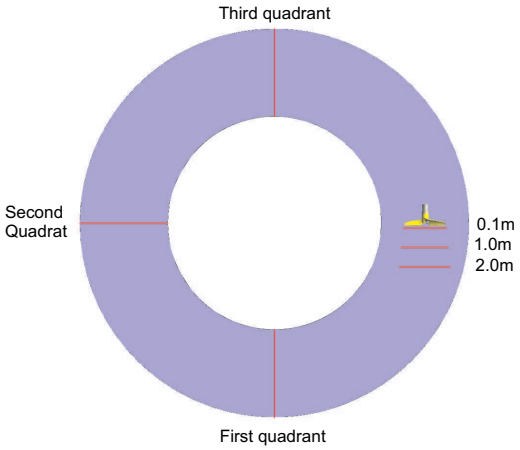

Figure 4.47 Outline of the six transversal profiles applied for the calibration of the momentum source model.

During the model calibration, the results of the momentum source model has been compared to the results of the sliding mesh model at six transversal profiles in the tank. An outline of the

positions of the six compared profiles is shown in figure 4.47. The red lines on figure 4.47 indicate the position of the profiles used for comparison between the propeller- and momentum model. The comparisons include three profiles 0.1m, 1m and 2m behind the propeller and three profiles one, two and three quadrants after the propeller.

The momentum source model has been calibrated against the fully developed flow obtained from long time running of the transient model until a stationary flow was obtained. The comparison between the impeller and the momentum model can be viewed in the plots of figure 4.48 - 4.50.

The axial velocity distributions of the two types of modelling of the propeller show both quantitatively and qualitatively correspondence for all modelled profiles (Figure 4.48). The trough effect behind the propeller is modelled fairly well, even though the velocity profiles of the momentum model are a little smoother than the profiles originating from the more rigorous propeller model. This discrepancy is most likely to be a consequence of a too simple expression of the source model.

For the profiles close to the propeller, very good agreement is obtained between the two models with regards to the modelled vertical velocity components, w, (Figure 4.49). The remainder of the profiles do however show less accuracy. Similar behaviour is for these profiles obtained between the two models, but the profiles one and three quadrants downstream of the impeller show too little vertical velocities, whereas the profile two quadrants after the impeller overestimate the w component. The reason why these profiles show relatively bad correlation between the models is likely to be found in the simplicity of the momentum model that probably can not completely resolve the swirling effect caused by the propeller.

The general level of the eddy viscosity is well correlated between the two models (Figure 4.50). Qualitatively, the momentum model does however not reproduce the eddy viscosity very well in the vicinity of the propeller. Again this is likely to be sought in the simplified momentum source model, which is not capable of reproducing the complexity of the flow in the vicinity of the propeller. Consequently, it has not been possible to accurately resolve the eddy viscosity in the complex flow field immediately behind the propeller. In the bulk of the tank, the eddy viscosity is however well correlated between the two models.

The pumping capacity, Q, has been estimated to $5.25 m^{3 \cdot s^{-1}}$ for the momentum source based *propeller*, almost perfectly matching Q in the sliding mesh model (Table 4.3).

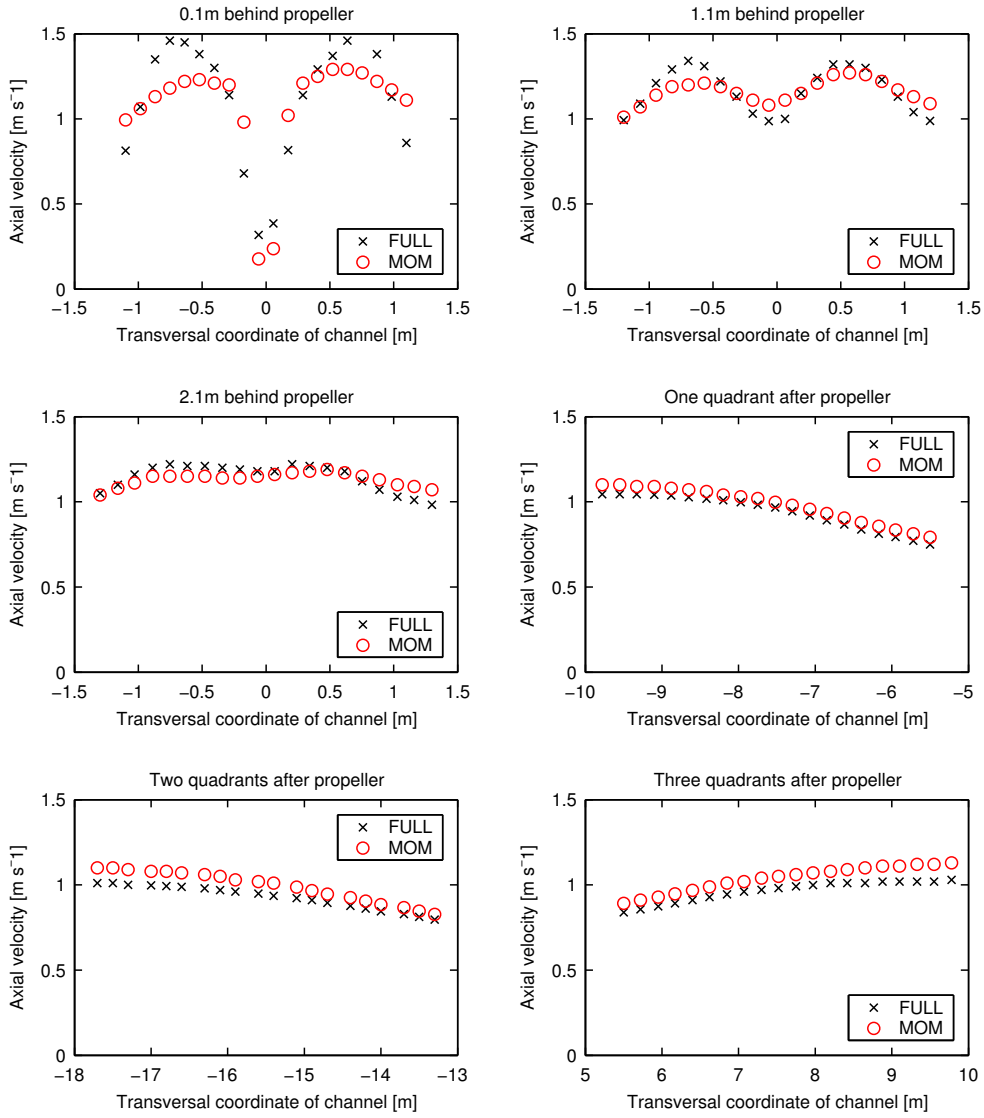

Figure 4.48 Comparisons of modelled axial velocities for the steady-state propeller model (legend: FULL) and the simplified momentum model (legend: MOM).

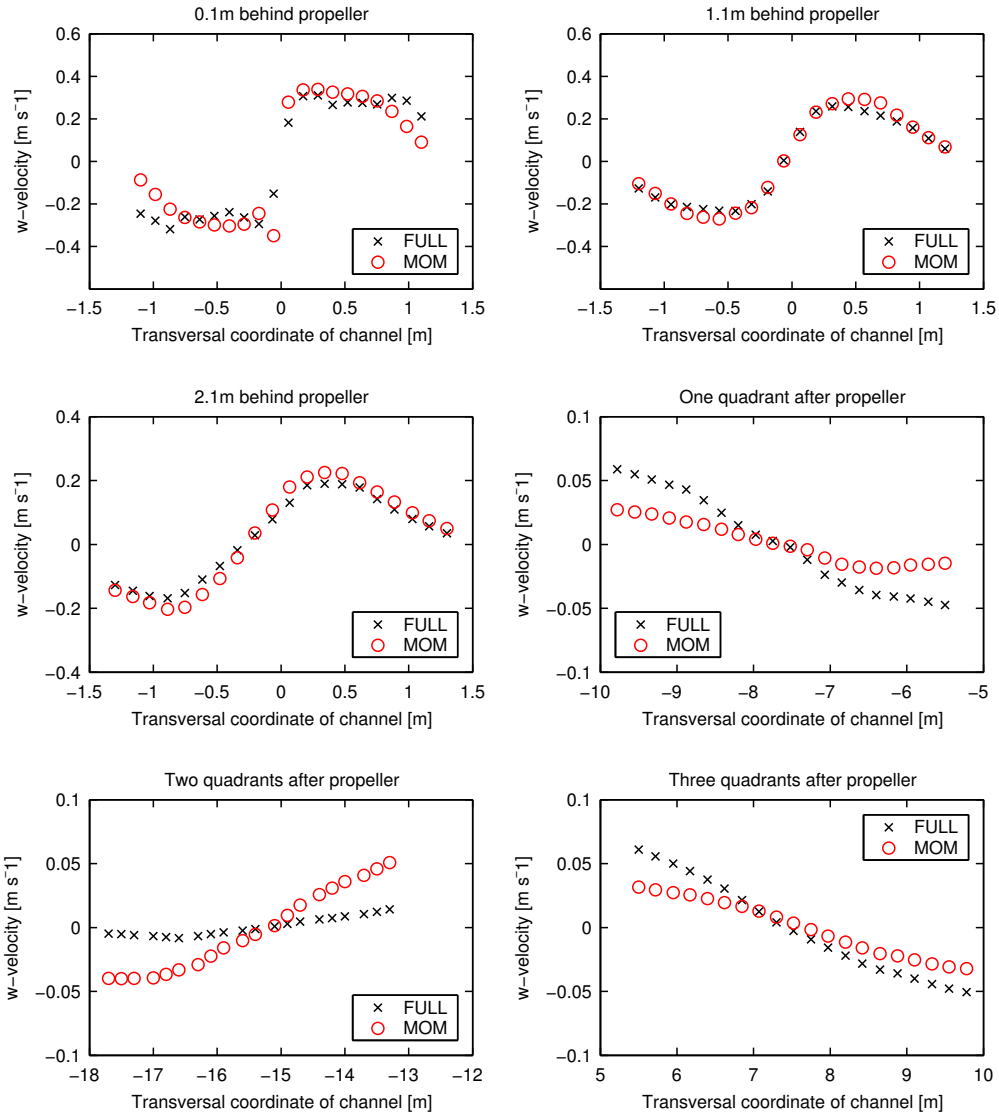

Figure 4.49 Comparisons of modelled vertical velocities, w, for the steady-state propeller model (legend: FULL) and the simplified momentum model (legend: MOM).

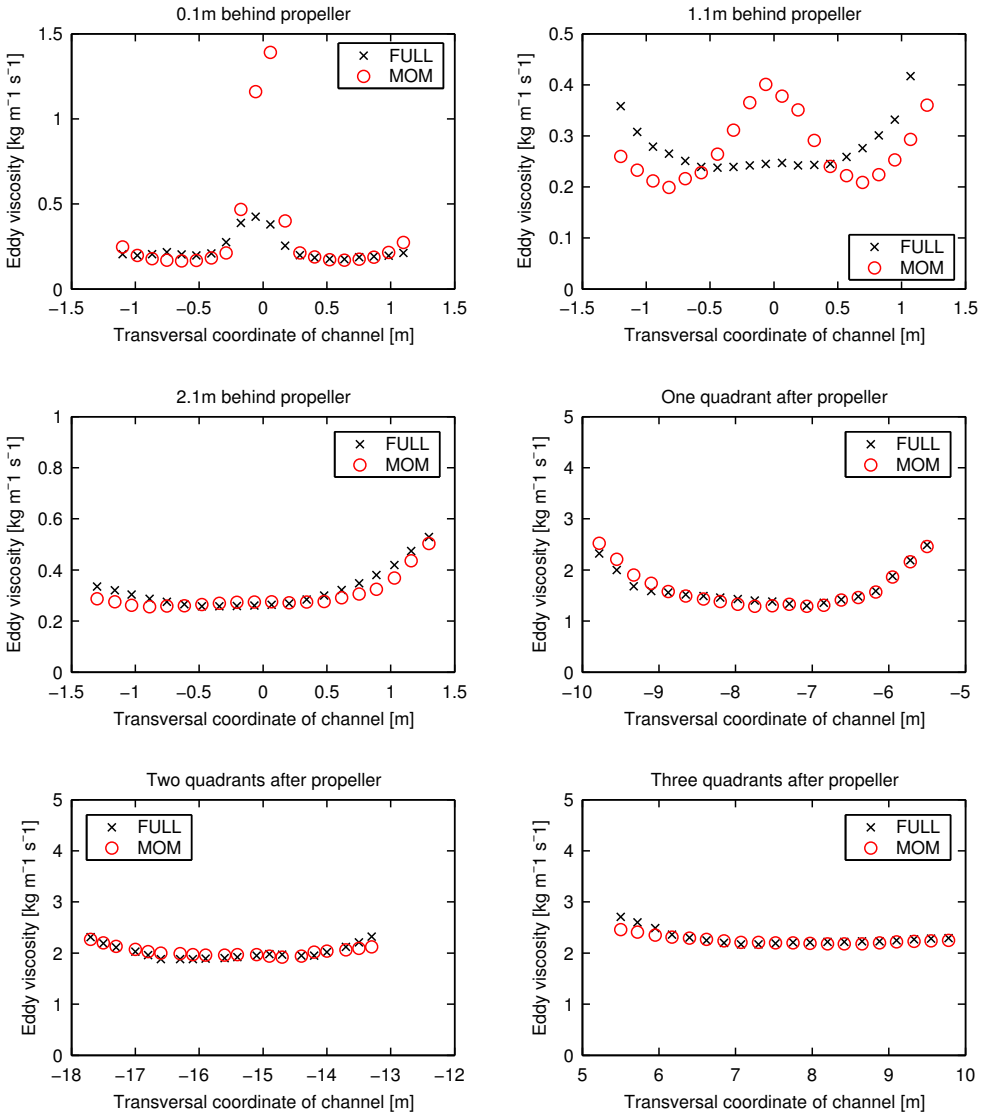

Figure 4.50 Comparisons of modelled eddy viscosities for the steady-state propeller model (legend: FULL) and the simplified momentum model (legend: MOM).

4.2.6 Summary

A Flygt 4430 hydrofoil shaped full-scale propeller operated at $35RPM$ has been investigated numerically. A comprehensive transient sliding mesh scheme, resolving the rotation of the propeller scheme, has been applied. The results of the sliding mesh computation show that the axial flow close to the propeller is highly dependent on the position of the propeller blades. A few propeller diameters downstream of the propeller, the jet show less dependency of the actual position of the propeller blades. This justifies the use of a more computationally cheap momentum source model instead of the rigorous sliding mesh model. Since the momentum model do not resolve the movement of the propeller geometry, even a transient momentum model will act as a steady-state model compared to the sliding mesh model. Since the blade dependency is only apparent close to the propeller, it is however believed that the momentum model can reproduce the effect of the rotating propeller in the remainder of the tank. This is supported by the fact that good correlation between axial flow velocities and eddy viscosities has been obtained for all profiles except very close to the propeller.

4.3 Modelling of the activated sludge processes

As presented in chapter 1, three versions of the IAWQ activated sludge models are applicable for modelling of municipal activated sludge tanks. ASM1 and ASM3 are applicable for systems where biological nitrogen removal is present, whereas the more complex ASM2 also includes biological removal of phosphorous. In order to keep the complexity of the numerical model on a reasonable level, the integrated model will only deal with removal of organic matter and nitrogen, whereas removal of Phosphorous is neglected.

For the modelling of biological removal of organic matter and nitrogen, the ASM1 or ASM3 are the most appropriate models. Compared with ASM1, ASM3 has several differences:

- ASM3 is intended to become the new standard model, correcting for the defects of ASM1 (Gujer *et al.*, 1999)
- In ASM3 readily biodegradable substances are taken up and stored into an internal cell component prior to cell growth
- ASM3 should be easier to calibrate than ASM1 due to the conversion of the circular growth-decay-growth model into a growth endogenous respiration model (Gernaey *et al.*, 2004)
- Cell growth limitations are not considered in ASM1, whereas nitrogen and alkalinity limitations are considered in ASM3

The uptake and storage of readily biodegradable substances into one internal cell component, X_{STO}, can not be observed in reality, but since no reliable model is available for describing the more detailed substrate fluxes of storage, assimilation and dissimilation, this option seems appropriate for the time being (Gujer *et al.*, 1999). Compared to ASM1, the addition of internal storage should make the ASM3 more suited towards adjustments of decay processes in environmental conditions (Gujer *et al.*, 1999).

The difference in model structure between the ASM1 and ASM3 is further visualized in figure 4.51.

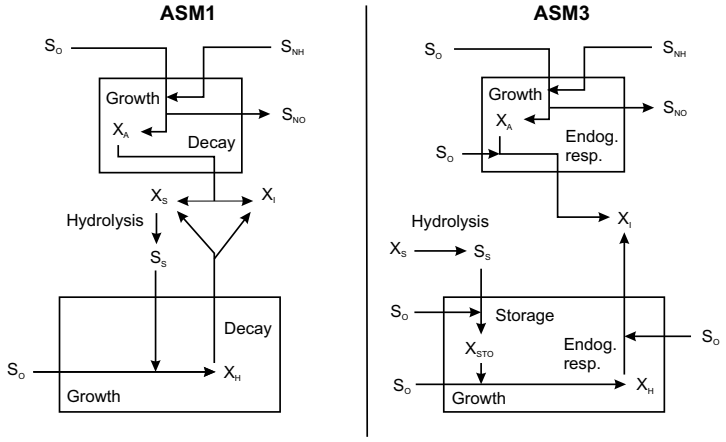

Figure 4.51 Principle layout of the model structure of ASM1 and ASM3 (Gernaey *et al.*, 2004).

From figure 4.51 the two big differences with the cancellation of the circular growth-decay-growth model and the switching from the traditional lysis model to the endogenous respiration model become obvious. As a consequence, a separation between the conservation processes of autotrophic and heterotrophic biomass occurs, which is opposite to the ASM1 where the two types of biomass are strongly interrelated through the decay regeneration cycles.

Due to the introduction of the internal storage of readily biodegradable substances, ASM3 is better than ASM1 for describing systems where storage of such components are significant (Koch *et al.*, 2000). (Koch *et al.*, 2000) also states that both ASM1 and ASM3 performs well for municipal WWTP's, and that ASM3 performs better for systems with substantiated non-aerated zones. In the article of (Koch *et al.*, 2000), a new set of stoichiometric and kinetic parameters was proposed on behalf of the application of the ASM3 on batch experiments and the modelling of several Swiss municipal wastewater treatment plants. Later (Wichern *et al.*, 2001) applied the calibrated version of (Koch *et al.*, 2000) for the modelling of three German WWTP.

(Rieger *et al.*, 2001) extended the ASM3 with the EAWAG-Bio-P module and modelled both batch experiments, pilot-scale and full-scale experiments from Swiss municipal wastewater treatment plants. Again, the values from the calibrated ASM3 version of (Koch *et al.*, 2000) was applied. The model predicted the removal of both Nitrogen and Phosphorous well for both the batch- and full-scale experiments.

(Mussati *et al.*, 2002) performed simulations of biological removal of Nitrogen on the COST benchmark simulation plant (Copp, 2002) with both the ASM1 and ASM3 model. The authors stated that ASM3 results were easier to interpret than ASM1 results due to a more transparent model structure with the simpler decay model principle. For the ASM3 model, model parameters at 15 $^{\circ}C$ were interpolated from the default sets at 10 and 20 $^{\circ}C$ in (Gujer *et al.*, 1999). Due to the different model structure in the two models, the steady-state effluent concentrations predicted by the two models showed distinctive differences. When subject to imposed disturbances on an otherwise steady-state system, the ASM3 required longer time to reach the new steady-state compared to ASM1. (Koch *et al.*, 2000) also stated that the ASM3 performed better for systems where storage of readily biodegradable substrates is dominating, systems with high

diurnal variations of COD or systems with substantial non-aerated zones.

4.3.1 Implementation of the ASM3 model

As indicated in chapter 2, the ASM3 consists of a rather complex system of equations, that needs to be solved in order to model the variation of substances in the activated sludge. The ASM3 model has been implemented in the CFD-model by associating the different ASM-components to either the water or the sludge phase:

- Soluble components and the particulate fraction of slowly degradable organic matter have been associated to the continuous water phase
- Biomass fractions and suspended solids have been associated to the sludge fraction
- The transport of the different components of the ASM3 have been modelled via the transport dispersion equation (Equation 3.11)
- The ASM3 processes have been implemented through the source term on the right-hand side of equation 3.11

In order to account for the fact that only a fraction of a cell might be filled with e.g. sludge and hence biomass, the process rates have been multiplied with the volume fraction of the phase to which the component has been associated.

4.3.2 Validation of model implementation

In order to validate the implementation of the ASM3 model into the CFD-model, a three-phase Multifluid model has been integrated with the ASM3 model in a 4mx4mx4m squared cube and evaluated against a spreadsheet model of the ASM3. The models have been tested for 5 minutes in real time, initialized with the identical initial conditions taken from a set of online measurements at Frederikshavn WWTP. The results of the validation is shown for the four soluble components: Oxygen (S_{O_2}), readily biodegradable organic matter (S_S), ammonium and ammonia (S_{NH}) and nitrate and nitrite (S_{NO}) (Figure 4.52). For the particulate fractions, the variation of the concentration of the heterotrophic biomass (X_H) is shown (Figure 4.53).

As indicated on figure 4.52 and 4.53, the implementation of the ASM3 model has been successful, with identical concentration variations for the integrated ASM3 model and the reference model.

Later, in a case study, the calibration procedure of the model is described, and an example of the application possibilities of the CFD-integrated ASM3 model is shown.

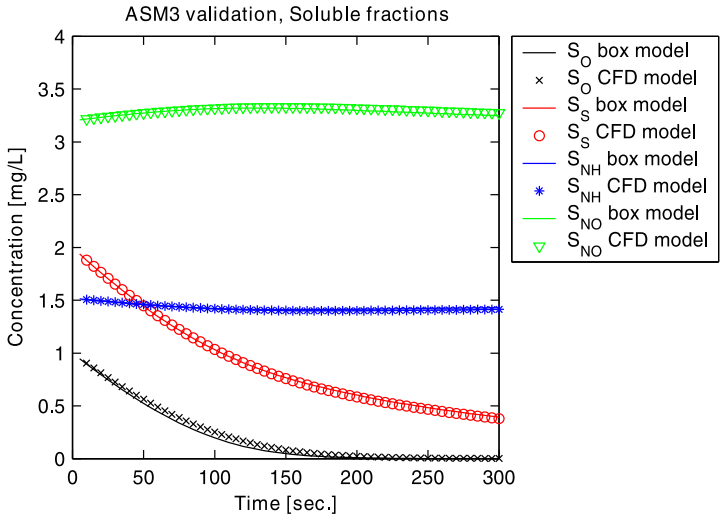

Figure 4.52 Comparison of the ASM3 model integrated into a three-phase multifluid model and a reference spreadsheet model.

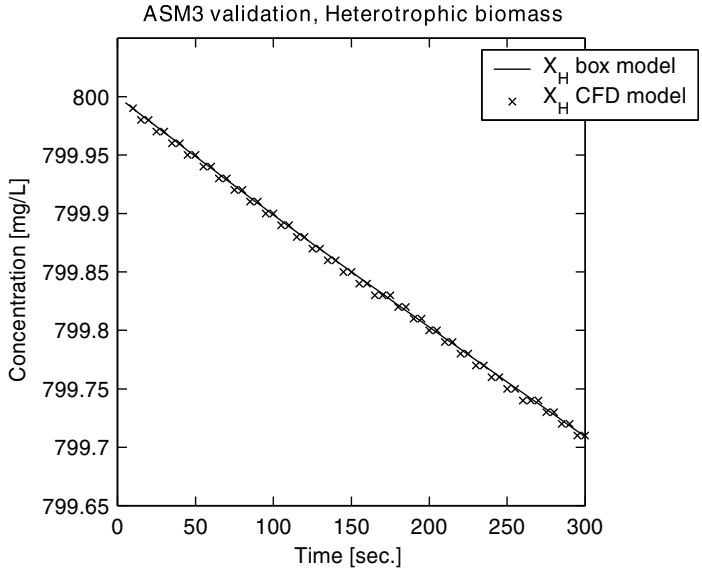

Figure 4.53 Comparison of the ASM3 model integrated into a three-phase multifluid model and a reference spreadsheet model.

4.4 Implementation of the sludge transport model

The present section describes the implementation of the sludge transport model. Special attention is headed towards the implementation of a sedimentation model and a non-Newton viscosity model for the activated sludge.

4.4.1 Settling velocity

As described in chapter 2 the settling of sludge particles is dependent both the local sludge concentration and the level of turbulence. Consequently, the model of (Rasmussen and Larsen, 1996) has been implemented into the hydrodynamic multifluid model:

$$W_s = W_0 \cdot e^{\beta \cdot X_{SS} + \gamma \cdot G} + \lambda \tag{4.59}$$

where β and γ are empirical constants with the units $[m^3 \cdot kg^{-1}]$ and $[s]$, respectively. λ is the minimal compression settling velocity $[m \cdot s^{-1}]$ and G is the velocity gradient as introduced by $[s^{-1}]$ (Camp and Stein, 1943).

Basically, the constants β and γ in equation 4.59 expresses sludge velocity dependency upon increased sludge concentration and turbulence, respectively. All the constants in equation 4.59 can be determined experimentally through the method developed by (Rasmussen and Larsen, 1996).

By combining equation 4.59 and 2.15, C_D was isolated and the expression for C_D was directly incorporated into the model. By making initial modelling on a cube geometry, it was verified that the CFD-model exactly resulted in the expected results, as performed by hand calculations.

Parameter estimation

The parameters in equation 4.59 has been estimated from previous experiments on Danish wastewater treatment plants (Rasmussen and Larsen, 1996), (Rasmussen, 1997), (Jensen, 2004). The experiments were performed in a settling column designed by (Rasmussen, 1997) (Figure 4.54 and 4.55).

The settling column is constructed in a way that allows a one dimensional steady-state settling of the sludge in the middle part of the column.

The inlet of sludge is located at the top of the column. The inlet is arranged with a diffuser that creates a local area of high turbulence that disintegrates the sludge particles (Figure 4.56). Due to the continuous pumping of sludge through the inlet, a small convective transport is apparent together with the transport due to sedimentation. As the sludge moves down through the column it flocculates into larger faster settling sludge flocs. Towards the middle of the column equilibrium between flocculation and deflocculation is present, which is equal to equilibrium between growth and decay of the particle sizes. Consequently, a uniform concentration of sludge is obtained. At the bottom of the column, the compressed sludge is taken out and recirculated to the top of the column.

The experiment can be compared to the flow in a settling tank, where the sludge is subject to a high level of turbulence at the inlet, after which it enters the more quiescent parts of the settling tank. In the transition between the high- and low turbulence areas flocculation is occurring. The

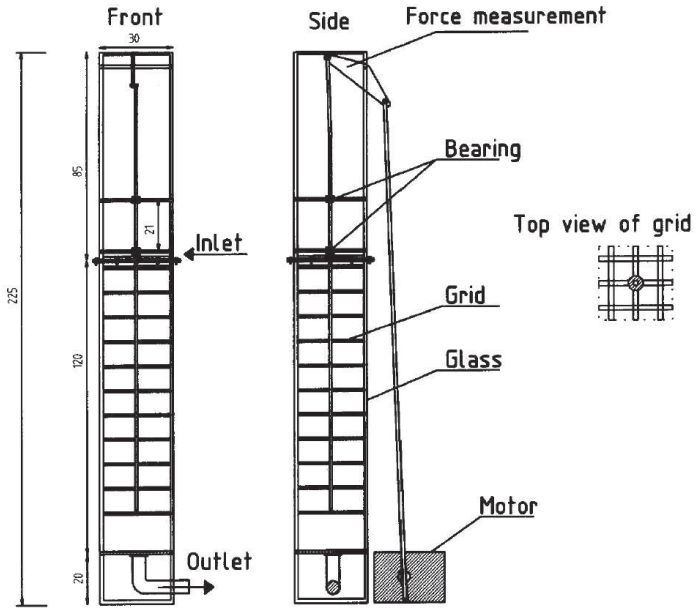

Figure 4.54 Outline of the settling column (All measures are in cm) (Rasmussen and Larsen, 1996).

turbulence level in the column can be varied on behalf of the speed of the oscillating sinusoidal movement of the grid.

Due to the steady-state and uniform conditions in the column, a mass conservation can be constructed on behalf on the assumed constant flux through cross-section of the inlet and the cross-section of measuring in the column (Rasmussen and Larsen, 1996):

$$W_0 C_i = (W_0 + W_s) \cdot C_{eq} \longleftrightarrow W_s = \frac{W_0 \cdot (C_i - C_{eq})}{C_{eq}} \tag{4.60}$$

where W_0 is the mean velocity due to pumping $[m \cdot s^{-1}]$, W_s is the settling velocity $[m \cdot s^{-1}]$, C_i is the sludge inlet concentration $[kgSS \cdot m^{-3}]$ and C_{eq} is the equilibrium sludge concentration at the measurement position in the column $[kgSS \cdot m^{-3}]$.

By the application of an OSLIM light sensor and a shifting valve, the sludge concentration can be measured at both the inlet and at different positions in column. On behalf of these measurements and by the application of equation 4.60 the settling velocity can be estimated.

In equation 4.59 the turbulent shear G is included as a measure of the turbulence level in the sludge. G is dependent on the dissipation of turbulent energy and the kinetic viscosity of the liquid:

$$G = \sqrt{\frac{\epsilon}{\nu}} \tag{4.61}$$

Figure 4.55 Pictures of the settling column as installed on Aalborg East WWTP in 2004.

where G is the turbulent shear $[s^{-1}]$, ϵ is the dissipation of kinetic turbulence energy $[m^2 \cdot s^{-3}]$ and ν is the kinetic viscosity of the suspension, water $[m^2 \cdot s^{-1}]$.

During the experiment ν is kept constant. At steady-state conditions, ϵ is equal to the work done by the oscillating grid per unit time. Over one cycle with period T, ϵ can accordingly be calculated as (Rasmussen and Larsen, 1996):

$$\epsilon = \frac{1}{T}\int_0^T \frac{W}{V\rho}dt = \frac{1}{V\rho}\frac{1}{T}\int_0^T F_D|u|dt \tag{4.62}$$

where T is the period $[s]$, W is the work applied on the water per mass $[W]$, F_D is the drag force on the grid $[kg \cdot m \cdot s^{-2}]$, u is the velocity of the grid $[m \cdot s^{-1}]$ and V is the volume $[m^3]$. For steady-state conditions, F_D can be calculated from (Rasmussen and Larsen, 1996):

$$F_D = \frac{1}{2}C_D\rho u^2 D \tag{4.63}$$

here C_D is the drag coefficient $[-]$ and D is the rod diameter in the grid $[m]$. During oscillating conditions, C_D varies due to changing wakes downstream of the rods. For the present grid velocities, C_D do consequently have to be determined from experiments. Based on grounds

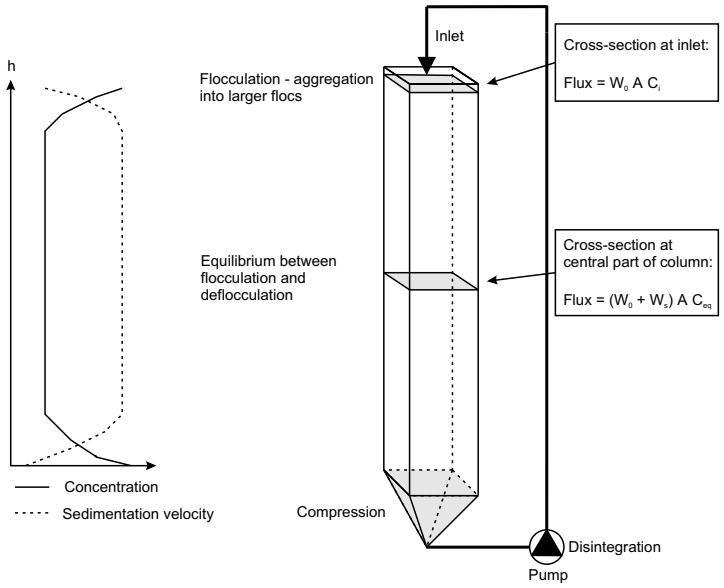

Figure 4.56 Outline of the settling column experiment.

of measurements of the force applied to the grid, C_D can be calculated for the oscillating grid, and C_D can accordingly be extracted (Figure 4.57).

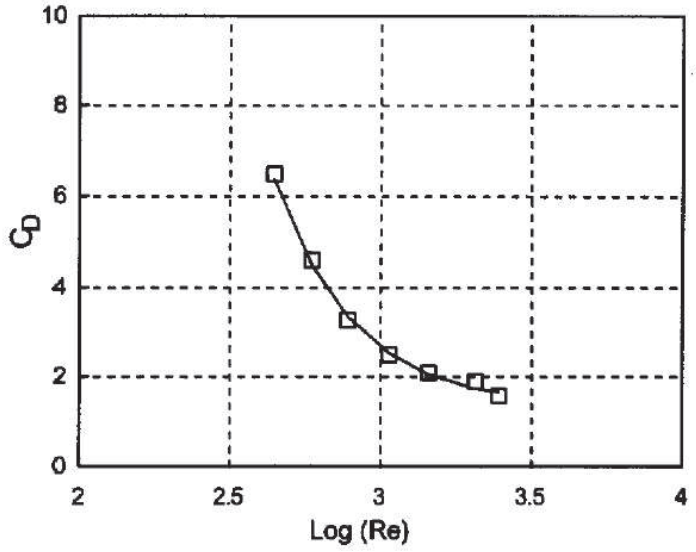

Figure 4.57 C_D measured in oscillating flow (Re = $(u_{max} D)/\nu$) (Rasmussen and Larsen, 1996).

When C_D and consequently F_D is known from the experiment, ϵ can be calculated from equation 4.62 under the assumption that the grid-velocity can be described by a cosine function:

$$\epsilon = \left(\frac{\frac{1}{2}C_D k A_{grid}}{V}\right)\left(\frac{a2\pi}{T}\right)^3 \underbrace{\frac{1}{T}\int_0^T cos^2\left(\frac{2\pi}{T}t\right)\left|cos\left(\frac{2\pi}{T}t\right)\right| dt}_{2\alpha=0.424} \tag{4.64}$$

where k is the number of grids in the column $[-]$, V is the volume of the column $[m^3]$ and A_{grid} is the cross sectional area of the grid rods $[m^2]$. The under braced part of equation 4.64 is an integral independent of the geometry. Consequently, this part is constant with the value: $2\alpha = 0.424$ (Rasmussen and Larsen, 1996).

Inserting equation 4.64 in equation 4.61 yields:

$$G = \sqrt{\left(\frac{\alpha C_D k A_{grid}}{\nu V}\right)\left(\frac{2\pi a}{T}\right)^3} \tag{4.65}$$

By monitoring the period T of the oscillating grid, the turbulent shear G can be calculated from equation 4.65. The sludge concentration apparent in the expression for the settling velocity of the sludge (Equation 4.59) comes directly out from the measurements on the suspended solids in the central part of the column.

In the present work, the results of settling column experiments previously performed on activated sludge from Aalborg East WWTP has been applied when adopting the settling model (Rasmussen and Larsen, 1996), (Jensen, 2004). The fitted model parameters, W_0, γ, β and λ from these experiments are listed in table 4.4.

Table 4.4 Fitted model parameters for the settling velocity at Aalborg East Wastewater Treatment Plant. $^+$: (Rasmussen, 1997), $^{++}$: (Jensen, 2004).

$Experiments$ $[-]$	W_0 $[m \cdot d^{-1}]$	γ $[s]$	β $[m^3 \cdot kg^{-1}]$	λ $[m \cdot d^{-1}]$
1996^+	147	-0.22	-0.48	3.53
2004^{++}	109	-0.003	-0.55	0.31

Distinct differences are observed between the two sets of data in table 4.4. The values of W_0 and γ are both lowest in the experiments of (Jensen, 2004), indicating that the settling characteristics at the period of time were worse than at the earlier experiments in 1996. Also the larger negative value of β indicate a higher sensitivity towards the suspended solids concentration. The small negative value of γ in the 2004 experiments are likely to be caused by a too narrow experimental ground. The majority of the 2004 experiments were run at a relatively high level of turbulence, where it is likely that W_s is relatively insensitive towards changes in G. If the experiments in 2004 had been performed at a broader range of G values, it is likely that a larger sensitivity towards turbulence would have been observed.

Besides natural variations, the reason for the worsened settling characteristics might be due to concurring experiments with the reject water and problems with keeping the suspended solids concentration down on the normal level of $5kg \cdot m^{-3}$.

With the above described considerations in mind, it is chosen to apply the values of (Rasmussen and Larsen, 1996) in the remainder of this work.

Field rheology experiments

In order to determine a proper rheology model for describing the viscosity of the activated sludge in a process tank, the equations 2.19 - 2.21 were in 2004 tested on sludge from Aalborg East WWTP (Jensen, 2004). The measurements were performed on a Tube Viscometer manufactured in-house at the Laboratory of Hydraulics and Coastal Engineering at Aalborg University (Figure 4.58). The Tube viscometer was designed as a simplified version of the one applied in (Frost, 1981), (Frost, 1982), (Frost, 1983).

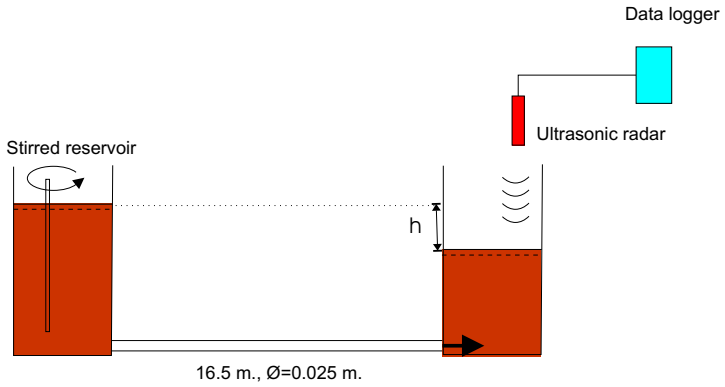

Figure 4.58 Outline of the tube viscometer.

Basically the experimental equipment consists of two 50L plastic barrels connected with a 16.5m long 1 inch diameter plastic hose. The relatively large diameter of the hose was chosen in order to accommodate the size of the sludge aggregates. Initially one of the barrels are full, whereas the other is only partly full. When the experiment is started, the pressure difference between the two reservoirs induces a flow from the full barrel to the empty one. The flow stops when equilibrium has reached between the driving force from the pressure difference and the viscous forces acting between the fluid and the pipe wall. If the fluid possesses a yield stress, the flow will theoretically stop when the pressure force has decreased to a level equal to the force required to the yield stress. Further details about the experimental layout is included later in this section.

If the fluid stops flowing with a resulting difference in pressure level between the two barrels, the yield stress can be determined by dividing the pressure force calculated from the pressure level difference with the surface area of the tube:

$$\tau_y = \frac{\Delta h \rho g \pi r^2}{2\pi r L} \tag{4.66}$$

where τ_y is the yield stress $[N \cdot m^{-2}]$, Δh is the difference in water level between the two barrels $[m]$, ρ is the density of the fluid $[kg \cdot m^{-3}]$, r is the radius of the tube $[m]$ and L is the length of the tube $[m]$.

A set of equations for describing the flow in the tube was set up. The equations are only applicable for laminar flow conditions. In order to investigate if laminar conditions are apparent, the Reynolds' number has been calculated, based upon a Herschel-bulkley fluid:

$$Re = \frac{2\rho U r}{K\left(\frac{3n+1}{4n}\right)^n} \cdot \left(\frac{4U}{r}\right)^{1-n} \tag{4.67}$$

where K and n are the parameters presented in connection with equation 2.19 - 2.21 and U is mean flow velocity in the tube $[m \cdot s^{-1}]$. The transition between laminar and turbulent pipe flow occur at Re of approximately 2300, where Re below 2300 indicate laminar flow.

Assuming that fluid properties are known and that the rheology of the fluid can be described by equation 2.21, the flow through the tube viscometer can be calculated as (Frost, 1982):

$$Q = \pi r^3 \cdot \frac{n}{3n+1} \cdot \left(\frac{\tau_w - \tau_y}{K}\right)^{1/n} \left\{1 - \frac{\tau_y/\tau_w}{2n+1} \cdot \left[1 + \frac{2n}{n+1} \cdot \frac{\tau_y}{\tau_w} \cdot \left(1 + n\frac{\tau_y}{\tau_w}\right)\right]\right\} \tag{4.68}$$

here τ_w is the wall shear stress $[N \cdot m^{-2}]$, for pipes calculated as:

$$\tau_w = \rho g R I = \frac{\Delta h \rho \cdot g r}{2L} \tag{4.69}$$

where Δh is the difference in pressure head between the two reservoirs $[m]$.

As for the Herschel-Bulkley model, expressions can be derived for calculating the flow in the tube viscometer by the use of the Bingham and the Casson equations (Barnes, 2000). These equations has however been omitted here.

The Bingham, the Casson and the Hershel-Bulkley model has been fitted to data from rheological experiments performed at Aalborg East WWTP. The experiments were performed with the tube viscometer described previously (Figure 4.58).

Figure 4.59 Experimental equipment used on rheology measurements at Aalborg East WWTP. From: (Jensen, 2004)

Throughout the experiments (Figure 4.59), each of the reservoirs were gently agitated in order to maintain fluid homogeneity. The agitation was kept gentle in order to maintain the

structure of the flocs in the flocculated suspension. The level of the suspension was monitored with a Honeywell 940 Ultrasonic meter. By logging the signal from the ultrasonic meter to an EXTECH ML720 data logger, the flow could be calculated based on the geometry of the reservoir. Before the experiment, the ultrasonic meter was calibrated to known water levels. The receiving reservoir was filled above the level of the inlet before the beginning of the experiment. Since the geometries of the two reservoirs were identical, the decrease in water level in one reservoir could be related to the increase in water level in the other. On behalf of the water level in the two reservoirs, the pressure drop was calculated. In order to ensure fresh and undisturbed sludge, the sludge was taken directly from the process tanks at Aalborg East WWTP. Approximately 30-40 liters of sludge was applied for each experiment. In total, eight experiments at three different suspended solids concentration were conducted (Table 4.5).

Table 4.5 Sludge concentrations for the 8 experiments conducted at Aalborg East WWTP.

Experiment	*Sludge concentration*
Experiment 1	1.94 $kgSS/m^3$
Experiment 2	1.94 $kgSS/m^3$
Experiment 3	1.94 $kgSS/m^3$
Experiment 4	2.95 $kgSS/m^3$
Experiment 5	2.95 $kgSS/m^3$
Experiment 6	2.95 $kgSS/m^3$
Experiment 7	5.00 $kgSS/m^3$
Experiment 8	5.00 $kgSS/m^3$

A typical graph of the sludge level versus time during the measurements is illustrated in figure 4.60.

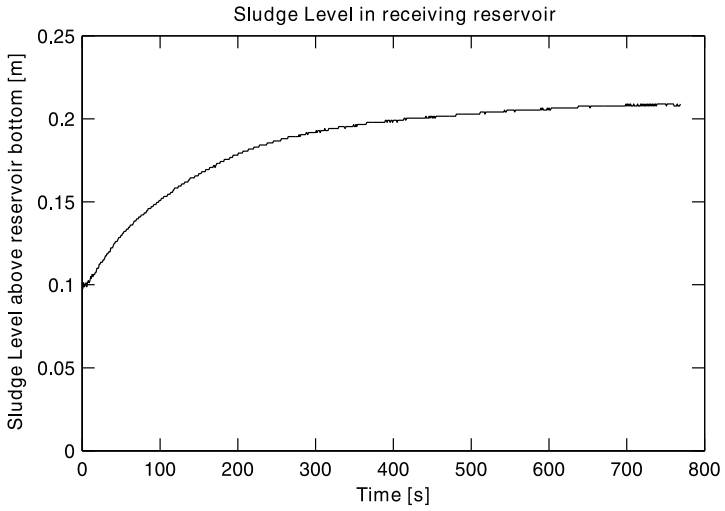

Figure 4.60 Water level as a function of time in the receiving reservoir. Data are from the measurements at Aalborg East WWTP.

As illustrated on figure 4.60, the water level gradually rises until it reaches a steady state level. The yield strength of the sludge can be estimated by application of equation 4.66.

After conducting the measurements, the data were processed and graphs of the wall shear stress τ_w (equation 4.71) as a function of the apparent velocity gradient at the wall, $8V/D$, were constructed.

Data fitting

When fitting the data to the Herschel-bulkley model, the approach suggested by (Frost, 1983) was applied: The shear stress at the wall against $(8V/D)$ were plotted on a log-log graph and the gradients of the tangents on this graph were calculated:

$$n' = \frac{d\log\tau_w}{d\log(8U/D)} \tag{4.70}$$

The shear rate $\dot{\gamma}$ of the non-Newtonian fluid can be calculated by correcting $(8V/D)$ with the gradient n', accounting for the variation in non-Newtonian viscosity as the shear varies across the cross section of the pipe:

$$\dot{\gamma} = \left(\frac{3n'+1}{4n'}\right)\left(\frac{8V}{D}\right) \tag{4.71}$$

Now $\tau_w - \tau_y$ against $\dot{\gamma}$ are calculated on a double logarithmic plot. The curve fitting is based on the fact that the correct yield stress will show a straight line of gradient n, where n is the coefficient in equation 2.21. Since now both τ_y and n are found, it is relatively straight-forward to estimate K from the data set.

Fitting of the Bingham and Casson equations are somewhat easier since these models only have two parameters and the fitting is easily done by the use of an ordinary spread sheet.

It is clear that the Herschel-Bulkley model is superior to the other mentioned equations for non-Newtonian fluids. This is due to the extra model flexibility introduced by the variable power exponent n. Figure 4.61 shows a typical plot of the pipe flow modelled with the 3 different models, the Bingham, the Casson and the Herschel-Bulkley model.

Apart from the first part of the flow curve, the curve fitted by the Herschel-Bulkley model is very close to the measurements, whereas the other models show slightly less accordance. This tendency also applies to the rest of the experiments, and thus it is assessed that the Herschel-Bulkley model is the most applicable model.

Consequently, the Herschel-Bulkley model has been fitted to the eight experiments described in table 4.5. An overview of the fitted model parameters can be seen in table 4.6.

From the fitted Herschel-Bulkley models with the parameters from table 4.6, the viscosities as a function of the shear rates have been plotted for the eight experiments (Figure 4.62).

When comparing table 4.5 and figure 4.62 it becomes evident that the viscosity increases with sludge concentration. The curves from experiment 7-8 clearly show higher viscosity than the curves from experiments with lower sludge concentrations. Also, the curves from experiment 4-6, where the sludge concentration had the lowest values, shows the smallest viscosities. The general trend with n-values close to one, is in compliance with the findings of (Sozanski *et*

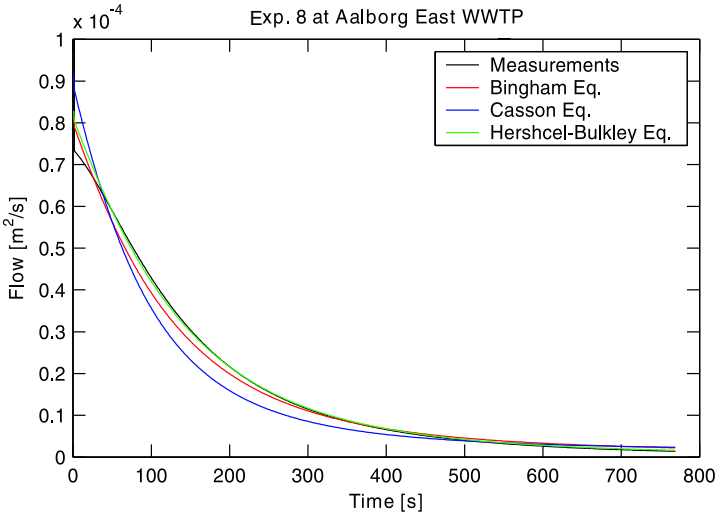

Figure 4.61 Non-Newtonian fluid models fitted to the flow curve of the pipe viscometer with activated sludge, from experiment 8 at Aalborg East WWTP.

Table 4.6 Fitted Herschel-Bulkley model parameters for the eight experiments performed at Aalborg East WWTP.

$Experiment$ $[-]$	τ_y $[N/m^2]$	K $[Ns^n/m^2]$	n $[-]$
Experiment 1	0.317	2.72E-3	1.047
Experiment 2	0.331	8.27E-4	1.334
Experiment 3	0.285	3.08E-3	1.02
Experiment 4	0.282	1.45E-3	1.221
Experiment 5	0.268	2.07E-3	1.130
Experiment 6	0.271	1.56E-3	1.174
Experiment 7	0.356	3.09E-3	1.091
Experiment 8	0.361	2.51E-3	1.172

al., 1997), who found that the viscosity of precipitated waterwork sludges approached Newtonian behavior for water contents above 98%.

In the remainder of the work, the rheology model has as widely as possible been applied to the modelling cases regarding activated sludge.

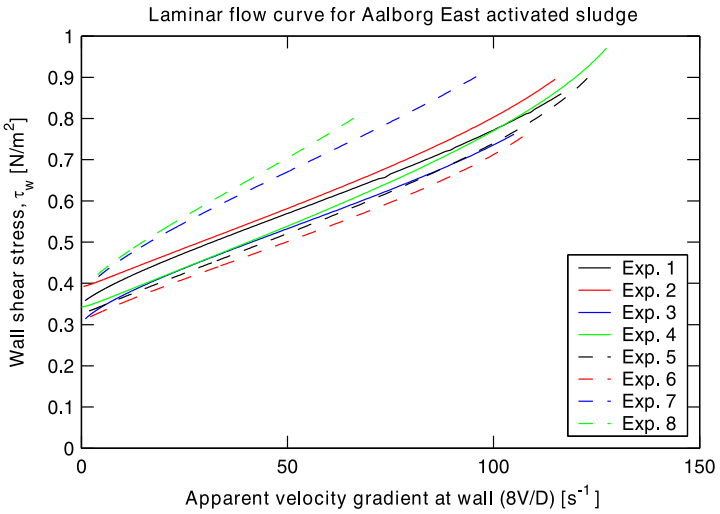

Figure 4.62 Wall shear stress, τ_w as a function of the apparent velocity gradient $(8V/D)$.

4.5 Summary

A range of important sub processes have been investigated in details with the purpose of a later integration into a complete hydrodynamic and biological model of a process tank.

1 A dish-shaped air-diffuser was investigated in the laboratory and a numerical two-phase multifluid model was constructed. Good accordance was obtained between measured and modelled mean liquid velocities and volume fractions of air inside the bubble plume

2 A large slow-rotating two-bladed hydrofoil shaped propeller was investigated numerically. The complex geometry of the blade was scanned with a laser, and a sliding mesh model, resolving the accurate movement of the propeller during operation was constructed. The results from the comprehensive propeller model were used for getting an insight into the complex flow generated by the propeller. Due to the excessive requirements in computational power, a lesser demanding momentum model describing the overall effect of the propeller was constructed on behalf of the information obtained from the detailed modelling. Good correlation between the detailed sliding mesh model and the simplified momentum model was obtained

3 The ASM3 model was successfully integrated into the three-phase multifluid model, and the model integration was validated through good agreement with a reference spreadsheet model

4 The sedimentation model of (Rasmussen and Larsen, 1996), (Rasmussen, 1997) was implemented into the three-phase multifluid model

5 The non-Newtonian properties of the activated sludge was investigated by the analysis of data from experiments in a simple tube rheometer in at Aalborg East Wastewater Treatment

Plant

In the next chapter, the above-discussed sub processes will be combined and tested on three case studies of increasing complexity.

CHAPTER 5
WWTP case studies

In the present chapter, the developed model framework is tested in case studies on wastewater treatment process tank at three WWTP in Denmark. The case studies are presented in order of increasing complexity:

1. Bjergmarken WWTP - investigation of the Aeration Tank Settling (ATS) properties of a process tank
2. Hals Central WWTP - investigations of a very dynamic process tank. A simple biological model for the bulk microbial uptake of oxygen is integrated into the model
3. Frederikshavn Central WWTP - investigations of a process tank. Here, the detailed ASM3 model for the description of the biological processes in the tank is incorporated in the hydrodynamic model

The principle of the structure of the chapter is illustrated in figure 5.1.

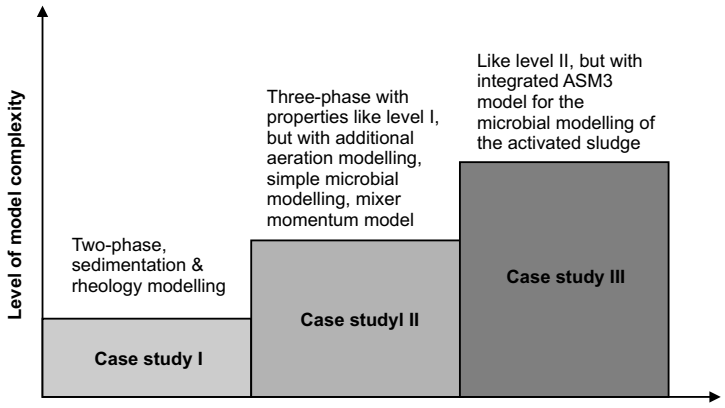

Figure 5.1 Principle layout of *staircase* illustrating the structure of the present chapter.

In the first case study at Bjergmarken WWTP, the settling properties of a tank operated according to a special storm weather operation scheme are investigated. During ATS operation, some of the process tanks are basically utilized for extra settling capacity in order to reduce the load on the secondary settling units during storm weather events.

The second case study regards a very dynamically operated process tank at Hals Central WWTP. The process tank constantly undergoes a distinct process cycle, where both the special

geometry of the OCO-tank and the varying operation of the aeration and mixing equipment are responsible for the complexity of the hydraulic and biological conditions in the tank.

The last case study involves the integration of the detailed ASM3 model with the three-phase multifluid model. The integrated model is used to predict the nitrogen concentrations of the process tank during alternating nitrification and denitrification operation.

5.1 Case study 1: ATS-operation at Bjergmarken WWTP

The first of three case studies involves the modelling of the Aeration Tank Settling (ATS) operation at Bjergmarken Wastewater Treatment Plant in Denmark. The present investigation is part of an external assignment performed on request of Krüger A/S, Denmark. Consequently, the case study has basis in a problem defined by Krüger A/S and solutions partly suggested by Krüger A/S and partly suggested by (Laursen and Rasmussen, 2004).

As presented in detail later, ATS-operation is an operational mode where some of the process tanks are applied for extra settling capacity, in order to reduce the wash-out of sludge to the recipient during storm weather events.

The ATS case will be used to calibrate the water-sludge two-phase model. Since the efficiency of the ATS concept depends highly on the efficiency of the sedimentation process, the natural focus of the present case study will be headed towards an accurate modelling of this process.

In order to optimize the ATS-operation of the process tank, the inlet arrangement of the tank has been retrofitted, with the purpose of finding the solution that results in the best conditions for optimal sedimentation in the process tank (Laursen and Rasmussen, 2004).

5.1.1 Presentation of location

Bjergmarken Wastewater Treatment Plant is located at the City of Roskilde (Figure 5.2). The WWTP had a load of $75821 PE$ in 2003. After the wastewater is treated in the plant, the cleaned water is discharged into Roskilde Fjord.

Bjergmarken WWTP is of the MBNDC type, where both mechanical treatment, heterotrophic biological turnover of organic matter, removal of nitrogen by nitrification and de-nitrification and chemical precipitation of phosphorous and also biological phosphorous removal are present on the plant. The present work involves the modelling of one of the process tanks at the WWTP during a cycle of ATS-operation.

The process tank at Bjergmarken WWTP

An outline of the investigated process tank is shown in figure 5.3. The length, width and depth of the tank are 40, 22 and $4.5 m$, respectively. Internally in the tank, a middle wall and several baffles at the ends of the middle wall are present, separating the tank in an inner and outer zone, where the sludge in the inner zone rotates slower than in the outer zone during periods of mechanical mixing. A circular inlet with a diameter of $1.2 m$ is located in the dividing wall between two tanks in a tank set. The inlet is connected to an identical neighbour process tank, where the wastewater and sludge passes through before it enters the tank undergoing investigations. At the one end of the tank a rectangular weir is located, from where the sludge is discharged to a distribution channel and further into the secondary settling units.

Figure 5.2 Map showing the location of Bjergmarken WWTP.

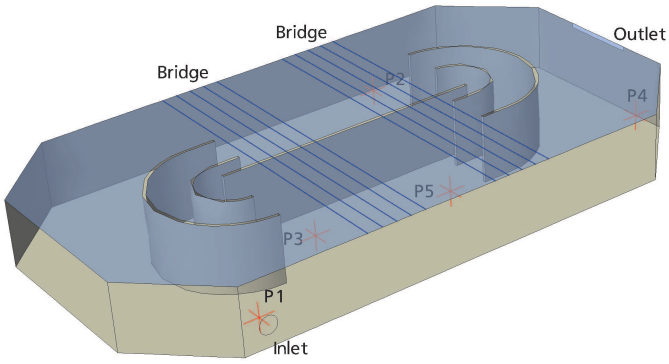

Figure 5.3 Outline of the process tank. The points P1 - P5 indicates the location of the measurements performed by Krüger A/S on the 20/9 - 2001.

ATS-operation

During Aeration Tank Settling (ATS) operation, sedimentation is in periods allowed in the aeration tanks, whereby the loading on the secondary settlers is lowered and the hydraulic capacity is increased (Bundgaard *et al.*, 1996), (Nielsen *et al.*, 1996) and (Nielsen *et al.*, 2000). When

the hydraulic capacity of the settler is increased, the point where a critical amount of sludge is discharged into the recipient, will occur at a higher hydraulic loading than would be the case with *normal* controlling strategies. The principle of the ATS controlling strategy is outlined in figure 5.4.

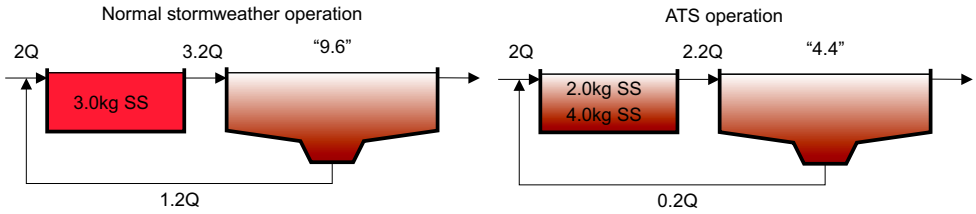

Figure 5.4 The principle of ATS-operation. In the shown example, the required settler volume is more than halved during ATS (Nielsen *et al.*, 1996).

By retaining a larger part of the sludge in the aeration tank, the loading on the settler is decreased. In the example on figure 5.4, it is assumed that the outlet concentration and flow from the process tank are reduced by 50% and 30%, respectively. As a result of this ATS operation scheme, the required settling volume of the settler is more than halved compared to the normal operation conditions during storm weather.

During steady-state operations, the capacity of the settler is inversely proportional to the suspended solids concentration at the outlet of the process tanks ($X_{SS,out}$) and the sludge volume index (SVI) (Nielsen *et al.*, 2000):

$$Q = \frac{V_{Settler}}{XSS_{out} \cdot SVI \cdot k} \tag{5.1}$$

where Q is the capacity of the settler $[m^3 \cdot s^{-1}]$, $V_{Settler}$ is the volume of the settler $[m^3]$, XSS_{out} is the concentration of suspended solids in the inlet to the settler $[kg\ SS \cdot m^{-3}]$, SVI is the sludge volume index $[mL \cdot g^{-1}]$ and k is a proportionality factor $[-]$, depending on the plant design. As indicated in equation 5.1, the capacity of the settler is highly dependent on the inlet concentration of suspended solids. The present numerical work, aims at finding means for keeping the concentration of suspended solids as low as possible at the outlet of the process tank at Bjergmarken during storm weather events.

In the present case study, one of the tank sets is operated in ATS-mode. During ATS, the tank set undergoes an alternating operation dependent on the inlet flow, the ammonium, nitrate and XSS concentration and the time elapsed of the different ATS phases. The alternating operation of a tank set is illustrated in figure 5.5.

As indicated on figure 5.5 the two tanks alternates between aeration and sedimentation during ATS-operation. In the present investigations the tank set was consistently running in the main phase, where the investigated tank was the one running in sedimentation mode.

5.1.2 Data collection

On the 20/9-2001 Krüger A/S performed a measurement campaign in one of the process tanks at Bjergmarken WWTP. The measurement campaign consisted of two investigations:

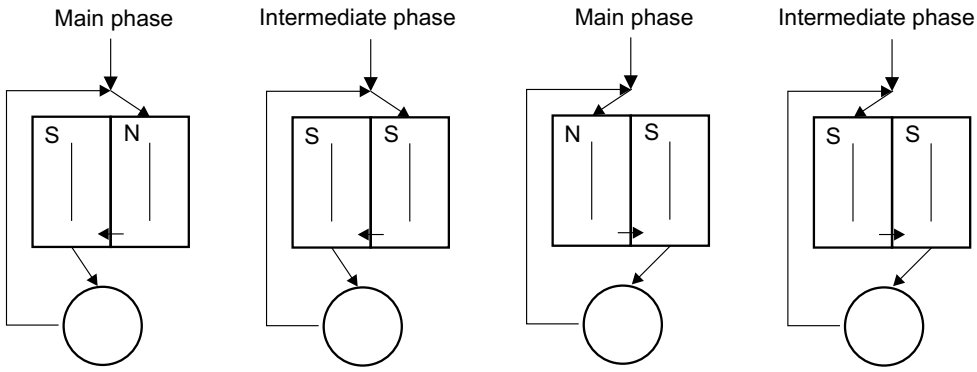

Figure 5.5 The principle of the different phases occurring during ATS-operation (Nielsen *et al.*, 2000).

1 No agitation in the tank, and no in- or outlet of sludge

2 Inlet to the tank: $1200 m^3 \cdot h^{-1}$ + a recirculation flow of $300 m^3 \cdot h^{-1}$. Otherwise no agitation in the tank

The duration of the two investigations were 65 and 105 minutes, respectively.

Investigation 1

Investigation 1 is based on a situation where a single aeration tank is considered isolated without either in- or outlet from other tanks. Furthermore, the tank is in a sedimentation phase, i.e. no aeration or stirring are turned on. Prior to the investigation, the tank is stirred, i.e. a circulating flow is initially occurring.

The measurement campaign contains velocity measurements in a selected point in the tank (P2 on figure 5.3). The locations of measurement points are estimated on behalf of approximate indications on a forwarded layout drawing of the plant. Hence, a certain amount of uncertainty is related to the exact location of the measurement points. Since relatively large velocity gradients are present at some locations in the tank, a small displacement in the estimated measurement position compared to the actual position could influence the magnitude of e.g. the modelled velocities. The above mentioned uncertainties should be taken into account when evaluating the compliance between measurements and model results.

Beside the measured flow velocities in P2, the sludge blanket was visually estimated to be positioned approximately $45 cm$ below the water surface at the end of the investigation. The sludge concentration in the tank was approximately 5.5 - $6.6 kg\ SS \cdot m^{-3}$.

Investigation 2

Investigation 2 is based upon measurements on an *artificial* ATS event. Bjergmarken WWTP is in its present form consisting of two identical set of tanks, with two process tanks in each set. In the *artificial* ATS event, the total of the dry weather flow is led through only one of the sets - the investigated set. The dry weather flow was during the investigations $1200 m^3 \cdot h^{-1}$. In

addition to the dry weather flow, a recirculation flow of $300m^3 \cdot h^{-1}$ was added, making a total of $1500m^3 \cdot h^{-1}$ in the inlet.

The investigated tank works as sedimentation tank during the measurements. The neighbour tank is operated as a normal aeration tank. The wastewater is initially led through the neighbour tank where it is aerated. Hereafter it is led through the aeration tank working as a sedimentation tank during ATS, after which it is led to separation in the secondary settling unit. The inlet to the investigated tank occurs through the circular inlet, as shown on figure 5.3. The outlet into the secondary settling unit is occurring through a traditionally designed outlet tilt at the end of the tank.

Like in investigation 1, the process tank is initially stirred, whereby the flow initially will decrease from a state of higher velocities to a state where the flow in the tank is controlled by the inlet jet.

Flow velocity measurements was conducted in five points (P1-P5 on figure 5.3). Furthermore, suspended solid concentrations are measured at P5 and the sludge blanket position in the tank was measured a couple of times through the measurement campaign.

Sedimentation characteristics

With the purpose of obtaining an estimate on the initial sedimentation velocity of the sludge flocs, cylinder glass measurements were performed on the Bjergmarken activated sludge in September 2004. During these measurements, the sludge blanket was measured at predefined time intervals, and from this the initial settling velocity was estimated. The initial settling velocity is an important property of the applied sedimentation model (Equation 4.59). Since significant differences in sludge characteristics may appear in time on a given wastewater treatment plant, uncertainties are connected with applying settling properties measured in 2004 on data from a measurement campaign performed in 2001. The obtained value is thus thought as an initial estimate on the initial velocity, and if necessary, modifications can be made during the numerical simulations. Prior knowledge on the values of the remainder of the constants in equation 4.59, have been obtained from the work of (Rasmussen and Larsen, 1996), (Rasmussen, 1997).

5.1.3 Numerical model

The level of detail in the present model was chosen with background in a weighing between the necessary level of detail and the relatively short time frame of the project (Laursen and Rasmussen, 2004). A higher level of detail, reflected in e.g. the resolution of the mesh, would require computational demands that would exceed the limits of the project.

Model setup

The hydrodynamics of the process tank is resolved through the solution of the multifluid model as presented in chapter 3. The multifluid model is based on a solution of the Navier-Stokes equations for the two phases: water and sludge flocs. The two phases interacts with each other through interfacial drag forces which are applied to the phases through the momentum equations. The sedimentation velocity is highly governed by the chosen drag model. For the present work the sedimentation model of (Rasmussen and Larsen, 1996), (Rasmussen, 1997) has been applied. The parameters of the model is partly built upon the data from Aalborg East Wastewater Treatment Plant (Rasmussen and Larsen, 1996), (Rasmussen, 1997), and partly built upon cylinder

glass experiment from Bjergmarken WWTP in 2004. The turbulence of the continuous water phase is modelled through the standard $k-\epsilon$ model (Chapter 3) and the eddy viscosity in the sludge phase is assumed proportional to the eddy viscosity in the water phase (Equation 3.12).

modelling of the initial mixed condition The process tank was prior to the measurements in the two investigations initially stirred. In order to obtain a correct initial condition, two sub-domains are constructed in the areas of the two slowly rotating propellers located in the tank. A momentum model of the same principle as the one constructed in chapter 4 has been constructed and implemented in the sub-domains. Since only constant axial momentum components where added to the sub-domains, the applied model was however simpler in its form than the one constructed in chapter 4.

Boundary conditions The model involves the following boundary conditions:

- A circular inlet in the dividing wall between the two tanks
- The rectangular outlet
- The water surface
- Concrete walls and tank floor

The inlet is modelled through a velocity boundary with constant inlet velocities perpendicular to the boundary. The outlet is modelled as a pressure boundary with a pressure corresponding to the atmospheric pressure, equivalent to a free outlet. The water surface has been modelled as a symmetry boundary, where the flow velocities are assumed to be identical above and below the water surface, corresponding to zero shear stresses at the surface, making this particular boundary type well suited for simulating a water surface. At the walls and the tank floor a roughness height of $3mm$ was applied. Beside the friction of the walls, friction to flow is also occurring at other installations in the tank. In order to account for this, additional resistance to the flow in the tank was added to the momentum equations.

Computational mesh the applied computational mesh is in the present computations within the size of 150,000 - 200,000 control volumes, dependent on the layout of the inlet arrangements during retrofitting. The control volumes are tetrahedron shaped, which allow for a flexible subdivision of the computational mesh. For all models, including the models with retrofitted inlets, identical configurations with respect to minimum and maximum control volume sizes and refinement parameters were applied.

5.1.4 Calibration and validation of the model

In the following, the numerical model is calibrated against the data of investigation 1 (Subsection 5.1.2), and validated against the data from investigation 2 (Subsection 5.1.2).

Calibration - investigation 1

The calibration is primarily performed by holding the modelled flow velocities up against the measured flow velocities obtained in P2 (Figure 5.3) during investigation 1. Furthermore the modelled position of the sludge blanket is compared with the measured sludge blanket position at the end of the investigation. Measured and modelled flow velocities in P2 are plotted in figure 5.6.

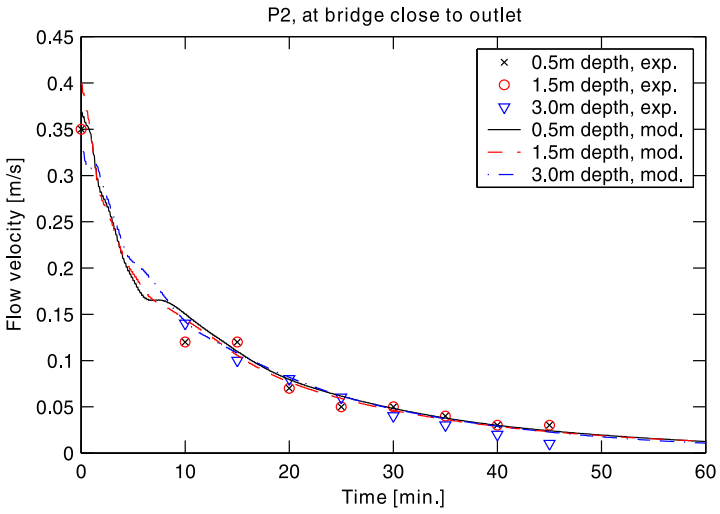

Figure 5.6 Time series of measured and modelled flow velocities at P2 during investigation 1.

From figure 5.6 a good agreement between measured and modelled velocities are apparent at all depths in P2, indicating that the model can describe slowdown of the flow satisfactory. The modelled sludge blanket at the end of the measurement campaign is plotted in figure 5.7.

The implemented sedimentation model, cause the sedimentation velocity of the sludge flocs to be dependent on both the level of turbulence and the suspended solids concentration, resulting in a lower settling velocity as either the turbulence level or the suspended solids concentration is increased. From figure 5.7 it appears that the sedimentation is better at the central part of the tank, whereas it is worse at the ends. This is caused by a higher level of turbulence at the end turns of the tank. In the inner part of the end turns this effect is not apparent, since the internal baffles have an attenuating effect on the turbulence, resulting in the best sedimentation inside the baffles. The available measurement campaign does not contain information regarding if there was a difference in sludge blanket level in different parts of the tank. In the measurement campaign the sludge blanket was just stated to be approximately $45cm$ below the water surface. For this reason the calibration is based on a mean sludge blanket position $45cm$ below the water surface.

The distribution of the suspended solids concentration has also been modelled and plotted, even though no measurements for evaluating this part of the model were available (Figure 5.8).

From figure 5.8 it is apparent that the sludge concentration is largest at the central part of the process tank.

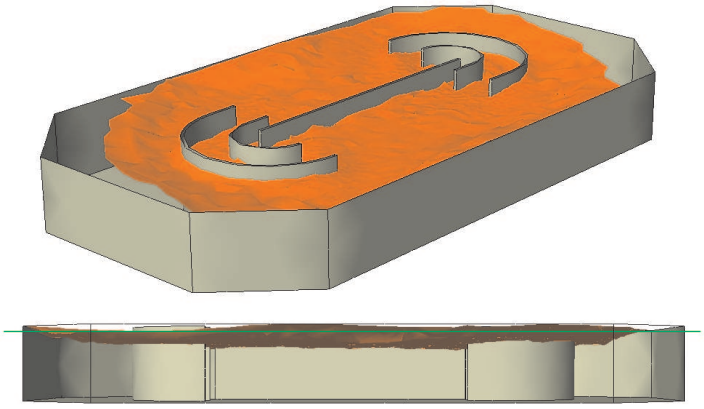

Figure 5.7 Modelled level of the sludge blanket at the end of investigation 1. The green line indicates a level of $0.45m$ below the water surface.

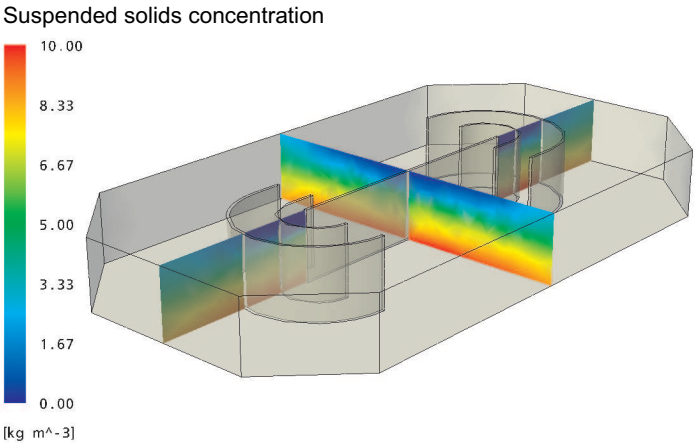

Figure 5.8 Modelled sludge concentration in the tank at the end of investigation 1.

Validation using investigation 2

In the model validation, the output of the model is compared against both flow velocities obtained in the measurement points indicated on figure 5.3, sludge concentrations in P5 and the level of the sludge blanket at the end of the investigation.

Flow velocities In P1 only flow velocities perpendicular to, and at a distance of $1m$ from the inlet in $3.0m$ depth was measured. The measurement in this point can be used as an indicator for the flow velocity through the inlet. If the assumption of an inlet flow of $1500m^3 \cdot h^{-1}$ holds, the flow velocity should be approximately $0.35m \cdot s^{-1}$, assuming that the flow is equally distributed

throughout the Ø1200 circular inlet. The measurements do however show significantly higher values (Figure 5.9).

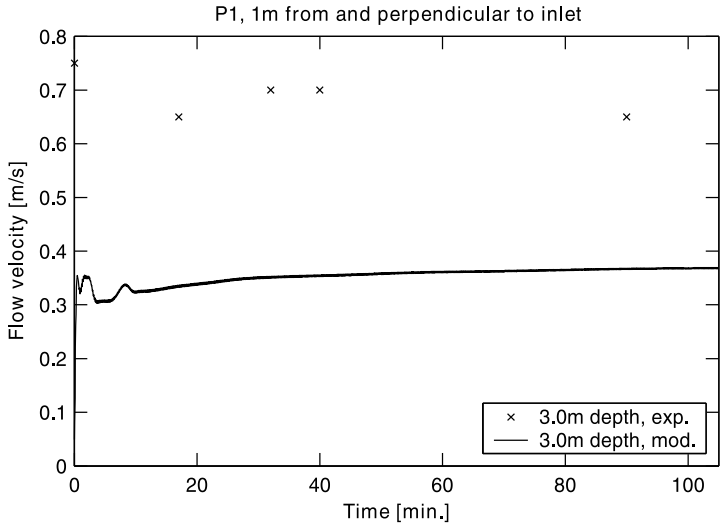

Figure 5.9 Time series of measured and modelled flow velocities at P1 during investigation 2.

The measured velocities are approximately twice as high as expected (Figure 5.9). This might be a result of contraction of the inlet flow, whereby the effective area of the inlet is smaller than the geometric area. The phenomena is probably caused by the acceleration of the sludge, where the sludge has to make a hard turn from the mean flow in the agitated neighbour tank, in order to pass through the inlet in the dividing wall. As a result of this, the sludge is pressed into one side of the inlet, whereby the main part of the flow occurs through a smaller effective area. Due to the sparse data material, it is hard to quantify the exact extent of the problem. Some of the difference in measured and modelled velocities could also be caused by measurement uncertainties.

In P2 time series of the flow velocities have been measured in 0.5, 1.5 and 3.0m depth. The measurements have been compared to the modelled velocities in figure 5.10.

From figure 5.10 it can be seen that the model does not capture the measured velocity gradient in the depth of the tank. At the beginning of the investigation, it appears like the flow velocity is largest at the bottom of the tank. At the end of the investigation, the trend is shifted towards largest velocities in the two upper points. This might be a consequence of stratification at the end of the investigation, with the highest sludge concentrations at the bottom of the tank. Since the inlet jet from the hole in the dividing wall between the tanks will have a lower sludge concentration than in the ATS tank in sedimentation mode, and thereby lower density, it is likely that the jet will be forced up on its way through the tank. This effect has not been captured by the model - but it could probably be resolved through a finer resolution of the computational mesh.

Also in P3 (Figure 5.3) flow velocities have been measured and modelled (Figure 5.11).

The model under estimates the flow velocities slightly in P3 (Figure 5.11). In P4 and P5 only a single measurement of the flow velocity has been performed, which is why it has been chosen to disregard this part of the data.

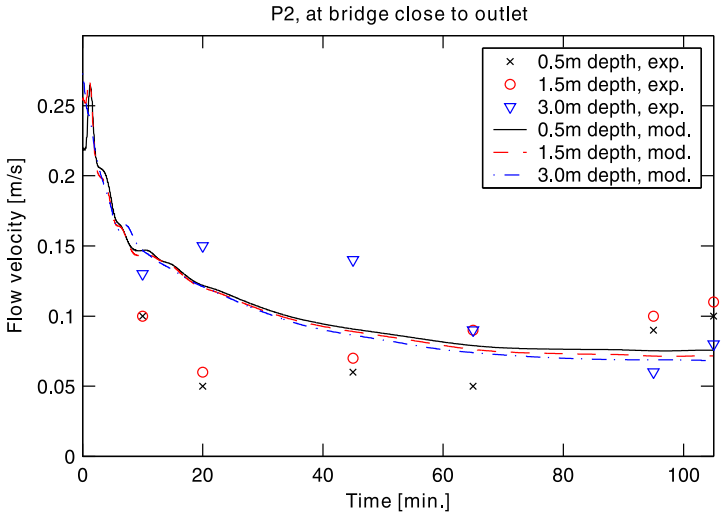

Figure 5.10 Time series of measured and modelled flow velocities at P2 during investigation 2.

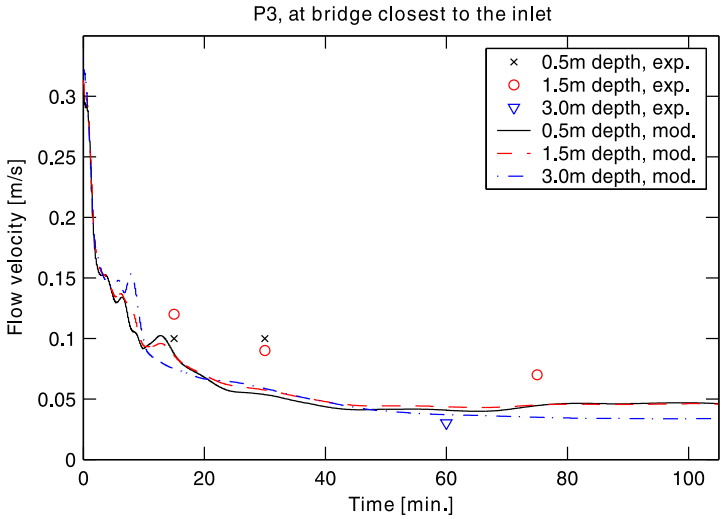

Figure 5.11 Time series of measured and modelled flow velocities at P3 during investigation 2.

The model do in general show that the flow during the two investigations proceeds as expected - in the same direction as during normal dry weather conditions where the mixers are applied. As examples of the flow behaviour, two vector plots have been constructed. Figure 5.12 show a horizontal vector plane intersecting the inlet.

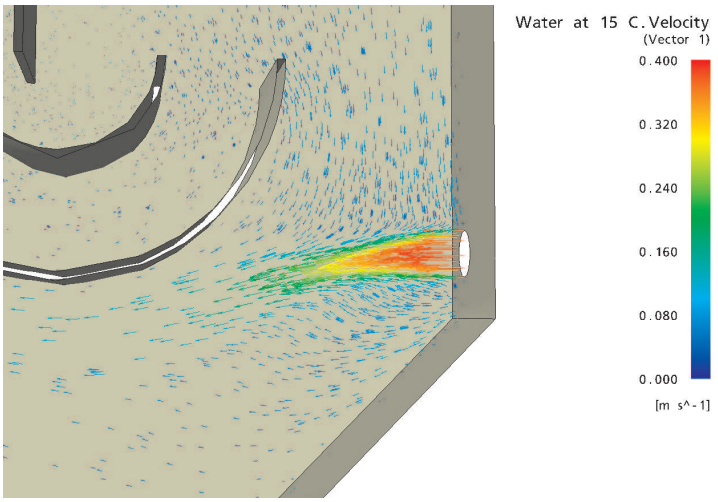

Figure 5.12 Vector plot showing velocity vectors in a horizontal plane intersecting the inlet during investigation 2.

In figure 5.13 a vector plot in a horizontal plane intersecting the outlet is shown.

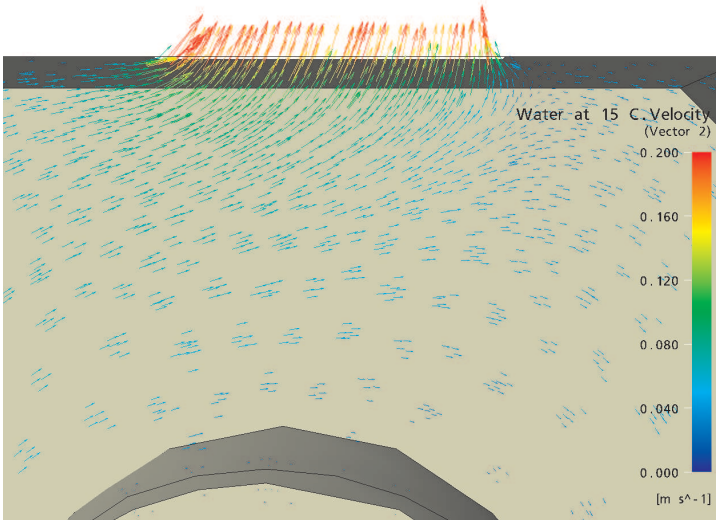

Figure 5.13 Vector plot showing velocity vectors in a horizontal plane intersecting the outlet during investigation 2.

Sedimentation Model and measurements have been compared for the two suspended solids concentration profiles measured in P5 30 and 90min after the start of investigation 2 (Figure 5.14).

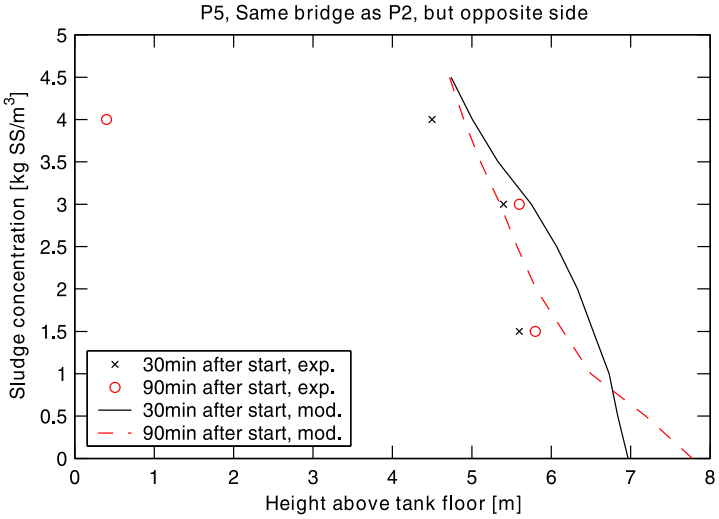

Figure 5.14 Profiles of measured and modelled suspended solids concentration profiles during investigation 2.

Model and measurements do in general show good agreement. In the top of the geometry the model does however not hit the right concentration correct. This is mainly due to the models relatively coarse computational mesh, resulting in an over estimation of the sludge concentration due to averaging over the relatively large control volumes. In order to have zero concentration in a control volume, the control volume do in principle have to be completely empty of sludge, which is why its hard to obtain zero concentrations with a relatively coarse mesh. The result of the sludge concentration modelling could possibly be improved by grid refinement and/or adjustments of the parameters in the sedimentation model.

The modelled sludge concentrations have been plotted in the same cross sections as in figure 5.8 (Figure 5.15). In compliance with investigation 1 (Figure 5.8), the sedimentation is again largest at the central part of the tank (Figure 5.15). Due to the additional flow passage through the tank, the separation is in general worsened compared to investigation 1. Like in investigation 1 (Figure 5.7), the sludge blanket position is modelled and visualized by the application of an iso-surface (Figure 5.16).

Again there is a trend towards better sedimentation in the central part of the tank. At the end of investigation 2, the sludge blanket position was in the measurements estimated to be approximately 18cm below the water surface. Only in the central part of the tank a sludge blanket is occurring in the model at this position.

With respect to the above discussed calibration and validation it is concluded that the hydrodynamic model is performing satisfactory regarding the modelling of flow velocities in the process tank. In both investigation 1 and 2, good accordance between modelled and measured flow velocities has been obtained. The measurements at the inlet indicate that there might be flow effects originating from contraction of the flow in the inlet.

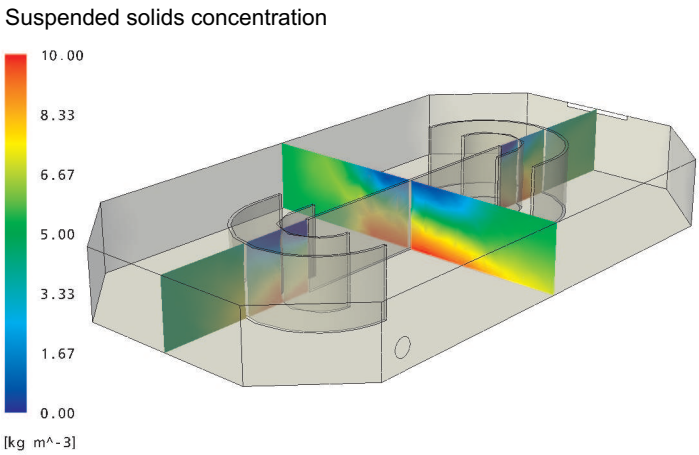

Figure 5.15 Modelled sludge concentration in the tank at the end of investigation 2.

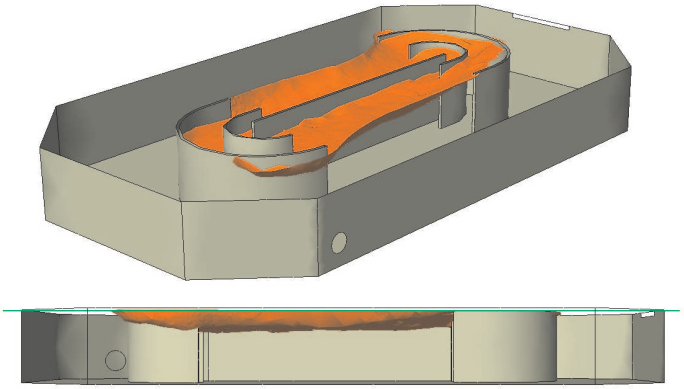

Figure 5.16 Modelled level of the sludge blanket at the end of investigation 2. The green line indicate a level of $0.18m$ below the water surface.

The modelling of the sedimentation shows that areas with low velocity are most favourable for the sedimentation. These areas are especially present in the central part of the tank and on the straight run of which the inlet is located. With regards of bringing the flow velocities down and thereby create more favourable conditions for sedimentation, it could be fruitful to change the hydrodynamic conditions regarding the inlet jet in the dividing wall between the tanks.

5.1.5 Alternative inlet configurations

With the optimization of the existing ATS-conditions at the process tank at Bjergmarken WWTP in mind, alternative inlet configurations as proposed by Krüger A/S have been tested in the CFD-model. Three different configurations have been tried out in the model. The setup of the three

configurations have aside from the different inlet layouts been identical to the setup of the validation regarding investigation 2 (Subsection 5.1.4).

In the attempt to decrease the flow velocities in the ATS-tank, alternative inlet configurations where a part of the exchange flow between the two tanks in a tank set are removed to one or more additional inlet holes, have been conceived. By increasing the effective inlet area, the same inlet flow to the tank should result in lower flow velocities in the inlet.

Inlet configuration 1

Inlet configuration 1 contains an extra inlet hole identical to the existing ø1200 circular hole in the dividing wall between the two tanks. The new hole is located upright of the existing hole (Figure 5.17). Since the effective flow area of the inlet is doubled in this configuration, the mean velocity in the inlet should be halved. This should have a positive effect with respect to reducing the circulation velocities in the sedimentation operated ATS-tank.

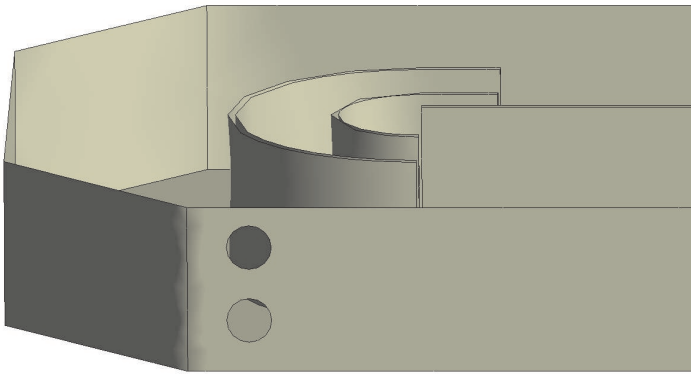

Figure 5.17 Inlet configuration 1.

Numerical results The numerical model does as expected show reduced flow velocities at the inlets. Figure 5.18 illustrates a horizontal vector plot intersecting the original inlet hole.

If figure 5.18 is compared to figure 5.12 a clear reduction of the flow velocities is apparent after the introduction of the extra inlet hole. It is now investigated if this reduction is a general trend applicable for the remainder of the tank. Modelling of the existing flow conditions and the conditions with inlet configuration 1 is compared through several plots of flow velocities and suspended solids concentrations. Flow velocities for the existing configuration and inlet configuration 1 in 0.1 and 3.0m depth are visualized in figure 5.19 and figure 5.20, respectively.

As illustrated in figure 5.19 and 5.20 it is apparent that the extra inlet has resulted in a reduction of the flow velocities in the tank. During the existing conditions, the flow velocities are in almost all of the tank affected by the jet from the inlet (Figure 5.19). At inlet configuration 1 the influence of the inlet jet has become less significant. This is especially apparent for the straight run after the outlet, but also in the zone in the vicinity of the outlet, the flow velocities seems to be reduced. It is expected that the reduction in flow circulation within the tank would

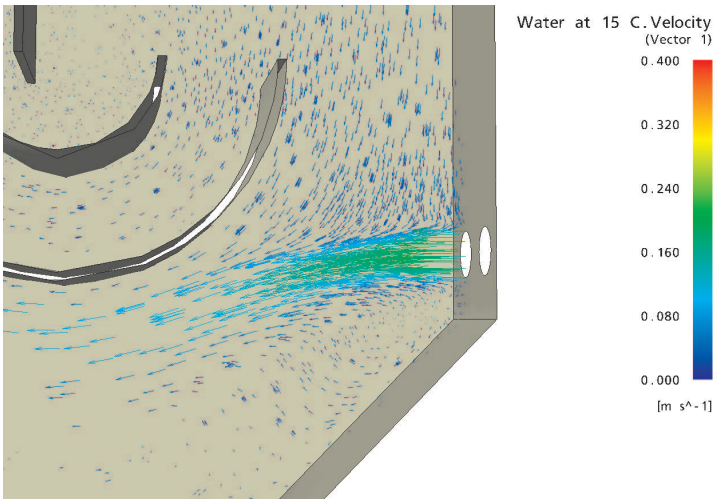

Figure 5.18 Vector plot showing velocity vectors in a horizontal plane intersecting the original inlet during numerical test of inlet configuration 1.

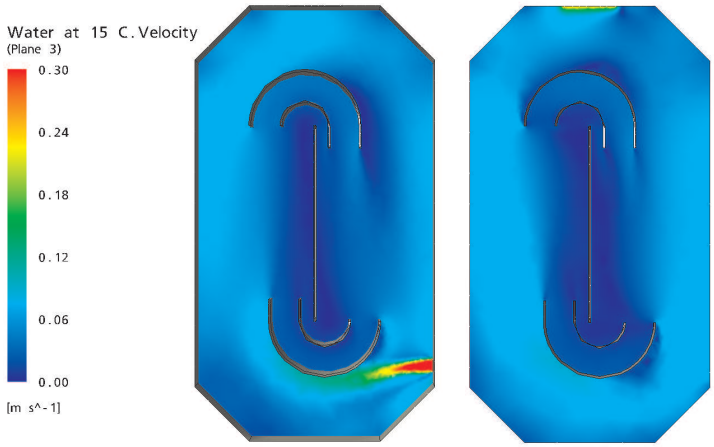

Figure 5.19 Flow velocities at the existing inlet configuration. The flow velocities are shown for a point in time corresponding to the end of investigation 2. The left plot is made in 3.0m depth, whereas the right plot is made in 0.1m depth.

have a positive effect on the sedimentation in the tank. This is investigated through a plot of the suspended solids concentration in the tank at the two cross section applied earlier (Figure 5.21).

A comparison between figure 5.15 and 5.21 indicates that the conditions for sedimentation will be substantially better at the implementation of an extra inlet hole in the dividing wall.

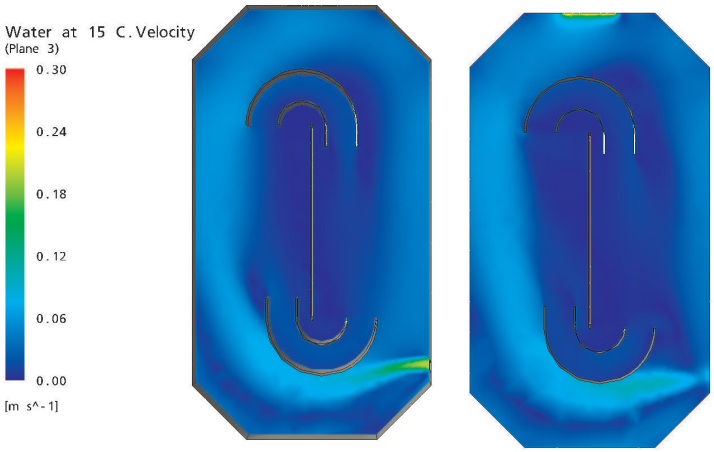

Figure 5.20 Flow velocities at inlet configuration 1. The flow velocities are shown for a point in time corresponding to the end of investigation 2. The left plot is made in $3.0m$ depth, whereas the right plot is made in $0.1m$ depth.

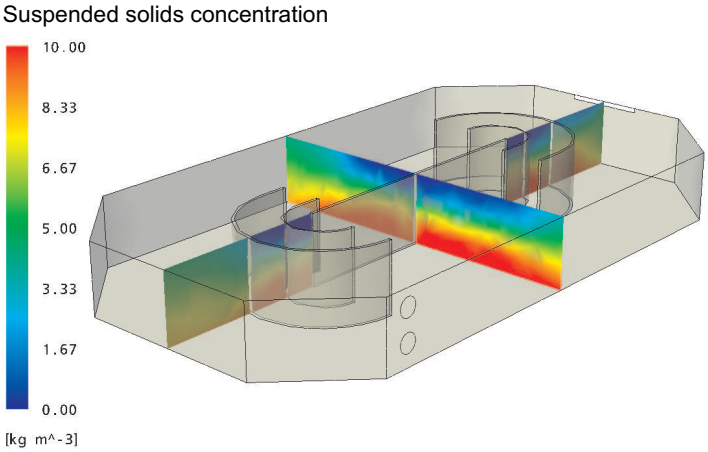

Figure 5.21 The modelled sludge concentration in the tank at inlet configuration 1. The plot is created at a time step corresponding to the end of investigation 2.

Inlet configuration 2

The motivation for inlet configuration 2 is originated in both economical and practical criteria. An obvious solution would be to place an extra rectangular inlet in the top of the dividing wall between the two neighbour tanks. Such an inlet could be cut out without emptying the tank completely, and the solution would also give rise to the smallest possible stability problems for the wall.

The position and the detailed layout of the additional inlet constitute of two degrees of freedom in which the system can be optimized. As a starting point it has been chosen to half

the flow through the existing inlet. I.e. the new inlet would have to deliver half of the inlet flow. With this flow in mind, the rectangular inlet has been dimensioned with basis in identical pressure losses over the inlets. From the existing conditions in the system, the pressure loss has been estimated to $2cm$. If the flow is halved through the existing inlet, the pressure loss would drop to $0.5cm$. The additional rectangular inlet has consequently been designed with basis in an identical pressure loss of $0.5cm$, resulting in a height and width of 0.45 and $1.9m$, respectively.

The location of the rectangular weir is chosen with the purpose of reducing the circulation in the tank as widely as possible. The existing walls and baffles have if possible been used to slow down the flow when it enters the tank. The location of the rectangular inlet can be viewed in figure 5.22.

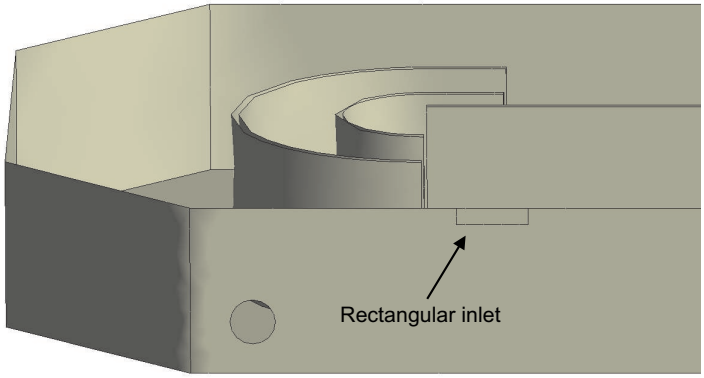

Figure 5.22 Inlet configuration 2.

Numerical results After the sludge has flown through the rectangular inlet it will be decelerated when it hits the middle wall in the tank. Simultaneously, the part of the flow that hits left of the middle wall will be decelerated by the two internal baffles at the end turn of the tank. This is substantiated by a vector plot of the flow velocities (Figure 5.23).

For inlet configuration 2 the modelled flow velocities are shown in figure 5.24. The point in time for figure 5.24 corresponds to the end of investigation 2. If figure 5.24 is compared to figure 5.19, a dramatic reduction in flow velocities is visualized. It is apparent that the flow velocities in general must be expected to be reduced if this solution is implemented. The only exception is naturally the zone in the vicinity of the new inlet. The model does furthermore indicate that the middle wall and the baffles as intended decelerates the jet from the rectangular jet.

The reduced flow velocities have a positive impact on the sedimentation in the tank (Figure 5.25). Comparing figure 5.15 and 5.25 the effect of the new inlet configuration can be viewed. Especially the straight run opposite of the side with the inlets show improved sedimentation after implementation of the new inlet. The zone in the vicinity of the new inlet does naturally show worsened sedimentation.

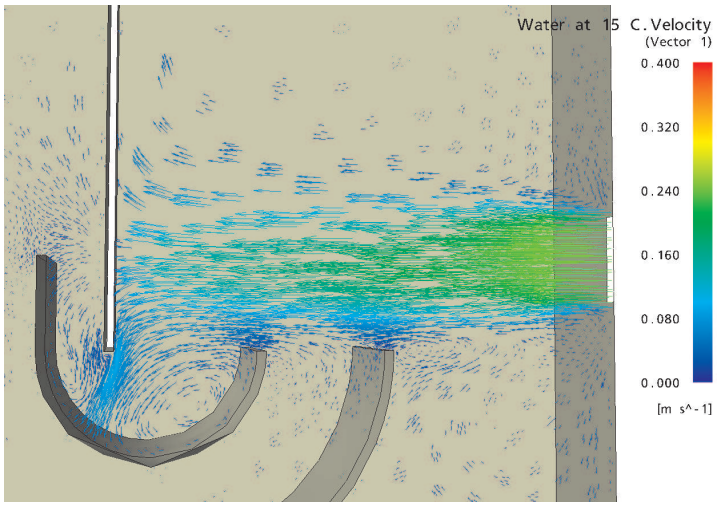

Figure 5.23 Vector plot showing velocity vectors in a horizontal plane intersecting the rectangular inlet during numerical test of inlet configuration 2.

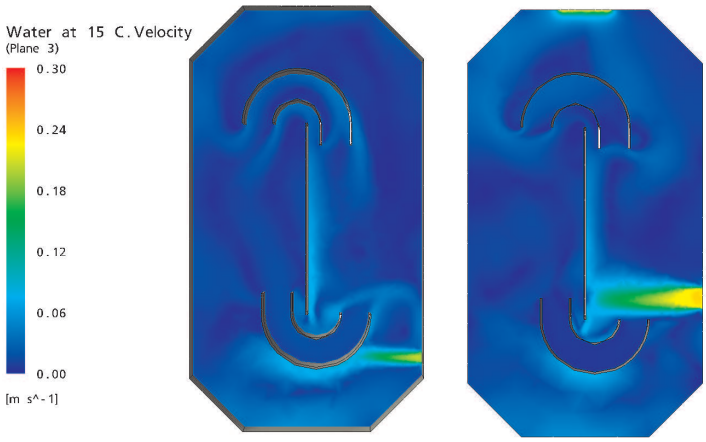

Figure 5.24 Flow velocities for inlet configuration 2. The flow velocities are shown for a point in time corresponding to the end of investigation 2. The left plot is representing $3.0m$ depth, whereas the right plot is representing $0.1m$ depth.

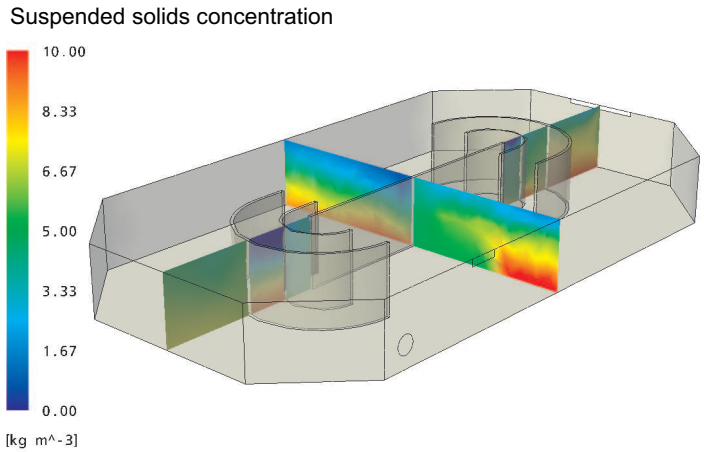

Figure 5.25 Modelled sludge concentration in the tank at inlet configuration 2. The plot is created at a time step corresponding to the end of investigation 2.

Inlet configuration 3

In inlet configuration 3 nine extra submerged circular inlets are introduced in approximately the same horizontal position as the rectangular inlet in configuration 2. The new holes are positioned significantly lower than in configuration 2. Each of the new additional holes have a diameter of $40cm$, and they have been positioned at a mutually interspaced distance of $80cm$, displaced with an offset above each other in two rows (Figure 5.26).

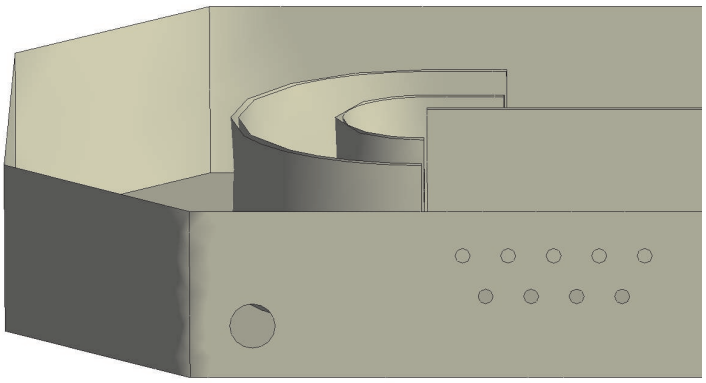

Figure 5.26 Inlet configuration 3.

Like in the case of inlet configuration 2, the flow distribution is assumed to be 50% on the existing inlet, and the remainder of the flow is distributed on the nine additional holes. The number of additional inlets have been determined with basis in an identical pressure loss of $0.5cm$ over the holes.

Numerical results In compliance with the same principle as for inlet configuration 2, the middle wall and the baffles are used for breaking down the inlet jet (Figure 5.27).

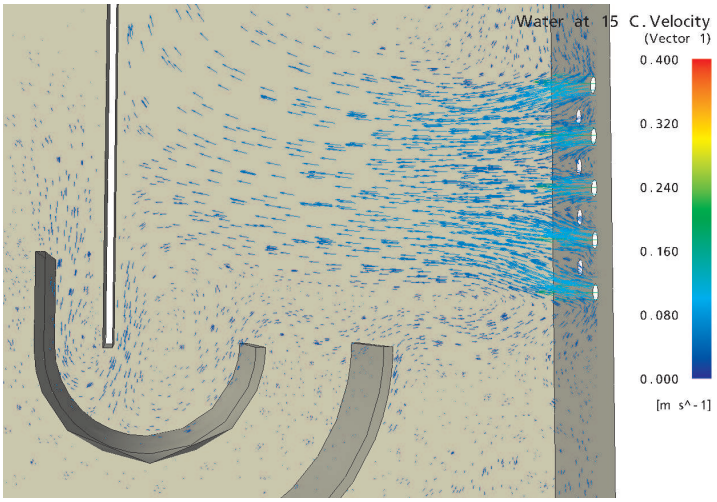

Figure 5.27 Vector plot showing velocity vectors in a horizontal plane in $1.0m$ depth, intersecting the upper row of additional circular inlets during numerical test of inlet configuration 3.

The vector plot in figure 5.27 is shown for $1.0m$ depth, intersecting the upper row of additional circular inlets. When comparing figure 5.27 with figure 5.23 it appears like the flow in configuration 3 has a greater tendency to be directed in the opposite direction as the normal flow direction. This is in general not wanted, since the sludge in this direction has a shorter way to the outlet, with a thereby derived higher risk of short-circuiting. The middle wall and the baffles at the end turn do however take a lot of the energy out of the water before it reaches the end of the middle wall, which is probably why the overall flow does not show tendencies towards short-circuiting (Figure 5.28).

Figure 5.28 show that the flow velocity is very low in most parts of the tank at a point of time corresponding to the end of investigation 2. Compared with the model of the existing conditions, a considerable decrease in flow velocity is obtained, like in the case of inlet configuration 2. The reduction in flow velocities does like in the preceding two alternative configurations have a positive effect on the separation of sludge (Figure 5.29)

The modelled sludge concentration is seen to qualitatively be of the same order of magnitude as in the case of the additional rectangular inlet. Again a significant improvement is obtained at the straight run opposite to the inlet holes, whereas the sedimentation is moderately worsened in the vicinity of the new inlet holes.

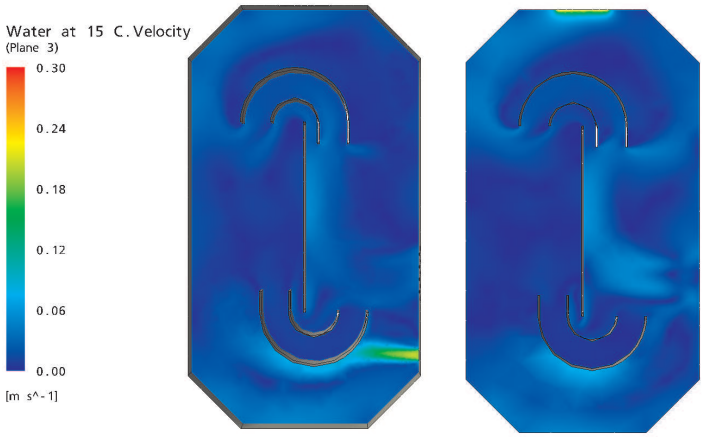

Figure 5.28 Flow velocities at inlet configuration 3. The flow velocities are shown for a point in time corresponding to the end of investigation 2. The left plot is made in $3.0m$ depth, whereas the right plot is made in $0.1m$ depth.

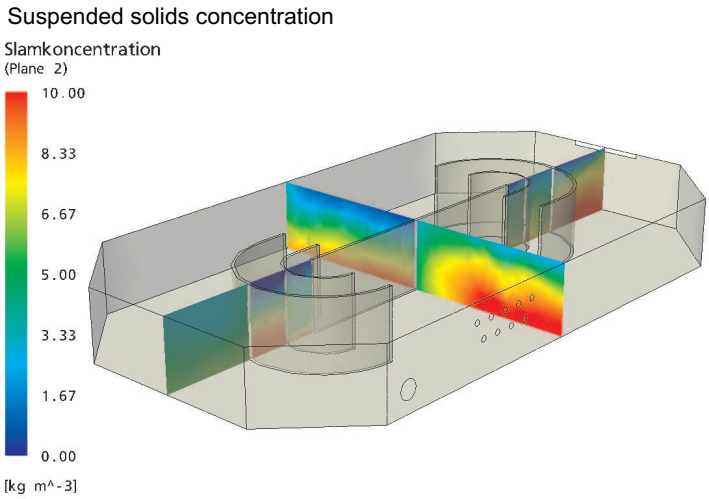

Figure 5.29 Modelled sludge concentration in the tank at inlet configuration 3. The plot is created at a time step corresponding to the end of investigation 2.

5.1.6 Summary

With basis in a measurement campaign performed on Bjergmarken Wastewater Treatment Plant in 2001, a numerical model of a process tank in ATS sedimentation operation has been constructed. The model was calibrated and validated satisfactory to two different parts of the measurement campaign. From the modelling of the existing conditions in the process tank it was in compliance with the measurements concluded that the sedimentation was poor during ATS-operation of the tank. Part of the reason for this probably originates from high circulating velocities in the tank. This was both confirmed by the measurements and the model. The circulating flow condition is mainly governed by the jet of the inlet between the two neighbouring tanks.

In order to solve the problems with unwanted high circulating velocities, numerical computations on three different retrofitted inlet configurations were performed by request of Krüger A/S. All three investigated solutions included the addition of extra inlet holes in the dividing wall between the two tanks. The idea was to increase the effective area of the inlet, and thereby lower the velocities in the inlets. As expected the numerical investigations with the alternative inlet configurations showed decreased flow velocities and improved sedimentation in the tank.

Inlet configuration 1, where an extra circular inlet identical to the existing inlet is implemented above the existing inlet, resulted in the most homogeneous distribution of suspended solids concentrations in the tank. There was however still tendencies towards recirculation in the tank with this configuration.

Inlet configuration 2 and 3 both slowed down the flow circulation in the tank significantly, which resulted in improved sedimentation in large parts of the tank. The areas in vicinity of the new inlet holes did however show worsened sedimentation conditions due to the extra induced momentum from the additional inlet jets. From a practical and economical point of view, configuration 2 seems attractive, since this solution involves an cutting in the wall near the surface of the tank. The implementation of solution 3 would involve operation beneath the normal sludge surface of the tank, which would complicate the process and might even demand an emptying of the tank.

The present numerical simulations are performed on the basis of a concentration and turbulence dependent sedimentation model. The sedimentation model and its incoming parameters is set up on basis in former comprehensive measurements performed on sludge from Aalborg East Wastewater Treatment Plant (Subsection 4.4.1). The initial sedimentation velocity, an important incoming parameter in the sedimentation model, was however estimated from cylinder glass experiments performed on Bjergmarken Wastewater Treatment Plant in 2004. The sludge characteristics are assumed to be somewhat different from plant to plant, and also in time on a given plant, resulting in uncertainties connected to the applied sedimentation model. It is however assessed that the application of the sedimentation model in general results in a strengthening of the model with respect to modelling the sedimentation in detail. Due to the above-mentioned uncertainties in the sedimentation model, the numerical results must in general be quantified as qualitative rather than quantitative. The model is believed to be sufficiently accurate to quantify if the given alternative configurations will result in either improvements or worsening of the flow conditions in the tank.

The model does not include contraction of the inlet jet. Even though the measurements in P1 indicate contraction, it is uncertain to what extend the contraction is occurring. Any contraction would result in a decreased effective area of the inlet, with resulting higher inlet velocities and higher circulating velocities in the tank.

5.2 Case study 2: Hals WWTP

Case study 2 includes the modelling of an OCO-tank, a design which at the same time utilizes anaerobic, anoxic and aerobic zones in the process tank. The investigations of the OCO process tank at Hals Central Wastewater Treatment Plant involve the coupling of a three-phase multifluid model with a simplified model for the microbial oxygen uptake during turnover of organic matter and nitrogen.

The concept of the OCO-tank results in complex flow structures, where the tank constantly alternates between aerobic and anoxic conditions through a predefined process cycle. The strongly varying flow conditions and switching of anoxic and aerobic conditions makes the process tank at Hals Central Wastewater Treatment Plant a challenging case for testing the model concept with respect to both the comprehensive flow model and the simple biological model.

In short, the purpose of the present model is to simulate the dynamics of the flow conditions and oxygen concentrations in the OCO-tank. The purpose of the model will be to obtain detailed information of these properties within a few process cycles, rather than less detailed modelling over a range of e.g. several sludge ages. The inner part of the process tank is occupied by an anaerobic zone, where the sludge passes through before it enters the remainder of the tank. Since the conditions in this part of the tank are much more static than in the following anoxic and aerobic zones, it is chosen not to model this zone.

In order to capture the dynamic behaviour of the hydrodynamics and biological conditions of the OCO-tank, detailed transient modelling over at least a couple of process cycles is necessary. In a multifluid configuration this can be very time consuming due to long computational times. To put things in perspective, the modelling of one process cycle (one hour in real-time), took three weeks on a pentium 4, 2.4GHz pc with 1Gb RAM internal memory. I.e. fine-tuning of the model is nearly impossible within a reasonable time frame - even for a Ph.D. project. Even though some of the computations have been performed on up to five pc's in parallel run, calibration is not an easy task. Thus, other set of calibration constants than the ones found in the present analysis could possibly be found.

5.2.1 Presentation of location

Hals Central Wastewater Treatment Plant is located just East of the small town, Hals, at the Eastern mouth of the Limfjord in the Northern Part of Jutland (Figure 5.30).

The town of Hals is occupied by approximately 2300 inhabitants, delivering domestic wastewater to the WWTP. Beside the wastewater originating from the city of Hals, wastewater is pumped into the plant from small towns in the catchment area of Hals Municipality. Since the coastal area of the municipality is built-up with summer houses, the load to the plant varies over the year. Sporadic locations of industry are present in the area. The daily flow and loads of nutrients and organic matter in 2001, can be viewed in Table 5.1.

The wastewater treatment plant in Hals is of the MBNDC-type, i.e. mechanical treatment, heterotrophic biological turnover of organic matter, removal of Nitrogen by nitrification and denitrification and chemical precipitation of Phosphorous and also biological Phosphorous removal are present on the plant. The process flow from inlet of wastewater to outlet of cleaned water is illustrated in figure 5.31.

As indicated on figure 5.31, the main flow of substances goes from the inlet through mechanical drum screens and sand and grease traps through the biological stage with two OCO-units, and

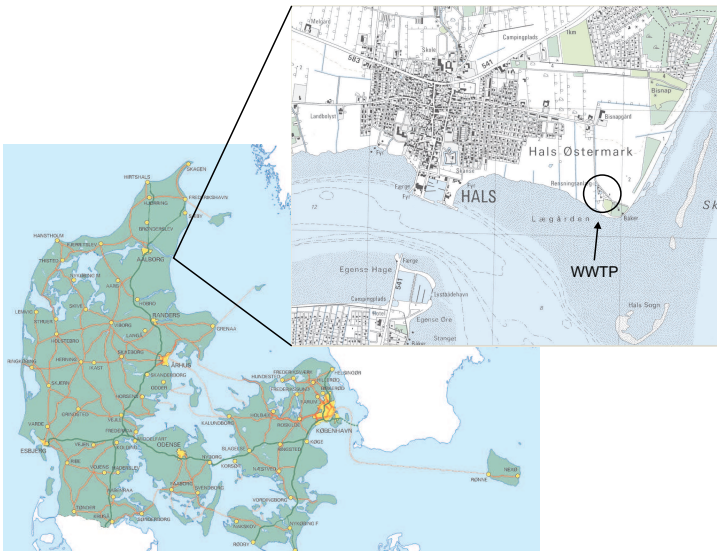

Figure 5.30 Map showing the location of Hals in Northern Jutland.

Table 5.1 Daily inflow and loads of nutrients and organic matter on Hals Central Wastewater Treatment Plant (Pedersen, 2001).

Parameter	*Value*
Daily inflow of wastewater	2250 $m^3 \cdot d^{-1}$
Daily BOD load	395 $kg\ BOD \cdot d^{-1}$
Daily Nitrogen load	85 $kg\ N \cdot d^{-1}$
Daily Phosphorous load	16 $kg\ P \cdot d^{-1}$

further through a settling unit before the clean water is disposed in the Limfjord. Departs from the mean flow of substances are present where surplus products like screenings, sand, grease and sludge are taken out of the system. Below photos of some of the operational units are presented (Figure 5.32, 5.33, 5.34 and 5.35).

As mentioned above, the OCO tanks illustrated by the photos in figure 5.34 and 5.35 are responsible for the biological removal of organic matter and nutrients. The OCO-tank is subject to the investigations in the remainder of this chapter.

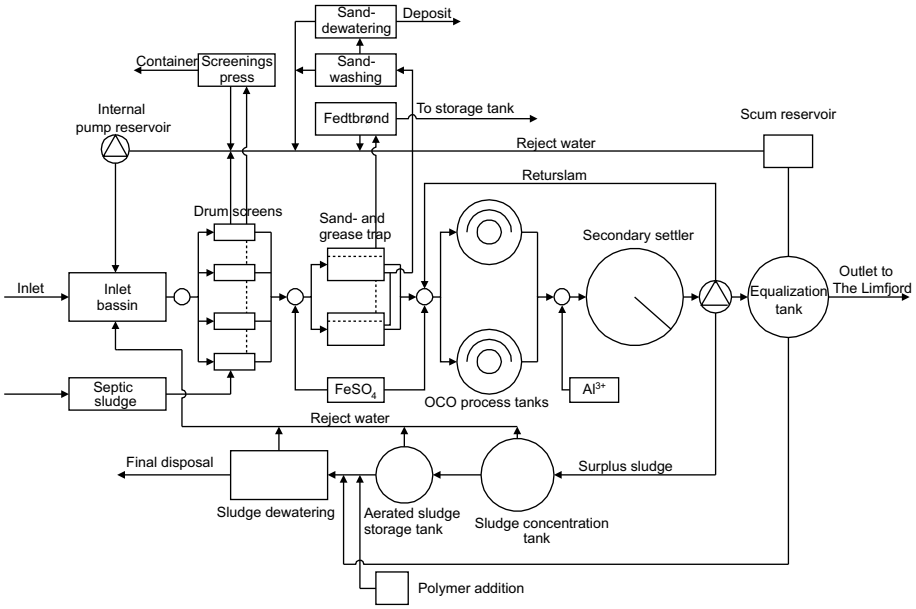

Figure 5.31 Outline of the flow of processes at Hals Central Wastewater Treatment Plant.

Figure 5.32 Drum screens at Hals Central Wastewater Treatment Plant.

Figure 5.33 Sand and grease trap at Hals Central Wastewater Treatment Plant.

Figure 5.34 Overview of the to OCO biological removal tanks at Hals Central Wastewater Treatment Plant.

Figure 5.35 Outlet weir of the OCO-tank at Hals Central Wastewater Treatment Plant.

5.2.2 The OCO-process tank

The layout of the OCO-tank makes it possible to have a number of different microbiological conditions occurring at the same time in the tank. The layout of the tank is illustrated in figure 5.36.

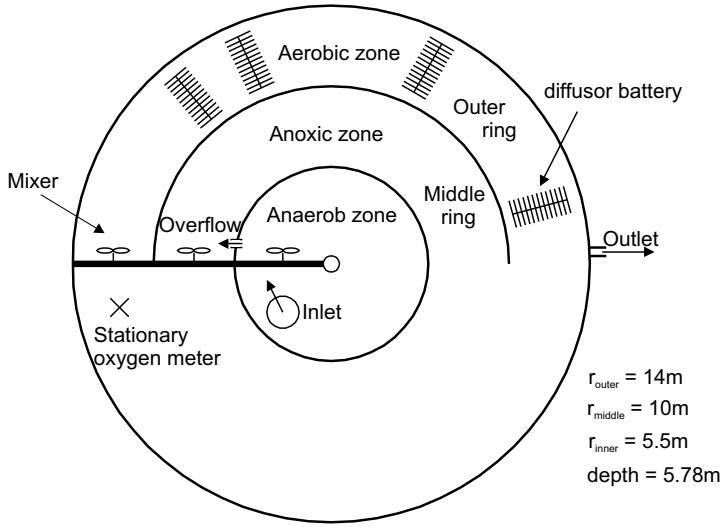

Figure 5.36 Layout of the OCO-tank.

From figure 5.36 it is apparent that the OCO-tank has been named from its design, consisting of two circles enclosing a half-moon shaped internal wall. The inner part of the OCO-tank is occupied by an anaerobic zone. When the wastewater is conveyed to the OCO-tank together with recirculated sludge from the settling unit, it is led through the inlet in the bottom of the inner cylinder. Since the inner cylinder is anaerobic, the main process occurring in this zone is hydrolysis. During the hydrolysis, readily biodegradable organic compounds are formed, resulting in increased reaction rates for the processes occurring in the remainder of the tank. Especially the denitrification process is dependent on sufficient availability of readily biodegradable material, in order to work properly. Beside hydrolysis, also denitrification and bio-P bacteria taking up storage of readily biodegradable substrate during release of orthophosphate can occur in the anaerobic inner zone of the tank. Due to the relatively constant biological conditions in this zone, the anaerobic zone is not very interesting from a modelling perspective. Under the act of gravity the mixture of sludge and wastewater is led from the anaerobic zone to the zone inside the internal half-moon shaped wall. This zone will be named the *middle ring*. During the main part of a process cycle, the middle ring is kept anoxic, hence nitrate will be reduced to free dinitrogen by the act of denitrifying heterotrophic biomass. Since air diffusers are mounted to the bottom of the outer ring, this zone will be working as an aerobic zone when the diffusers are active (Figure 5.37).

During the aerobic conditions, biodegradable organic material is turned over by heterotrophic biomass, while nitrificating autotrophic biomass is oxidating ammonium to nitrate. From the outer ring sludge is displaced to the settler by a weir under the act of gravity. Obviously the air

Figure 5.37 Part of the outer ring of the OCO tank during aeration.

diffusers play a main role in controlling the processes occurring in the tank, but also the mixers are key elements in this sense. By switching on and off the mixers, the mixing between the aerobic and anoxic zone can be controlled. The interplay between aerators and mixers is illustrated in figure 5.38.

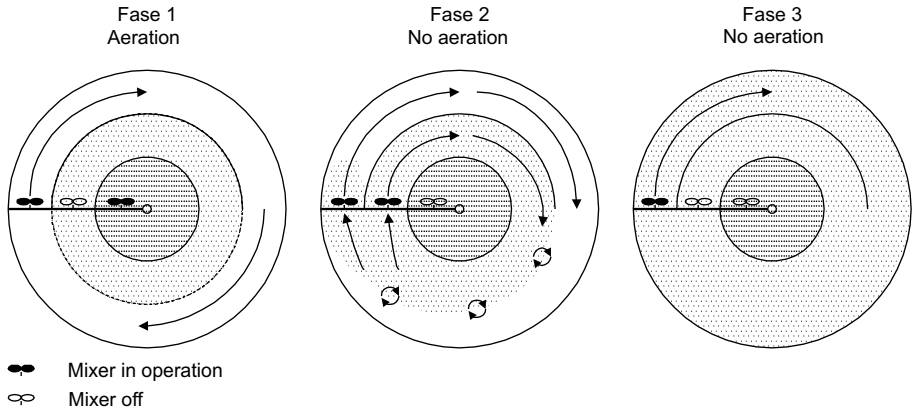

Figure 5.38 Layout of the principle functions of the OCO-tank. The hatching illustrate the level of oxygen in the tank, where non-hatched areas are aerated zones, mildly hatched areas are anoxic zones and densely hatched areas are anaerobic zones

During aeration (Phase 1 in figure 5.38), the mixer in the outer ring is active, while the mixer in the middle ring is turned off. This operational mode minimizes the mixing between the aerobic zone and the anoxic zone, making both nitrification and denitrification possible at the same time. Immediately after the aeration is turned off, the mixer in the middle ring is switched on (Phase 2 in figure 5.38). In this way sludge from the two zones are mixed, and amongst

others, nitrificated sludge is delivered to the middle anoxic ring while the more ammonium rich sludge is conveyed to the outer ring. In the last phase of a process cycle, only the outer mixer is turned on while aeration is turned of, ensuring anoxic conditions in the whole of the tank (Phase 3 in figure 5.38). At Hals WWTP the length of one process cycle going through all three phases is approximately one hour, after which the process cycle is restarted. All though not important to the present modelling of the processes occurring from the middle ring and out, it should be mentioned that the two mixers located in the inner anaerobic zone on figure 5.38 are turned on and off intermittently in order to insure mixing of the anaerobic sludge. The mixers in the middle and outer ring are identical to the slow rotating propeller investigated in chapter 4, while the two mixer located in the anaerobic zone are smaller fast rotating mixers.

The air going through the air diffusers are delivered from two separate blowers; an Aerzner GM-30-L/DN 150 (Blower 1) and an Aerzner GMA-12.6 (Blower 2). Blower 1 can operate in two settings at two different aeration intensities. Dependent on which of the settings it is operated at, it can deliver 14.7 or 19.8 $m^3\ air \cdot min^{-1}$ at a back-pressure of 0.6 bar. Blower 2 has one setting, where it can deliver 19.5 $m^3\ air \cdot min^{-1}$ at 0.6 bar. Each of the diffusor batteries illustrated in figure 5.36 is consistent of diffusor elements at which the air is diffused through oblong fine pored flexible rubber membranes. The controlling strategy of the air blowers is based on a mix of the length of the operational period and the measured level of oxygen saturation. From the point when aeration starts, the aeration is continued until a set point of 22.5% oxygen saturation is reached. In order to reach that point, several aeration steps with increasing aeration intensity are passed:

1. First 7 minutes: Blower 1 at low intensity
2. Next 8 minutes: Blower 2
3. Next 9 minutes: Blower 1 at high intensity
4. Next 10 minutes: Blower 1 at low intensity and blower 2
5. Until the set point is reached: Blower 1 at high intensity and blower 2

During the measurements in 2002 (Kunnerup *et al.*, 2002), no higher level than aeration level 3 was observed. A typical process cycle as observed during measurements at the plant in 2002 is listed below:

- 00.00: Outer ring mixer is turned on
- 00:09: Aeration (Level 1) is turned on
- 00:16 Aeration (Level 2) is turned on
- 00:23 Mixers in anaerobic zone is turned on
- 00:24 Aeration (Level 3) is turned on
- 00:31 Upper oxygen set point reached - aeration turned off
- 00:31 Middle ring mixer is turned on

- 00:37 Lower oxygen set point is reached - 10 minutes to switch-off of middle ring mixer
- 00:38 Mixers in anaerobic zone is turned off
- 00:47 Middle ring mixer is turned off
- 00:57 Outer ring mixer is turned off
- 00:59 Outer ring mixer is turned on
- —— The process cycle is restarted

The length of the process cycle may differ from the above-mentioned dependent on the time it takes to aerate before upper set point is reached, and the time it takes to reach lower set point after aeration is discontinued.

5.2.3 Data collection

During the period of April 30th to May 7th 2002, an intensive measurement campaign was performed at Hals Central WWTP (Kunnerup *et al.*, 2002). The measurement campaign that forms the basis for the calibration of the numerical model will be briefly described in this section. The measurements consisted of both point measurements across selected cross sections and time series measured over typically a couple of process cycles. Only the measured time series will be applied in the present discussion.

The measured time series parameters are:

- Flow velocities
- Oxygen concentrations

The flow velocities were measured as 1 minute averages, obtained by the use of a small OTT impeller (Figure 5.39).

Figure 5.39 OTT impeller used for the measurements of time-averaged flow velocities. From: (Kunnerup *et al.*, 2002).

The oxygen concentrations were measured with an oxygen electrode (YSI model 58).

When the results of the measurements are displayed below, a small thumbnail beside the figure will indicate the location at which the time series has been performed.

Presentation of measured time series

Time series of flow velocities were performed at 4 different positions in the OCO-tank (Figure 5.40).

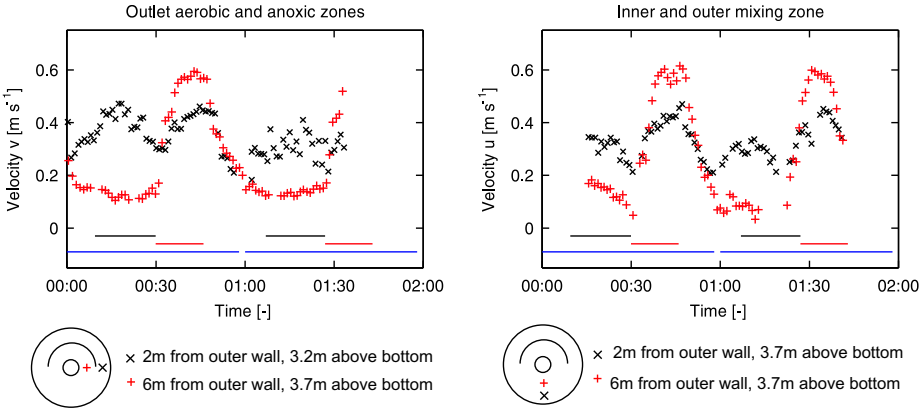

Figure 5.40 Time series of the measured velocities in the OCO-tank during two process cycles on Hals WWTP. (——) indicates when the aeration is turned on, (——) indicates when the mixer in the middle ring is turned on and (——) illustrates when the mixer in the outer ring is turned on.

As indicated in figure 5.40, the flow velocities are strongly dependable of the operational mode of the mixers. When the mixer in the middle ring is operational, the measured flow obtained from positions inside the middle ring are accelerated up to flow velocities of a factor 5-6 higher than the base flow originating from the outer mixer. Also the measured flow velocities obtained in the outer positions are higher when the impeller in the middle ring is turned on. When the aeration is turned on, the flow velocities also increase, and strong fluctuations are occurring at the outer position closest to the diffuser batteries. The increment in flow velocities during periods of aeration is caused by the secondary flow generated by the injection of air bubbles.

The measured time series of dissolved oxygen concentrations and the read outs of the stationary oxygen meter is shown in figure 5.41. As expected, the oxygen concentrations in the positions located in the outer parts of the tank start to increase shortly after the aeration is turned on (Figure 5.41). In the anoxic zone inside the internal wall bounding the middle ring, the increase in oxygen concentration is however delayed considerable compared to the outer positions. The concentration in this position slowly starts to built up halfway through the aeration process. After the aeration is stopped and the mixer inside the internal wall is turned on, the oxygen concentration increases rapidly to its maximum due to the mixing with more oxygen rich sludge.

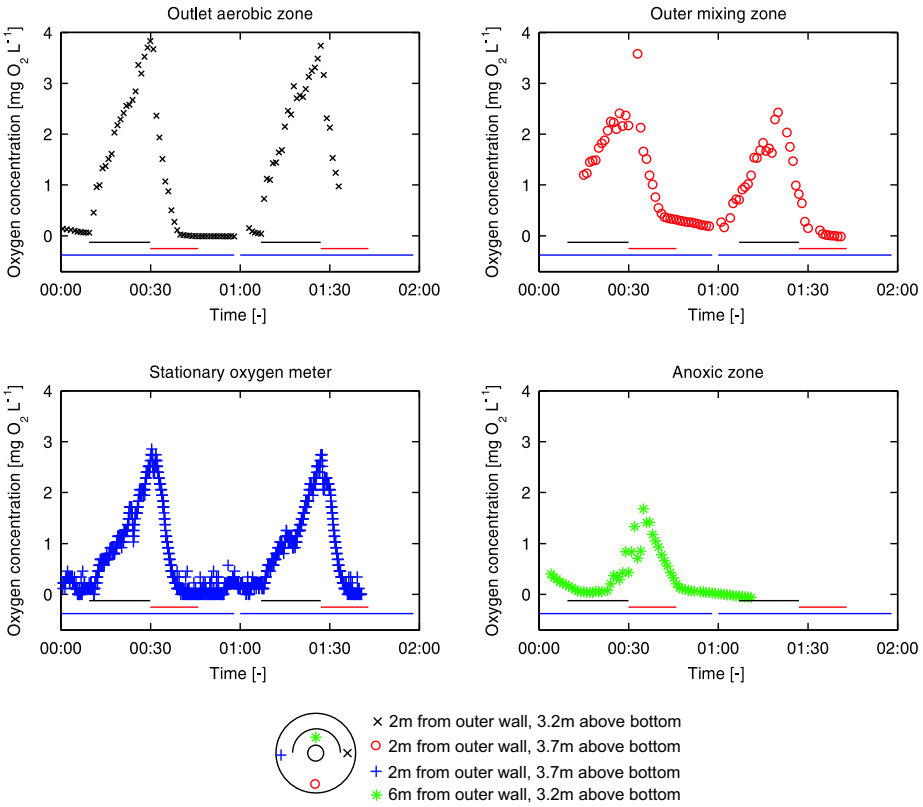

Figure 5.41 Time series of the measured oxygen concentrations and the read out of the stationary oxygen meter during two process cycles in the OCO-tank at Hals WWTP. (——) indicates when the aeration is turned on, (——) indicates when the mixer in the middle ring is turned on and (——) illustrates when the mixer in the outer ring is turned on.

5.2.4 Numerical model

Compared to the numerical two-phase CFD-model applied for the Bjergmarken case, the present model involves the solution for one more phase; the bubble phase. The features of the numerical model applied in the present chapter are listed below:

- 3-dimensional three-phase multifluid model, solving the Navier-Stokes equations for all three phases
- The Shear Stress Transport (SST) turbulence modelling
- The sedimentation of sludge is governed by settling velocity expression as derived by (Rasmussen and Larsen, 1996)
- The model describing the bubble phase and the interactions between this phase and the other phases are identical with model described in section 4.1

- A simple model describing the oxygen concentration in the tank as a function of reoxygenation and a bulk model for the turnover of oxygen originated from nitrification of ammonium and biological turnover of biodegradable organic matter, has been integrated into the CFD-model
- An altered viscosity of the suspension, expressing the result from the measurements on Aalborg East sludge
- The mixer model described in section 4.2 is applied
- Boundary and initial conditions are based upon data from measurements on the plant and estimations from the literature

The multifluid model, solving the interactions between the continuous water phase and the disperse phases, sludge flocs and air bubbles, by the application of a set of Navier-Stokes equations for each phase, have been applied to the current flow problem. The multifluid model includes interfacial force interactions between the continuous phase and the disperse phases (For more details, see chapter 3). Due to the rotational properties of the flow in the OCO-tank, the Shear Stress Transport (SST) turbulence model has been applied (Chapter 3). Again, the settling model of (Rasmussen and Larsen, 1996) as applied in the preceding Bjergmarken WWTP case study has been used with the coefficients obtained at Aalborg East WWTP (Rasmussen, 1997). The model for the bubble plume in chapter 4 has been applied to the present model, ie. the Grace drag-model (Clift *et al.*, 1978) is used for describing the drag force between air bubbles and water phase. The oxygen uptake due to nitrification and microbial turnover of organic matter and also reoxygenation of the sludge has been modelled through a simple first-order expression for the reoxygenation, combined with a bulk Monod-like expression describing the bulk biological uptake of oxygen. As described in section 4.1, detailed modelling of the slowly rotating hydrofoil-shaped propellers utilized in the OCO-tank has been performed. In order to minimize computational times, the simplified and less computational demanding momentum source impeller model has been applied to the present OCO-tank model.

Optimally, the non-Newton rheology model presented in chapter 2 should have been applied to the present model of the OCO-tank. The rheological model was thought to be implemented through an expression for the viscosity, incorporated in the properties of the fluid specification for the continuous fluid, water. The chosen type of non-Newton rheological model do however apply the concept of a yield stress, making the viscosity go towards infinity for shear rates going towards zero. This particular property of the rheology model is believed to cause the numerical model to crash, possible due to instabilities when the shear rate is low in the tank. Even though a limiter ensuring that the value of the shear rate in the expression for the viscosity could not be too low was introduced, the problems seemed to sustain when applying the non-Newtonian model. From the measurements performed on sludge from Aalborg East Wastewater Treatment Plant, it is apparent that the viscosity of sludge is higher than the viscosity of water, especially at low shear rates. In order to account for the extra viscosity, it has been chosen to apply a constant dynamic viscosity of the continuous phase of $0.01 kg \cdot m^{-1} \cdot s^{-1}$. This value was estimated by the application of the non-Newton model of Aalborg East Wastewater Treatment Plant and the mean shear rate in the tank estimated from initial modelling. The chosen assumption of Newton sludge is an assumption compared to reality, where the sludge is believed to be of non-Newton nature. The rheology experiments conducted in the present work do however indicate that the

investigated activated sludge was only mildly non-Newtonian with a n coefficient close to unity. This partly justifies the assumption of applying Newtonian like properties to the sludge. Further investigations are suggested in order to obtain a better description of this sub-process.

Finally, the boundary- and initial conditions have as widely as possibly been determined from the available data from the plant. When no data have been present for a given input parameter, estimations have been made from experiences and literature values. The remainder of this section will describe the setup of the model in details.

Setup of numerical model

The following subsection describes the setup of the numerical model for the OCO-tank at Hals Central WWTP in details. The details of modelling the mixer, the air diffusers and the sedimentation will not explicitly pointed out. Instead the reader is referred to the previous chapter that deal with the modelling of these processes in detail.

Oxygen concentration modelling The concentration of soluble oxygen is modelled through an additional variable for which an additional differential equation describing the transport of the variable is solved. Hence, the advection-dispersion equation (3.11) is governing the transport of soluble oxygen.

As described in chapter 2 (Equation 2.9), the concentration of soluble oxygen is dependent on the reoxygenation originating from the air bubbles delivered by the air diffusers and the removal of oxygen due to microbial activity. A more detailed version of equation 2.9 is presented below:

$$\frac{dC_{O_2}}{dt} = K_L \cdot \frac{A}{V} \cdot \left(C_{O_{2,s}} - C_{O_2}\right) - r_{O_2} \cdot X_{SS} \cdot \frac{C_{O_2}}{K_{O_2} + C_{O_2}} \tag{5.2}$$

where K_L is the aeration parameter $[s^-]$, C_{O_2} and $C_{O_{2,s}}$ is concentration and saturation concentration of oxygen, respectively $[mg\ O_2 \cdot L^{-1}]$, r_{O_2} is a measured respiration rate $[g\ O_2 \cdot kg\ SS^{-1} \cdot s^{-1}]$, X_{SS} is the suspended solids concentration $[kg\ SS \cdot m^{-3}]$ and K_{O_2} is the saturation constant for oxygen $[mg\ O_2 \cdot L^{-1}]$. From oxygen uptake rate (OUR) laboratory experiments, the respiration rate was determined to 1.16E-3 $gO_2 \cdot kgSS^{-1} \cdot s^{-1}$ (Kunnerup *et al.*, 2002). Since the OUR experiments were performed under conditions without oxygen limitation, it has been chosen to correct the first-order expression for the removal of oxygen due to microbial activity with a Monod term, accounting for that type of limitation. At low oxygen concentrations the Monod term will approach zero. The value of the saturation constant, K_{O_2} has been set to 0.75 $[mg\ O_2 \cdot L^{-1}]$ on behalf of values from (Henze *et al.*, 1992).

Boundary conditions The wall boundary conditions are modelled as described in chapter 6, regarding the case of Bjergmarken WWTP.

Due to the air bubbles that inevitable will escape to the surrounding air through the *water* surface of the tank, a special formulation of this boundary has been applied. A special *degassing* boundary condition was setup to ensure that only the air bubbles would see the outlet, whereas the disperse sludge particles and the continuous water phase would see the upper surface as a normal free slip wall. When this boundary was applied, unwanted loss of sludge flocs to the surroundings could be avoided. The boundary was set up as a constant air-velocity outlet

boundary of 0.3 $[m \cdot s^{-1}]$ normal to the boundary for the air bubbles. The outlet velocities of water and sludge phases were set to zero and a free-slip boundary was applied for these phases, making the boundary frictionless.

The inlet of wastewater from the sand and grease trap and return sludge from the secondary settler is delivered to the OCO-tank through a 600mm diameter pipe. Due to pumping, the flow is not constant. No direct measurements of the flow through the inlet to either the plant itself or the OCO-tank were available. From measurements of the outlet flow, a diurnal variation was apparent. Due to the relatively short modelling period of only a couple of process cycles, it was chosen to model the inflow rate as constant. Because the energy connected to the inlet jet of sludge and wastewater is negligible compared to the energy delivered by the mixer and the aeration process, the neglect of inflow variation is believed a reasonable assumption with respect to the hydrodynamic impact on the system. The average daily flow through the WWTP was approximately 2,250 $m^3 \cdot d^{-1}$, but the two OCO-tanks were not evenly loaded. From suspended solids concentration differences in the two tanks, it was estimated that the flow to the investigated tank was approximately 1,050 $m^3 \cdot d^{-1}$. Since the flow of return sludge from the secondary settler was approximately of the size of the flow of wastewater, the total average flow to the tank has been estimated to 2,100 $m^3 \cdot d^{-1}$. Due to the mixing of wastewater with a low X_{SS} content and return sludge with a high X_{SS} concentration, it is estimated that the X_{SS} concentration in the inlet will be approximately 5.0 $kgX_{SS} \cdot m^{-3}$; roughly the same concentration as in the OCO-tank itself.

The boundary through the outlet weir is defined as an opening boundary with an applied atmospheric pressure, where water and sludge in principle can be freely transported both in and out of the boundary. A *pure* outlet boundary condition where only transport out is allowed and with an applied atmospheric pressure was also tested. When the normal pressure outlet boundary was applied, the model did however suffer from instabilities, making the solver diverge with a resulting breakdown. The change into an opening boundary stabilized the computation. The reason for this is probably due to the built in flexibility of the opening boundary that equalizes instabilities occurring in the model during start up.

The diffuser boundary has been constructed on basis of the blower operational scheme as described previously. The boundary has been defined as a fluid dependent inlet velocity boundary, with a constant velocity of 0.25 $m \cdot s^{-1}$ normal to the boundary, approximately corresponding to the rise velocity of a freely rising bubble in quiescent water (Clift *et al.*, 1978). For the two remaining phases, the flow velocity has been set to zero. The time dependent inlet of air has been controlled by varying the volume fraction of air, corresponding to the given flow of air delivered by the blower.

Initial conditions Initial conditions of flow velocities, the pressure distribution, the suspended solids and oxygen concentrations and turbulence parameters (k and ω) have been delivered to the model.

All flow velocities except the settling velocity of the sludge flocs have been initialized to zero. By applying a small initial velocity to the settling sludge flocs, which is also physical correct, the start up of the model is stabilized. If no form of energy or driving force is input to the system at start up, the solution might suffer from divergence, with a resulting solver break down. Also in order to stabilize the model at start up, an initial hydrostatic pressure distribution has been applied. The initial concentrations of oxygen and suspended solids has been set to 0,0 $mg\ O_2 \cdot L^{-1}$ and 4.6 $kg\ SS \cdot m^{-3}$, in accordance with the measured values. For k and ω values

of 1E-9 $m^2 \cdot s^{-3}$ and 1E-9 $[s^{-1}]$ has been applied. These values are low, but they quickly find their natural level when the computation is running.

Computational mesh The computational mesh has been constructed on the basis of an unstructured mesh of tetrahedrons with prismatic layers at the wall boundaries (Figure 5.42)

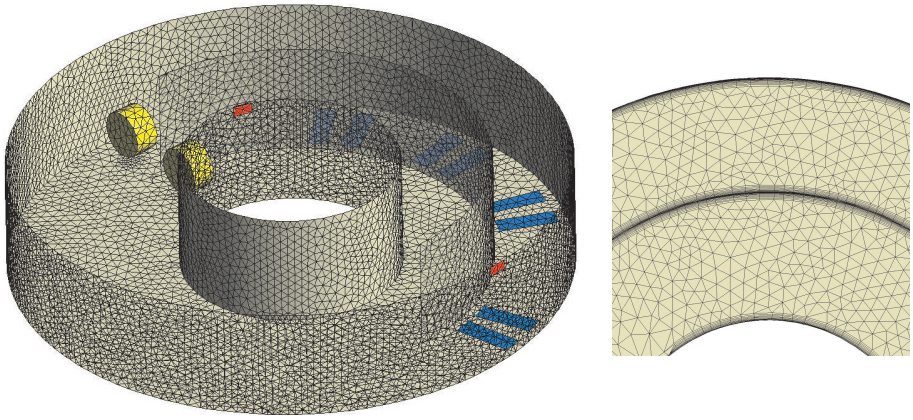

Figure 5.42 Computational mesh of the numerical model of the process tank at Hals Central WWTP.

The total number of cells for the present model of the OCO-tank was approximately 480,000. The blue rectangles on figure 5.42 indicate the diffuser batteries, whereas the red rectangles shows the in and outlets locations. The two yellow cylinders represent the subdomains in which the momentum model simulating the effect of the large slowly rotating hydrofoil-shaped propellers is applied. The right side of figure 5.42 shows a cutting of the tank across the middle and the outer ring. In order to resolve the flow at the wall, the mesh is refined with prismatic layers of cells close to the wall. As indicated on the figure the internal wall is surrounded by the prismatic layer on both sides. By making the internal wall a *thin surface* with zero thickness, a considerable amount of cells could be saved and a smoother mesh could be obtained.

5.2.5 Modelling results

The present section contains the numerical results of the model of the OCO-tank at Hals WWTP. Initially the calibration, where the model is compared to the results of the time series measurements, is presented.

Model calibration

Since the two mixers in the middle and outer ring are identical to the propeller investigated in chapter 4.2, the findings of that investigation were initially directly transferred to the model of the OCO-tank. It did however quickly turn out that the size of the terms in the momentum model from chapter 4.2 were too small compared to what was needed in the OCO-tank model. This could be caused by several factors:

- The OCO-tank model is run at an approximately 10 times higher dynamic viscosity
- The mixers do in average have to move a relatively larger volume of fluid
- Grid dependency

As the fluid that needs to be moved has a higher viscosity, a larger force has to be applied in order to create the same movement in the fluid.

Furthermore, the two propellers do in average have to move more fluid than was the case for the setup of the propeller in chapter 4.2, demanding for a larger momentum source.

Finally the momentum model might be grid dependent. Even though the grids in the two models have densities in the same order of magnitude, they are not totally identical. A grid analysis performed on the tank in a single phase configuration, showed that grid independency was approximately obtained at a total cell number of 800.000 for the OCO-tank. At 480,000 cells in the present model, grid dependency can not be entirely ruled out. Due to the massive computational effort already apparent at the current cell number, it has been chosen to change the parameters of the momentum model rather than performing a very time consuming grid dependency test.

The calibration of the momentum model was performed by scaling up the axial and tangential momentum terms by a factor of 6 compared to the results in chapter 4.2, obtaining the same proportionality between the axial and tangential component.

The aeration process was calibrated by fine-tuning the aeration parameter K_L until the right level in oxygen concentrations were obtained.

The biological oxygen uptake rate was not touched during the calibration, i.e. the value obtained from OUR experiments was applied.

Calibration results The modelled velocities appears to be overestimated for the time series obtained at the position immediately after the aeration zone and the position in the outer part of the mixing zone (Figure 5.43). Qualitatively, the modelled flow in the outlet of the aerobic zone captures the large fluctuations as observed during measurements. The overestimated flow velocities in the outer parts of the tank are probably caused by a combination of a too high flow generated by the outer impeller and a too high influence from the impeller inside the half-moon shaped wall.

At the measurement point at the outlet of the anoxic zone, the velocity peak caused by the operation of the inner propeller is well captured. The base flow is however slightly underestimated. Furthermore the acceleration and deceleration of the suspension is overestimated in the model.

For the time series in the inner part of the mixing zone, the peak values are underestimated, meanwhile the base flow is slightly overestimated.

From figure 5.44, the time series of oxygen concentrations appear to be reproduced fairly well. Modelled oxygen concentrations are slightly overestimated in the positions at the outlet of the aerobic zone and the outer part of the mixing zone, whereas it is slightly underestimated in the anoxic zone.

The calibration of the model has been performed with mixed success. It has not been possible to obtain an optimal relationship between the flow velocities in the outer and the middle ring of the process tank. In order to get a sufficiently high base flow in the middle ring, the momentum addition of the outer propeller had to be turned up at a level where the velocities in the outer ring

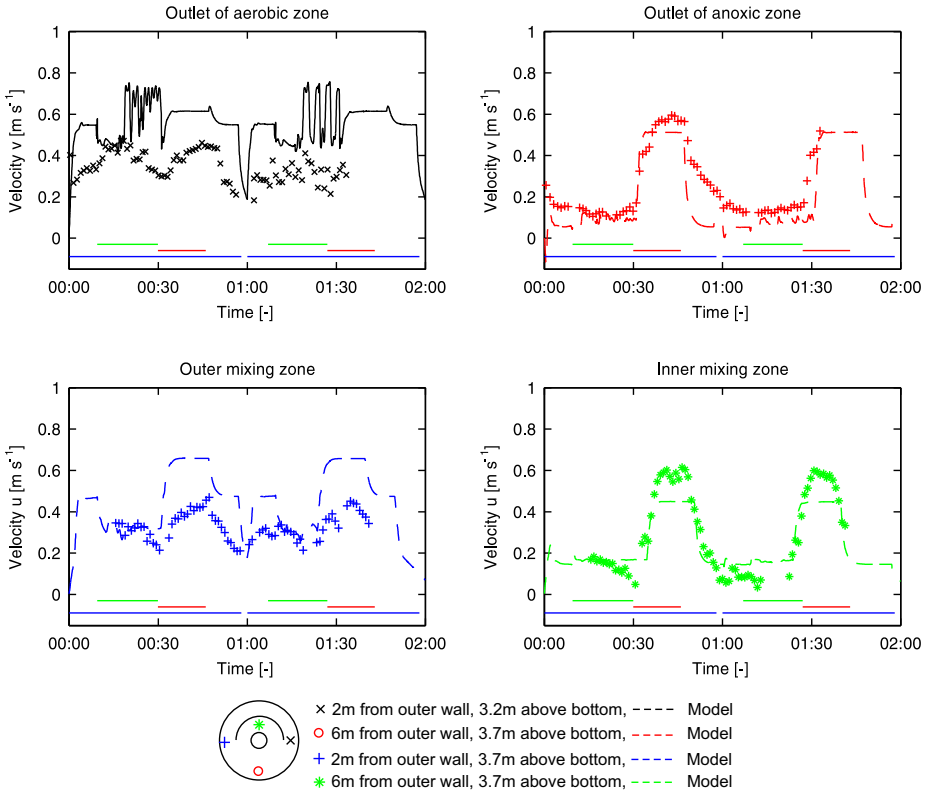

Figure 5.43 Comparisons of measured and modelled time series of flow velocities during two process cycles on Hals WWTP. (——) indicates when the aeration is turned on, (——) indicates when the mixer in the middle ring is turned on and (——) illustrates when the mixer in the outer ring is turned on.

became overestimated. Since the oxygen concentration in the anoxic zone is highly controlled by the inflow of aerated water from the outer ring, an underestimating of the base flow inside the middle ring would result in an underestimation of the oxygen concentration in the anoxic zone. Due to this issue, it has been chosen to continue with the present setup of the model.

Additional modelling results

In order to investigate the sub-processes and the functioning of the tank into further detail, the present subsection contains additional plots withdrawn from the model.

Flow properties During the process cycle, the hydrodynamics of the OCO-tank is highly governed by the action of the propellers. This is illustrated in slice plane plots of the flow velocities, showing the complete tank sliced through at a depth of $4m$ at different time steps in a process cycle (Figure 5.45).

At the start of a process cycle, the outer propeller is responsible for building up the flow in the outer *ring* of the OCO-tank. When the aeration starts the flow enter a more chaotic state

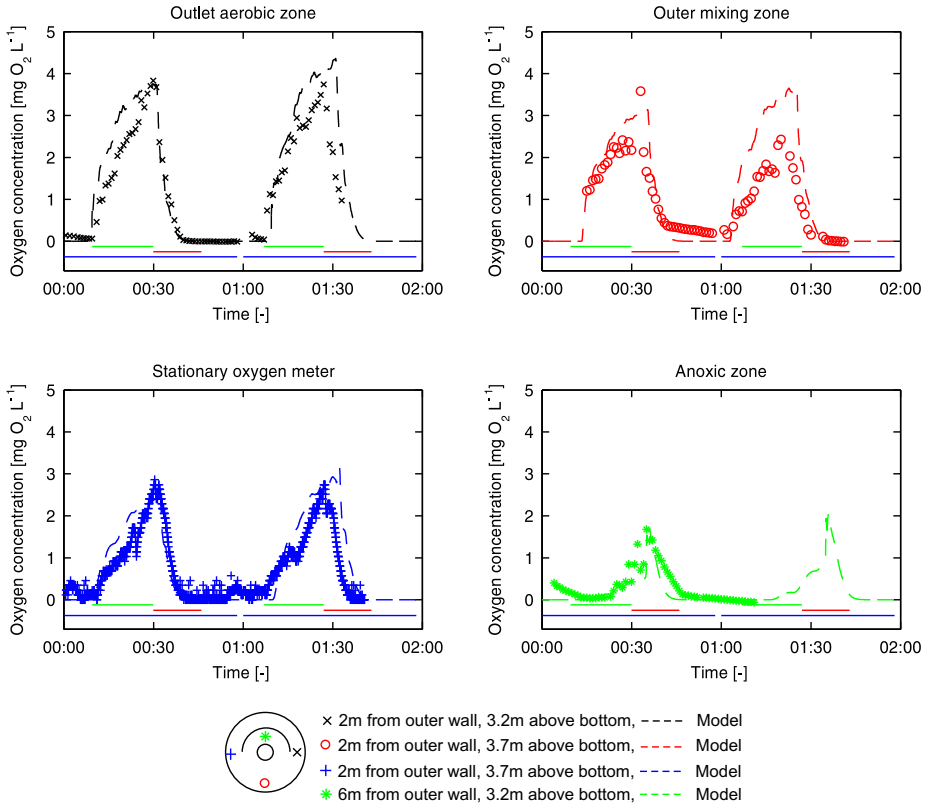

Figure 5.44 Comparisons of measured and modelled time series of the oxygen concentration during two process cycles in the OCO-tank at Hals WWTP. (———) indicates when the aeration is turned on, (———) indicates when the mixer in the middle ring is turned on and (———) illustrates when the mixer in the outer ring is turned on.

where mixing is enhanced. The enhanced mixing results in a slight break-through of aerated water into the anoxic zone towards the end of the aeration process. As the propeller in the middle ring is started immediately after the stop of the aeration, the flow velocities quickly equals out in the tank. At the end of the process cycle, the flow is decelerated in the whole of the tank, due to the temporary stopping of the outer propeller.

As indicated, the mixing zone, in the area where no internal wall is present, can during some parts of the process cycle be thought of as being composed of two isolated zones where only little exchange of e.g. flow is occurring. This is further illustrated in figure 5.46.

As shown in figure 5.46, a distinct zone differentiation exist between the inner and outer part of the mixing zone when only the outer propeller is turned on (Figure 5.46 left). When the propeller in the middle ring is turned on, the clear velocity gradient between the two zones is destroyed (Figure 5.46 right), substantiating the flows dependency upon the operation of the propellers in the tank.

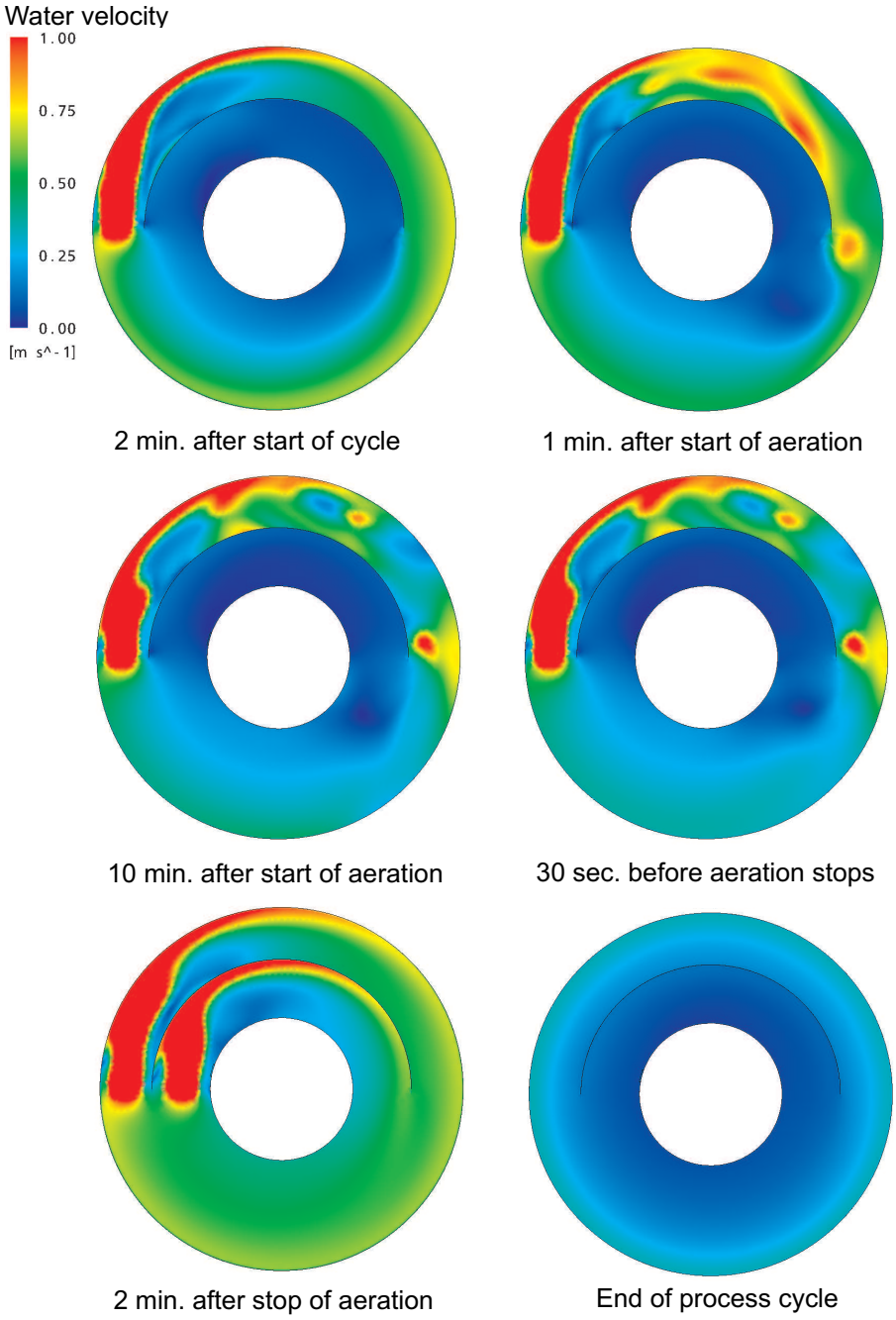

Figure 5.45 Plots of the distribution of water velocities at $4m$ depth at different time steps during a process cycle.

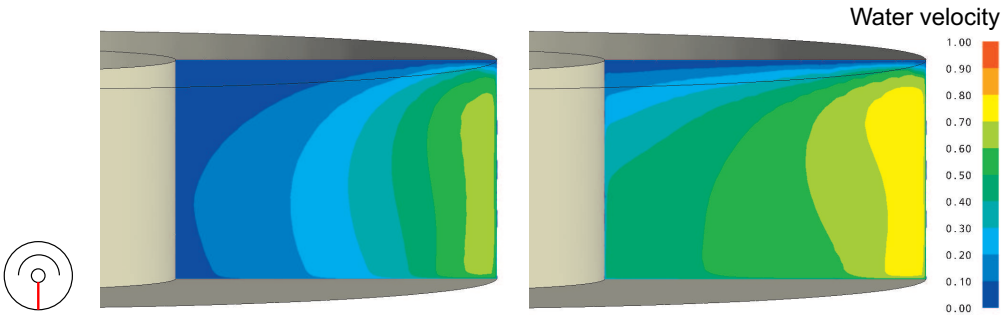

Figure 5.46 Iso surfaces of water velocities. Left: At beginning of aeration with only outer propeller operational. Right: $8min$ after stop of aeration, where both propellers are operational.

Transient behaviour of aeration process The aeration process occurring in the OCO-tank is of the same general type as for the diffuser investigated in chapter 4.1. The flow in the present case do however differ from the diffuser experiment in chapter 4.1 in some properties. The generated bubble plumes are in OCO-tank subject to a turbulent co-flow generated by the mixers, and also the secondary flows originating from the many closely spaced air-diffusers adds to the complexity of the flow. The above-listed properties of the flow in the OCO-tank results in a swirling complex movement of the bubble plume above the diffuser batteries (Figure 5.47). As indicated in figure 5.47, the volume fractions of air show a distinct transient variation, adding further to the mixing properties of the tank.

In order to quantify the mixing conditions in the OCO-tank, the concentration of soluble oxygen has been plotted at different time steps in a process cycle. As apparent in figure 5.48, the oxygen concentration distribution in the tank undergoes a distinct variation throughout the duration of the aeration process. The zone inside the internal half moon shaped wall remains anoxic throughout most of the aeration process. At the end of the aeration cycle, after approximately 15-20 minutes, oxygen rich water do however start to enter the anoxic zone. Immediately after the aeration is stopped, the mixer inside the internal wall is turn on, and almost immediate mixing of oxygen depleted and oxygen rich sludge occurs.

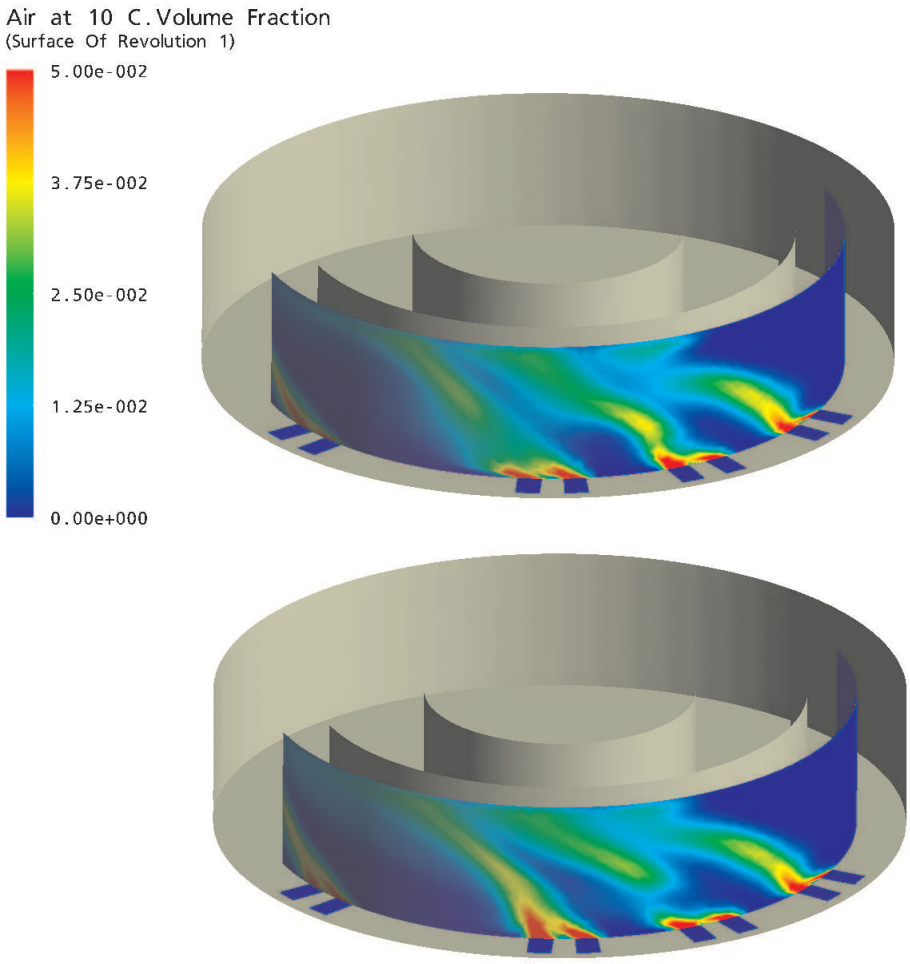

Figure 5.47 Volume fraction plot at two different time steps during the aeration process

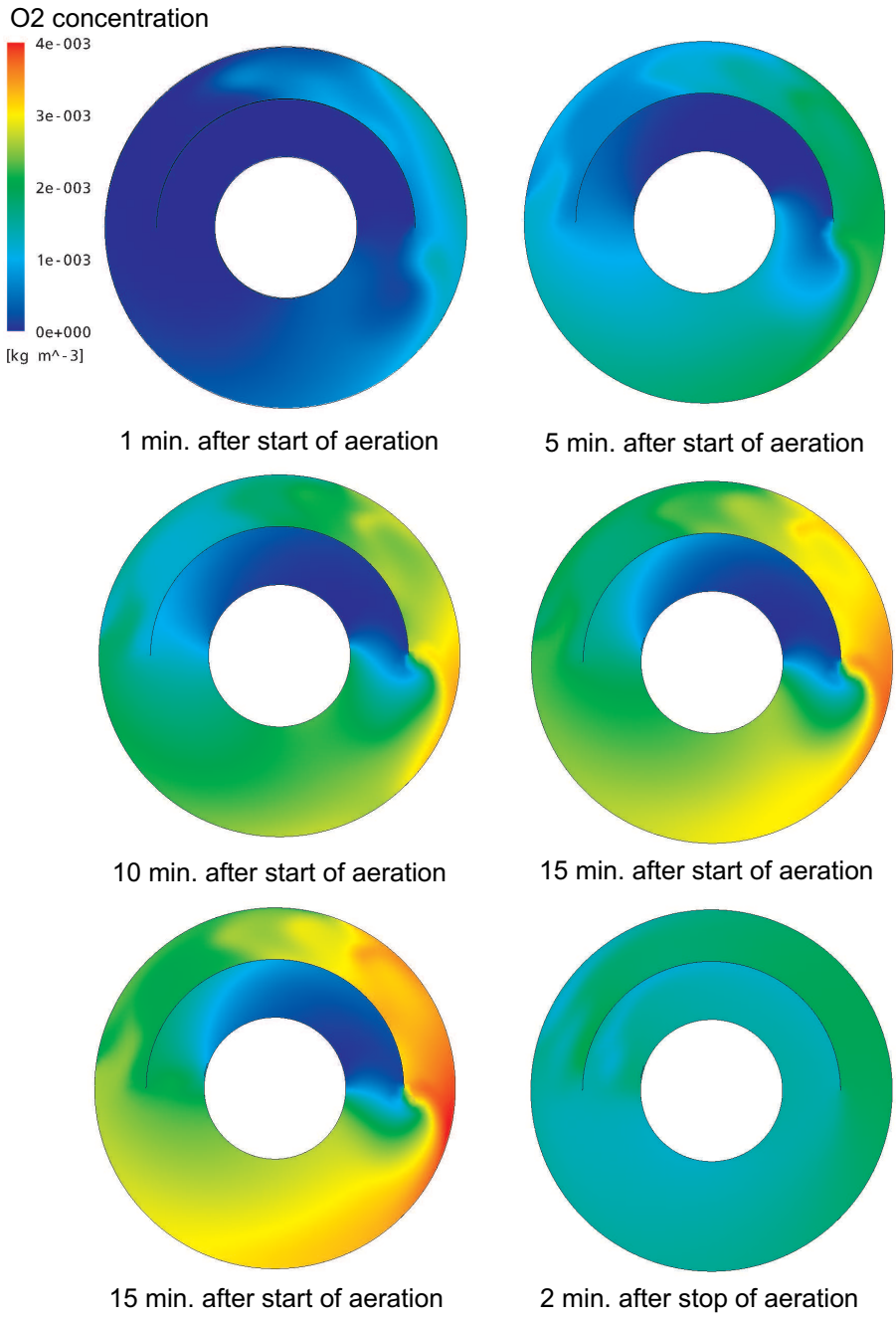

Figure 5.48 Plots of the distribution of soluble oxygen concentration at $3m$ depth at different time steps during the aeration process. The total duration of the aeration is $22min$

Sedimentation modelling The modelled suspended solids concentrations are in accordance with the observations on the plant in 2002 (Kunnerup *et al.*, 2002) nearly constant throughout the tank (Not shown here). The reason for the constant conditions with respect to the sludge concentration is to be found in the hydrodynamic conditions in the tank, where the main part of the tank is subject to agitation, and thereby conditions with high levels of shear in the majority of the time. The only place where stratification may appear is in the anoxic zone inside the internal wall. In this zone sedimentation of sludge may appear over several process cycles, and a balance may built up, where the sludge concentration is higher at the bottom of the tank. It is however believed that the built up of sludge will occur at a rate where more than the two operation cycles modelled in this investigation are necessary to say something about at what extent such a stratification may be apparent.

With the apparent almost constant concentration of the suspended solids concentration in mind, a disregarding of variations of the sludge concentration might seem a plausible solution, resulting in a possible reduction of the model from a three-phase to a two-phase model. Such a model reduction would result in less computational times and an increased stability of the model.

5.2.6 Summary

A three-phase model of one of the OCO-tanks at Hals Wastewater Treatment Plant, Denmark has been constructed. The model was calibrated against time series of flow velocities and oxygen concentrations measured in 2002 (Kunnerup *et al.*, 2002). The model showed good correlation between the measured and modelled soluble oxygen concentrations, whereas the compliance between the measured and modelled flow velocities was only partly satisfactory.

Like also indicated at the measurements in 2002, the suspended solids concentrations are only weakly varying throughout the tank during normal operation. This is not surprising since the OCO-tank almost constantly is subject to some kind of agitation. The almost completely mixed conditions with respect to suspended solids concentration raise questions whether the hydrodynamics could be approximated by a two-phase model regarding only the modelling of the water and bubble phase, and disregarding the modelling of the sludge phase. The two-phase model would reduce the computational effort and enhance the stability of the model.

Additional numerical investigations, as expected show that the flow in the tank is highly governed by the operational mode of the mixers, where especially the operation of the mixer in the middle ring determines whether or not a clear concentration gradient between the inner and outer part of the mixing zone will occur. When only the propeller in the outer ring is operational, the clear velocity gradient across the mixing zone assures that the anoxic zone will survive from the aerated zone, until the additional turbulence and built up of base flow originating from the aeration process slowly starts to induce mixing between the inner and outer zones. The application of a detailed hydrodynamic model clearly helps with additional understanding of the functioning of the OCO-tank.

5.3 Case study: ASM modelling at Frederikshavn central WWTP

The last case study involves the integration of the multiphase CFD-model with an enhanced biological model for the simulation of the biological processes occurring in the activated sludge. The background of the present case study is to combine the strength of the well-approved Activated Sludge Models with the detailed multiphase CFD-model, resulting in a powerful tool for a better understanding of the combined physical and biological behavior of a process tank. The resulting model is also meant to be a tool for optimization of non-ideal tanks, where assumptions of e.g. fully mixed conditions or plug flow are not realizable. The last case study in this work involves a process tank at Frederikshavn WWTP. Equipped with several diffuser batteries and a large mixer for keeping the sludge in suspension, it is fair to expect that the tank is fully mixed during operation. At least during aeration this assumption should be true. The results of the present study do however show that especially during periods where the aeration and mixing equipment is stopped, the tank is far from being fully mixed. More interestingly the results do also indicate that even during aeration periods, the fully mixed conditions are questionable.

One important aspect when applying a complex model like an Activated Sludge Model is proper model validation. Because a complex model often involves many unknown variables, such models can be hard to interpret, if sufficient data are not available for comparisons. For that reason one important demand for a proper case study, is the availability of a sufficient amount of data, in this case concentrations of nutrients, oxygen and suspended solids.

During the last years the Danish wastewater treatment plants has in general been subject to investments with respect to increased process control and optimization. One of the main means for this has been online measurements in the process tanks. Typically the process control is performed by turning on and off mixing equipment, aeration and chemical dosing with background in set points related to the online measurements. Such online measurements are well suited for comparisons with numerical models.

5.3.1 Presentation of location

The third case study involves an activated process tank at Frederikshavn Central Wastewater Treatment Plant. The plant is located in Frederikshavn, one of the larger cities (25,000 inhabitants) in the northern part of Jutland, Denmark (Figure 5.49).

The wastewater treatment plant is of the MBDNC type, where both mechanical, biological and chemical treatment is present, and the biological treatment include biological removal of organic matter, removal of Nitrogen by nitrification and denitrification and lastly biological removal of Phosphorous. The biological removal system comprise of two parallel removal units; an activated sludge unit and a biofilter unit. The flow of wastewater is split in half between the two units. A flow diagram of the processes in the WWTP is shown in figure (5.50).

The PE load on the plant was in 2004 114,000 $PE \cdot year^{-1}$, and the removal efficiencies of organic matter measured in COD, Suspended solids, Nitrogen and Phosphorous was 91, 97, 82 and 86$\%$, respectively.

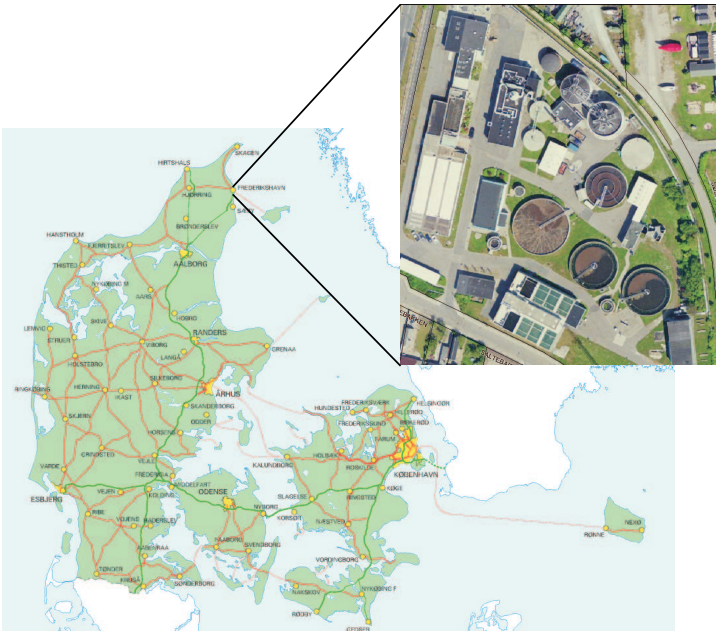

Figure 5.49 Map showing the location of Frederikshavn in Northern Jutland. The over layer shows an air photo of the structure of the wastewater treatment plant (Source: www.frederikshavn.dk).

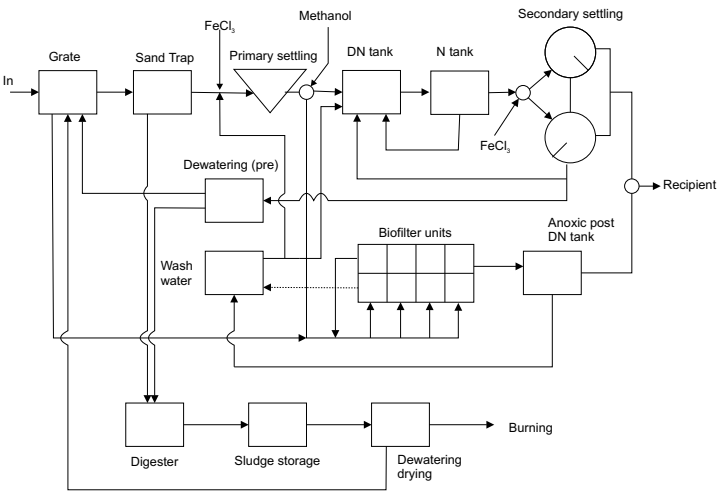

Figure 5.50 Flow diagram of the unit operations at Frederikshavn Central Wastewater Treatment Plant.

The unit operation in focus here is the aeration, or nitrification tank (Figure 5.51). At the plant in Frederikshavn, the aeration tank works in alternation. Hence, the mixing equipment and the aeration units are turned on and off on behalf of advanced process control. The operation of the tank is determined by set points relating to the signal of online sensors of O_2, NO_3^-, NH_4^+, S_S and PO_4^{-1}.

Figure 5.51 Picture showing part of the aeration tank at Frederikshavn Central WWTP during aeration.

The tank consists of 10 batteries of dish shaped air diffusors (total: 850 pieces), a slowly rotating three-bladed mixer and the above-mentioned online sensors (Figure 5.52). The mixer is manufactured by Lind Jensens Maskinfrabrik A/S (LJM).

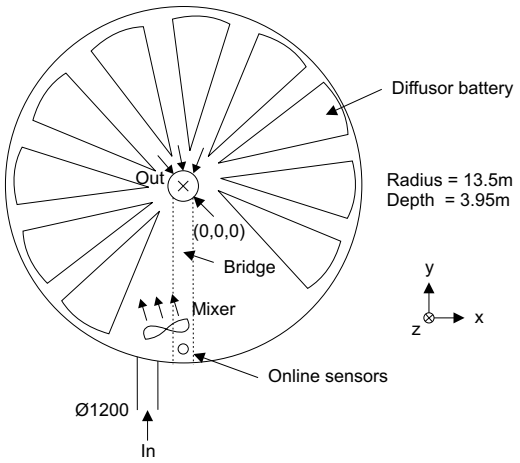

Figure 5.52 Outline of the investigated process tank at Frederikshavn Central Wastewater Treatment Plant.

Even though the tank is designed to be a nitrification tank, it works anoxic more than half the time of operation during normal dry weather conditions. In this way the over capacity of the

aeration equipment is used to obtain extra sedimentation capacity in the system. The changing cycle between aerobic and anoxic conditions, fully mixed and stratified conditions and the high energy contra low energy system, makes the process tank at Frederikshavn a complex system - and a challenging case study. In general the process cycle of the process tank is controlled via predefined responses to the signal of the online sensors indicated in figure 5.52.

5.3.2 Data collection

Beside the online measurements of O_2, NO_3^-, NH_4^+, S_S and PO_4^{-1} at the point at the surface of the tank (indicated on Figure 5.52), additional measurements were performed during the period: 2. -3. of August, 2005. During the measurement campaign flow velocities and oxygen concentrations were measured from the bridge on top of the tank (Figure 5.52). Since the bridge could not be moved due to the presence of the online sensors, only the area in vicinity of the bridge could be used for the measurements. From the bridge, time series of the flow velocities were measured at different depths and distances from the outer tank wall. Like in the case study of Hals Central Wastewater Treatment Plant, small OTT measurement impellers were applied for the measurements (Chapter 7). Also time series measurements of the oxygen concentration were performed just below the water surface. The additional oxygen concentration measurements were mainly performed at a distance of 10m from the outer wall, supplementing the stationary online oxygen measurements close to the outer wall. On August 3rd a monitoring of the sludge blanket position was performed during settling in a part of the cycle where neither mixing nor aeration were occurring. Details of the measurements can be viewed in detail in table 5.2. The coordinates of the measurement positions in the table are relative to the reference point in figure 5.52.

Table 5.2 Measured time series during the period 2. - 3. August 2005.

Date [−]	Ref. nr. [−]	Time [−]	Parameter [−]	Meas. position ($[m, m, m]$)
2. Aug. 2005	1	09:11 - 12:41	u	(0.0,-11.5,-1.0)
2. Aug. 2005	2	09:13 - 09:45	u	(0.0,-5.5,-2.0)
2. Aug. 2005	3	11:05 - 12:36	C_{O_2}	(0.0,-8.5,-0.2)
2. Aug. 2005	4	11:06 - 11:40	v	(0.0,-10.5,-1.0)
2. Aug. 2005	5	13:50 - 14:49	C_{O_2}	(0.0,-3.5,-0.2)
2. Aug. 2005	6	13:52 - 14:41	v	(0.0,-5.5,-1.0)
2. Aug. 2005	7	13:57 - 14:39	u	(0.0,-6.0,-1.0)
3. Aug. 2005	8	08:30 - 09:11	u	(0.0,-5.5,-2.0)
3. Aug. 2005	9	08:30 - 11:49	C_{O_2}	(0.0,-3.5,-0.2)
3. Aug. 2005	10	08:38 - 09:11	v	(0.0,-6.0,-2.0)
3. Aug. 2005	11	09:21 - 10:26	u	(0.0,-11.5,-2.0)
3. Aug. 2005	12	09:21 - 10:26	v	(0.0,-11.0,-2.0)
3. Aug. 2005	13	10:29 - 10:58	$Sludge\ blanket$	(0.0,-11.0,-2.0)
3. Aug. 2005	14	11:12 - 11:49	u	(0.0,-8.0,-2.0)
3. Aug. 2005	15	11:12 - 11:49	v	(0.0,-7.5,-2.0)

Measurement results

Below an example of the measurement data is shown in figure 5.53. The shown measurements correspond to the ones chosen as calibration and validation data for the CFD-model.

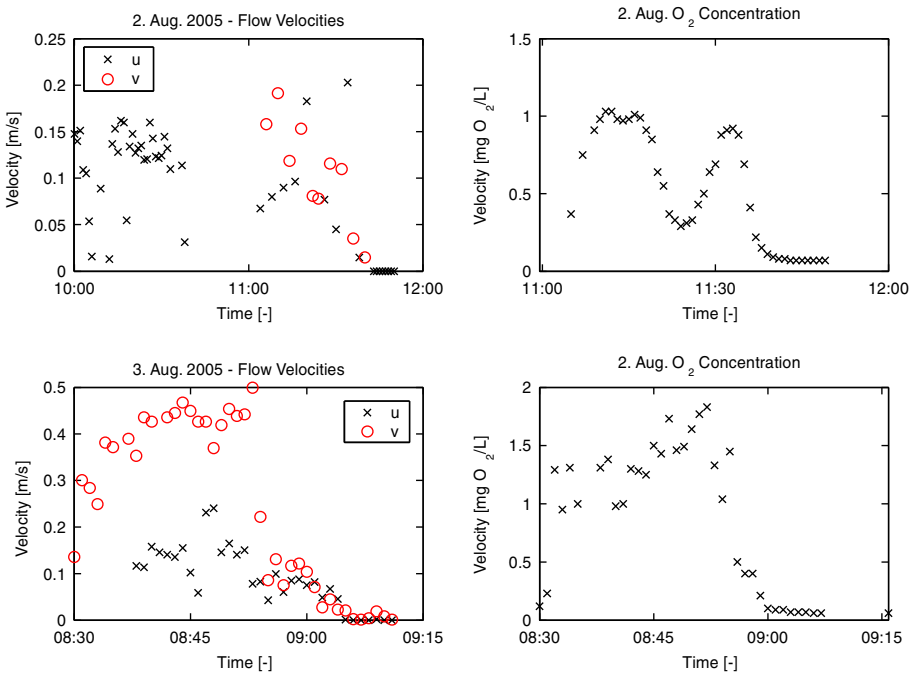

Figure 5.53 Data from the measurements at Frederikshavn Wastewater Treatment Plant in the period 2. August - 3. August 2005.

On the left top on figure 5.53, displaying the flow velocities on the late morning of August 2. 2005, a distinct variation in flow velocities can be seen as a function of time. In this particular period the mixer is turned on until approximately 10:38, after which it is turned off until the aeration is initiated at approximately 11:05. As a consequence of the mixer operation, the measured velocities are highest before approximately 10:40, after which they decrease fast until approximately 11:05 when the aeration and mixer is turned on. Due to the action of the mixer and the excessive secondary flow resulting from the bottom mounded air diffusors, the flow velocities increase again during aeration. Especially the velocity component v, perpendicular to, and away from the tank wall, pointing in direction towards the areas with air diffusors, seems to be dependent on these secondary flow effects. Naturally, the measured oxygen concentration increase rapidly as soon as the aeration begins (Top right of figure 5.53), whereas it due to the massive biological activity decreases almost immediately after shutdown of the aeration.

The example from August 3. 2005, is dominated of both aeration and mixing from the propeller from the beginning of the measurements (Figure 5.53 bottom left and right). The aeration stops at approximately 8:52, and the mixer stops shortly after. From this moment both flow velocities and oxygen concentration decreases rapidly. Again, especially the flow component v is

strongly influenced by the secondary flow originating from the diffusor.

Beside the above-mentioned measurements of flow velocities and oxygen concentrations, the location of the sludge blanket where estimated during one of the sedimentation phases of the aeration tank (Figure 5.54).

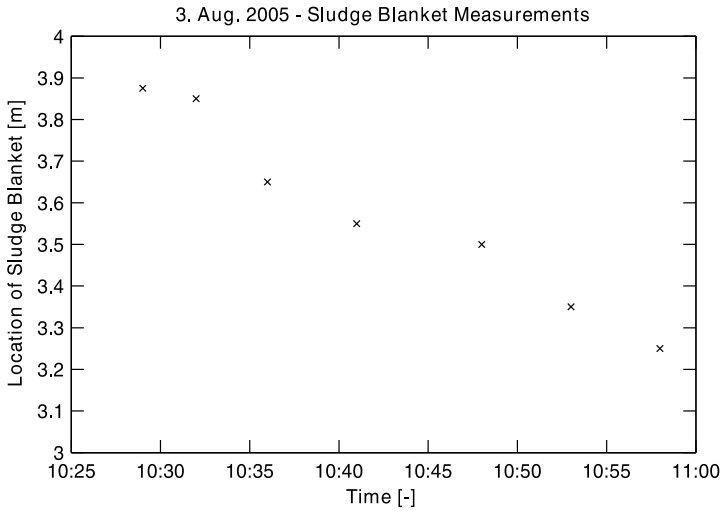

Figure 5.54 Sludge blanket position during measurements at Frederikshavn Wastewater Treatment Plant on August 3. 2005.

In the approximate period of 30 minutes with no aeration or stirring, the surface of the sludge blanket moved fairly linearly down to a distance of approximately 70cm below the water surface in the tank. At the approximate time of 11:05 aeration started again and the sedimentation process was consequently discontinued.

In order to further characterize the sedimentation properties of the sludge, additional investigations where performed in a cylinder shaped glass of 0.6m height and 10 cm diameter (Figure 5.55). The glass was filled to the 50cm mark with a sludge sample consisting of a suspended solids concentration of 4.9 $[kg\ S_S \cdot m^{-3}]$.

From the cylinder glass settling experiments, it can be concluded that the sedimentation properties of the activated sludge in general was good at the time of the investigation. This was substantiated by observations of the sludge blanket positions during quiescent conditions in the tank.

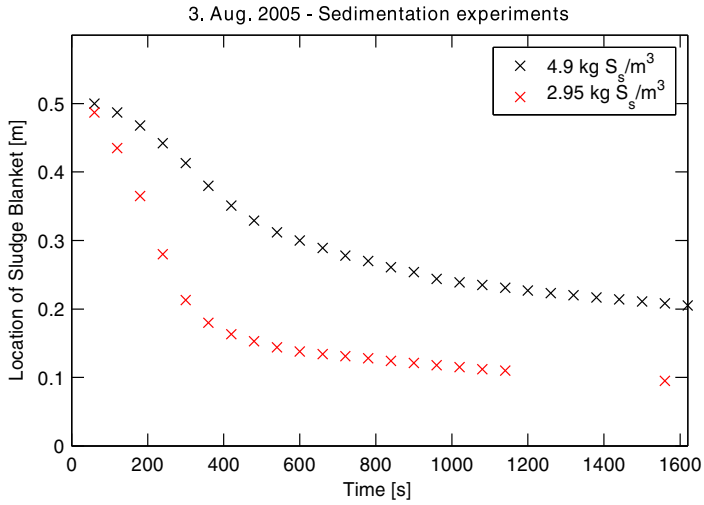

Figure 5.55 Sedimentation experiments during measurements at Frederikshavn Wastewater Treatment Plant on August 3. 2005.

Online measurements

The online measurements are continuously delivered with a resolution of five seconds. For the same period as the shown example of time series measurements shown in figure 5.53, the online measurements are shown in figure 5.56 and 5.57.

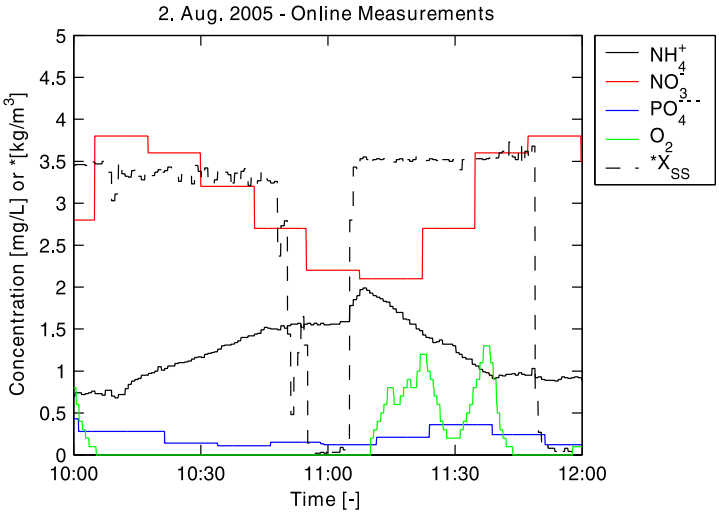

Figure 5.56 Extract of the online data measurements in the aeration tank at Frederikshavn Wastewater Treatment Plant at August 2. 2005.

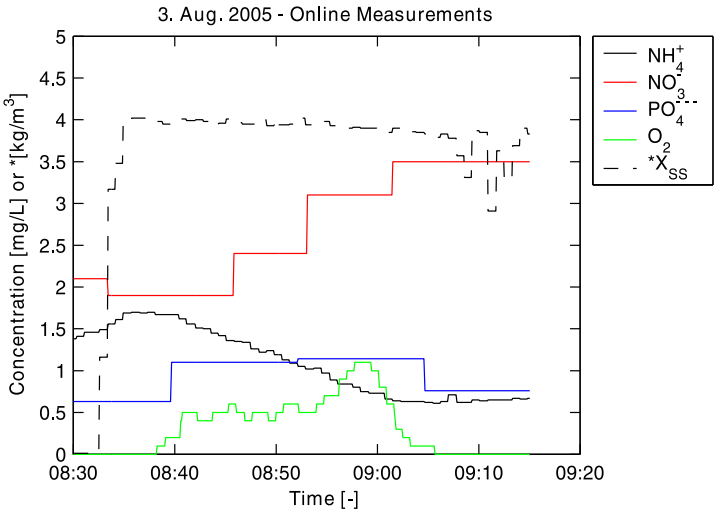

Figure 5.57 Extract of the online data measurements in the aeration tank at Frederikshavn Wastewater Treatment Plant at August 3. 2005.

From the online measurements (Figure 5.56 and 5.57) it can be observed that the concentrations of oxygen and nutrients behave like expected with respect to the aeration cycle. Aeration starts at 10:05 and 8.32, respectively, on figure 5.56 and 5.57. The concentration of NH_4^+ decrease during aeration, while it slowly builds up during anoxic conditions. The decrease during aeration is due to the nitrification, and the increase during anoxic/anaerobic conditions is partly caused by hydrolysis and partly caused by the inlet of more ammonium rich sludge from the neighbour tank. Also, as a consequence of nitrification the concentration of NO_3^- increases during aeration, even though the effect is blurred out visually by a poor resolution of the NO_3^- probe. Both the NO_3^- and the PO_4^{3-} probes seem to measure with a far lower resolution than the remainder of the probes. The concentration of PO_4^{3-} seem to increase slightly during aeration. This is in contrary to the work of the biological phosphorous removal mechanism, where the biological phosphorous removal bacteria, *Acinetobacter*, during aerobic conditions are expected to take up soluble phosphorous during the depletion of stored *polyhydroxybutyrates* (Henze *et al.*, 1992). On the other hand, the observed increase might be due to variations in the inlet during the measurement period. No measurements are however confirming this, and the model is not setup with inlet variations of PO_4^{3-}.

The measured concentration of suspended solids, X_{SS} follows a distinct pattern with very abrupt concentration changes. The probe for online logging of the S_S concentration is located just below the water surface in the aeration tank, resulting in a zero readout during quiescent conditions, i.e. during sedimentation when no stirring or aeration occurs. Hence, only during periods of aeration or mechanical mixing, the online measurement of S_S is expected to give representative values for the suspended solids concentration in the bulk of the tank.

5.3.3 Numerical model

In the present section the setup of the integrated numerical model is presented. The model is calibrated for the period matching figure 5.56 and validated for the period matching figure 5.57.

Model setup

The setup of the numerical model is basically identical with the setup presented in the case study representing Hals Central Wastewater Treatment Plant (Section 5.2). I.e. a three-phase multifluid model solving three sets of Navier-Stokes equations in three dimensions are put up for a continuous water phase and the disperse air bubble and sludge floc phases. The one significant difference compared to the model presented in section 5.2 is to be found in the implementation of the more complex biological model; ASM3. Below the setup of the model is described in further details.

Discretization The geometry of the model is divided into a mesh of 96.000 prisms in the boundary layer and 238.000 tetrahedrons in the remainder of the tank, resulting in a total of 334.000 elements. In order to resolve the flow close to the wall, a layer of 10 flat prisms with logarithmical increasing height has been placed along the walls of the tank. An outline of the computational surface mesh is presented in figure 5.58.

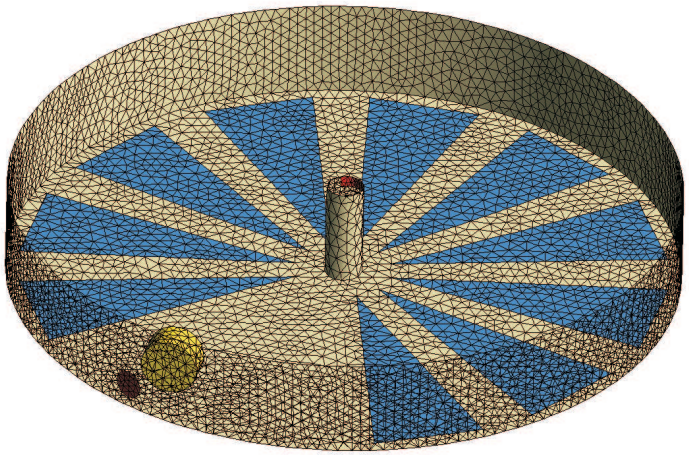

Figure 5.58 Presentation of the computational surface mesh constructed for the modelling of the aeration tank at Frederikshavn Central WWTP.

The blue triangles on figure 5.58 represent the boundaries describing the air diffusers. The inlet of air is controlled through a time dependent boundary condition with a constant velocity of 0.3 $m \cdot s^{-1}$ and varying volume fractions of air. During aeration the volume fraction is set corresponding to an inflow of 600 $m^3 air \cdot hr^{-1}$, whereas the volume fraction is switched to zero during periods where the aeration is turned off. The inflow rate of air was estimated from logged flow rates of the blowers. The red colored faces indicates the location of the in and

outlet of the tank. Since no direct data exists for the inlet flow and concentrations, mean values obtained from the outlet of the primary settling tanks have been applied to the inlet. Beside the normal flow of wastewater going through the plant, an extra flow contribution originating from the recirculation of sludge from the secondary settler is passing through the tank. The time variation of the recirculation flow has been accounted for through a time varying mass flow rate through the inlet. Since a pressure corresponding to the atmospheric pressure has been applied to the outlet, the outlet in principle works as a free outlet. The yellow cylinder shows the subdomain corresponding to the volume where sources are added in order to describe the effect of the propeller. The propeller is modelled with the same type of expression as described in chapter 4, section 4.2. Even though the propeller in the present process tank is different than the propeller investigated in chapter 4, it is assumed that the type of expression found during these investigations is adequate for describing the flow generated by the present propeller. This is justified in the fact that, the propeller in the present case study also is a slow rotating type constructed with the main purpose of keeping a large body of water/sludge in suspension.

Setup of ASM3 The fundamental difference between the model setup for the case study of Hals Central Wastewater Treatment Plant and the present model in the case of Frederikshavn Wastewater Treatment Plant is to be found within the complexity of the biological model. In the former case a simple model describing the bulk uptake of oxygen was presented, where as the Activated Sludge Model 3 (ASM3) (Gujer *et al.*, 1999) is incorporated in the present case. Details about the structure of ASM3 are given in chapter 2.

Due to the complex structure of ASM3, a large number of constants and components need to be determined before the model will be applicable to a given case. Among these are the soluble and particulate constituents of the wastewater and the activated sludge and the kinetics constants of the model.

The soluble and particulate components need to be determined for both the initial conditions and the boundary conditions of the model. Since many of the components are not available through the regular measurements performed at the plant, the use of default values and values obtained from the literature have been applied. The initial and boundary values of the soluble and particulate components are presented in table 5.3, and further explained below.

Since the oxygen concentration decrease rapidly after the end of the aeration period, and both of the cycles that are to be modelled start with a previous anoxic period, the initial concentrations of dissolved oxygen, S_O, are likely to be zero. Because the inlet to the aeration tank comes directly from the outlet on an anoxic/anaerobic tank, S_O is also assumed to be zero at the inlet boundary.

The concentration of readily biodegradable organic matter, S_S, is assumed to be low in the aeration tank due to its volatility. Like in the aeration tank, no information about the level of S_S is available for the inlet to the tank. The nearest location where measurements of COD are performed on a regular basis, is at the outlet of the primary settling tank. In between the primary settling and the aeration tank an anoxic tank is located (Figure 5.50). No information about concentrations of nutrients or fractions of organic matter is available in the anoxic tank. Hence, the values from the outlet of the anoxic tank, identical with the inlet to the aeration tank, needs to be estimated on basis of the values at the outlet of the primary settling unit (mean value of readily biodegradable organic matter: 88 $gCOD \cdot m^{-3}$) and common knowledge about the processes occurring in the anoxic tank. With respect to the concentration of readily biodegradable substrates, S_S the concentration at the outlet of the anoxic tank is assumed to be low compared to the outlet

Table 5.3 Initial and boundary values for the soluble and particulate components appearing in ASM3 as applied to the process tank at Frederikshavn Central Wastewater Treatment Plant at August 2. and 3., 2005. When two values are present in a column, the first value is from August 2. and the last value is from August 3.

Component	Component name	Initial value	Value at inlet
S_O	Dissolved oxygen	0 $g\ O_2 \cdot m^{-3}$	0 $g\ O_2 \cdot m^{-3}$
S_S	Readily biodegradable substrates	2 $g\ COD \cdot L^{-3}$	2 $g\ COD \cdot L^{-3}$
S_I	Soluble inert organic matter	15 $g\ COD \cdot m^{-3}$	15 $g\ COD \cdot m^{-3}$
S_{NH}	Ammonium	0.76/1.38 $g\ N \cdot m^{-3}$	0.76/1.38 $g\ N \cdot m^{-3}$
S_{NO}	Nitrite and nitrate	2.8/2.1 $g\ N \cdot m^{-3}$	0 $g\ N \cdot m^{-3}$
S_{N2}	Dinitrogen, product of denitrification	0 $g\ N \cdot m^{-3}$	0 $g\ N \cdot m^{-3}$
S_{HCO}	Alkalinity, Bicarbonate	5 $mole\ HCO_3^- \cdot m^{-3}$	5 $mole\ HCO_3^- \cdot m^{-3}$
X_S	Slowly biodegradable substrates	37.5 $g\ COD \cdot m^{-3}$	75 $g\ COD \cdot m^{-3}$
X_I	Inert particulate organic matter	3000 $g\ COD \cdot m^{-3}$	3000 $g\ COD \cdot m^{-3}$
X_H	Heterotrophic biomass	800 $g\ COD \cdot m^{-3}$	800 $g\ COD \cdot m^{-3}$
X_A	Autotrophic biomass	200 $g\ COD \cdot m^{-3}$	200 $g\ COD \cdot m^{-3}$
X_{STO}	Storage in heterotrophic biomass	8 $g\ COD \cdot m^{-3}$	8 $g\ COD \cdot m^{-3}$
X_{TS}	Total suspended solids	4.9 $kg\ X_{SS} \cdot m^{-3}$	4.9 $kg\ X_{SS} \cdot m^{-3}$

of from the primary settling tank. Furthermore, it is assumed that the consumption of readily biodegradable substrates due to denitrification is larger than the release of readily biodegradable matter due to hydrolysis. In case of anaerobic conditions, biological phosphorous removing bacteria might also take up readily biodegradable substrates during release of orthophosphate (Henze *et al.*, 1992).

The concentration of inert soluble matter, S_I, is set to 15 $g \cdot m^{-3}$, corresponding to the value in thin domestic wastewater (Henze *et al.*, 1992). The level of inert soluble material does not have any effect on the biological processes apparent in ASM3.

The initial values of the ammonium and nitrate concentrations are chosen on behalf of the value of the online sensor at the given time of day. Since no turnover of ammonium is expected in the anoxic tank, the inlet concentration of ammonium is set equal to the mean value measured at the outlet of the primary settler on the 2. of August 2005. By applying this inlet condition, it is assumed that the increase in ammonium due to hydrolysis is negligible compared to the inlet concentration in the raw wastewater. The inlet concentration of nitrate is set to zero since the sludge is coming directly from the anoxic tank.

The initial and inlet concentration of dinitrogen is set to zero, corresponding to the value of the outlet of primary effluents as suggested by (Gujer *et al.*, 1999). Since the sludge passes the anoxic tank before it enters the aerobic tank, some degree of attachment of N_2 to the sludge flocs might be present when it enters the aeration tank. Since the N_2 component is without influence on the biological processes simulated by ASM3, it is however chosen not to take the N_2 component into regard.

The concentration of HCO_3^- is modelled as a measure for the alkalinity availability in the process tank. Alkalinity is introduced into the model in order to be able to capture early indications of low pH conditions (Gujer *et al.*, 1999). As such the alkalinity feature is not used in the present work and since no data for HCO_3^- are present for the process tank at Frederikshavn the default value of 5 $moleHCO_{3^-} \cdot m^{-3}$ as suggested in the original ASM3 paper is applied (Gujer *et al.*, 1999). Since the concentration of HCO_3^- do affect some of the processes included

in ASM3 the chosen value of HCO_3^{-1} is however not without significance for the model results.

No value for the initial concentration of particulate slowly biodegradable substrates, X_S, is readily available for the process tank. A reasonable value would be somewhat in between the values at the in- and outlets of the tank. The inlet concentration is chosen to 75 $gCOD \cdot m^{-3}$, identical with the value in the outlets of primary effluents as suggested by (Gujer *et al.*, 1999). On behalf of the discussion above, the initial concentration is set to 37.5 $gCOD \cdot m^{-3}$. Since the mean total COD concentration measured at the outlet of the primary effluent is 191 $gCOD \cdot m^{-3}$, a X_S concentration of 75 $gCOD \cdot m^{-3}$ also seems reasonable from this perspective.

The approximate concentrations of heterotrophic and autotrophic biomass (X_H and X_A) and inert particulate matter X_I have been chosen on behalf of the investigations of (Kristensen *et al.*, 1992), presented in (Henze *et al.*, 1992).

In ASM3 it is assumed that all substrate is taken up into stored material before it is assimilated into growth. During the uptake and growth on the stored substrate, X_{STO}, oxygen may be used, making the oxygen uptake dependent on the concentration of stored substrate available in the heterotrophic biomass. Since no data are available for X_{STO}, this component needs to be estimated. As a rough estimate, the concentration of X_{STO} have been set to 1% of the heterotrophic biomass concentration X_H.

The value of total suspended solids, X_{SS} is taken directly from measurements performed by the staff at the plant on sludge from the aeration tank while on the days of the measurement campaign.

Since the introduction of additional variables representing the components of ASM3 results in the solution of one extra transport equation for each component, it has been chosen to rule out the solution for the inert fractions of substrates and the dinitrogen fraction. The exclusion of these two components seems reasonable, since neither of the components have influence on the modelling of the remainder of components. Furthermore, as pointed out in table 1.1 and the thereof related discussion, the growth of the microorganisms and suspended solids concentration occur at a considerable larger timescale than the real time modelling of e.g. 1 or 2 hours. Hence, X_A, X_H and X_{SS} are included in the model, but the sources including the processes for updating the concentrations of the variables have been ruled out. The concentrations of X_A, X_H and X_{SS} can however still change during modelling due the in- and outlet of these quantities. Since the alkalinity feature is not used in the present work, the S_{HCO} is not updated during the modelling, whereby the initial value has been hold constant through the simulation.

5.3.4 Modelling results

The model has been calibrated and validated against the two parts of the measurements shown in figure 5.59 and 5.60.

Model calibration

The model has been calibrated to the data from the late morning of the 3. of August 2005. Initially the default sets of the ingoing kinetic parameters of the ASM3, as suggested by (Gujer *et al.*, 1999) for wastewater temperatures of 10 and 20°C (Table 2.3) was applied to the model. When it turned out that the best values of kinetic parameters was lying somewhere between the 10 or 20°C sets, a systematic adjustment of the kinetic parameters was performed. Only the parameters that varies with temperature in (Gujer *et al.*, 1999) was adjusted, while the remainder of

the parameters were kept constant. The idea behind the calibration was to multiply the difference in parameter values between the 10 and 20 °C sets with the same factor between 0 and 1 after which this new set of parameter differences were added to the existing 10 °C set of (Gujer *et al.*, 1999). It turned out that satisfactory results were obtained with a factor of 0.25, i.e. the 10 °C set was to weighted higher than the 20 °C set. The final values of the changed parameters is shown in table 5.4.

Table 5.4 Calibrated values of kinetic parameters applied in the Activated Sludge Model 3 (ASM3).

Symbol	Characterization	Value	Units
k_H	Hydrolysis rate constant	2.25	$g\ X_s\ g^{-1}\ X_H\ d^{-1}$
$Heterotrophic\ organisms, denitrification, X_H$			
k_{STO}	Storage rate constant	3.125	$g\ S_s\ g^{-1}\ X_H\ d^{-1}$
μ_H	Heterotrophic max. growth rate	1.25	d^{-1}
K_{NH}	Saturation constant for Ammonium, S_{NH}	0.01	$g\ N\ m^{-3}$
$b_{H,O2}$	Aerobic endogenous respiration rate of X_H	0.125	d^{-1}
$b_{H,NO}$	Anoxic endogenous respiration rate of X_H	0.0625	d^{-1}
$b_{STO,O2}$	Aerobic respiration rate for X_{STO}	0.125	d^{-1}
$b_{STO,NO}$	Anoxic respiration rate for X_{STO}	0.0625	d^{-1}
$Autotrophic\ organisms, nitrification, X_A$			
μ_A	Autotrophic max. growth rate of X_A	0.5125	d^{-1}
$b_{A,O2}$	Aerobic endogenous respiration rate of X_A	0.075	d^{-1}
$b_{A,NO}$	Anoxic endogenous respiration rate of X_A	0.0275	d^{-1}

The modelled concentrations of soluble oxygen, ammonium and nitrate are compared to the online time series (Figure 5.59).

It can be concluded that the model captures the variations of NH_4^+, NO_3^- and S_{O_2} satisfactory. Hence, the release of NH_4^+ by hydrolysis and the consumption by nitrification are well described. Also the denitrification of NO_3^- during anoxic conditions seems to be reproduced at the right rate of change. Furthermore, the modelling of the nitrification appear to reproduce the correct increase in NO_3^- during aeration. The variation in S_{O_2} concentration, with slightly increasing concentration from the beginning of the aeration process until the discontinuation of aeration, is very well correlated with the measurements from the stationary oxygen meter. The modelled S_{O_2} concentration do however appear to be slightly underestimated at measurements performed with the transportable oxygen meter. The modelled velocities appear to possess a more dynamic nature than the measured ones, and the modelled velocities appear to be slightly underestimated. It should be pointed out that the applied propeller anemometer might have shortcomings towards capturing the dynamic nature of the flow of the suspension during especially aeration. Since the modelled velocities have a resolution of 2 seconds, and the measurements have a resolution of 1 minute, the shown modelled velocities have accordingly been averaged over a 1 minute interval.

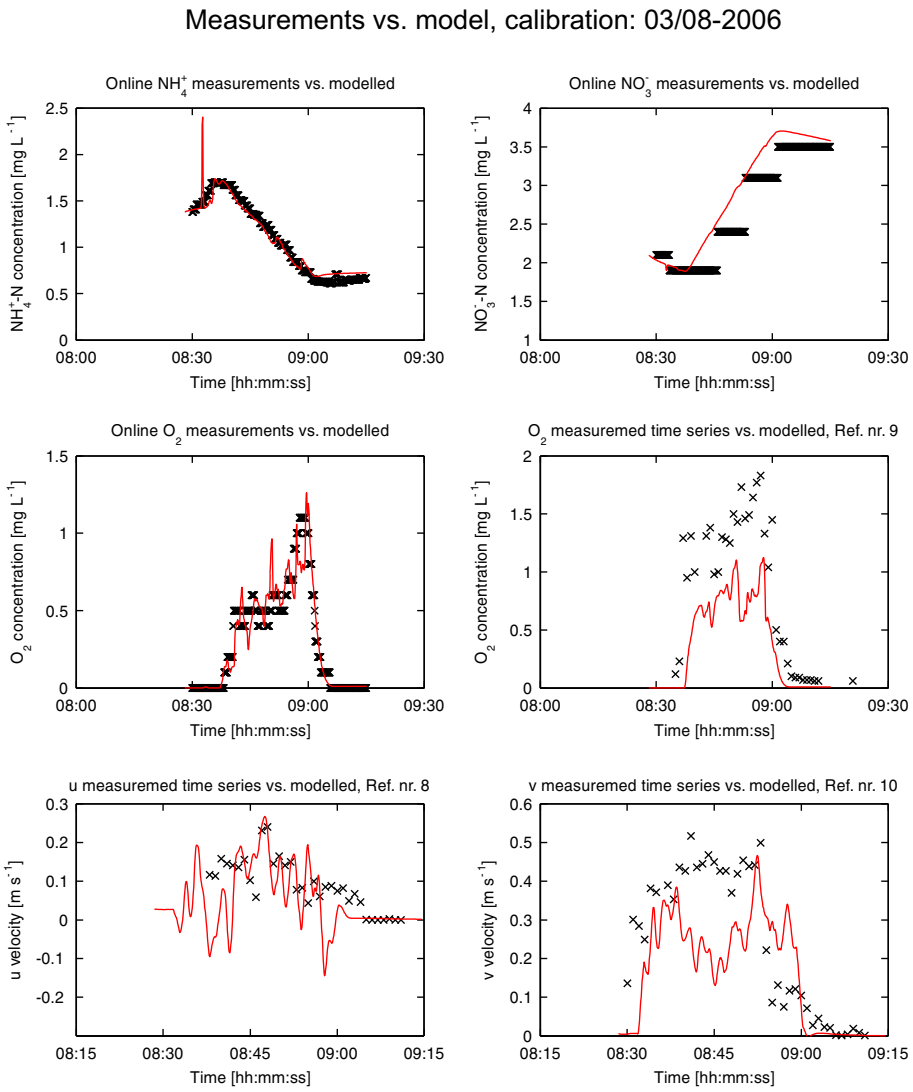

Figure 5.59 Measured and modelled time series during calibration; ×: Measurements, —: Model. The ref number of the measurements corresponds to table 5.2.

Model validation

The model has been validated for a part of the measurement period shown in figure 5.56 (Figure 5.60).

In the model validation, the accordance between measurements and model is not as good as for the calibration. The modelled concentration of NH_4^+ and NO_3^- do not fit the measurements perfectly, and the modelled S_{O_2} concentration is slightly underestimated. Again, the modelled velocities have a more dynamic nature than the measured ones meanwhile they appear to be

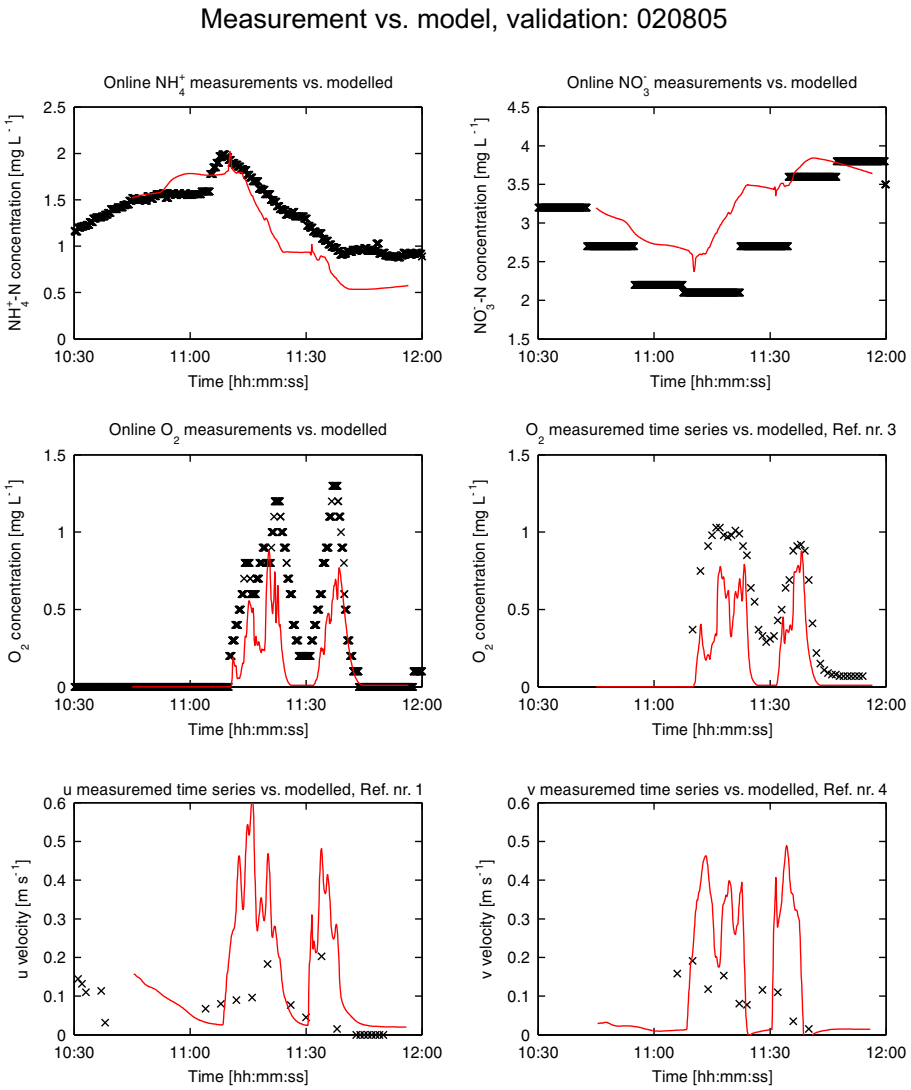

Figure 5.60 Measured and modelled time series during validation; ×: Measurements, —— : Model. The ref number of the measurements corresponds to table 5.2.

slightly overestimated.

Additional modelling results

In order to better show the functionality of the process tank, additional plots and figures are presented and discussed below. Especially the mixing conditions of the tank are discussed.

The controlling strategy of the investigated tank, results in very varying flow conditions, ranging from very dynamic conditions during operation of the mechanical mixer and the diffuser

batteries to almost quiescent conditions during the sedimentation period. As a consequence of the broad range in flow conditions, the sludge concentration also varies in both space and time during the process cycles. During aeration and mechanical mixing, the tank is assumed to be fully mixed with respect to the concentration of suspended solids. As the aeration and mechanical mixing is stopped, the sludge flocs starts to settle out and a suspended solids concentration stratification slowly starts to developed as the suspension decelerates. Such stratified conditions are shown in figure 5.61, where the suspended solids concentration is plotted after a 45 min. sedimentation period. The situation corresponds well to an observed period during the measurement campaign on the 3rd of August 2005. The simulation was initialized with conditions corresponding to the situation immediately after the turn off of the diffusers and the mechanical mixer, i.e. a circulating flow with velocities of approximately 10-12 cm/s was used as initial conditions.

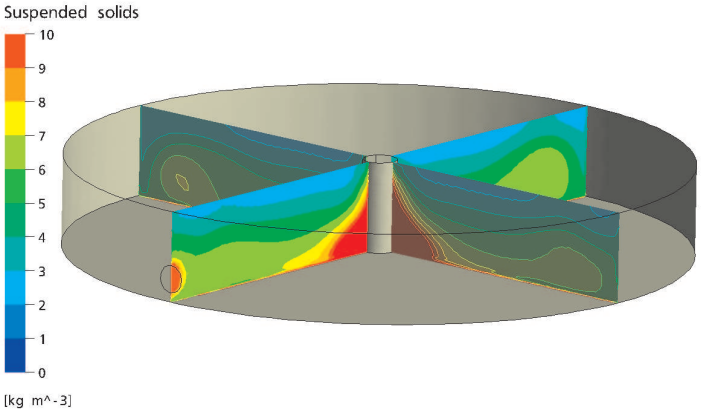

Figure 5.61 Suspended solids concentration at the end of a 45min sedimentation period.

From the sludge blanket monitoring, the sludge blanket was located approximately 0.7m below the water surface after 45min of sedimentation. With reference to the 3.95m deep tank in figure 5.61 this corresponds to a sludge volume of 82% of the tank. As discussed in Case Study 1 (Section 5.1), a relatively coarse mesh is not adequate to resolve the sharp interface between sludge flocs and supernatant. The suspended solids stratification plot do however show the qualitative trends as observed during the measurement campaign. In the circumferential zone, midway between the centre of the tank and the outer walls, the sedimentation of the sludge particles seems to be best. Also as experienced during the measurements, the sludge blanket is raised at the centre of the tank. This is partly due to the presence of the outlet, that drags up particles and partly due to the extra amount of the sludge deposited at the centre. The deposition at the centre is due to the *teacup* effect occurring in circulating flows. At the bottom and sides of the tank, the frictional resistance counteracts the centrifugal forces, making the radial flow weaker compared to the top of the tank, thus creating a radially inward directed flow at the bottom of the tank. Furthermore, due to the circulation in the clockwise direction the sludge from the inlet moves in doughnut shaped jet, as indicated in the stratification plot. Due to the higher sludge concentration in the inlet, the centre of the inlet jet shows a higher suspended solids concentration than the surrounding suspension. The shape of the jet can be identified at least halfway round in the tank, counting from the inlet.

When the modelled sludge blanket position is plotted against the measurements at August 3., it is however revealed that the model underestimates the settling velocity considerably (Figure 5.62).

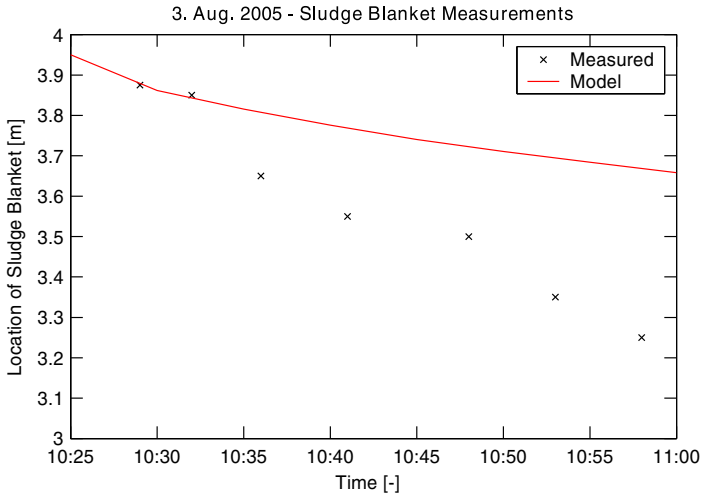

Figure 5.62 Modelled sludge blanket positio versus measurements at Frederikshavn Wastewater Treatment Plant on August 3. 2005.

Instead of the measured 70cm sludge blanket displacement at the end of the investigation, the model estimates the displacement to approximately 30cm. This relatively large deviation is probably due to the non-calibrated settling model, where the values of (Rasmussen, 1997) is not capable of capturing the settling properties of the faster settling sludge at the Frederikshavn process tank.

Due to the cyclic operation of the aeration equipment, the oxygen concentration in the process tank varies significantly with time. Figure 5.63 show the variation of the soluble oxygen concentration over time at a horizontal slice plane fixed at $2m$ above the tank bottom. The tank is on the remainder of the plots oriented as in the outline on figure 5.52.

As expected the oxygen concentration increases through the aeration cycle, after which it quickly decreases due to the rapid microbiological uptake (Figure 5.63). Furthermore, it is apparent that the configuration of the air diffusers influences the distribution of oxygen in the tank. The agitation of the suspension results in a clockwise flow in the tank. As the activated sludge passes over the diffusers, the oxygen concentration increases, whereas it decreases again when the sludge passes through the part of the tank at the inlet, where no diffusers are mounted. Some of the reason for the lower oxygen concentrations in this region of the tank, might also be due to the inlet of oxygen depleted sludge from the anoxic tank upstream in the system.

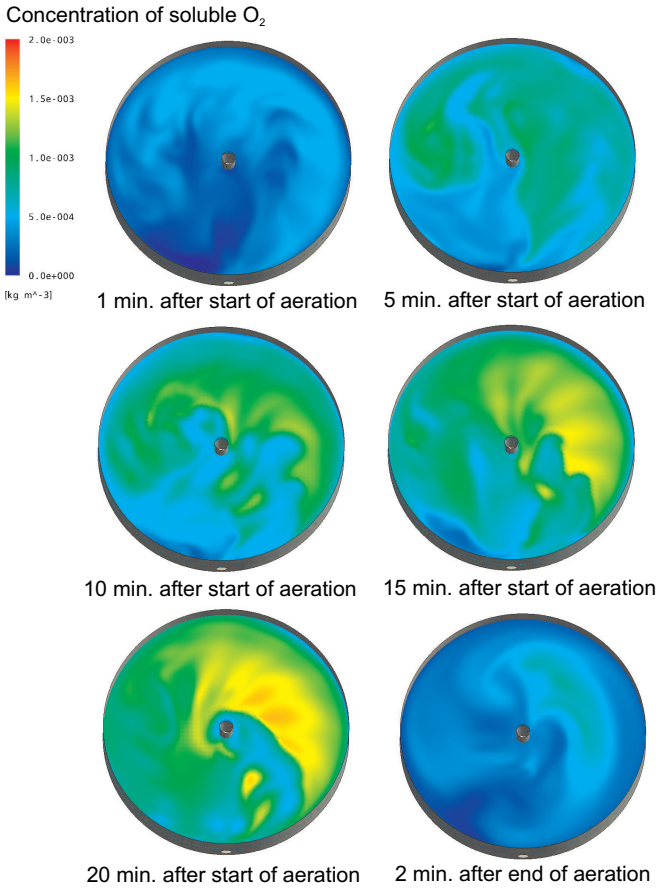

Figure 5.63 The variation of the modelled concentration of soluble oxygen $2m$ above tank bottom during and right after the aeration process.

The complex flow in the process tank during aeration and agitation is illustrated by two vector plots in figure 5.64.

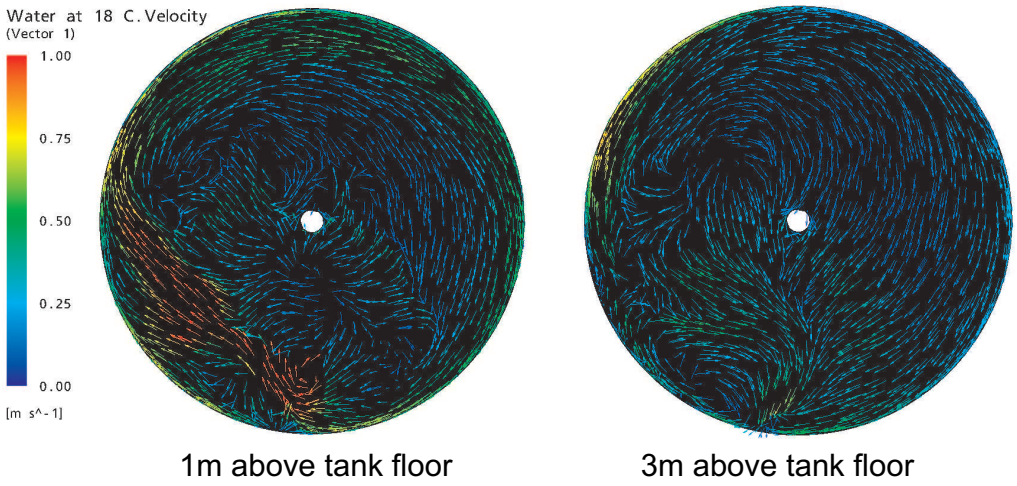

Figure 5.64 Vector plots showing the velocity of the continuous water phase.

As indicated on the left vector plot of figure 5.64, the flow is guided in a clockwise direction by the propeller. The flow is very complex due to both the action of the impeller and the complex secondary flows generated by the air diffusers. The many large eddies apparent in the tank are in agreement with the visual observations of the movement of the water surface in the tank during the measurement campaign. The presence of the many eddies contributes to the mixing of substances in the tank.

Also the mixing conditions with respect to NO_3^- and NH_4^+ can be investigated by plotting these two components at the same slice plane, $2m$ above the tank floor, as for S_{O_2}. The NO_3^- concentration varies significantly through the different parts of the process cycle (Figure 5.65).

At the period before the aeration is started, the tank is anoxic, and denitrification occurs under the turnover of readily degradable organic matter. As a consequence the NO_3^- concentration decreases in the period before the aeration starts (Figure 5.65 top left - top right). When the aeration is started, the NO_3^- concentration naturally increases due to the nitrification of the sludge (Figure 5.65 top right - bottom right). In order to obtain a global scale where the NO_3^- concentration could fit within during the different parts of the process cycle, it had to be made relatively broad. Due to the broad scale of the plots in figure 5.65, the variations of the NO_3^- concentration in a slice plane is blurred out at a given point in time.

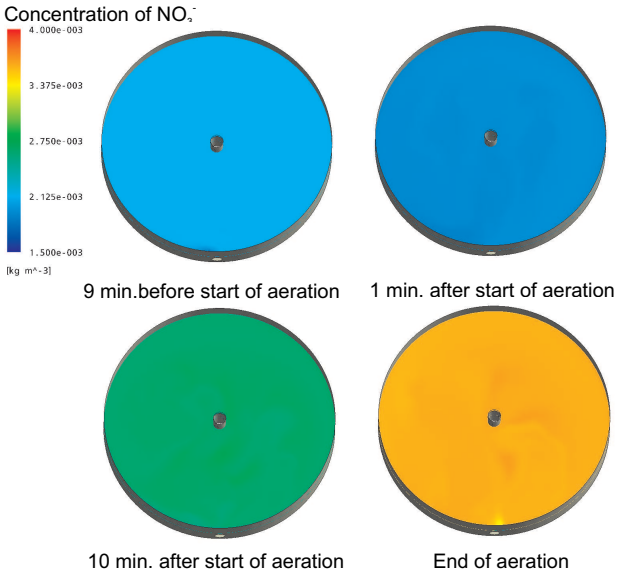

Figure 5.65 The variation of the modelled concentration of NO_3^- $2m$ above tank bottom during and before the 22 minutes long aeration process.

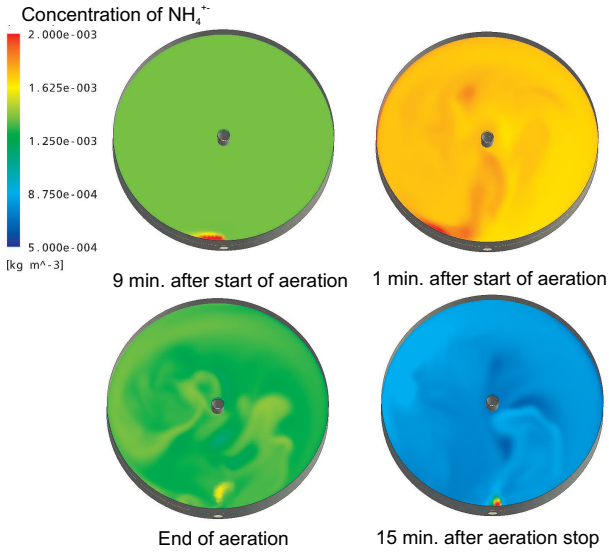

Figure 5.66 The variation of the modelled concentration of NH_4^+ $2m$ above tank bottom during and before the 22 minutes long aeration process.

Also the NH_4^+ concentration varies significantly within a process cycle (Figure 5.66). Due to hydrolysis and the admixture of NH_4^+ rich sludge from the inlet, the NH_4^+ concentration increases from the start of the simulation until the time when aeration is turned on (Figure 5.66 top left - top right). As the aeration is turned on, the nitrifying biomass converts NH_4^+ into NO_3^-, with a resulting drop in NH_4^+ concentration in the tank. Again, due to the relatively broad scale of the legend in the plots, the NH_4^+ concentration variations are blurred out in each slice plane. Changing the range of the legend and plotting the NH_4^+ concentration variations with depth do however clearly show the local concentration variations (Figure 5.67).

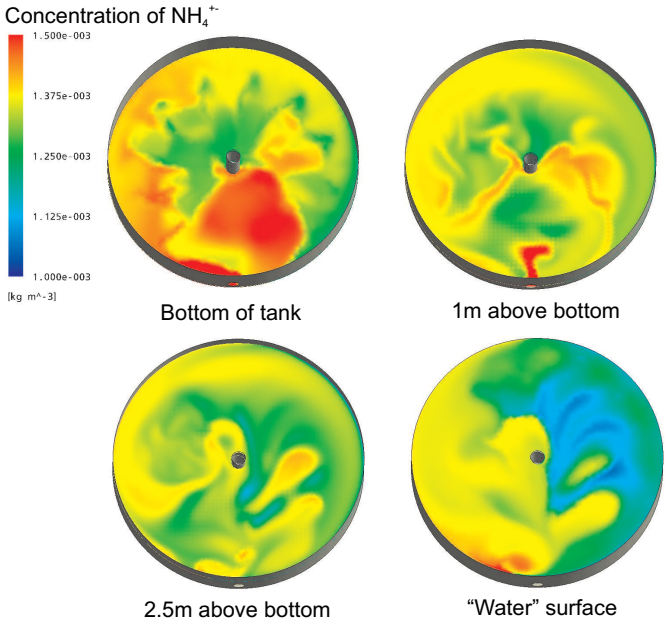

Figure 5.67 The variation of the modelled concentration of NH_4^+ at different depths after 10 minutes of aeration.

At the bottom of the tank, high concentrations of NH_4^+ appear in the region in the vicinity of the inlet. This is probably due to the high NH_4^+ concentration and a slightly higher density of the inlet jet (Figure 5.67 top left). Moving to a slice plane $1m$ above the tank floor, the influence of the inlet can still be registered (Figure 5.67 top right). Continuous threads originating from the inlet jet can be seen across the slice plane. At the surface layer of the process tank, the influence of the aeration process is most apparent (Figure 5.67 bottom right). The blue areas with the lowest concentrations of NH_4^+ are located approximately above the area of the last sections of diffusers, counting from the inlet and clockwise around in the same direction as the flow.

The above discussed plots of S_{O_2}, NO_3^- and NH_4^+ concentrations all indicate that the process tank during some parts of the process cycle is far from being fully mixed. Another way of showing the mixing conditions with respect to the biological properties of the tank, would be to directly plot the process rates for the creation/removal of the different components in the activated sludge model. In figure 5.68 the nitrification rate is plotted at different depths, 2 minutes after the beginning of aeration.

From figure 5.68 it is seen that the nitrification rate varies significantly both horizontally

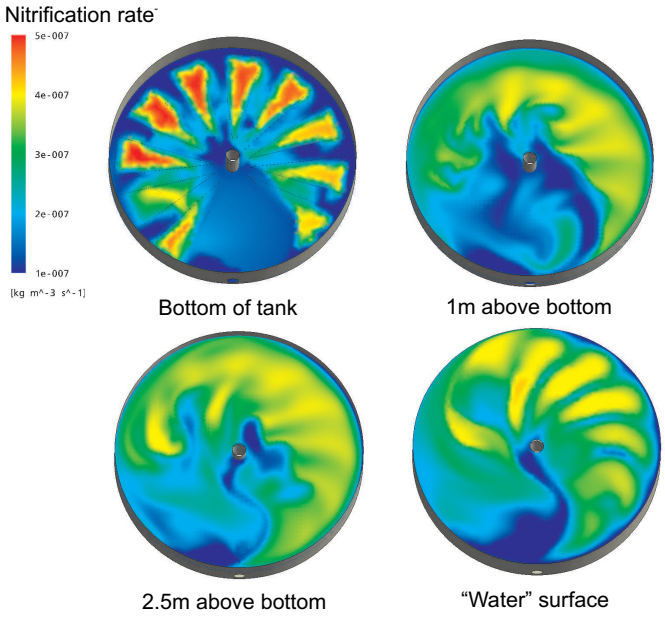

Figure 5.68 The nitrification rate at different depths after 2 minutes of aeration.

and vertically. Since the nitrification rate is highly dependent on the available amount of dissolved oxygen in the water, the areas above the diffuser do naturally show high rates. Due to the clockwise flow direction the nitrification rates are highest after the last sections of diffusers. In the area in the vicinity of the inlet where oxygen depleted sludge are flowing in and no diffuser batteries are present, the nitrification rates are lowest. Also the amount of NH_4^+ available for conversion have impact on the nitrification rate. This effect do however only vaguely appear compared to the large effect of the S_{O_2} variation. The modelled volume average, minimum and maximum values in the process tank at the same time step as for figure 5.68 are 2.6E-7, 2.4E-9 and 5.2E-7 $kg \cdot m^{-3} \cdot s^{-1}$, respectively. A lot of the large difference between the largest and the smallest value of the nitrification rate is probably to be found in the very different properties of the areas close to the inlet and close to the diffuser, representing the smallest and the largest value of the rate, respectively. Nevertheless, it is inquestionable that large variations of the nitrification rate are occurring in the tank. This is substantiated when plotting the relative tank volume as a function of the nitrification rate (figure 5.69).

Figure 5.69 expresses how large a volume of the process tank that possesses less than a given value of the nitrification rate. The ideally fully mixed tank, visualized by the continuous red line, possesses a constant nitrification rate in the tank, whereas the current tank has a wide distribution of sizes of nitrification rates in the tank. Hence, from figure 5.69 it can be concluded that the tank can not be considered as fully mixed.

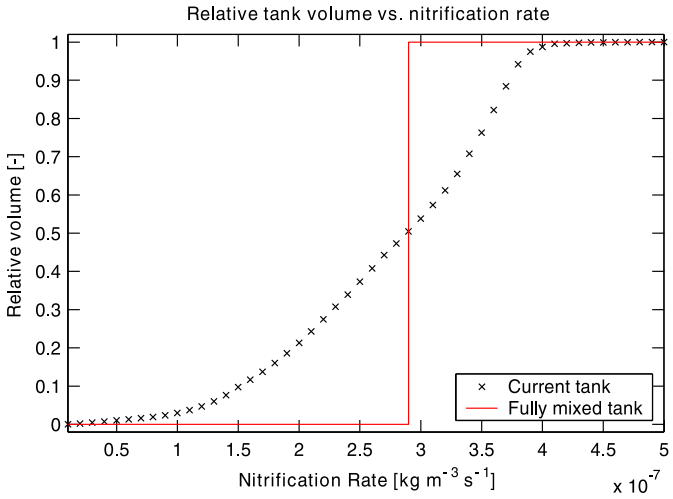

Figure 5.69 The relative tank volume as a function of nitrification rate.

5.3.5 Discussion

The comprehensive three-phase multiphase model has been integrated with the Activated Sludge Model 3 and compared to measurements in a process tank at Frederikshavn WWTP. Despite a sparse calibration set, the model was calibrated and validated with reasonable success.

The obtained measurement and modelling results indicate that the flow conditions are very dependent upon the operation of the propeller for mechanical agitation and the operation of the aeration system. Furthermore, the concentration distributions of S_{O_2}, NH_4^+ and NO_3^{-1} are largely controlled by the location and operation of the aeration system. In fact, the process tank can be considered to be split into different parts with different biological properties. This is due to the very different properties of the regions above the air diffusers and the region close to the inlet. This is substantiated by the fact that the rate of e.g. the nitrification rate is largely varying across the tank, indicating a large diversity in conditions for nitrification in the tank. Other process rates than the nitrification rate are subject to larger combinations of substrate limitations, and it is likely that these process rates will posses even larger variations in the tank, depending on the local values of the different substrate levels. The considerable variations of the process rates, have the effect that the tank cannot be accounted for as fully mixed. If a commercial compartment model was applied instead of the present detail hydrodynamic model, it is likely that the outcome would be incorrect, due to necessary assumptions about the hydrodynamics of the tank.

For more complicated tank configurations where the flow conditions and mixing properties are possessing more complicated behaviour, the concentration variations of the different compounds are believed to possess even larger variations, making the demand for an integration of hydrodynamic and biological modelling even higher.

Even though the model is only calibrated and validated over a very short period of time, the results indicate a wide usage of the model in future wastewater treatment plant modelling. The ability to predict the local flow conditions and sedimentation properties results in better

overviews of the physical operation of the tank. As a consequence, the distribution of activated sludge and the mixing properties can be better predicted than other less hydrodynamically sophisticated models. By overlaying ASM3 on top of the hydrodynamic model, a powerful tool for obtaining information on the biological operation of activated sludge process tanks has been evolved. The integrated model gives information on e.g. the local concentrations of oxygen and nutrients in the tank, an information that would not have been available without knowledge of the local flow and sedimentation properties in the tank.

CHAPTER 6
Conclusion

Activated sludge tanks are an important part in modern domestic wastewater treatment plants. The activated sludge tank is a complex mixture of both hydrodynamical, biological and chemical processes, making a clear understanding of the functioning of the tank as a whole troublesome. In addition to this, many different design concepts are currently available on the market.

Until now, modelling of wastewater treatment plants, and consequently also activated sludge tanks, have mainly been based on simple models like e.g. mass balance models for completely mixed reactors. As these types of models does not give any detailed information about the processes occurring inside the different unit operations of the treatment plant, troubleshooting and plant optimisation can be troublesome. In the present work, an integrated model, combining a detailed hydrodynamic modelling via Computational Fluid Dynamics, is proposed. The model includes:

- A three-phase CFD model, including the phases of: wastewater, sludge flocs and air bubbles
- A simple model for the oxygenation of wastewater on behalf of local air volume fraction
- Either a simple model for the bulk microbial consumption of soluble oxygen in the wastewater, or a comprehensive activated sludge model describing the wealth of microbiological processes in the suspension
- A computationally faster momentum source model, applied for the modelling of a large slow rotating hydrofoil-shaped propeller often used in activated sludge tanks
- A settling model that determines the local settling velocity on behalf of local suspended solids concentration and turbulence level
- A rheology model that takes the transport properties of the suspension into account

Prior to the implementation in the complete model of the activated sludge tank, several of the above-listed models where tested or developed against simpler cases or experiments. Measurements were performed on a dish-shaped rubber membrane air-diffuser similar to the ones often used in Danish treatment plants. Both the measurements and a matching two-phase model agreed well with the theory of Gaussian shaped far wake profiles of plume velocity and volume fractions of air.

A spare blade of a large slow rotating propeller used for keeping the sludge in suspension in an activated sludge tank of a Danish WWTP was borrowed and measured with an in-house laser

profiler. Subsequently the propeller was directly modelled in a transient sliding mesh model and the flow and turbulence quantities generated by the propeller could be resolved. Since this type of model is computationally demanding, and as such not applicable for long real-time simulations of complete activated sludge tank cases, a momentum source model was calibrated to the flow generated in the direct model. Even though the momentum model produces a steady-state like flow, the far wake flow could be reproduced satisfactory for further application in a complete activated sludge model.

The sedimentation model was implemented on the basis on the experimental data and model as proposed by (Rasmussen and Larsen, 1996). The model proved useful for describing the alternating mixing and settling cycle of an activated sludge tank undergoing a dedicated stormwater controlling strategy.

In order to determine the proper transport properties of activated sludge suspensions, a simple tube viscometer was constructed. The viscometer was built upon an assumption of laminar pipe flow and the pipe dimension was chosen to accommodate the sizes and structures of the sludge flocs. Experimental data obtained from the viscometer was fitted to a non-Newtonian Herschel-Bulkley rheology model. As widely as possible, the results from the fitted rheology model was transferred to the subsequent models of activated sludge tanks.

The Activated Sludge Model 3 (ASM3) was implemented into the CFD model and tested for implementation errors against a spread-sheet model of a fully mixed reactor.

The integration of the above listed sub models has resulted in a comprehensive model able to describe the functioning of many different tank configurations and controlling strategies. Three different case studies were performed with increasing case and model complexity:

A two phase model was applied for the modelling of an activated sludge rank running in the sedimentation phase of an Aeration Tank Settling (ATS) controlling scheme. Different inlet configurations were tested, to find the optimal layout with respect to obtaining optimal settling conditions in the tank. It was concluded that an additional rectangular inlet near the surface of the tank, would lower the impulse from the inlet jets and the thereby derived circulation velocities in the tank significantly, whereby the settling performance and the detention of sludge was enhanced.

Secondly, the activated sludge model was tested in a three-phase version against at test case of an OCO-tank with a rather complex controlling strategy. The model included the sedimentation of a sludge phase, the aeration of the wastewater fraction in the suspension and a simple model for the bulk microbial turnover of oxygen. The alternating shifts between aerobic and anaerobic conditions were well captured, and also the strong gradient in both flow velocities and biological conditions between the outer aerobic zone and an inner mostly anoxic zone could be accounted for in the model.

The final case study included the full three-phase model with the integrated ASM3 model. The model was calibrated and validated against a short period of online and manually measured data. By adjusting the values of the kinetic parameters as originally proposed by (Gujer, 2006), the model could capture the dynamics of the microbial processes relatively well over the short-term period the model was run. Even though the process tank with its current layout and configuration under normal circumstances might be considered as completely mixed, there were indications that the process rates of e.g. the nitrification rate would vary largely throughout the tank. Longer term simulations do however need to be performed before a general conclusion can be made on the subject.

The developed model is not restricted only to the cases tested in this study. Since the model

in principle can handle any geometries or controlling strategies, the possibilities seem endless.

CHAPTER 7
discussion

The proposed integrated hydrodynamic and microbial model has proven capable of modelling activated sludge tanks of different designs and controlling strategies. The models obvious strength is the linking between the detailed hydrodynamic model and the activated sludge model, a feature that makes local information on both flow properties and biological parameters available.

In this final chapter, the strengths and weaknesses of the model will be pinpointed, and suggestions for model applications and further research will be given.

The Navier-Stokes multiphase solver proved adequate to model periods of quiescent conditions during sedimentation phases of activated sludge tanks quite well. Even though the sedimentation model is empirical of nature, a transferring of model constants from different sites but of similar activated sludge types could be performed with a reasonable result. Modelling of the flocculation process would be optimal for a better understanding of the sedimentation process, and should be subject to further research, but until so, the model of (Rasmussen and Larsen, 1996) seems suitable for engineering purposes.

The model could successfully model hydrodynamically complicated process tanks like the OCO-tank in Hals Central WWTP. This is big advantage with respect to troubleshooting and upgrading process performance. Combined with the activated sludge model, the model seems suitable for simulating design concepts involving challenging biological processes. From the present investigations it was indicated that even process tanks that usually would be counted as fully mixed in reality can be far from this assumption when observing the variability in process rates. In the light of these indications, it might in many cases be questionable whether a calibrated mass balance model really represents the biological processes occurring in a given process tank, or the calibration instead is a result of the interaction between the biological model and a poor hydrodynamic model. Having said that, it is obvious that mass balance models have had their strengths in describing the overall performance of a wealth of wastewater treatment plants all over the world.

During the model development, several sub process investigations where initiated. These investigations all reflect the means of getting sufficient overview from a practical engineering point of view. As such these sub process investigations is not to be regarded as state of the art measurement investigations. Rather they should be seen as a means of obtaining measurements in conditions that from a practical standpoint are very hard to reach. The ultrasound probe applied for the measurements of large-scale bubble plume gas holdups, was chosen due to the poor visibility and size of the diffuser generated bubble plume. For the same reasons the measurement propeller was chosen for the measurements of flow velocities inside the bubble plume.

Due to the floc structure and diverse composition of the activated sludge, ordinary rotational rheometers was avoided due to the associated risks of destroying the natural structure of the sludge. The inadequacy of the rotational rheometers was confirmed in experiments prior to the tube viscometer experiments. Instead a tube viscometer was constructed, since this type of measurement allows the sludge to flow with a minimum of disturbance of the sludge structure. The tube viscometer is however not without drawbacks since sludge sedimentation cannot be ruled out at low shear rates toward the end of the experiment. When transferring the fitted non-Newtonian viscosity model to the numerical model, the hydrodynamic model in some instances was prone to numerical instabilities. In other earlier studies of non-Newtonian flow in a much thicker sludge from aquaculture fish farms, the model worked without any problems (Rasmussen *et al.*, 2004). Putting a rather large limiter on the shear stress in the viscosity relation did not help in the cases of instability. It is unclear whether the instabilities originated from the more complex three-phase model or from the regions of high shear generated in the vicinity of the propeller or the diffuser batteries. Since the rheological model is an important model for adequately describing the transport processes of the suspension, further development of the model is recommended.

Ideally the solely numerical investigation of the large-scale propeller should have been backed up by an experimental investigation. The experimental work could possible clear up the rather questionable trends of the modelled eddy viscosity in the near wake of the propeller. In future use of the model, a catalogue of different propellers and their belonging momentum source models should be available for easy and fast setup. Such a library demands both extra computations and detailed experiments.

Similarly only one of the main types of aeration equipments was investigated - the bottom mounted diffuser. The inclusion of a top mounted surface aerator demands a totally different modelling concept. This concept is not necessarily more computationally demanding, since this type of aerator could possibly be implemented by applying a source of soluble oxygen at subdomains near the top surface of the tank. Further research into the concept is suggested.

One main weakness of the model is the inability to model long term periods over e.g. one or several sludge ages. On a small cluster of 5 relatively large workstations, the usual modelling time for one process cycle (approx. 1hr. in real-time) was in the order of weeks to months depending on the complexity of the model and the size of the computational mesh. Thus, without the application of super computers, long term modelling is not realistic.

With the above described deficiencies in mind, the model still has its relevance in future modelling of wastewater treatment plants. From the present investigations several applications of the model seems possible:

- Optimisation of tank layouts and controlling strategies
- Estimation of the optimal localisation of online sensors in order to give representative values.
- A tool for learning students about process optimisation and in general gaining more insight in the functioning of wastewater treatment plants
- Integration of multiple operational units to construct a total CFD wastewater treatment plant model

The ATS case study in section 5.1 is a good example of both tank layout and controlling strategy changing and optimisation.

Currently large investments are conducted on online measurement equipment among the wastewater treatment industry. The online sensors give valuable information to the more and more advanced controlling units for e.g. the process tanks. In order to get the full value of these investments, the online sensors need to be located at places representative for the overall conditions in the tanks. In hydrodynamically complex process tanks the optimal location of the online sensors may not necessarily be straightforward. In these situations a detailed process tank model can help gaining the necessary insight.

With the standard of modern post-processing tools, the visualisation possibilities are nearly endless, and alone on this basis a CFD model is a very useful tool for learning and understanding the functioning of the many processes occurring in process tanks.

Finally it should be pointed out that the present activated sludge model is only one of the building blocks of a complete wastewater treatment model. Consequently, the optimisation has been performed on behalf of the individual unit operation, rather than as a part of a larger group of dependent processes. Ideally the process tank model should get its values at the inlet boundary from upstream located unit operations like e.g. other process tanks or a primary clarifier. Likewise the outlet from the activated sludge process tank should be working as inlet in downstream located unit operations like e.g. a secondary clarifier, and so on. This way the individual processes would be optimised on behalf of the optimisation of the treatment plant as a whole. Also the activated sludge process tank is only one of several process tank types available at WWTP's. Other process tank types, like the fixed bed biofilter, demands a totally different model setup due to the stationary nature of the biofilter media. One way of modelling a biofilter process would be to treat the biofilter as a media with a porosity corresponding to the real porosity.

The present work is another step towards the development of detailed wastewater treatment models. The complete model concept might however still be too complex for industrial applications. Consequently, a detailed hydrodynamic single phase CFD model coupled with an activated sludge model and treatment of the sludge and air bubble phases as soluble phases might for a start have a higher practical value for the industry.

Bibliography

Anderson, J.D.Jr. (1995). *Computational fluid dynamics: the basic with applications*. McGraw-Hill, New York.

Anderson, J.S., Hyunook Kim, T.J. McAvoy and O.J. Hao (2000). Control of an alternating aerobic-anoxic activated sludge system - part 1: development of an linearization-based modelling approach. *Control Engineering Practice* **8**, 271–278.

Antal, S., R. Lahey and J. Flaherty (1991). Analysis of phase distribution in fully-developed laminar bubbly two-phase flow. *International Journal of Multiphase Flow*.

Armenante, P.M., C. Luo, C.-C. Chou, I. Fort and J. Medek (1997). Velocity profiles in a closed, unbaffled vessel: comparison between experimental ldv data and numerical cfd predictions. *Chemical Engineering Science* **52**(20), 3483–3492.

Barnes, H.A. (2000). *A handbook of elementary rheology*. The University of Wales Institute of Non-Newtonian Fluid Mechanics, Department of Mathematics, University of Wales Aberystwyth.

Barth, T.J. and D.C. Jesperson (1989). The design and application of upwind schemes on unstructered meshes. *AIAA Paper 89-0366, in 27th Aerospace Sciences Meeting, Reno, USA*.

Becker, S., H. De bie and J. Sweeney (1999). Dynamic flow behaviour in bubble columns. *Chemical Engineering Science* **54**, 4929–4935.

Bernard, R.S., R.S. Maier and H.T. Falvey (2000). A simple computational model for bubble plumes. *Applied Mathematical Modelling* **24**, 215–233.

Bingham, E.C. (1916). An investigation og the laws of plastic flow. *U.S. Bureau of Standard Bulletins* **13**, 309–353.

Blackburn, H.M., J.R. Elston, D.A. Niclasen, M. Rudman and J. Wu (2000). A hybrid method for simulation of axial flow impeller driven mixing vessels. *Applied Mathematical Modelling* **24**, 795–805.

Borchers, O., C. Busch, A. Sokolichin and G. Eigenberger (1999). Application of the standar k-epsilon turbulence model to the dynamic simulation of bubble columns. part ii: Comparison of detailed experiments and flow simulations. *Chemical Engineering Science* **54**, 5927–5935.

Bröder, D. and M. Sommerfeld (1998). Simultaneous measurements of continuous and dispersed phase in bubble columns in pda. *Proceedings of the nineth international symposium on applications on laser techniques to fluid mechanics, Lisbon, Portugal*.

Bröder, D. and M. Sommerfeld (2002). An advanced lif-plv system for analysing the hydrodynamics in a laboratory bubble column at higher void fractions. *Experiments in Fluids* **33**, 826–837.

Brdjanovic, Damir, Mark C.M. van Loosdrecht, Paul Versteeg, Christine M. Hooijmans, Guy J. Alaerts and Joseph J. Heijnen (2000). Modeling cod, n and p removal in a full-scale wwtp haarlem waarderpolder. *Water Research*.

Brenn, G., H. Braeske and F. Durst (2002). Investigations of the unsteady two-phase flow with small bubbles in a bubble column using phase-doppler anemometry. *Chemical Engineering Science* **57**, 5143–5159.

Brevik, I. and R. Killie (1996). Phenomenological description of the axisymmetric air-bubble plume. *International Journal of Multiphase Flow* **22**(3), 535–549.

Börjesson, T. and M. Fahlgren (2001). Mechanics of fluids in mixing - bringing mathematical modeling close to reality. *Scientific Impeller, published by ITT Flygt AB, Sweden* **6**, 55–68.

Brouckaert, C.J. and C.A. Buckley (1999). The use of computational fluid dynamics for improving the design and operation of water and wastewater treatment plants. *Water Science and Technology* **40**(4-5), 81–89.

Bruun, H.H. (1996). Hot-film anemometry in liquid flows. *Measurement Science and Technology* **7**, 1301–1312.

Bundgaard, E., M.K. Nielsen and M. Henze (1996). Process development by full-scale on-line tests and documentation. *Water science and Technology* **33**(1), 281–287.

Burns, A.D.B., T. Frank, I. Hamill and J-M. Shi (2004). Drag model for turbulent dispersion in eulerian multiphase flows. *Proceedings of the Fifth International Conference on Multiphase flow (ICMF), Yokohama, Japan*.

Buscaglia, G.C., F.A. Bombardelli and M.H. Garcia (2002). Numerical modelling of large-scale bubble plumes accounting for mass transfer effects. *International Journal of Multiphase Flow* **28**, 1763–1785.

Camp, T.R. and P.C. Stein (1943). Velocity gradients and internal work in fluid motion. *Journal of the Society of Civil Engineering* **30**, 219–237.

Carregal-Ferreira, J., A. Holzwarth, F. Menter, T. Esch and A. Luu (n.d.). Advanced cfd analysis of aerodynamics using cfx.

Casson, N. (1957). *Br. Soc. Rheol. Bull.*

CFX, ANSYS (2003). *CFX-5.6 documentation*.

CFX, ANSYS (2005). *CFX-5.7.1 documentation*.

Chaouki, Jamal, Larachi, Faïcal and Dudukovict', Milorad P., Eds.) (1997). *Non-invasive monitoring of multiphase flows*. Elsevier Science B.V.. Sara Burgerhartstraat 25, P.O. Box 211, 1000 AE Amsterdam, The Netherlands.

Cinar, Ozer, Glen T. Daigger and Stephen P. Graef (1998). Evaluation of iawq activated sludge mode no. 2 using steady-state date from foru full-scale wastewater treatment plants. *Water Environment Research*.

Clift, R., J.R. Grace and M.E. Weber (1978). *Bubbles, drops and particles*. Academic Press.

Cockx, A., Z. Do-Quang, J.M. Audic, A. Line and M. Roustan (2001). Global and local mass transfer coefficients in waste water treatment process by computational fluid dynamics. *Chemical Engineering and Processing* **40**, 187–194.

Coen, F., B. Petersen, P.A. Vanrolleghem, B. Vanderhaegen and M. Henze (1998). Model-based characterisation of hydraulic, kinetic and influent properties of and industrial wwtp. *Water Science and Technology* **37**(12), 317–326.

Copp, J. (2002). The cost simulation benchmark: Description and simulator manual. Technical report. Office for official publications of the European Union, Luxembourg.

Crowe, C.T. (2000). On models for turbulence modulation in fluid-particle flows. *International Journal of Multiphase Flow* **26**, 719–727.

Dahl, C. (1993). Numerical modelling of flow and settling in secondary settling tanks. Ph.d. thesis, series paper no. 8, issn: 0909-4296. Aalborg University, Department of Civil Engineering.

Davidson, L. (2003). An introduction to turbulence models. Technical report. Department of Thermo and Fluid Dynamics, Chalmers University of Technology, Göteborg, Sweden.

de Clercq, B. (2003). Computational fluid dynamics of settling tanks: development of experiments and rheological, settling, and scraper submodels. Ph.d. thesis. University of Gent.

Deen, N.G. and B.H. Hjertager (2002). Particle image velocimetry measurements in an aerated stirred tank. *Chemical Engineering Communications* **189**, 1208–1221.

Deen, N.G., T. Solberg and B.H. Hjertager (2000). Numerical simulation of the gas-liquid flow in a square cross-sectioned bubble column.

Deen, N.G., T. Solberg and B.H. Hjertager (2001). Large eddy simulation of the gas-liquid flow in a square cross-sectioned bubble column. *Chemical Engineering Science* **56**, 6341–6349.

Delnoij, E., , J. WesterWeel, N.G. Deen, J.A.M. Kuipers and W.P.M. van Swaaij (1999*a*). Ensemble correlation piv applied to bubble plumes rising in a bubble column. *Chemical Engineering Science* **54**, 5159–5171.

Delnoij, E., J.A.M. Kuipers and W.P.M. van Swaaij (1999*b*). A three-dimensional cfd model for gas-liquid bubble columns. *Chemical Engineering Science* **54**, 2217–2226.

Devanathan, N., M.P. Dudukovic, A. Lapin and A. Lübbert (1995). Chaotic flow in bubble column reactors. *Chemical Engineering Science* **50**(16), 2661–2667.

Ditmars, J.D. and K. Cederwall (1974). Analysis of air-bubble plumes. *Proceedings of the Fourteenth Coastal Engineering Conference, Copenhagen, Denmark* pp. 2209–2226.

Do-Quang, Z., A. Cockx, A. Liné and M. Roustan (1999). Computational fluid dynamics applied to water and wastewater treatment facility modeling. *Environmental Engineering and Policy* **1**, 137–147.

Edwards, C.H.Jr. and David E. Penney (1994). *Calculus with analytic geometry*. 4th ed.. Prentice Hall International, Inc.

Friberg, P.C. and B.H. Hjertager (1998). Simulation of a 3-dimensional large-scale fermenter with four rushton turbines using a two-fluid model.

Friberg, P.C. and B.H. Hjertager (1999). Simulation of a 3-dimensional large-scale fermenter with four rushton turbines.

Friberg, P.C. and B.H. Hjertager (2000*a*). Commonly used mathematical models for bubble columns; a computational comparison.

Friberg, P.C. and B.H. Hjertager (2000*b*). Computational investigations of impeller stirred gas/liquid tank reactors.

Friberg, P.C. and B.H. Hjertager (2000*c*). An investigation of mathematical models for impeller stirred tank reactors.

Frier, J.O. (1998). *Compendium in water streams*. Department of Environmental Technique, Aalborg University.

Frost, R.C. (1981). First report on the wrc sewage sludge pumping project. Technical report TR 162. WRC Water Research Centre.

Frost, R.C. (1982). Prediction of the friction losses for the flow of sewage sludges in straight pipes. Technical report TR 175. WRC Water Research Centre.

Frost, R.C. (1983). How to design sewage sludge pumping systems. Technical report TR 185. WRC Water Research Centre.

Gernaey, K.V., M.C.M. van Loosdrecht, M. Henze, M. Lind and S.B. Jørgensen (2004). Activated sludge wastewater treatment plant modelling and simulation: state of the art. *Environmental modelling and software* **19**, 763–783.

Glover, G.C., C. Printemps, K. Essemiani and J. Meinhold (2006). Modelling of wastewater treatment plants - how far shall we go with sophisticated modelling tools?. *Water science and Technology* **53**(3), 79–89.

Gore, R.A. and C.T. Crowe (1989). The effect of particle size on modulating turbulent intensity. *International Journal of Multiphase Flow* **15**, 279–285.

Groen, J.S., R.F. Mudde and H.E.A Van Den Akker (1999). On the application of lda to bubbly flow in the wobbling regime. *Experiments in Fluids* **27**, 435–449.

Gujer, W. (2006). Activated sludge modelling: past, present and future. *Water science and Technology* **53**(3), 111–119.

Gujer, Willi, Mogens Henze, Takahashi Mino and Mark Van Loosdrecht (1999). Activated sludge model no. 3. *Water Science and Technology* **39**(1), 183–193.

Gupta, A.K. (1984). *Swirl flows*. Abacus Press.

Haas, U., h. Schmidt-Traub and H. Brauer (1972). Flow round spherical bubbles with internal circulation. *Chemie Ingenieur Technik*.

Harlow, F.H. and J.E. Welch (1965). Numerical calculation of time-dependent viscous incompressible flow of fluid with free surface. *Physics of Fluids* **8**, 2182–2189.

Henze, M., C.P.L. Grady, W. Gujer, G.v.R Marais and T. Matsuo (1987). Activated sludge model no.1. IAWPRC Scientific and Technical Report 1. IAWPRC. London.

Henze, M., P. Harremoës, J. la Cour Jansen and E. Arvin (1992). *Spildevandsrensning - Biologisk og kemisk*. 2nd ed.. Polyteknisk Forlag.

Henze, M., W. Gujer, T. Mino, T. Matsuo, M.C. Wentzel and G.v.R Marais (1995). Activated sludge model no.2. IAWQ Scientific and Technical Report 3. IAWQ. London.

Henze, Mogens, Willi Gujer, Takahashi Mino, Tomonori Matsuo, Mark C. Wentzel, Gerrit v.R. Marais and Mark C.M. Van Loosdrecht (1999). Activated sludge model no.2d, asm2d. *Water Science and Technology* **39**(1), 165–182.

Herschel, W.H. and R. Bulkley (1926). Measurement of consistency as applied to rubber benzen solutions. *Proceedings to the American Society for testing materials*.

http://www.aquasim.eawag.ch (2005). Webpage.

http://www.dantecdynamics.com (2005). Webpage.

http://www.dhisoftware.com/efor (2005). Webpage.

http://www.envirosim.com (2005). Webpage.

http://www.flygtus.com/115917.asp (2005). Webpage.

http://www.hemmis.com (2005). Webpage.

http://www.hydromantis.com (2005). Webpage.

http://www.hydrosoft.civil.aau.dk/epro/index.htm (2005). Webpage.

http://www.ifak system.com (2005). Webpage.

http://www.wldelft.nl/inst/sed/uhcm/index.html (2004). Webpage.

http://www.wrc plc.co.uk/software (2005). Webpage.

Isaacs, S., J.A. Hansen, K. Schmidt and M. Henze (1995). Examination of the cativated sludge model no. 2 with an alternating process. *Water Science and Technology* **31**(2), 55–66.

Ishii, M. (1975). Thermo-fluid dynamics theory of two-phase flow. *Eyrolles, Paris*.

Ishii, M. and N. Zuber (1979). Drag coefficient and relative velocity in bubbly, droplet or particulate flows. *AIChE Journal* **25**(5), 843–855.

Janex, M.L., P. Savoye and Z. Do-Quang (1998). Impact of water quality and reactor hydrodynamics on wastewater disinfection by uv, use of cfd for perfomance optimization. *Water Science and Technology* **38**(6), 71–78.

Jenne, M. and M. Reuss (1999). A critical assessment on the use of $k - \epsilon$ turbulence models for simulation of the turbulent liqiud flow induced by a rushton-turbine in baffled stirred-tank reactors.. *Chemical Engineering Science* **54**, 3921–3941.

Jensen, M.D. (2004). Modellering af transportprocesser - under ats drift af renseanlæg. Masters thesis. Aalborg University, Department of Civil Engineering.

Jensen, M.D., P. Ingildsen, M.R. Rasmussen and J. Laursen (2006). Computational fluid dynamics modelling of hydraulics and sedimentation in process reactors during aeration tank settling. *Water Science and Technology* **53**(12), 257–264.

Jones, W.P. and B.E. Launder (1972). The prediction of laminarization with a two-eqution model of turbulence. *International Journal of Heat and Mass Transfer* **15**, 301–314.

Karama, A.B., O.O. Onyejekwe, C.J. Brouckaert and C.A. Buckley (1999). The use of computational fluid mechanics (cfd). technique for evaluating the efficiency of an activated sludge reactor. *Water Science and Technology* **39**(10-11), 329–332.

Keulegan, G.H. (1957). An experimental study of the motion of saline water from locks in fresh water channels. Report 5168. U.S. Department of Commerce, National Bureau of Standards.

Kobus, H.E. (1968). Analysis of the flow induced by air-bubble systems. *Proceedings of Coastal Engineering Conference* pp. 1016–1034.

Koch, G., M. Kühni, W. Gujer and H. Siegrist (2000). Calibration and validation of activated sludge model no. 3 for swiss municipal wastewater. *Water Research* **34**(14), 3580–3590.

Krebs, P. (1991). Hydraulics of final settling tanks. *Water Science and Technology* **23**(4), 1037–1046.

Krebs, Peter, Anastasios I. Stamau, Jaime L. García Heras and Wolfgang Rodi (1996). Influence of inlet and outlet configuration on the flow in secondary clarifiers. *Water Science and Technology* **34**(5-6), 1–9.

Kristensen, G.H., P.E. Jørgensen and M. Henze (1992). Characterization of functional groups and substrate in activated sludge and wastewater by aur, nur and our. *Water Science and Technology* **25**(6), 43–57.

Kunnerup, T., J. Laursen and S.B. Pedersen (2002). Cfd-modellering af strømninger og processer i aktiv-slam anlæg - analyse af oco-tank på hals centralrenseanlæg. Masters thesis. Aalborg University, Department of Civil Engineering.

Ladiges, G., C. Günner and R. Otterpohl (1999). Optimisation of the hamburg wastewater treatment plants by dynamic simulation. *Water Science and Technology* **39**(4), 37–44.

Lain, S., D. Bröder and M. Sommerfeld (1999). Experimental and numerical studies of the hydrodynamics in a bubble column. *Chemical Engineering Science* **54**, 4913–4920.

Lain, S., D. Bröder and M. Sommerfeld (2001). Numerical simulations of the hydrodynamics in a bubble column: Quantitative comparisons with experiments. *Proceedings of the Fourth International Conference on Multiphase flow (ICMF), New Orleans, USA*.

Lain, S., D. Bröder, M. Sommerfeld and M.F. Göz (2002). Modelling hydrodynamics and turbulence in a bubble column using the euler-lagrange procedure. *International Journal of Multiphase Flow* **28**, 1381–1407.

Lakehal, D. (2002). On the modelling of multiphase turbulent flows for environmental and hydrodynamic applications. *Internatioanl Journal of Multiphase Flow* **28**, 823–863.

Lankford, D. (1974). *Aeration of activated sludge in sewage treatment*. Chap. 7, pp. 65–88. Pergamon Press Inc.

Larsen, P. (1977). On the hydraulics of rectangular settling basins: Experimental and theoretical studies. Repor / Lunds Universitet, Lunds Tekniska Högskola, Institutionen för teknisk vattenresurslära 1001. University of Lund.

Launder, B.E. and D.B. Spalding (1974). The numerical computation of turbulent flows. *Computer methods in applied mechanics and engineering* **3**, 269–289.

Laurien, E. and J. Niemann (2004). Determination of the virtual mass coefficient for dense bubbly flows by direct numerical simulation. *Proceedings of the Fifth International Conference on Multiphase flow (ICMF), Yokohama, Japan*.

Laursen, J. and M.R. Rasmussen (2004). Modellering af ats-forhold på bjergmarken renseanlæg. Report in: Hydraulics and coastal engineering, issn 1603-9874. Aalborg University, Department of Civil Enigineering.

Loosdrecht, Mark C.M. Van and Mogens Henze (1999). Maintenance, endogeneous respiration, lysis, decay and predation. *Water Science and Technology* **39**(1), 107–117.

Loth, E. (2000). Numerical approaches for motion of dispersed particles, droplets and bubbles. *Progress in Energy and Combustion Sciences* **26**, 161–223.

Magnaudet, J. and I. Eames (2000). The motion of high-reynolds-number bubbles in inhomogeneous flow. *Annual Review of Fluid Mechanics* **32**, 6659–708.

Manga, M., J. Castro, K.V. Cashman and M. Loewenberg (1998). Rheology of bubble-bearing magmas. *Journal of Volcanology and Geothermal Research* **87**, 15–28.

McDougall, T.J. (1978). Bubble plumes in stratified environments. *Journal of Fluid Mechanics* **85**(4), 655–672.

Menter, F.R. (1996). A comparison of some recent eddy-viscosity turbulence models. *Journal of Fluids Engineering* **118**, 514–519.

Menter, F.R., M. Kuntz and R. Langtry (2003). *Turbulence, Heat and Mass Transfer 4*. Chap. Ten years of industrial experience with the SST turbulence model. Begell House Inc.

Miljøministeriet, Danmark (1987). *Handlingsplan mod forureningen af det danske vandmiljø med næringssalte*. Miljøministeriet, Danmark.

Morud, K.E. and B.H. Hjertager (1996). Lda measurements and cfd modelling of gas-liquid flow in a stirred wessel. *Chemical Engineering Science* **51**(2), 233–249.

Mussati, M., K. Gernaey, R. Gani and S.B. Jørgensen (2002). Computer aided model analysis and dynamic simulation of a wastewater treatment plant. *Clean Technologies and Environmental Policy* **4**(2), 100–114.

Newton, Sir I. (1687). *Philosophiae naturalis principia mathematica*. Londini, jussi societatus Regiae ac typis Josephi Streater, prostat apud plures bibliopolas.

Nielsen, M.K., H. Bechmann and M. Henze (2000). Modelling and test of aeration tank settling (ats). *Water science and Technology* **41**(9), 179–184.

Nielsen, M.K., J. Carstensen and P. Harremoës (1996). Combined control of sewer and treatment plant during rainstorm. *Water science and Technology* **34**(3-4), 181–187.

Nielsen, P.H. (1994). Slamkarakterisering of -identifikation. In: *Kompendie i Biologisk Spildevandrensning -Et model- og computerorienteret kursus*. Laboratoriet for Miljøteknik.

Nielsen, P.H. (2002). *Encyclopedia in Environmental Microbiology*. Chap. The activated sludge floc. Wiley.

Nielsen, P.H., T.R. Thomsen and J.L. Nielsen (2004). Bacterial composition of activated sludge - importance for floc and sludge properties. *Water Science and Technology* **49**(10), 51–58.

Nowak, O., A. Franz, K. Svardal, V. Müller and V. Kühn (1999). Parameter estimation for activated sludge models with the help of mass balances. *Water Science and Technology* **39**(4), 113–120.

Oda, T., T. Yano and Y. Niboshi (2006). Development and exploitation of a multipurpose cfd tool for optimisation of microbial reaction and sludge flow. *Water science and Technology* **53**(3), 110–110.

Patankar, S.V. (1980). *Numerical heat transfer and fluid flow*. Hemisphere Publishing Corporation.

Patankar, S.V. and D.B. Spalding (1972). A calculation procedure for heat, mass and momentum transfer in three-dimensional parabolic flows. *International Journal of Heat and Mass Transfer* **15**, 1787.

Pedersen, P. (2001). Annual report of hals central wastewater treatment plant. Technical report. Hals Central Wastewater Treatment Plant.

Petersson, P., M. Larson and L. Jönsson (1996). Measurements of the velocity field downstream of an impeller. *Journal of Fluids Engineering* **118**, 602–610.

Petersson, P., M. Larson and L. Jönsson (2000). Development of a turbulent jet generated by a mixer in weak co-flow and counter-flow. *International Journal of Heat and Fluid Flow* **21**, 1–10.

Pfleger, D. and S. Becker (2001). Modelling and simulation of the dynamic flow behaviour in a bubble column. *Chemical Engineering Science* **56**, 1737–1747.

Poirier, M.R. (2004). Mixing in srs closure business unit applications. Report WSRC-TR-2004-00153 REv. 0. U.S. Department of Energy.

Rasmussen, Michael R. (1997). Solid dynamics in secondary settling tanks. Series paper no.5. Aalborg University, Hydraulics and Coastal Engineering, Department of Civil Engineering.

Rasmussen, M.R. and T. Larsen (1996). A method for measuring sludge settling characteristics in turbulent flows; water. *Water Research* **30**, 2363–2370.

Rasmussen, M.R., J. Laursen and E. McLean (2004). Development of efficient sludge cones for the concentration of raceway-derived solids in recirculating aquaculture systems. *Proceedings of the 5th International Conference on Recirculating Aquaculture, Roanoke, Virginia, USA, July 22-25, 2004* pp. 400–410.

Reichert, P. (1994). Aquasim - a tool for simulation and data analysis of aquatic systems. *Water Science and Technology* **30**(2), 21–30.

Revstedt, J., L. Fuchs and C. Trägårdh (1998). Large eddy simulations of turbulent flow in a stirred reactor. *Chemical Engineering Science* **53**(24), 4041–4043.

Rhie, C.M. and W.L. Chow (1983). Numerical study of the turbulent flow past and airfoil with trailing edge separation. *AIAA Journal* **21**, 1525–1532.

Rieger, L., G. Koch, M. Kühni, W. Gujer and H. Siegrist (2001). The eawag bio-p module for activated sludge model no. 3. *Water Research* **35**(16), 3887–3903.

Salter, H.E., C.T. Ta, S.K. Ouki and S.C. Williams (2000). Three-dimensional computational fluid dynamic modelling of a facultative lagoon. *Water Science and Technology* **42**(10-11), 335–342.

Sato, Y. and K. Sekoguchi (1975). Liquid velocity distribution in two-phase bubbly flow. *International Journal of Multiphase flow*.

Schiller, L. and A. Naumann (1933). Über die grundlegenden berechnungen bei der schwerkraftaufbereitung. *Vereines Deutscher Ingenieure* **77**, 318–320.

Shilton, A. (2000). Potential application of computational fluid dynamics to pond design. *Water Science and Technology* **42**(10-11), 327–334.

Simiano, M., R. Zboray, F. de Cachard, D. Lakehal and G. Yadigaroglu (2004). Extensive measurements of the hydrodynamic characteristics of large-scale bubble plumes. *Proceedings of the Fifth International Conference on Multiphase flow (ICMF), Yokohama, Japan*.

Simonin, O. and P.L. Viollet (1988). On the computation of turbulent two-phase flows in the eulerian formulation. *Proceedings of the Conference, EUROMECH, Toulouse, France*.

Sincero, A.P. and G.A. Sincero (2003). *Physical-chemical treatment of water and wastewater*. IWA Publishing, CRC Press.

So, S., H. Morikita, S. Takagi and Y. Matsumoto (2003). Laser dopper velocimtry measurement of turbulent bubbly channel flow. *Experimental in Fluids* **92**, 111–122.

Sokolichin, A. and G. Eigenberger (1999). Applicability of the standard $k - \epsilon$ turbulence model to the dynamic simulation of bubble columns: Part i. deatiled numerical simulations. *Chemical Engineering Science* **54**, 2273–2284.

Sokolichin, A., G. Eigenberger, A. Lapin and A. Lübbert (1997). Dynamic numerical simulation of gas-liquid two-phase flows. euler/euler versus euler/lagrange. *Chemical Engineering Science* **52**, 611–626.

Solbakken, Trond and Bjørn H. Hjertager (1998). A computational and experimental study of flowpattern in a pilot and full scale column.

Sozanski, M.M., E.S. Kempa, K. Grocholski and J. Bien (1997). The rheological experiment in sludge properties research. *Water science and Technology* **36**(11), 69–78.

Speziale, C.G. (1991). Analytical methods for the development of reynolds-stress closures in turbulence. *Annual Review of Fluid Mechanics* **23**, 107–157.

Stamou, A., A. Katsiri, I. Mantziaras, K. Boshnakov, B. Koumanova and S. Stoyanov (1999). Modelling of an alternating oxidation ditch system. *Water Science and Technology* **39**(4), 169–176.

Sun, X., S. Kim, T.R. Smith and M. Ishii (2002). Local liquid velcity measurement in air-water bubbly flow. *Experiments in Fluid* **33**, 653–662.

Sundaresan, Sankaran (2000). Modeling the hydrodynamics of multiphase flow reactors: Current status and challenges. *AIChE Journal* **46**(6), 1102–1105.

Suzanne, C., K. Ellingsen, F. Risso and V. Roig (1998). Local measurements in turbulent bubbly flows. *Nuclear Engineering and Design* **184**, 319–327.

Takacs, I., G.G. Patry and D. Nolasco (1991). Dynamic model of the clarification-thickening process. *Water Research* **25**, 1263–1271.

Tchobanoglous, G. and F.L. Burton (2003). *Wastewater engineering: treatment and reuse*. 4th ed.. Metcalf & Eddy.

Thomsen, F. (2000). Modellering af procestanke i rensningsanlæg. integreret 3d model af hydrodynamik og mikrobielle processer i oco-anlæg. Masters thesis. Aalborg University, Department of Civil Engineering.

Tyack, J.N. and R.A. Fenner (1999). Computational fluid dynamics modelling of velocity profiles within a hydrodynamic separator. *Water Science and Technology* **39**(9), 169–176.

Vanderhasselt, A. and P.A. Vanrolleghem (2000). Estimation of sludge sedimentation parameters from single batch settling curves. *Water Research* **34**, 395–406.

Vassallo, P.F. and Ranganathan Kumar (1999). Liquid and gas velocity measurements using ldv in air-water duct flow. *Experiments in Fluids* **19**, 85–92.

Vega, G.P., M.R. Peña, C. Ramirez and D.D. Mara (2003). Application of cfd modelling to study the hydrodynamics of various anaerobic pond configurations. *Water Science and Technology* **48**(2), 163–171.

Versteeg, H.K. and W. Malalasekera (1995). *An introduction to Computational Fluid Dynamics*. 1st ed.. Prentice Hall.

Vesilind, P.A. (1968). Design of prototype thickeners from batch settling tests. *Water Sewage Works* **115**(7), 302–307.

Wang, Tiefeng, Jinfu Wang, Fei Ren and Yong Jin (2003). Application of doppler ultrasound velocimetry in multiphase flow. *Chemical Engineering Journal* **92**, 111–122.

Wichern, M., F. Obenaus, P. Wulf and K.-H. Rosenwinkel (2001). Modelling of full-scale wastewater treatment plants with different treatment processes using the activated sludge model no. 3. *Water science and Technology* **44**(1), 49–56.

Wilcox, D.C. (2000). *Turbulence modeling for CFD*. 2nd ed.. DCW Industries, Inc.

Winther, L., M. Henze, J.J. Linde and H.T. Jensen (1998). *Spildevandsteknik*. Polyteknisk Forlag.

Wood, M.G., P.F. Greenfield, T. Howes and M.R. Johns abd J. Keller (1995). Computational fluid dynamic modelling of wastewater ponds to improve design. *Water Science and Technology* **31**(12), 111–118.

Wörner, M. (2003). A compact introduction to the numerical modeling of multiphase flows.

Wu, J. and L. Pullum (2000). Performance analysis of axial-flow mixing impellers. *AIChE Journal* **46**(3), 489–498.

Zboray, R. and F. de Cachard (2005). Simulating large-scale bubble plumes using various closure and two-phase turbulence models. *Nuclear Engineering and Design* **235**, 867–884.

Zhao, Hong, Oliver J. Hao and Thomas J. McAvoy (1999). Approaches to modeling nutrient dynamics: Asm2, simplified model and neural nets. *Water Science and Technology* **39**(1), 227–234.

Appendix

APPENDIX A
Numerical solution methods

Due to the strong non-linearity of the governing Navier-Stokes equations, analytical solutions are only possible for very simple flow problems. As a consequence other solutions must be applied. Computational Fluid Dynamics (CFD) is such a technique, where the governing equations are solved numerically. The present section concerns the numerical solution of the above-mentioned governing differential equations.

A.1 Terminology

The solution of a given flow problem typically involves several processes:

- Pre-processing
- Solving
- Post-processing

During pre-processing, the geometry is transformed into a computational mesh in a mesher. Also the definition of the flow problem is created during pre-processing, i.e. fluid data, boundary conditions, turbulence model etc. are defined. The computational mesh is in the solver discretized into a system of algebraic equations, usually solved by comprehensive iterative techniques during the solving process. When a converged solution is obtained, a result file is created, and the result are ready for post-processing.

A.2 Discretization

The solver is typically structured on basis of one of three distinct solution techniques:

- The finite difference technique
- The finite volume technique
- The finite element technique

The difference between the three types of solution techniques is mainly to be found within the approximation procedures for the unknown variables and the method of discretizing. Many of the first CFD schemes were built upon the finite difference method, whereas currently the main part of the commercial solvers, including the one used in the present work, CFX-5.7.1 (CFX, 2005), is constructed with basis in the finite volume method. The finite element method has mainly been focused towards structural analysis in e.g. the construction and building sectors. Due to the focus in this thesis, the following brief review will exclusively concern the finite volume method.

A.3 The finite volume method

The finite volume method is build upon control volume integrations, resulting in expressions expressing conservation of fluid variables and flow properties for each finite volume. Thus, balances describing the conservation of e.g. a velocity component can be expressed for every control volume. For details about the finite volume method, see any CFD textbook, e.g. (Patankar, 1980), (Anderson, 1995) and (Versteeg and Malalasekera, 1995).

A.3.1 Basic equations

For the sake of simplicity, the most basic equations will be shown in the case of the finite volume solution of the Navier-stokes equations. The coverage of the review will roughly be pointed towards the actual solution technique used in the commercial CFD model CFX-5.7.1 (CFX, 2005), applied for the work of this thesis.

Again, the governing Navier-Stokes equations for single phase flows are written; this time for a compressible fluid in the absence of external sources:

The continuity equation:

$$\frac{\partial \rho}{\partial t} + \frac{\partial}{\partial x_j}\left(\rho U_j\right) = 0 \tag{A.1}$$

The momentum equations:

$$\frac{\partial}{\partial t}\left(\rho U_i\right) + \frac{\partial}{\partial x_j}\left(\rho U_i U_j\right) = -\frac{\partial p}{\partial x_i} + \frac{\partial}{\partial x_j}\left(\mu\left(\frac{\partial U_i}{\partial x_j} + \frac{\partial U_j}{\partial x_j}\right) - \rho\overline{u_i' u_j'}\right) + S_{U_i} \tag{A.2}$$

As indicated earlier, the main part of the finite volume method is the control volume integration. The integration involves the application of Gauss' divergence theorem (described in any calculus textbook, e.g. (Edwards and Penney, 1994)), in order to convert relevant volume integrals into surface integral. Since no mesh deformation is applied in the present simulations, the time derivatives are moved out of the volume integrals:

The finite volume integral continuity equation:

$$\frac{d}{dt}\int_V \rho dV + \int_S \rho U_j dn_j = 0 \tag{A.3}$$

The finite volume integral momentum equations:

$$\frac{d}{dt}\int_V \rho U_i dV + \int_S \rho U_i U j dn_j = \\ -\int_S P dn_j + \int_S \left(\mu\left(\frac{\partial U_i}{\partial x_j}+\frac{\partial U_j}{\partial x_j}\right) - \rho\overline{u_i' u_j'}\right) dn_j + \int_V S_{U_i} dV \quad \text{(A.4)}$$

where the indexes V and S respectively represent the volume and surface regions over which integration is performed. dn_j is the differential cartesian components of the outward normal surface vector.

After performing the integration, the equations become:

The finite volume integrated continuity equation:

$$V\left(\frac{\rho-\rho^\circ}{\triangle t}\right) + \sum_{ip}\left(\rho U_j \triangle n_j\right)_{ip} = 0 \quad \text{(A.5)}$$

The finite volume integrated momentum equations

$$V\left(\frac{\rho U_i - \rho^\circ U_i^\circ}{\triangle t}\right) + \sum_{ip}\dot{m}_{ip}\left(U_i\right)_{ip} = \\ \sum_{ip}\left(P\triangle n_i\right)_{ip} + \sum_{ip}\left(\left(\mu\left(\frac{\partial U_i}{\partial x_j}+\frac{\partial U_j}{\partial x_i}\right) - \rho\overline{u_i' u_j'}\right)\triangle n_j\right)_{ij} + \overline{S_{U_i}}V \quad \text{(A.6)}$$

here, the subscript ip refers to an integration point (Figure A.1) and $^\circ$ denotes the old time level; the previous time step. $\triangle n_j$ is the discrete outward surface vector. As indicated in equation A.5 and A.6, the summations are performed over all the integration point surrounding a particular node. $\dot{m}_{ip}$ represents the surface mass flow through the finite volume $[kg \cdot s^{-1}]$:

$$\dot{m}_{ip} = \left(\rho U_j \triangle n_j\right)_{ip}^\circ \quad \text{(A.7)}$$

The transient terms in equation A.5 and A.6 are approximated by first order backward euler approximation. The approximation procedure is first order accurate, hence it can suffer from numerical diffusion in time. The approximation is fully implicit and robust, hence obvious advantages are present for choosing this approximation method despite of it limitations with respect to numerical accuracy. Greater accuracy, but less robustness can however be obtained by the application of the second order backward euler approximation, where both values from time steps forward and backward in time are used in the approximation. Details are not shown here, but can be viewed in (CFX, 2005).

A.3.2 Approximation of derivatives

One main property of a discretization scheme is the approximation of the derivatives in the governing equations. The difference in approximation method is in general termed by the way

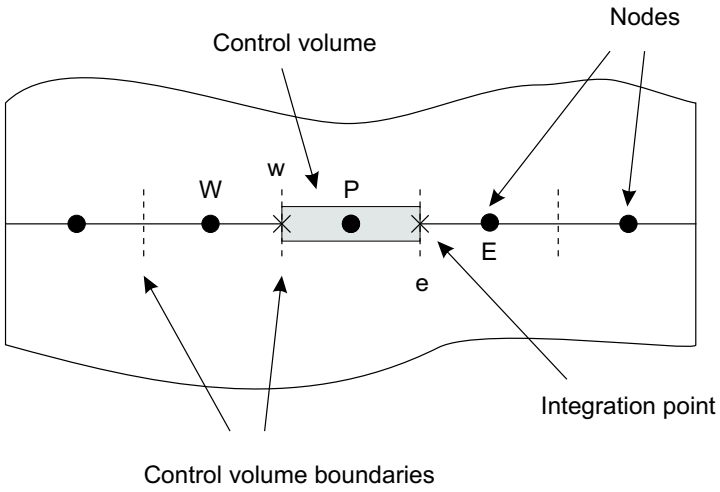

Figure A.1 Definition of control volume, control volume boundaries and node.

interpolation is performed and how many of the neighbouring nodes that are applied in the interpolation procedure. Special attention will be given to the approximation of the advection terms. Usually, the difference schemes are based on a Taylor-expansion, where the accuracy of the approximation method is depending on the number of terms casted away from the expansion. In the present model the following ways of discretising the advection term are available:

- The UPWIND scheme
- The Central Differencing Scheme
- The Numerical Advection Correction Scheme
- The High Resolution Scheme

As a result of equation A.6 terms of the type $(\rho U_i U_j \triangle n_j)_{ip}$ has to be determined at the integration points (the cell faces). With reference to figure A.1, and assuming a convective flow from left to right, expressions approximating the value of ϕ on cell face w can be derived. One simple assumption is that the value of ϕ at the integration point w is equal to the value of ϕ at the upstream located node W. This can be expressed through UPWIND differencing:

$$\phi_w = \phi_W \tag{A.8}$$

As indicated, the UPWIND scheme assigns a high priority to the upstream node P, resulting in a value at the cell face equal to the value at the upstream node. Thus, the downstream node is without any influence on the value of ϕ at the cell faces. The method seems rational in flow dominated by strong convection, whereas the method seems questionable in flow with weak convection. The upside of the method is mainly robustness, whereas the scheme is only first order accurate, making the scheme prone to numerical diffusion.

Opposite to the UPWIND scheme, the Central Differencing Scheme weighs nodes at up- and downstream nodes equal when determining the value of ϕ at the cell faces. Again, ϕ is approximated at cell face w Figure A.1:

$$\phi_w = \frac{\phi_W + \phi_P}{2} \tag{A.9}$$

The main advantage of the Central Differencing Scheme compared to the UPWIND scheme is its nature of second order accuracy, which makes it much less prone to numerical diffusion. The drawback is however that the scheme may suffer from divergence. If the flow is strongly dominated by convection, the scheme is not physical correct, since the downstream node will be weighed too much, resulting in classical problems regarding bad convergence and numerical dispersion in the form of *wiggles*.

In the Numerical Advection Correction Scheme, available in CFX-5.7.1, a blending factor, β, can be specified, determining how much upstream nodes are to be weighed:

$$\phi_{ip} = \phi_{up} + \beta \nabla\phi \cdot \triangle\vec{r} \tag{A.10}$$

where ϕ_{ip} and ϕ_{up} are the variables at the integration point (corresponding to the cell face) and at the upstream node, respectively. β is the weighing factor $[-]$, $\nabla\phi$ is the gradient of ϕ and $\vec{r}$ is the vector from the upstream node to the integration point. With the UPWIND schemes problems with numerical diffusion in mind, the second term might be considered as an anti-diffusive flux added to the UPWIND scheme (CFX, 2005). The advantage compared to the UPWIND scheme is less numerical diffusion, whereas the disadvantages are as discussed under the paragraph concerning the Central Differencing Scheme.

The default advection scheme in CFX-5.7.1 is the High Resolution Scheme. In the High Resolution Scheme, β in equation A.10 is locally computed to be as close to 1 without violating the boundedness criteria, where β is updated as in (Barth and Jesperson, 1989). When the boundedness criteria is violated, the solution might not converge, and if it does, *wiggles* might dominate the results (Versteeg and Malalasekera, 1995). Roughly, the value of β will be close to 1 (equal to second order accuracy) in areas of low variable gradients, whereas β will be adjusted towards 0 in areas with high variable gradients. Hence, the high resolution scheme is a mix of first and second order schemes depending of the nature of the flow.

A.3.3 Pressure-velocity coupling

Since all velocity components occur in both the continuity equation and the momentum equations, the system of of Navier-Stokes equation are not only non-linear, but also strongly coupled. Furthermore, the pressure appears in all the momentum equations all though no separate transport equation exists for the pressure, and if the flow is incompressible, no equation of state can be used to determine the pressure. If the pressure field on the other hand is known and applied to the momentum equation, a solution of flow velocities satisfying the continuity equation would be obtained. In the CFD codes the problem is often solved by introducing an iterative process where the unknown pressure field is obtained through some sort of a guess and correct algorithm.

Usually, all the variables are stored at the centroid of the finite volumes. This can however give rise to problems when the pressure gradients in the momentum equations or the velocity

gradients in the continuity equations are to be found. The problems arise because the discretised form of the pressure and velocity differentials under such configurations result in a relationship between alternate nodes rather than adjacent ones. Thus an envisaged *checkerboard* pressure field (Figure A.2) would during evaluation of the pressure gradients appear as a uniform pressure distribution. This can be illustrated by evaluating the pressure gradient at node P in the x-direction on figure A.2.

$$\frac{\partial p_P}{\partial x} = \frac{p_e - p_w}{\triangle x} = \frac{\frac{p_P + p_E}{2} - \frac{p_W + p_P}{2}}{\triangle x} = \frac{p_E - p_W}{2\triangle x} \tag{A.11}$$

From equation A.11 it is evident that the calculation would result in a zero gradient of the pressure at node P, even though it is apparent that this is not the case. Such nonphysical behavior of the solver is unwanted, and hence procedures to avoid the *checkerboard* problem has been constructed.

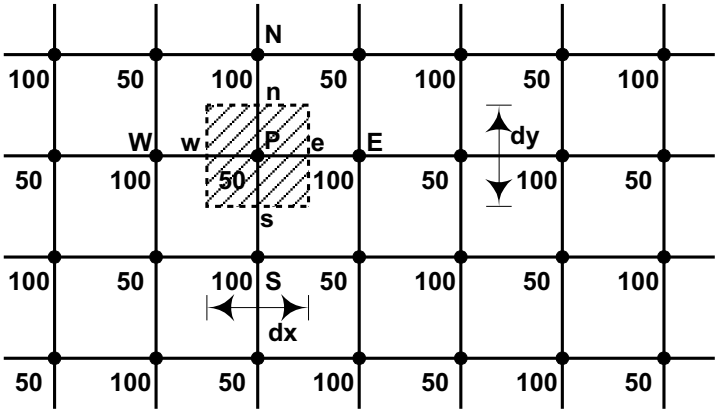

Figure A.2 Checkerboard velocity field

One such preventive tool is the use of a staggered grid (Harlow and Welch, 1965), where the velocities are evaluated at staggered grids centred around the cell faces. The staggered grid is also the basis of the Semi-Implicit Method for Pressure-Linked Equations (SIMPLE) algorithm (Patankar and Spalding, 1972), a *guess and correct* procedure for resolving the pressure-velocity coupling problem. The grid staggering has had a wide success within modelling with structured meshes, whereas the method is not to extend to systems with unstructered meshes. As a consequence, other methods involving collocated grids, where collocated, finite volume centre values are used to calculate the velocities at the finite volume cell faces. The extended Rhie-Chow approximation (Rhie and Chow, 1983) applied in the current version of the CFX software is such a method. In the Rhie-Chow algorithm, checkerboard oscillations are damped by adding a fourth order derivative of the pressure in the continuity equation:

$$\left(\frac{\partial U}{\partial x}\right)_i + \frac{\triangle x^3 A}{4\dot{m}} \left(\frac{\partial^4 p}{\partial x^4}\right)_i = 0, \quad \dot{m} = \rho U_j \triangle n_j \tag{A.12}$$

The above-described continuity equation are written in the one-dimensional case. As indicated above, the fourth order derivative of the pressure works as a dissipative term, levelling out checkerboard oscillations.

A.3.4 Solution of the system of coupled equations

For every node, discretized equations are setup, resulting in a large system of linear algebraic equations. For the fully implicit one-dimensional case with no additional cources as a very simple example, with indexes as presented in figure A.1, the discretized equations are of the following form:

$$a_P\phi_P = a_W\phi_W + a_E\phi_E + a_P^\circ\phi_P^\circ \tag{A.13}$$

Where the ϕ's with indexes P, W, E refer to the directions on figure A.1, and $^\circ$ refer to values from the previous time step. The coefficients, a_i, in equation A.13 consists of everything but the unknown variables.

With basis in equation A.13, the system of linear algebraic equations can be written as:

$$\sum_{nb_i} a_i^{nb}\phi_i = b_i \tag{A.14}$$

Where, a_i^{nb}, in the two-dimensional case can be written as:

$$a_i^{nb} = \begin{vmatrix} a_P & a_E & 0 & 0 & 0 \\ a_W & a_P & a_E & 0 & 0 \\ . & . & . & . & . \\ 0 & 0 & a_W & a_P & a_E \\ 0 & 0 & 0 & a_W & a_P \end{vmatrix}_i^{nb}, \quad \phi_i = \begin{vmatrix} \phi_1 \\ \phi_2 \\ . \\ \phi_{n-1} \\ \phi_n \end{vmatrix}_i, \quad b_i = \begin{vmatrix} a_P^\circ\phi_1^\circ \\ a_P^\circ\phi_2^\circ \\ . \\ a_P^\circ\phi_{n-1}^\circ \\ a_P^\circ\phi_n^\circ \end{vmatrix}_i \tag{A.15}$$

Traditionally, solvers for finding solutions to the system of algebraic linear equations have been built up in a segregated manner, where each equation is solved one at a time. One way to work a segregated solver would be to start with an initial guess, then solve the momentum equations one at a time, before finally correcting the continuity equation with a modified pressure equation. When the cycle is finished it starts over at the new time step or iteration level.

However, for strongly coupled flow systems, a segregated solving method do not converge very efficiently. For this reason coupled solvers, like the one in CFX-5.7.1, have been developed. In a coupled solver all equations are solved at the same time, resulting in one big matrix. The drawback of the coupled solver compared to the segregated one is beside an increased memory demand, primarily due to the increased complexity, making the programming of the scheme more cumbersome. The structure and flow of the coupled solver in the present model can be viewed in figure A.3

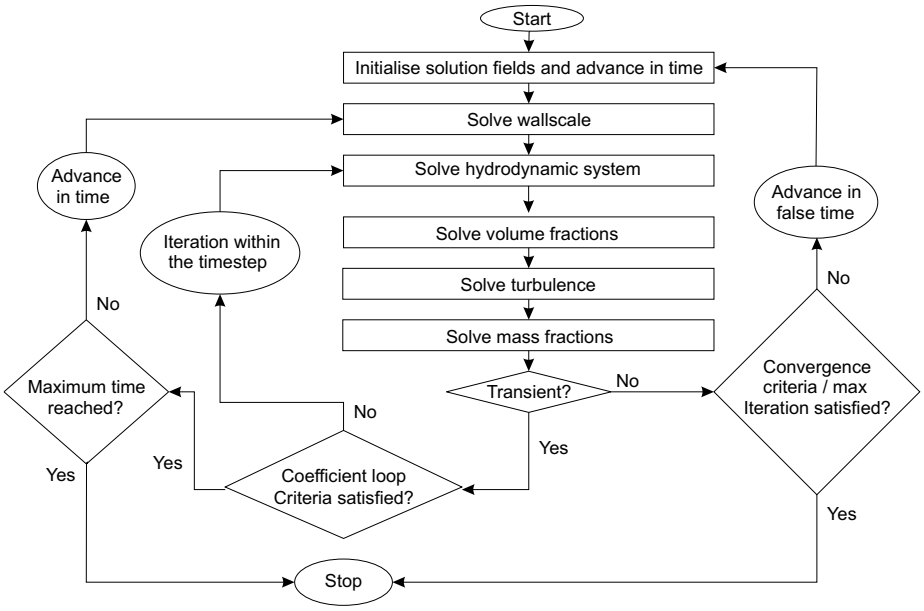

Figure A.3 Outline of the structure and flow of relevant parts of the coupled solver in CFX-5.7.1. From: (CFX, 2005)

A.3.5 Mesh types

As indicated above, the fluid domain is spatially discretised into a number of finite control volumes using a mesh. The control volumes, or cells, can be of different types, where the most common types are listed below:

- Hexahedral shaped
- Tetrahedral shaped
- Prismatic shaped

The different shapes can be viewed in figure A.4.

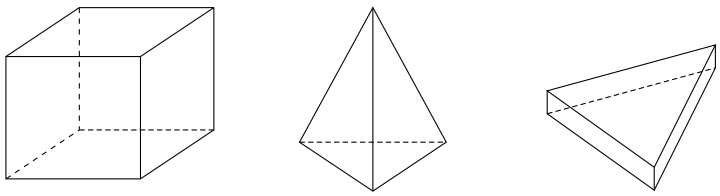

Figure A.4 Outline of different mesh types

The different mesh types have their advantages and drawbacks. The most important property is probably the accuracy of the computation. It turns out that the hexahedral mesh is not well suited for flow where the flow direction is not coinciding with the alignment of the hexahedral mesh (Figure A.5 left). This is because the flow then has to move from one element to two elements downstream, creating a *smearing* effect. However, if the flow direction is coinciding with the alignment of the mesh, the results will not suffer from the above-mentioned *smearing* effect, and hence, the results are likely to be more accurate. With the above-mentioned issue in mind, the design of a structured mesh should as widely as possibly be made such that the main flow direction is normal to the cell faces.

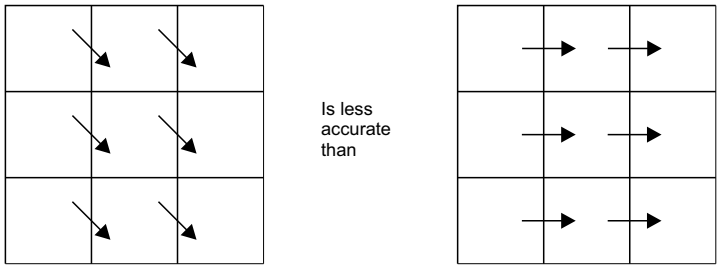

Figure A.5 Structured hexahedral mesh. The flow direction's influence on the accuracy

On the other hand, if an unstructered mesh is applied, the accuracy will not be dependent on the main flow direction (Figure A.6). The disadvantage is however that the unstructured mesh, independently of the flow direction, inherently will possess a certain degree of *smearing* effect. This is because of the nature of the unstructured mesh, where the flow is bound to be split from one element to several other elements downstream, creating the *smearing*. For this reason it is common that more tetrahedral cells are needed to get a certain accuracy of the results in a flow dominated by on flow direction, compared to hexahedral cells.

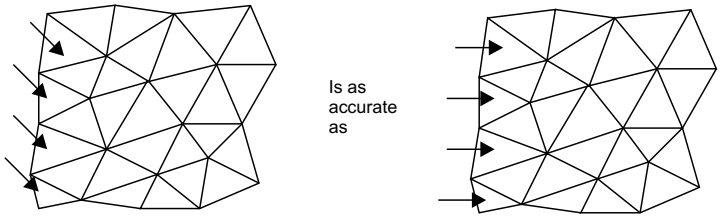

Figure A.6 Unstructured tetrahedral mesh. The flow direction's influence on the accuracy